University of Cyprus, Cyprus

Department of Mechanical and Manufacturing Engineering

Doctoral Thesis

Structure-Based Turbulence models: inclusion of additional physics and development of improved engineering closures.

Author:
Constantinos Panagiotou

Supervisor:
Stavros Kassinos

Prepared with the support of the US Army International Technology Center
and the US Air Force European Office of Aerospace Research
and Development (EOARD) under grant W911NF-11-1-0425.

December 28, 2015

Copyright © Constantinos F. Panagiotou, 2016

APPROVAL PAGE

Doctoral Candidate:
Constantinos F. Panagiotou

Doctoral Thesis Title:
Structure-based turbulence models: inclusion of additional physics and development of improved engineering closures

The present Doctorate Dissertation was submitted in partial fulfillment of the requirements for the Degree of Doctor of Philosophy at the **Department of Mechanical and Manufacturing Engineering** and was approved on the 14th of December of 2015 by the members of the **Doctoral Committee.**

Doctoral Committee:

Research Advisor: Stavros Kassinos, Associate Professor ....
University of Cyprus, MME Department

Committe Member: Andreas Alexandrou, Professor ....
University of Cyprus, MME Department

Committe Member: Dimokratis Grigoriadis, Assistant Professor ....
University of Cyprus, MME Department

Committe Member: Suad Jakirlic, Professor ....
Darmstadt University, GER

Committe Member: Bjorn Anders Petterson Reif, Dr. ....
Norwegian Defence Research, NOR

‘”Learn from yesterday, live for today, hope for tomorrow. The important thing is to not stop questioning.”

Albert Einstein

Περίληψη

Τα δομικά μοντέλα (SBMs) περιέχουν πληροφορίες σχετικά με τη δομή της τύρβης, πληροφορίες οι οποίες χρειάζονται για τη σωστή πρόβλεψη των πολύπλοκων και ασταθών τυρβώδων ροών. Μολονότι τα δομικά μοντέλα έχουν χρησιμοποιηθεί επιτυχώς για την πρόβλεψη κανονικών ροών, η ευρεία χρήση τους σε υπάρχοντες κώδικες έχει εμποδιστεί λόγω της διαφοροποίησής τους από τα συμβατικά μοντέλα. Στην παρούσα διατριβή, ιδιαίτερη προσοχή έχει δοθεί στην ανάπτυξη ενός ακριβούς και ευσταθούς μηχανικού μοντέλου τύρβης. Για τον σκοπό αυτό, αναπτύξαμε τη σύζευξη μεταξύ ενός Αλγεβρικού Δομικού Μοντέλου (ASBM) και του μοντέλου τύρβης των Spalart-Allmaras (SA), η οποία παρέχει σε μηχανικά μοντέλα τη δυνατότητα χρησιμοποίησης πληροφορίας σχετικά με τη δομή της τύρβης. Ταυτόχρονα, για να φέρουμε τη συγκεκριμένη σύζευξη σε ολοκληρωμένη μορφή, η τυρβώδη κινητική ενέργεια και ο ρυθμός απόσβεσής (dissipation) της χρησιμοποιήθηκαν ως οι δύο κλίμακες της τύρβης. Το τελικό μοντέλο δοκιμάστηκε σε μια σειρά από απλές περιπτώσεις, εξασφαλίζοντάς μας ενθαρρυντικά αποτελέσματα.

Παράλληλα, έχουμε αναπτύξει, για πρώτη φορά, ένα δομικό μοντέλο για τη μελέτη της εξέλιξης παθητικών βαθμωτών μεγεθών (passive scalars) σε τυρβώδεις ροές. Τόσο η διασπορά του παθητικού μεγέθους (passive scalar variance), όσο και η μεγάλης κλίμακα κλίση αυτής της διασποράς προτείνονται στην περίπτωση αυτή ως οι δύο κλίμακες που χαρακτηρίζουν τη συγκεκριμένη εξέλιξη. Ακολούθως, το δομικό μοντέλο ενσωματώθηκε στο λεγόμενο 'Σωματιδιακό Μοντέλο Αλληλεπίδρασης' (IPRM), προσάγοντάς το σε μια ολοκληρωμένη μορφή. Ο ρυθμός απόσβεσης της βαθμωτής διασποράς (passive scalar dissipation rate) μοντελοποιείται με βάση τη βαθμωτή διασπορά καθώς και τη μεγάλης κλίμακας ενστροφία (enstrophy). Το εν λόγω μοντέλο δοκιμάστηκε σε ένα σημαντικό αριθμό περιπτώσεων, συμπεριλαμβανομένου διαφόρων παραμορφώσεων του μέσου πεδίου (mean field), σε στάσιμα και περιστρεφόμενα συστήματα αναφοράς, παρέχοντας μας ενθαρρυντικές προβλέψεις. Το ολοκληρωμένο μοντέλο είναι σε καλή συμφωνία με DNS αποτελέσματα της περίπτωσης μέσης διάτμισης στη παρουσία είτε εγκάρσιας είτε διαμηκούς κλίσης του μέσου βαθμωτού πεδίου. Ταυτοχρόνως, το μοντέλο ορθώς προβλέπει την ύπαρξη μεταφοράς διασποράς από τις μεγαλύτερες στις μικρότερες κλίμακες της τύρβης μέσω ενός μηχανισμού γνωστού ως 'μηχανισμός χιονοστιβάδας' σε δισδιάστατη ισοτροπική τυρβώδη ροή.

Τέλος, μελετήσαμε τη δυνατότητα σύζευξης ανάμεσα στο Αλγεβρικό Δομικό Μοντέλο (ASBM) και στο μοντέλο τύρβης SST. Κατά πόσο δηλαδή η σύζευξη αυτή παρέχει ακριβείς προβλέψεις για ροές γύρω από δισδιάστατες αεροτομές και συγκεκριμένα των αεροτομών NACA0015 και VR7. Για τον σκοπό αυτό, διεκπεραιώθηκε επιτυχώς μια σειρά από στατικές προσομοιώσεις για ένα

μεγάλο εύρος γωνιών προσβολής (angle of attacks) και οριακών συνθηκών. Για να διασφαλίσουμε τη σύγκλιση των προσομοιώσεων, αναπτύξαμε ένα αριθμό τεχνικών σταθερότητας, οι οποίες συνέβαλαν στο να επιτευχθούν, για πρώτη φορά, ευσταθείς προβλέψεις για ροές γύρω από αεροτομές οι οποίες υπόκεινται σε μη-στατικές κινήσεις και συγκεκριμένα σε περιοδική περιστροφή γύρω από το αεροδυναμικό τους κέντρο (pitching motions). Για τις στατικές περιπτώσεις, το συζευγμένο μοντέλο παρέχει βελτιωμένα αποτελέσματα σε σχέση με το SST μοντέλο για τους συντελεστές πίεσης και άντωσης (lift). Αντίθετα για τις μη-στατικές περιπτώσεις, το συζευγμένο μοντέλο συστηματικά υπερεκτιμά τη τιμή του συντελεστή άντωσης, γεγονός που οδηγεί στη δραστικότερη μείωση του συντελεστή οπισθέλκουσας από ό,τι αναμενόταν.

Abstract

Structure-based turbulence models (SBM) carry information about the turbulence structure that is needed for the prediction of complex non-equilibrium flows. SBM have been successfully used to predict a number of canonical flows, yet their adoption rate in engineering practice has been relatively low, mainly because of their departure from standard closure formulations, which hinders easy implementation in existing codes. Through this thesis, we demonstrate the coupling between the Algebraic Structured-Based Model (ASBM) and the one-equation Spalart-Allmaras (SA) model, which provides an easy route to bringing structure information in engineering turbulence closures. As the ASBM requires correct predictions of two turbulence scales, which are not taken into account in the SA model, Bradshaw relations and numerical optimizations are used to provide the turbulent kinetic energy and dissipation rate. Attention is paid to the robustness and accuracy of the hybrid model, showing encouraging results for a number of simple test cases.

In addition, a structure-based model has been constructed, for the first time, for the study of passive scalar transport in turbulent flows. The scalar variance and the large-scale scalar gradient variance are proposed as the two turbulence scales needed for closure of the scalar equations in the framework of Interacting Particle Representation Model (IPRM). The scalar dissipation rate is modeled in terms of the scalar variance and the large-scale enstrophy of the velocity field. Model parameters are defined by matching the decay rates in freely isotropic turbulence. The model is validated for a large number of cases of deformation in both fixed and rotating frames, showing encouraging results. The model shows good agreement with DNS results for the case of pure shear flow in the presence of either transverse or streamwise mean scalar gradient, while it correctly predicts the presence of direct cascade for the passive scalar variance in two dimensional isotropic turbulence.

A series of static computations for a wide range of angle of attacks and freestream parameters were performed in order to ascertain the performance of the ASBM-SST hybrid model, for a flow over two types of airfoils, NACA0015 and VR7. In order to obtain smooth, fully converged solutions, we developed advanced filtering schemes suitable for both 2D and 3D highly stretched grids. Additional stability techniques were developed, needed to obtain converged solutions, such as zonal separation and blending methods. For the first time, successful computations were performed for a flow over an airfoil undergoing pitching motions. For all static computations, ASBM-SST provided improved predictions for the lift and pressure coefficient respectively, while in all pitching computations, ASBM-SST showed a strong tendency to overestimate the lift coefficient around the stall angle, yielding a faster decrease of the drag coefficient than it should.

Acknowledgements

Grateful acknowledgment goes to the financial supporters of this work, particularly the US Army International Technology Center and the US Air Force European Office of Aerospace Research and Development (EOARD) under grant W911NF-11-1-0425, and Euratom's research and training programme 2014-2018.

Many thanks go to Prof. Karthik Duraisamy who provided our group with his algorithm during his visit here, a help that was crucial on successfully complete a number of computations. Additionally, his valuable guidance during the first months of familiarization with the code accompanied with the fact that he was always friendly and ready to provide us with any support he was asked during the whole time of this Thesis, is greatly appreciated.
A big thanks goes to Prof. Rene Pecnik, who gave me the encouragement I needed to start numerical development of CFD codes, and for his flawless assistant during his visit here, as well during our collaboration during Summer Program 2012 at the Center of Turbulence Research. Another thanks goes to Dr. John Sullivan for providing us with both experimental and computational data and for making my stay at Center of Turbulence Research even more pleasant with his great sense of humour.

A special thanks goes to Dr. Xavi-Albets Chico, who closely guided me during the first months of my avocation with CFD codes. I would like to also thank Prof. Dimos Grigoriadis for being there for us whenever we needed him, answering our questions. Also, thanks goes to Dr. Hari Radhakrishnan, whose computational knowledges are vital for the functionality of our group. I also want to thank Prof. Evangelos Akyllas for providing me with valuable advice in many different subjects. Thank you to all the other members in the group, namely Dr. Nikolas Kanaris, Pantelis Koullapis, Stratos Fonias and Charalambos Frantzis, for making our co-existence in the same floor very pleasant. I really feel that I have gained some truly good friends there.

In addition, I feel the need to say a big thanks to Fotos Stylianou who I believe will be among the rising stars in the field of turbulence research, and with whom I have interacted the most during my staying in the group. Our scientific discussions, as well as additional discussions for many other subjects, were and will be an inspiration for me.

Lastly, I would like to say a huge thank you to Prof. Stavros Kassinos, who gave me the opportunity to fulfill my PhD under his supervision. Under his guidance, I have acquired valuable knowledge regarding my field of interest. In addition, he gave me the opportunity to travel and meet many important people all around the world.

Dedicated to my parents Foivos and Evangelia, and my sweet Lyzia.

Contents

List of Figures

List of Tables

NONMENCLATURE

Roman Symbols

A_i	Eddy-axis vector.
a_i	Normalized eddy-axis vector, or passive scalar gradient vector.
a^2	passive scalar gradient magnitude squared.
A_{ij}	Eddy-axis tensor.
b_{ij}	Flattening tensor.
C	Anisotropic reference total strain, defined as $\exp(\int S dt)$.
c	Chord length.
c_s	Sound speed.
c_p	Specific heat at constant pressure.
C_D	Drag coefficient.
C_L	Lift coefficient.
C_P	Pressure coefficient.
C_{ij}	Inhomogeneity tensor.
c_{ij}	Normalized inhomogeneity tensor.
D_i	Dimensionality vector property in the particle representation model.
D_{ij}	Dimensionality tensor.
D^s_{ij}	Passive scalar dimensionality tensor.
d	Nearest wall distance.
d_{ij}	Normalized dimensionality tensor.
d^s_{ij}	Passive scalar normalized dimensionality tensor.
dW_i	Stochastic force vector denoting the Wiener process.
e	Total energy, the sum of kinetic and internal energy.
E	Internal energy.
E_κ	Energy spectrum function.
E_ϕ	Passive scalar spectrum function.
E_{ij}	Velocity energy spectrum tensor.
E^m_{ij}	Magnetic energy spectrum tensor.

F_{ij}	Circulicity tensor.
f_{ij}	Normalized circulicity tensor.
G_{ij}	Mean velocity gradient tensor.
$G_{ij}^{v,n,a}$	Effective mean gradient tensor based on **v**, **n**, **a** vectors respectively.
H_{ij}	Rotational transformation tensor.
h_j	Diffusive flux vector.
k_i	Wavenumber vector.
k	Magnitude of wave-vector, reduced frequency.
ℓ_i	Line segment along the axis of independence.
L	Turbulence length scale.
M_∞	Farfield Mach number.
M_{ijpq}	Fourth rank pressure strain-rate tensor.
N_i	Gradient vector property in the particle representation model.
N	Magnitude of the gradient property vector N_i.
n_i	Normalized gradient vector property.
P	Pressure property in the particle representation model.
p	Pressure field.
Pe	Peclet number.
Pr	Prandtl number.
q^2	Twice the turbulent kinetic energy.
q_j	Heat flux vector.
$\tilde{Q}_{ij}$	Scalar gradient co-spectrum.
R_{ij}	Reynolds stress tensor.
r_{ij}	Normalized Reynolds stress tensor.
R	Gas constant.
Re	Reynolds number.
S	Invariant of mean strain rate tensor, or the largest in magnitude eigenvalue of the mean strain rate tensor.
S_{ij}	Mean strain rate tensor.
$S_{ij}^{a,v,n}$	Effective mean strain rate tensor based on **a**,**v**,**n** vectors respectively.
$u_i\phi$	Passive scalar-flux vector.
t	Actual computational time.
T	Temperature variable.
T_∞	Freestream temperature.
u_i	Velocity field.
u_τ	Friction velocity.
U_∞	Magnitude of the freestream velocity.
V_i	Velocity property vector in the particle representation model, or

	Volume of the -i th cell.
W_{ij}	Vorticity spectrum tensor.
W_{ijpqmn}	Sixth moment of eddy-axis vector a_i.
x	Chordwise distance.
X_{ij}	Cross-helicity spectrum tensor.
$Z^{a,n}_{ijpq}$	Fourth moment based on **a**, **n** vectors respectively.

Greek Symbols

α	Blending factor, or angle of attack.
β	Prandtl-Glauert factor.
Γ	Molecular (or thermal) diffusivity.
γ	Jetal-vortex correlation parameter, or ratio of the specific heats.
γ_i	Stropholysis vector.
δ	Boundary layer thickness.
δ_{ij}	Kronecker delta tensor.
ϵ	Energy dissipation rate.
ϵ_ϕ	Scalar dissipation rate.
ϵ_{ijk}	Levi-Civita alternating tensor.
ζ_*	Structure equillibrium parameter.
Θ_i	Eddy effective rotation rate vector.
κ	Turbulent kinetic energy, thermal conductivity.
κ_T	thermal coefficient.
κ_v	von-Karman constant.
λ	Half passive scalar variance.
μ	Dynamic viscosity.
μ_T	Dynamic turbulent (eddy) viscosity.
ν	Kinematic viscosity.
ν_T	Turbulent eddy viscosity.
$\hat{\nu}$	Pseudo-eddy viscosity turbulent variable.
ξ_i	Irrotational vector, defined in equation (3.6).
ρ	Fluid density.
τ	Turbulence time scale.
ϕ	Passive scalar variable, or jetal parameter, or model parameter of the LSE model, defined in Table 3.2.
Φ	Blocking scalar parameter.
χ	Eddy flattening parameter,

	or model parameter of the LSE model, defined in Table 3.2.
ψ_i	Stream-function vector.
ω	Angular velocity of the pitching motion, or specific turbulence dissipation rate.
ω^2	Enstrophy.
Ω_i	Mean vorticity vector.
Ω^*	Rms effective eddy rotation rate.
Ω_i^f	Frame rotation vector.
Ω_i^T	Total rotation vector. given in equation (2.101).
Ω^s	Magnitude of the rotational randomization vector Ω_i^s.
Ω_{ij}	Mean rotation rate tensor.

Abbrevations

ADI	Alternating direction implicit method.
ASBM	Algebraic structure-based model.
AXC	Axisymmetric contraction.
AXE	Axisymmetric expansion.
BSL	Menter baseline turbulence model.
CFD	Computational fluid dynamics.
DRSM	Differential reynolds stress models.
EASM	Explicit algebraic stress model.
EVM	Eddy viscosity model.
IPRM	Interactive particle representation model.
LHS	Left hand side.
MHD	Magnetohydrodynamic.
MPI	Message passing interface.
POD	Proper orthogonal decomposition.
PRM	Particle representation model.
PS	Plane strain.
RANS	Reynolds averaged navier stokes.
RDT	Rapid distortion theory.
RHS	Right hand side.
SA	Spalart-allmaras turbulence model.
SBM	Structure-based model.
SST	Shear stress transport turbulence model.

Other Symbols

$(\,)^{\vert b}$	Conditioned on indicated vector.

$\langle(\,)\vert b\rangle$	Conditioned averaging on a given vector b_i.
$\langle(\,)\rangle$	Scale filtering, also denoted as bracket averaging.
$(\,)'$	Fluctuating quantity based on Reynolds decomposition.
$\overline{(\,)}$	Mean quantity based on Reynolds decomposition.
$(\,)''$	Small-scale fluctuating quantity based on triple decomposition method, or fluctuating quantity based on Favre decomposition.
$\tilde{(\,)}$	Large-scale fluctuating quantity, Favre averaging, anisotropic part of the tensorial variable.
$\hat{(\,)}$	Fourier mode of a turbulent variable.
$(\,)^+$	Variable given in wall units, or normalized by friction velocity.
$(\,)_{rms}$	Root-mean-square of a variable.
$(\,)_{press}$	Pressure part of a variable.

Chapter 1

Introduction

1.1 Background

Despite substantial progress in aerodynamics during the last century, knowledge about the physics of turbulent flows is still deficient. In fact, turbulence remains one of the great challenges of engineering and natural sciences, a fact which is particularly true for the turbulence near solid surfaces. For flows at very high Reynolds number (e.g. aircrafts, wind turbines etc.) the geometrical scales of the flow are several orders of magnitudes larger compare to the smallest turbulence scales, which influence pressure drag only indirectly by influencing separation. Since the full computation of such flows by solving directly the Navier Stokes equations is being out of reach for the foreseenable future, scientists and engineers must develop and use models in order to represent the effect of turbulence on the mean flow. Consequently, nowdays the computation of turbulent flows in industrial design and engineering applications relies heavily on the use of simple turbulence models in the Reynolds-Averaged Navier Stokes (RANS) equations. This has been a long-standing trend and is sustained by practical considerations.

The class of RANS models most often used in engineering applications is that of Eddy Viscosity Models (EVM). One of the most popular EVM is the Spalart-Allmaras (SA) one-equation model [1]. The SA model is often favored by practicing engineers because it exhibits superior robustness, low CPU time requirements and substantially lower sensitivity to grid resolution compared to two-equation models. On the other hand, one has to recognize that, despite its computational and implementational attractiveness, the eddy viscosity assumption is also the source of some of the most important performance limitations. For example, like other EVM, the SA model fails to capture important flow features, such as turbulence anisotropy or the effects of mean or system rotation.

The widespread use of EVM in engineering practice, despite their inherent limitations, is sustained by the lack of clearly superior alternatives that would justify the extra computational complexity required. For example, efforts to circumvent the limitations of the eddy viscosity assumption usually proceed along one of three paths. One path is that of Differential Reynolds Stress Models (DRSM), where the closure carries the Reynolds Stress Transport (RST) equations. DRSM closures allow the prediction of stress anisotropy, account for history effects on the anisotropy, and afford improved handling of rotational and curvature effects. However, robustness issues and performance inconsistencies have prevented this class of models from penetrating further into the mainstream of engineering practice. For example, a number of large European research projects were aimed at introducing DRSM models in industrial codes (FLOMANIA and ATAAC), but did not lead to a significant change in industrial CFD practice. A second common choice is to use one of the Explicit Algebraic Reynolds Stress Models (EARSM), which are based on a weak equilibrium assumption that leads to a constitutive equation between the turbulence stresses and the mean deformation field. In addition, EARSM involve the transport of two turbulence scales. The anisotropy equilibrium assumption that is inherent to EARSM has been a known source of performance limitations in complex non-equilibrium flows. A third option is resort to Nonlinear Eddy Viscosity Models (NLEVM), where the stress-strain relation is extended with additional terms. NLEVM and EARSM models can be made to show sensitivity to curvature and rotation, but cannot handle consistently complex rotational effects.

A common feature of the classical closure approaches described so far is the assumption that all key information about the turbulence is contained in the scales of the turbulence and in the turbulence stress tensor. However, one should consider that the turbulent stresses contain information only about the componentality of the turbulence, i.e. about the directions in which the turbulence fluctuations associated with large-scale eddies are most energetic. Thus, traditional closures do not take into account the morphology of the energy-containing eddies. Yet, eddies tend to organize spatially the fluctuating motion in their vicinity. In doing so, they eliminate gradients of fluctuation fields in some directions (those in which the spatial extent of the structures is significant) and enhance gradients in other directions (those in which the extent of the structures is short). Thus, associated with each eddy are local axes of dependence and independence that determine the dimensionality of the local turbulence structure. This structure dimensionality information is complementary to the componentality information contained in the Reynolds stresses, and as Kassinos and Reynolds [2, 3] have shown it is dynamically important.

Reynolds and Kassinos identified this common limitation of classical closures and introduced an alternative modeling approach, the Structure-Based Models (SBM), which today provide a promising route for devising improved RANS turbulence closures. The main feature of this type of models is that they provide a complete tensorial representation of turbulence structure. SBM can be envisioned in two complementary ways. The first is to use directly the structure tensors that characterize the morphology of the turbulence. The transport of these tensors is governed by exact partial differential equations that have been derived and this provides the starting point for differential SBMs, such as the Q-model [4]. In general, differential SBMs involve a large number of transport equations, which can be unattractive for routine engineering computations. Hence, a second way is to assume that the turbulence can be mimicked by ensembles of simplified structures, hypothetical 2D eddies, whose axis of independence is given by an eddy-axis vector. The orientation of the eddy-axis can be obtained through model equations, either differential or algebraic. These eddies are 2D, but they can be jetal 2D-1C (motion only along the eddy-axis), vortical 2D-2C (motion in planes normal to the eddy-axis) or helical 2D-3C (correlated motion along and normal to the eddy axis). Averaging over ensembles of eddies produces statistical quantities representative of the field and allows one to relate the Reynolds stress tensor to the statistics of the turbulence structure.[2, 5] The Algebraic Structure-Based Model (ASBM)[6] is an engineering structure-based model that follows this second approach. It is a fully realizable two-equation structure-aware model that provides the full Reynolds stress tensor.

In the ASBM, the eddy-axis is obtained through an algebraic equation that takes into account asymptotic rapid distortion theory (RDT) limits. Under RDT, the governing equations are linearized by neglecting products of turbulent fluctuations. This linearization is based on the assumption that the turbulence does not have time to interact with itself because the eddy turnover timescale is much longer than that of the mean distortion. Near solid boundaries, the model is sensitized to the wall-blocking effect through an elliptic relaxation equation that is based on the physical argument that eddies must be realigned parallel to the wall as the wall is approached. While the ASBM comes with its own transport equations for the turbulence scales (notably the Large-Scale Enstrophy Equation LSE),[7] it has recently been successfully coupled with the scale equations of popular Eddy-Viscosity Models (EVM), such as the v^2-f,[8] the κ-ε-ϕ-α [9] and the κ-ω models.[6, 8, 10]

1.2 Motivation

The work presented in this thesis has been motivated by the current status of Structure-Based Models (SBMs). The formulation of the Algebraic Structure-Based Model (ASBM) has provided an engineering simplification of the general Structure-Based Modeling (SBM) framework, but its impact has so far been limited by two constraints. The first is that until recently, ASBM had been applied only to canonical flows, such as fully-developed channel flows, turbulent boundary layers over flat plates and the backward facing step. Thus, we were motivated to explore the performance of the closure in more complex two-dimensional (2D) flows, such as flows in an asymmetric diffuser, smooth hills with and without flow control and airfoils. These are flows where adverse and favorable pressure gradients have a significant effect on flow development. The second constraint is related to a number of stability issues associated to the ASBM closure. These issues have become apparent to us during previous unpublished work. Thus, we have put significant effort into identifying the root causes of these stability issues and into increasing the overall stability of the model.

Work has also been directed at enriching and improving the physical content of SBMs. For example, the structural anisotropy of turbulence is known to have a significant effect on scalar transport. Hence, the expectation has been that SBMs could provide improved predictions for passive scalar transport and heat transfer phenomena. However, until now this potential has remained largely unexplored as the main development effort has been directed towards devising engineering simplifications of the SBM framework, such as the ASBM. In this work, we have taken the first step into exploring this potential by using the IPRM framework to formulate a structure-based model for passive scalar transport. In the same line of fundamental work, we constructed a differential SBM providing better predictions for homogeneous turbulence subjected to weak irrotational deformations, a category of flows for which the original eddy-axis based differential SBM is known to exhibit poor performance.

1.3 Passive scalars

The terminology passive it refers to the simplified case where a scalar is in such low concentration so that does not influence the evolution of the fluid. The study of the passive scalars is of great importance in engineering applications including pollution contaminants, temperature or elements concentration, since this simplification is a first step in understanding scalar behavior in these applications. The significance of this idealized case has motivated a lot of researchers in trying to construct a theory which would provide a starting point for these studies. The predominant theory for the description of the energy statistics in a turbulent flow in high Reynolds numbers is based on Kolmogorov's [11] idea of local isotropy, meaning that the small scales are isotropic, independently of the presence of any large scale anisotropies. In analogy to the velocity field case, similar arguments were extended to account also passive scalar statistics by Obuknov [12] and Corrsin [13] for a scalar in the presence of homogeneous and isotropic turbulent flow field at high Reynolds and Peclet numbers. The elegance of the formulation based on local isotropy, a case at which the transport equations are severely simplified, have motivated a large amount of works [14, 15], and similarity solutions for both scalar and velocity fields have been obtained, even in the presence of mean scalar gradients [16].

However, this aspect has undergone drastic reinterpretation from a number of works reported in literature [17, 18] which denote the impact of the large scale turbulent structures at the small scales. One of the key quantities characterizing this impact is the dissipation rate of the scalar variance. Specifically, the majority of current models for passive scalar transport require knowledge of both the turbulence and the scalar dissipation time scales, since the initial conditions of these time scales and their ratio can severely affect the evolution of the turbulent scalar field [19]. An elegant approach used by many workers is to solve directly for the scalar dissipation rate through the use of empirical equations [20, 21]. However, even though the terms that occur in the exact equation are related to the small-scale processes, it is common that these terms are modeled solely based on large-scale quantities.
Reynolds et al. [7] developed a structure-based model for the velocity field by modeling the small-scale processes based on a set of one-point tensors, which contain physical information with regards to the large-scale structure of the turbulent field. All of these yielding promising results. Thus, part of this work is motivated by the belief that a good turbulence model for the passive scalar transport must be build based on structural information about the most energetic eddies. Hence, the most immediate need is for a robust homogeneous model, and that is the focus of this work.

1.4 Objectives

Based on the above considerations, we have devoted large effort to the fundamental development of Structure Based models, in order to extend the range of their applicability. Thus, the main objective is to construct a one-point, passive scalar model for homogeneous turbulence which incorporates information about turbulent structure through the use of tensors related to turbulent structure, called *structure tensors*. The model matches the decay rates in freely isotropic turbulence, while it provides excellent predictions for isotropic turbulence in the presence of mean scalar gradient and for the case of pure homogeneous shear flow. Therefore, the proposed model may serve as the backbone of a more general one-point inhomogeneous model. Another goal of the current thesis is the engineering development of the ASBM for practical applications. This development deals with the known stability issues of the closure, while it proposes a new coupling of ASBM, that with SA. Moreover, another objective was to investigate the performance of the structure-based models in weakly compressible flows. The test cases that were chosen are those of flows passing over smooth airfoil surfaces at low Mach number.

1.5 Contributions

The most important contributions of the current work are the following:

- The development, for the first time, of a complete structure-based model for the study of the transport of passive scalar, consisting of two different types of models. An extended IPRM model which provides turbulent statistics of a passive scalar field in homogeneous turbulence. In order to "feed" the extended IPRM model with suitable turbulence scales, a two-equation model based on the triple decomposition scheme is constructed, sensitized to the anisotropy of the turbulent field. The complete model has been validated in a large number of test cases, involving either shear flows or irrotational deformations, at stationary and rotating frames. The closure was tested at both the RDT and slow limit, providing very promising results.

- The construction of a new stochastic structure-based model for the case of homogeneous turbulence. This scheme revises the main issues that were encountered in the previous version, as described in the work of Kassinos and Reynolds [22]. The proposed model incorporates additional physical information through the use of more sophisticated expressions for the turbulent parameters. It provides improved results compare to the previous model for all the irrotational benchmark cases, accompanied with a more consistent physical behavior. In addition, the model shows excellent agreement at the limit of rapid deformations.

- We demonstrate, for the first time, a coupling between an algebraic simplification of the structure-based models, called Algebraic Structured-Based Model (ASBM), and an one-equation turbulence model, particularly the Spalart-Allmaras (SA) model. The current coupling provides an easy route to bringing structure information in engineering turbulence closures. As the ASBM requires correct predictions of two turbulence scales, which are not taken into account in the SA model, Bradshaw relations and numerical optimizations are used to provide the turbulent kinetic energy and dissipation rate. Attention is paid to the robustness and accuracy of the hybrid model, showing encouraging results for a number of two-dimensional test cases.

- The demonstration that a coupling of the Algebraic Structure-Based Model with the SST model has the potential to lead to improved aerodynamic computations. The coupled closure has been implemented in a compressible solver and validated against experiments for low Mach number flows over rotor-craft airfoils. A number of stability techniques were constructed and implemented in the solver in order to improve the stability of the closure, leading to converged solutions for pitching cases, for the first time. For all the static cases considered, the ASBM provides notably improved predictions for the lift forces when compared to the SST closure.

1.6 Overview

Chapter 2 provides an overview of the mathematical background upon which the developments in the subsequent chapters are built. In Chapter 3, we discuss the development of a structure-based model for the passive scalar field. A stochastic generalization, as discussed in Arnold's book [23] and in Kassinos and Reynolds [24], is used to extend the original IPRM so as to account for passive scalar statistics in homogeneous turbulence. In order to bring the IPRM model into a closed form, a set of transport equations for the passive scalar turbulence scales is derived based on the triple decomposition method. Accordingly, a term-by-term modelling process is discussed for the simplified case of homogeneous turbulence, accompanied by physical justifications. The modeling parameters are evaluated by matching simple isotropic cases in the absence of mean gradients, whereas the performance of the model has been ascertained through comparison between model predictions with DNS, LES and experimental results for more complex homogeneous flows involving imposed mean deformations. Some preliminary results are also shown for the newly proposed coupling of the structure-based scalar model with the algebraic structure based model (ASBM). In this case, the ASBM provides the structure tensors and their products that are needed in the scalar model.

In Chapter 4, we develop a new stochastic extension of the original differential structure-based model of Kassinos and Reynolds [2]. We discuss the derivation of modified transport equations in respect to an earlier stochastic extension of the model [24] and we focus on physical considerations. Subsequently, the performance of the proposed model is tested on flows that are subjected to both rapid and slow deformations. The next two chapters are devoted to the description of the coupling procedure between the ASBM and the one-equation SA model. The SA model is implemented in an incompressible solver and its validity is verified through a series of 2D flows, for which DNS and experimental data are available.

Consequently, we provide a brief and comprehensive summary of a suitable set of algebraic expressions, used to couple the SA model with the ASBM closure. Concurrently, known refinement issues from prior couplings of ASBM with Eddy Viscosity Models are examined one by one, leading to useful outcomes. The validity of the proposed ASBM-SA model is tested for the same benchmark cases. The closure preserves the superior robustness of the SA closure, providing smooth converged solutions with a good convergence rate. It has been able to capture effectively the turbulence anisotropy, whereas it remains fully realizable in all test cases.

Chapter 7 investigates the potential to extend ASBM applicability to weakly compressible flows. The algebraic model is implemented in a compressible solver and combined with the SST model. A discussion about the stability treatment of the hybrid model is presented. Static and dynamic computations are performed for flows over different types of rotorcraft airfoils at low Mach number, for which the compressibility effects are weak. Comparison is made with experimental works which reveals the ability of ASBM to provide notably improved predictions for the lift forces when compared to the SST closure.

Chapter 2

Mathematical Background

2.1 Cartesian tensors.

2.1.1 Outline

This chapter introduces the mathematical tools that will be needed in subsequent chapters. After introducing the Cartesian tensors accompanied with their basic properties, the basic conservation laws are introduced in Section 2.3. In Section 2.4, two decomposition methods, which are excessively used in this thesis are mentioned, whereas in Section 2.5 we introduce the governing equations for incompressible and compressible flows. Next, in Section 2.6 we provide details for a number of popular Eddy Viscosity Models that have been used in this thesis to perform numerical simulations. In Section 3.2.2, we introduce the one-point structure tensors, while in Sections 2.8-2.10 we give details for three different structure-based models that will be used as the starting point for the developments we present in this work.

Notation

Throughout the thesis, the Einstein summation convention is used. Thus, repeated indices imply summation. For example,

$$a_{ij}b_j = a_{i1}b_1 + a_{i2}b_2 + a_{i3}b_3 \,. \tag{2.1}$$

The general definition and laws of operation of Cartesian tensors are given below:

Definition The tensor **A**, of rank n, is a quantity defined by 3^n components which may be written $A_{ijk} \dots n$, which under rotation is linearly transformed to a new coordinate frame through the identity

$$\bar{A}_{pq\dots t} = l_{ip} l_{jq} \dots l_{nt} A_{ij\dots n} \,, \tag{2.2}$$

where l_{ij} is the orthonormal rotation matrix.

Symmetries If interchange of two of the indices does not change the value of the component, then the tensor is said to be symmetric with respect to these indices. If the absolute value is unchanged but the sign is reversed, then the tensor is antisymmetric with respect to the indices.

Contraction The 3^{n-2} quantities formed by identifying two of the indices of an n^{th} rank tensor and invoking the summation convention are components of a tensor of order $n-2$.

Scalar Multiplication If α is any scalar, **A** and **B** are tensors of the same order, they obey to the following laws

$$\alpha \mathbf{A} = \mathbf{A} \alpha \,, \qquad \alpha(\mathbf{A} + \mathbf{B}) = \alpha \mathbf{A} + \alpha \mathbf{B} \,. \tag{2.3}$$

Addition If **A**, **B** and **C** are tensors of the same order, they obey to the following laws

$$\mathbf{A} + \mathbf{B} = \mathbf{B} + \mathbf{A} \,, \qquad \mathbf{A}(\mathbf{B} + \mathbf{C}) = \mathbf{AB} + \mathbf{AC} \,. \tag{2.4}$$

Multiplication If **A** and **B** are tensors of order n and m respectively, the product **A B** yields to a tensor of order $n+m$.

Isotropic tensors Isotropic tensors are those tensors whose components are unchanged by rotation of the frame of reference. The fundamental second order isotropic tensor, called Kronecker delta, given by

$$\delta_{ij} = \begin{cases} 1 & i = j, \\ 0 & i \neq j, \end{cases}$$

whereas the basic third order isotropic tensor, also called Levi-Civita tensor, is expressed as

$$\epsilon_{ijk} = \begin{cases} 1 & \text{if } (i,j,k) \text{ is a cyclic permutation of } (1{,}2{,}3)\,, \\ -1 & \text{if } (i,j,k) \text{ is an anti-cyclic permutation of } (1{,}2{,}3)\,, \\ 0 & \text{if any of } i,j,k \text{ are equal.} \end{cases}$$

A useful identity is given by

$$\epsilon_{kij}\epsilon_{klm} = \delta_{il}\delta_{jm} - \delta_{im}\delta_{jl}\,, \tag{2.5}$$

which can be extracted through the following generalized expression

$$\epsilon_{ijk}\epsilon_{lmn} = det \begin{pmatrix} \delta_{il} & \delta_{im} & \delta_{in} \\ \delta_{jl} & \delta_{jm} & \delta_{jn} \\ \delta_{kl} & \delta_{km} & \delta_{kn} \end{pmatrix}\,,$$

or

$$\epsilon_{ijk}\epsilon_{lmn} = \delta_{il}\delta_{jm}\delta_{kn} + \delta_{im}\delta_{jn}\delta_{kl} + \delta_{in}\delta_{jl}\delta_{km} - \delta_{il}\delta_{jn}\delta_{km} - \delta_{im}\delta_{jl}\delta_{kn} - \delta_{in}\delta_{jm}\delta_{kl}\,, \tag{2.6}$$

2.1.2 Invariants

The invariants of a tensor are variables that are independent of the coordinate system, insensitive to rotation. The theory of invariants states that there exist three invariants of a second order tensor A_{ij}

$$I = A_{jj}, \quad II = \frac{1}{2!}(A_{ii}A_{jj} - A_{ij}A_{ji}), \quad III = \frac{1}{3!}(A_{ii}A_{jj}A_{kk} - 3A_{ii}A_{jk}A_{kj} + 2A_{ij}A_{jk}A_{ki})\,. \tag{2.7}$$

An important theorem that is deduced from this theory is the *Cayley-Hamilton theorem.* This theorem states that a second order tensor satisfies its own characteristic equation, given by

$$A^3_{ij} - IA^2_{ij} + IIA_{ij} - III\delta_{ij} = 0\,, \tag{2.8}$$

where $A^2_{ij} = A_{ik}A_{kj}$ and $A^3_{ij} = A^2_{ik}A_{kj}$.

2.2 Equivalence between Euler and Langrangian coordinates.

At some instant $t = 0$ a certain fluid particle is at a position ξ_i and at a later time the same particle is at position x_i , where x_i is a function of t and the initial position ξ_i

$$x_i = x_i(\xi_i, t)\,. \tag{2.9}$$

The initial coordinates ξ_i are the *material coordinates*, also called *Lagrangian coordinates*, whereas x_i are the *spatial coordinates*, or *Eulerian coordinates*, also called position or space. Eq. (2.9) is a curve and these type of curves are called *particle paths.* Any property of the fluid, say F may be followed along the particle path. The equivalence between the material and spatial description is depicted by

$$F(x_i, t) = F[\xi_i(x_i, t), t]\,. \tag{2.10}$$

Associated with the above descriptions are two time derivatives, denoted by

$$\frac{\partial}{\partial t} = (\frac{\partial}{\partial t})_x\,, \qquad \frac{d}{dt} = (\frac{\partial}{\partial t})_\xi\,. \tag{2.11}$$

Thus $\frac{\partial F}{\partial t}$ is the rate of change of F as observed at a fixed point x_i, whereas $\frac{dF}{dt}$ is the rate of change as observed when moving with the particle, also called *material derivative.* The connection between the two derivatives is established by

$$\begin{aligned}\frac{dF}{dt} &= \frac{\partial}{\partial t}F(\xi_i, t) = \frac{d}{dt}F(x_i, t) \\ &= \frac{\partial F}{\partial x_i}(\frac{\partial x_i}{\partial t})_\xi + (\frac{\partial F}{\partial t})_{x_i} = v_i\frac{\partial F}{\partial x_i} + \frac{\partial F}{\partial t}\,,\end{aligned} \tag{2.12}$$

where $v_i = \frac{dx_i}{dt}$.

2.3 Conservation laws

Let $\rho(x_i, t)$ be the mass per unit volume at position x_i and time t. Also let's assume $\Im$ being the mass m of a volume V. Use of Reynolds theorem can leads to the integral form of mass conservation law

$$\frac{dm}{dt} = \int\int\int_{V(t)} \{\frac{\partial \rho}{dt} + \frac{\partial(\rho v_i)}{\partial x_i}\} dV\,, \tag{2.13}$$

or to the differential form

$$\frac{\partial \rho}{\partial t} + \frac{\partial(\rho v_i)}{\partial x_i} = 0\,. \tag{2.14}$$

The forces acting on an element can be separated into two kinds. The *external or body forces* per unit volume denoted by f_i, such as gravitational or electromagnetic forces, and the *internal forces* per unit area denoted by t_i, which act on the fluid element through its bounding element.

The principle of the momentum conservation states that these two kinds of forces define the rate of change of the linear momentum of the volume V, that is

$$\frac{d}{dt}\int\int\int_{V(t)} \rho v_i dV = \int\int\int_{V(t)} \rho f_i dV + \int\int_{S(t)} t_i dS\,. \tag{2.15}$$

Denoting by n_i the outward unit vector of the element surface and using the identity

$$t_i = n_i T_{ij}\,, \tag{2.16}$$

yields the integral form of the conservation law for an arbitrary stress tensor T_{ij}

$$\frac{d}{dt}\int\int\int_{V(t)} \rho v_i dV = \int\int\int_{V(t)} \{\rho f_i + \frac{\partial T_{ji}}{\partial x_j}\} dV\,, \tag{2.17}$$

or to the differential form, also called Cauchy's equation of motion

$$\frac{d(\rho v_i)}{dt} = \rho f_i + \frac{\partial T_{ji}}{\partial x_j} \,. \tag{2.18}$$

The stress tensor may always be written

$$T_{ij} = -p\delta_{ij} + \tau_{ij} \,, \tag{2.19}$$

where p is the pressure τ_{ij} is the viscous stress tensor.

Assuming Newtonian fluid, the viscous stress depends linearly on strain rate, that is

$$\tau_{ij} = \mu(\frac{\partial u_i}{\partial x_j} + \frac{\partial u_j}{\partial x_i}) + \lambda[\frac{\partial u_q}{\partial x_q}]\delta_{ij} \,, \tag{2.20}$$

where λ and μ are the two coefficients of viscosity. Based on Stokes assumption $\lambda = -2\mu/3$, whereas the μ is estimated through the Sutherland equation

$$\mu = C_1 \frac{T^{3/2}}{T + C_2} \,, \tag{2.21}$$

where $C_1 = 1.458 \times 10^{-6}\ kg\, m^2/(s\sqrt{^oK})$ and $C_2 = 110.4\ ^o K$ for air at moderate temperatures. The velocity gradient tensor can be written as the sum of symmetric and antisymmetric parts

$$\frac{\partial u_i}{\partial x_j} = \frac{1}{2}(\frac{\partial u_i}{\partial x_j} + \frac{\partial u_j}{\partial x_i}) + \frac{1}{2}(\frac{\partial u_i}{\partial x_j} - \frac{\partial u_j}{\partial x_i}) \,, \qquad \frac{\partial u_i}{\partial x_j} = S_{ij} + \Omega_{ij} \,, \tag{2.22}$$

where S_{ij} is the symmetric strain rate tensor and Ω_{ij} is the antisymmetric rotation rate tensor. The latter tensor is related to the vorticity vector through the identities

$$\Omega_{ts} = \frac{1}{2}\omega_m \epsilon_{mst} \,, \quad \omega_i = \epsilon_{ist}\Omega_{ts} \,. \tag{2.23}$$

The law of energy conservation states that the increase of total energy (kinetic and internal) in a material volume is the sum of the heat transfered and the work done on the volume

$$\frac{d}{dt}\int\int\int_{V(t)}\rho(\frac{1}{2}v^2+E)dV=\int\int\int_{V(t)}[\rho f_i v_i+\frac{\partial(v_iT_{ji})}{\partial x_j}-\frac{\partial q_i}{\partial x_i}]dV\,, \tag{2.24}$$

where q_i is defined by the Fourier law of heat conduction

$$q_k=-\kappa_T\frac{\partial T}{\partial x_k},\quad \kappa_T\qquad \text{is coefficient of thermal conductivity.} \tag{2.25}$$

Another important expression is the conservation equation of a passive, conservative scalar, say ϕ. Passive means that scalar does not influence the properties of the flow and conservative refers to the absence of sink/source terms at the RHS. The integral form is given by

$$\frac{d}{dt}\int\int\int_{V(t)}(\rho\phi)dV=\int\int\int_{V(t)}[-\frac{\partial h_j}{\partial x_j}]dV\,, \tag{2.26}$$

where h_j is the diffusive flux vector.

2.4 Decomposition methods.

The most common decomposition method is the procedure first introduced by Reynolds [25], in which an instantaneous variable is decomposed into a mean and a fluctuating part through time (or spatial averaging)

$$u_i=\overline{u}_i+u_i'\,. \tag{2.27}$$

Additionally, Reynolds [26] introduced an averaging process (denoted by angled brackets) which extracts the large-coherent motions from the fluctuating field. Applying this approach leads to the triple decomposition of an instantaneous variable. It is decomposed into a mean part, denoted by an overbar, and a fluctuating part that consists of a large-scale part, denoted by a tilde, corresponding to the large-scale coherent motions and a small-scale part which corresponds to small-scale fluctuations, denoted by a double prime.

Thus, the contributions to an instantaneous quantity β_i, are

$$\beta_i=\bar{\beta}_i+\beta_i'=\bar{\beta}_i+\tilde{\beta}_i+\beta_i''\,, \tag{2.28}$$

and satisfy the following averaging properties,

$$\langle \beta_i \rangle = \bar{\beta}_i + \tilde{\beta}_i \,, \tag{2.29a}$$

$$\overline{\langle \beta_i \rangle} = \bar{\beta}_i \,, \tag{2.29b}$$

$$\overline{\tilde{\beta}_i} = 0 \,. \tag{2.29c}$$

It is also assumed that the commutative property is satisfied between the averaging and the differentiation operators and that contribution at different scales are not correlated,

$$\overline{\tilde{\beta}_i \beta''_j} = 0, \quad \overline{\bar{\beta}_i \tilde{\beta}_j} = \bar{\beta}_i \overline{\tilde{\beta}_j} = 0, \quad \langle \tilde{\beta}_i \beta''_j \rangle = \tilde{\beta}_i \langle \beta''_j \rangle = 0 \,. \tag{2.30}$$

2.5 Governing equations.

2.5.1 Incompressible flows.

For incompressible flows, the conservation laws are summarized as:

$$\frac{\partial u_i}{\partial t} + u_j \frac{\partial u_i}{\partial x_j} = -\frac{1}{\rho}\frac{\partial p}{\partial x_i} + \frac{\mu}{\rho}\frac{\partial^2 u_i}{\partial x_j^2} \,, \tag{2.31a}$$

$$\frac{\partial u_i}{\partial x_i} = 0 \,, \tag{2.31b}$$

$$\frac{\partial \phi}{\partial t} + u_i \frac{\partial \phi}{\partial x_i} = -\Gamma \frac{\partial^2 \phi}{\partial x_i^2} \,, \tag{2.31c}$$

$$\tau_{ij} = \mu\left(\frac{\partial u_i}{\partial x_j} + \frac{\partial u_j}{\partial x_i}\right) , \tag{2.31d}$$

where the pressure p can be extracted by combining eqs. (2.31a), (2.31b). Since pressure can be solely determined through the momentum, the energy equation is not considered, while a constant dynamical viscosity is assumed.

2.5.2 Compressible flows.

For compressible flows, the conservation laws take the following forms

$$
\begin{aligned}
\frac{\partial \rho}{\partial t} + \frac{\partial(\rho u_i)}{\partial x_i} &= 0\,, \\
\frac{\partial(\rho u_i)}{\partial t} + \frac{\partial}{\partial x_j}(\rho u_i u_j + p\delta_{ij}) &= \frac{\partial \tau_{ij}}{\partial x_j}\,, \\
\frac{\partial(\rho e)}{\partial t} + \frac{\partial}{\partial x_i}[\rho u_i(e + \frac{p}{\rho})] &= \frac{\partial}{\partial x_j}[u_i\tau_{ij} + \kappa_T \frac{\partial T}{\partial x_j}]\,, \\
\frac{\partial(\rho \phi)}{\partial t} + \frac{\partial(\rho u_i \phi)}{\partial x_j} &= -\frac{\partial}{\partial x_j}(\Gamma \frac{\partial \phi}{\partial x_j})\,,
\end{aligned}
\tag{2.32}
$$

where Γ is the diffusivity coefficient of the scalar ϕ. The pressure is evaluated through the equation of state

$$
p = (\gamma - 1)\rho\left[e - \frac{1}{2}u_i u_i\right], \tag{2.33}
$$

where γ is the ratio of the specific heats. The thermal coefficient and the temperature are determined by

$$
\kappa_T = \frac{c_p \mu}{Pr}\,, \quad T = \frac{p}{R\rho}\,, \tag{2.34}
$$

where Pr is the Prandtl number, c_p is the specific heat at constant pressure, and R is the gas constant.

2.6 Eddy Viscosity Models.

2.6.1 Boussineq Approximation.

In 1877, Boussineq postulated that the Reynolds stress tensor can be modeled as being proportional to the deformation rate tensor through the following expression

$$
-\overline{\rho u_i' u_j'} = \mu_T(\frac{\partial \bar{u}_i}{\partial x_j} + \frac{\partial \bar{u}_j}{\partial x_i} - \frac{2}{3}\frac{\partial \bar{u}_k}{\partial x_k}\delta_{ij}) - \frac{2}{3}\overline{\rho}\kappa\delta_{ij}\,. \tag{2.35}
$$

Adding eqs. 2.35 and eq. 2.20 yields the following model expression for the total stress tensor

$$\overline{\tau}_{ij_{total}} = \overline{\tau}_{ij} + \Big[-\rho\overline{u'_i u'_j}\Big]_{aniso} = (\mu+\mu_T)\{\frac{\partial\tilde{u}_i}{\partial x_j} + \frac{\partial\tilde{u}_j}{\partial x_i} - \frac{2}{3}\frac{\partial\tilde{u}_k}{\partial x_k}\delta_{ij}\}\,, \tag{2.36}$$

where the pressure $\tilde{p}$ absorbs the isotropic part of (2.35), leading to a modified pressure in the momentum equations, defined by

$$\hat{p} = \tilde{p} + \frac{2}{3}\overline{\rho}\kappa\,. \tag{2.37}$$

2.6.2 κ-ω Models.

The κ-ω model is an EVM commonly used in aerodynamic applications and it was developed independently by Kolmogorov [27] and Saffman [28]. Since then, improved versions of the κ-ω model have been proposed, such as the model of Wilcox [29, 30] which has been one of the most used models widely during the last decades. The κ-ω family consists of two transport equations and a set of algebraic expressions. As in κ-ϵ models, κ is used as the first turbulence scale, while ω is chosen as the second scale, defined as $\epsilon/(\beta^*\kappa)$, where in standard versions of the model the choice β^*=0.09 is made. These models are designed so that they produce inappropriate profiles for the turbulent kinetic energy κ, which is in general underestimated in magnitude, without exhibiting the characteristic near-wall peak. These erroneous profiles are tolerated in order to obtain reasonable distribution of the eddy viscosity ν_t and shear stress $\overline{u'v'}$ accordingly. The model equations are

$$\begin{aligned}
\frac{\partial\kappa}{\partial t} + \overline{u}_j\frac{\partial\kappa}{\partial x_j} &= \underbrace{P - \beta^*\omega\kappa}_{\text{source/sink}} + \underbrace{\frac{\partial}{\partial x_j}[(\nu+\sigma_k\nu_t)\frac{\partial\kappa}{\partial x_j}]}_{\text{diffusion terms}}\,,\\
\frac{\partial\omega}{\partial t} + \overline{u}_j\frac{\partial\omega}{\partial x_j} &= \underbrace{\frac{\gamma P}{\nu_t} - \beta\omega^2}_{\text{source/sink}} + \underbrace{\frac{\partial}{\partial x_j}[(\nu+\sigma_\omega\nu_t)\frac{\partial\kappa}{\partial x_j}]}_{\text{diffusion terms}}\\
&\quad + \underbrace{2\frac{(1-F_1)}{\omega}\sigma_{\omega 2}\frac{\partial\kappa}{\partial x_j}\frac{\partial\omega}{\partial x_j}}_{\text{near wall correction}}\,,
\end{aligned} \tag{2.38}$$

where the source term $P = \overline{\tau_{ij}}\frac{\partial\overline{u}_i}{\partial x_j}$ is transformed through the use of the Boussineq aprroximation into the form

$$\tau_{ij} = \nu_t(2S_{ij} - \frac{2}{3}\frac{\partial\overline{u}_k}{\partial x_k}\delta_{ij}) - \frac{2\kappa}{3}\delta_{ij}\,. \tag{2.39}$$

Menter [31] proposed extended versions of the κ-ω models, namely κ-ω-SST and κ-ω-BSL. Even though these versions were originally used for aeronautic applications, they became widely used also in other fields, such as commercial and many research codes. The κ-ω-SST and κ-ω-BSL models consist of a combination between the κ-ω and the κ-ϵ models such that the κ-ω is used in the inner region of the boundary layer and switches to the κ-ϵ in the freestream region. That way they are benefited from the superior near-wall behavior of the κ-ω model, whereas they use the κ-ϵ behavior away from the walls, avoiding that way the use of the κ-ω model which is known to encounter numerical difficulties in that region. The switching between the two zones is done smoothly through the use of blending function F_1, which drops near unity in the inner half of the boundary layer, while decreasing through the outer region. This intricate function is given by

$$\begin{aligned} F_1 &= \tanh(arg_1^4), \\ \arg_1 &= \min[\max(\frac{\sqrt{\kappa}}{\beta^* \omega d}, \frac{500\nu}{d^2\omega}), \frac{4\sigma_{\omega 2}\kappa}{CD_{\kappa\omega} d^2}]\,, \\ CD_{\kappa\omega} &= \max(\frac{2\sigma_{\omega 2}}{\omega}\frac{\partial \kappa}{\partial x_j}\frac{\partial \omega}{\partial x_j}, A)\,, \end{aligned} \tag{2.40}$$

where d is the nearest distance of the point to a wall. To prevent an increase of the stress-intensity ratio $|\overline{u'v'}|/\kappa$, Menter introduced a limiter for the estimation of the eddy viscosity, such as

$$\nu_t = \begin{cases} \frac{a_1 \kappa}{\max(a_1\omega, SF_2)} & \text{for SST} \\ \frac{\kappa}{\omega} & \text{for BSL, Wilcox} \end{cases}$$

where

$$F_2 = \tanh(arg_2^2), \quad \arg_2 = \max(\frac{2\sqrt{\kappa}}{\beta^*\omega d}, \frac{500\nu}{d^2\omega})\,. \tag{2.41}$$

Also, a production limiter is used in the SST model to prevent the build-up of turbulence in stagnation regions:

$$P = \min(P^*, X\beta^*\omega\kappa)\,, \tag{2.42}$$

where X is a constant, which depends on the particular model choice.

Model coefficients

In Menter's models, a blending expression is used of the form

$$\phi = F_1\phi_1 + (1 - F_1)\phi_2 \,. \tag{2.43}$$

This expression is used to ensure the smooth transition between the zones of the model parameters appearing in the transport equations. A set of values chosen for some of these parameters is given below:

$$A = \begin{cases} 10^{-10} & \text{SST} \\ 10^{-20} & \text{BSL} \end{cases} , \qquad \gamma_1, \gamma_2 = \begin{cases} 5/9, 0.44 & \text{for SST} \\ \frac{\beta_1}{\beta^*} - \frac{\sigma_{\omega 1}\kappa^{*2}}{\sqrt{\beta^*}}, \frac{\beta_2}{\beta^*} - \frac{\sigma_{\omega 2}\kappa^{*2}}{\sqrt{\beta^*}} & \text{for BSL} \end{cases} ,$$

$$\sigma_{k1} = \begin{cases} 0.85 & \text{SST} \\ 0.5 & \text{BSL} \end{cases} , \qquad \sigma_{\omega 2} = \begin{cases} 0.856 & \text{SST, BSL} \\ 0 & \text{Wilcox} \end{cases} , \qquad X = \begin{cases} 10 & \text{SST} \\ 20 & \text{BSL} \\ 0 & \text{Wilcox} \end{cases} .$$

In addition, the parameters that have common values in both Menter's models were chosen to be

$$\begin{aligned} &\sigma_{\omega 1} = 0.5 \,,\ \beta_1 = 0.075 \,,\ \beta_2 = 0.0828 \,, \\ &\sigma_{k2} = 1.0 \,,\ \alpha = 0.31 \,,\ \kappa^* = 0.4 \,, \end{aligned} \tag{2.44}$$

whereas for Wilcox's κ-ω model, the respective constants were chosen to be

$$\sigma_k = 0.5 \,,\ \sigma_\omega = 0.5 \,,\ \beta = 3/40 \,,\ \gamma = 5/9 \,. \tag{2.45}$$

2.6.3 Spalart-Allmaras Model.

Spalart-Allmaras (SA) is a one-equation turbulence model which is mostly used in aerodynamic flows. It is elegant for industrial applications because it provides superior stability, it is faster and it is less sensitive to the grid choice compared to other popular EVM, such as κ-ω model. On the other hand, as it is commonly the case for one equation models, its main disadvantage is that it lacks of physical content, making it weak for a number of turbulent flows, such as massively separated flows, free-shear flows and complex internal flows.

The transport equation of the working variable $\hat{\nu}$ is derived by using empiricism and arguments of dimensional analysis, Galilean invariance and selected dependence on the molecular viscosity and is given by

$$\frac{\partial \hat{\nu}}{\partial t} + \bar{u}_j \frac{\partial \hat{\nu}}{\partial x_j} = \underbrace{c_{b1}(1-f_{t2})\hat{S}\hat{\nu}}_{\text{Production}} - \underbrace{[c_{w1}f_w - \frac{c_{b1}}{\kappa_v^2}f_{t2}](\frac{\hat{\nu}}{d})^2}_{\text{Destruction}} + \underbrace{\frac{1}{\sigma}[\frac{\partial}{\partial x_j}((\nu+\hat{\nu})\frac{\partial \hat{\nu}}{\partial x_j}) + c_{b2}\frac{\partial \hat{\nu}}{\partial x_i}\frac{\partial \hat{\nu}}{\partial x_i}]}_{\text{Diffusion}}, \tag{2.46}$$

where κ_v is the von-Karman constant, while the turbulent eddy viscosity is computed from

$$\mu_T = \overline{\rho}\hat{\nu}f_{v1}\,, \tag{2.47}$$

where f_{v1} is a damping function, which is defined in a way that ensures that $\hat{\nu}$ equals $\kappa y u_\tau$ in the log layer, where u_τ is the friction velocity,

$$f_{v1} = \frac{\chi_{sa}^3}{\chi_{sa}^3 + c_{v1}^3}\,, \qquad \chi_{sa} = \frac{\hat{\nu}}{\nu}\,. \tag{2.48}$$

The vorticity magnitude $\Omega = \sqrt{2\Omega_{ij}\Omega_{ij}}$ is used so that $\hat{S}$ maintains its log-layer behavior ($\hat{S} = \frac{u_\tau}{\kappa_v y}$)

$$\hat{S} = \Omega + \frac{\hat{\nu}}{\kappa_v^2 d^2}f_{v2}\,, \tag{2.49}$$

where d is the distance from the field point to the nearest wall. Additional functions are

$$\begin{aligned} f_{v2} &= 1 - \frac{\chi}{1+\chi f_{v1}}\,, \quad f_w = g\left[\frac{1+c_{w3}^6}{g^6+c_{w3}^6}\right]^{1/6}\,, \\ g &= r + c_{w2}(r^6 - r)\,, \quad r = \min[\frac{\hat{\nu}}{\hat{S}\kappa_v^2 d^2}, 10]\,, \\ f_{t2} &= c_{t3}\exp(-c_{t4}\chi^2)\,, \end{aligned} \tag{2.50}$$

where function f_w is used for obtaining the correct decay rate of destruction in the outer region of the boundary layer, g acts as a limiter that prevents large values of f_w. As a consequence, both r and f_w are tuned to equal unity in the log-law layer and decrease in the outer region. The constants of the model are given in Table 2.1

Table 2.1: Constants for the SA Closure

$c_{b1} = 0.1355$	$\sigma = 2/3$
$c_{b2}=0.622$	$\kappa_v=0.41$
$c_{w2}=0.3$	$c_{w3}=2$
$c_{v1}=7.1$	$c_{t3}=1.2$
$c_{t4}=0.5$	$c_{w1}= \frac{c_{b1}}{\kappa_v^2} + \frac{1+c_{b2}}{\sigma}$

2.7 Turbulence structure tensors.

In the context of Reynolds Averaged Navier-Stokes (RANS), it is important to have good one-point measures of turbulence anisotropy. As shown by Kassinos and Reynolds [2, 3], such anisotropy measures must take into account the morphology of the large energy-containing eddies. These coherent structures tend to organize the fluctuating motion in their vicinity and in the process create anisotropy in both the componentality and the dimensionality of the turbulence. Here, componentality refers to information about the directions in which turbulent fluctuations are most energetic, while dimensionality refers to information about the alignment and extent of the coherent structures. One has to distinguish between the turbulence componentality and dimensionality because they are two distinct aspects of turbulence anisotropy that affect the dynamics of the turbulence in different ways [3]. The structure of the turbulence field, i.e. the morphology of the large energy-containing eddies, can be characterized through a set of one-point turbulence structure tensors. Here, we summarize the key features of these tensors, but more details can be found in several works, such as [32–34].

The one-point structure tensors are defined through the fluctuating stream function vector ψ'_i, which is related to the fluctuating velocity u'_i and vorticity ω'_i through the expressions,

$$u'_i = \epsilon_{ijk}\psi'_{k,j}\,, \qquad \psi'_{i,i} = 0\,, \qquad \psi'_{i,nn} = -\omega'_i\,. \tag{2.51}$$

The Reynolds stress tensor R_{ij}, also called componentality tensor in the terminology of Kassinos et al. [3], describes the spatial orientation of the velocity fluctuations, i.e. it allows one to know in which direction the velocity fluctuations are most energetic. The componentality tensor is related to the stream function vector through the identity

$$R_{ij} = \overline{u'_i u'_j} = \epsilon_{ist}\epsilon_{jpq}\overline{\psi'_{t,s}\psi'_{q,p}}\,, \qquad r_{ij} = R_{ij}/R_{qq} = R_{ij}/(2\kappa)\,, \tag{2.52}$$

where κ is the turbulent kinetic energy. Applying isotropic tensor identities [35] to eq. (2.80a) leads to a constitutive equation,

$$R_{ij} + D_{ij} + F_{ij} - (C_{ij} + C_{ji}) = R_{kk}\delta_{ij}\,. \tag{2.53}$$

Equation (2.53) leads to the definitions of the one-point structure tensors,

$$\begin{aligned}
&\text{Componentality} && R_{ij} = \overline{u'_i u'_j}, && r_{ij} = R_{ij}/R_{kk}, && \tilde{r}_{ij} = r_{ij} - \delta_{ij}/3\,, && (2.54\text{a})\\
&\text{Dimensionality} && D_{ij} = \overline{\psi'_{k,i}\psi'_{k,j}}, && d_{ij} = D_{ij}/D_{kk}, && \tilde{d}_{ij} = d_{ij} - \delta_{ij}/3\,, && (2.54\text{b})\\
&\text{Circulicity} && F_{ij} = \overline{\psi'_{i,k}\psi'_{j,k}}, && f_{ij} = F_{ij}/F_{kk}, && \tilde{f}_{ij} = f_{ij} - \delta_{ij}/3\,, && (2.54\text{c})\\
&\text{Inhomogeneity} && C_{ij} = \overline{\psi'_{i,k}\psi'_{k,j}}, && c_{ij} = C_{ij}/D_{kk}, && \tilde{c}_{ij} = c_{ij} - \delta_{ij}/3\,. && (2.54\text{d})
\end{aligned}$$

The dimensionality tensor D_{ij}, describes the spatial orientation of the energy containing eddies, allowing one to determine the directions in which the eddies tend to be aligned. If in a given direction, let's say x_α, the structures are long, then gradients of the turbulence stream function tend to be eliminated in that direction, and as a result $d_{\alpha\alpha} \to 0$ (no summation is implied over Greek indices). On the other hand, when the turbulence is organized in a stack of thin two dimensional sheets normal to the x_α direction, then stream function gradients occur primarily in this direction and as a result $d_{\alpha\alpha} \to 1$. The circulicity tensor F_{ij} describes the structure of the large-scale circulation field. When large-scale circulation is concentrated along a particular axis x_α, then $f_{\alpha\alpha} \to 1$.

The inhomogeneity tensor, as its name indicates, describes the degree of inhomogeneity of a flow and it vanishes at the limit of homogeneous turbulence, as is shown easily if we re-express the tensor such as

$$C_{ij} = (\overline{\psi'_i\psi'_{k,j}})_{,k}\,. \tag{2.55}$$

In contrast to the other structure tensors, the trace C_{kk} can take zero or negative values in some regions of a turbulent flow, leading to an ill-defined normalized tensor. Instead of C_{kk}, the trace D_{kk} is used to normalized this tensor instead of R_{kk}, to avoid singularities at the wall of wall bounded flows.

2.7.1 The special case of homogeneous turbulence.

Next, we consider the case of homogeneous turbulence, in which the statistics of the turbulent field are independent of position. The concept of homogeneous turbulence is an idealization, in that there is no known method of realizing such a motion exactly. Nevertheless, this idealization is useful for modeling development, since it can be used as an intermediate step towards the construction of a turbulence model, suitable for general inhomogeneous flows.

In this limit, the one-point structure tensors of the velocity field can be expressed in terms of an equivalent Fourier representation involving the following integrals,

$$R_{ij} = \int E_{ij}(\mathbf{k}) d^3\mathbf{k} \,, \tag{2.56a}$$

$$D_{ij} = \int \frac{k_i k_j}{k^2} E_{qq}(\mathbf{k}) d^3\mathbf{k} \,, \tag{2.56b}$$

$$F_{ij} = \int \frac{W_{ij}(\mathbf{k})}{k^2} d^3\mathbf{k} \,, \tag{2.56c}$$

where $E_{ij} \sim \langle \hat{u}_i \hat{u}_j^* \rangle$ is the velocity energy spectrum, $W_{ij} \sim \langle \hat{\omega}_i \hat{\omega}_j^* \rangle$ is the vorticity spectrum tensor and $\mathbf{k}$ is the wave-number vector. Here, the upper-script $(^*)$ denotes a complex conjugate. Eq. (2.56c) clearly reveals the connection between the circulicity tensor and the large-scale circulation.

An interesting observation can be also deduced through the simplified constitutive equation

$$R_{ij} + D_{ij} + F_{ij} = R_{kk}\delta_{ij} \,. \tag{2.57}$$

Eq. (2.57) implies that even in the case of homogeneous turbulence, two of the three tensors are linearly independent, supporting the argument that knowledge of the componentality tensor alone does not suffice to completely characterize the turbulence field. Furthermore, it is important to note that the diagonal components of trace-normalized tensors can attain values only in the range zero to unity.

In homogeneous turbulence, Fourier expansions can be used to represent turbulent variables. Thus, the following fluctuating quantities are represented by the Fourier series,

$$u_i' = \sum_k \hat{u}_i(\mathbf{k}, t) e^{-ik_m x_m} \,, \tag{2.58a}$$

$$\omega_i' = \sum_k \hat{\omega}_i(\mathbf{k}, t) e^{-ik_m x_m} \,. \tag{2.58b}$$

The spectra satisfy the incompressibility conditions as follows

$$k_j E_{ij} = 0\,, \tag{2.59a}$$

$$k_j W_{ij} = 0\,. \tag{2.59b}$$

Eq. (2.59a) is a consequence of the incompressibility requirement. Since the turbulent variables are real quantities, the following identities must be satisfied by their Fourier coefficients

$$\hat{u}_i^*(\mathbf{k}, t) = \hat{u}_i(-\mathbf{k})\,, \quad \hat{\omega}_i^*(\mathbf{k}, t) = \hat{\omega}_i(-\mathbf{k})\,. \tag{2.60}$$

The componentality tensor is connected to the velocity spectrum through the equation

$$R_{ij} = \int E_{ij}(\mathbf{k}, t) d^3\mathbf{k}\,, \tag{2.61}$$

whereas the Fourier representation of the dimensionality tensor is given by the integral form

$$D_{ij} = \int \frac{k_i k_j}{k^2} E_{nn}(\mathbf{k}, t) d^3\mathbf{k}\,. \tag{2.62}$$

The circulicity tensor is related to the vorticity spectrum through the relation

$$F_{ij} = \epsilon_{inm}\epsilon_{jts} \int \frac{k_n k_t}{k^2} E_{ms}(\mathbf{k}, t) d^3\mathbf{k} = \int \frac{W_{ij}}{k^2} d^3\mathbf{k}\,. \tag{2.63}$$

Another important tensor which is defined in terms of the velocity spectrum tensor is the fourth-rank tensor M_{ijpq} given by

$$M_{ijpq} = \int \frac{k_p k_q}{k^2} E_{ij}(\mathbf{k}, t) d^3\mathbf{k}\,. \tag{2.64}$$

Different contractions of the fourth rank tensor can yield the structure tensors through the expressions

$$\begin{aligned} & R_{ij} = M_{ijss} = \int E_{ij} d^3\mathbf{k} \quad D_{ij} = M_{iipq} = \int \frac{k_i k_j}{k^2} E_{nn} d^3\mathbf{k}\,, \\ & F_{ij} = \epsilon_{ipq}\epsilon_{jrs} M_{qspr}\,, \end{aligned} \tag{2.65}$$

revealing that M_{ijpq} is linearly dependent not only on R_{ij} but also on D_{ij}.

At the limit of large $S\kappa/\epsilon$, meaning the time scale of the mean deformations (1/S) is much shorter than the characteristic turbulence time scale (κ/ϵ), the equations can be linearized in terms of the turbulent variable, leaving as the only non-linear term the product involving the pressure and velocity variables

$$\frac{dR_{ij}}{dt} = -G_{ik}R_{kj} - G_{jk}R_{ki} + T^r_{ij}\,, \tag{2.66}$$

where the upper-script (r) refers to the rapid part of the pressure related term, which is related to the M_{ijkp} through the equation

$$T^r_{ij} = 2G_{kn}(M_{inkj} + M_{jnki})\,. \tag{2.67}$$

2.8 The Interactive particle representation model (IPRM) for homogeneous turbulence.

The Particle Representation Model (PRM) was introduced by Kassinos and Reynolds [2] as a means of carrying out efficiently exact simulations of general deformations of homogeneous turbulence in the limit of Rapid Distortion Theory (RDT). In the RDT regime, the time scale of the turbulence is assumed to be much larger than the characteristic mean deformation time scale, leading to a linearization of the governing equations by neglecting terms involving products of fluctuating quantities. Even in the RDT limit, the governing equations are not closed at the one-point level because of the non-locality of the pressure fluctuations. One way to carry out exact RDT computations is to resort to spectral or pseudo-spectral simulations. While this is of course a valid approach, it is computationally costly and an overkill if one only needs to compute one-point statistics of turbulence. The PRM is based on the recognition that a full Fourier representation is unnecessary if all one is interested in is to compute exactly the one-point statistics of turbulence in the RDT limit. One can achieve this goal through a reduced representation that retains only a subset of the information normally carried in a spectral computation. In a sense, the PRM retains the minimal amount of information beyond one-point that enables a self-consistent closure of the RDT governing equations without resort to the use of a model and without resorting to full two-point formulations. Furthermore, Kassinos and Reynolds [2] cast this minimal representation in terms of “hypothetical particles”, thus avoiding the formality of Fourier transforms. Further details about the PRM framework are given in a number of publications [24, 36].

Each PRM “particle” is equivalent to a one-dimensional one-component (1D-1C) sheet of turbulence. In essence, particles are building blocks that can be used to construct more complex turbulence fields. Each of the PRM particles is assigned a number of properties, the exact set of properties depending on the application. In this work, we extend the original PRM by adding to the set of particle properties the passive scalar. Here, the complete set of particle properties is taken to be,

N_i	gradient vector
V_i	velocity vector
W_i	vorticity vector
S_i	stream function vector
P	pressure
Φ	passive scalar .

The gradient vector N_i represents a physical space abstraction of the wavenumber vector. The plane of each particle (the sheet of turbulence) is a plane of independence, in the sense that properties do not vary within the sheet. The gradient vector points in the direction of dependence, that is normal to the particle plane. Properties vary only in the direction normal to the sheet of turbulence.

In the PRM framework, one computes one-point statistics by taking ensemble averages over all the particles being tracked. For example, the one-point structure tensors of (B.9) are obtained through

$$R_{ij} = \langle V^2 v_i v_j \rangle \,, \qquad D_{ij} = \langle V^2 n_i n_j \rangle \,, \qquad F_{ij} = \langle V^2 s_i s_j \rangle \,, \qquad D^s_{ij} = \langle \Phi^2 n_i n_j \rangle \,, \tag{2.68}$$

where the angled brackets denote an ensemble average, and where we have used lower case to indicate the components of the unit vectors, for example $n_i = N_i/N$ where $N = \sqrt{N_s N_s}$.

2.8.1 PRM evolution equations

The particle properties are evolved in time according to simple differential equations that emulate the exact governing equations (3.4) in the limit of inviscid RDT,

$$\begin{aligned} \frac{dN_i}{dt} &= -G_{zi}N_z\,, && (2.69a)\\ \frac{dV_i}{dt} &= -(G_{iz}+2\Omega^f_{iz})V_z + PN_i\,, && (2.69b)\\ \frac{d\Phi}{dt} &= -\Lambda_i V_i\,. && (2.69c) \end{aligned}$$

The rapid pressure is determined by enforcing the incompressibility condition $V_iN_i = 0$,

$$P = 2(G_{mk}+\Omega^f_{mk})\frac{V_kN_m}{N^2}\,, \tag{2.70}$$

where Ω^f_{ik} is the frame rotation tensor, if present. The form of the pressure solution in (2.70) means that the velocity evolution depends only on the unit gradient vector n_i. Thus, one can replace equation (2.69a) by

$$\frac{dn_i}{dt} = -G_{ki}n_k + G_{km}n_kn_mn_i\,. \tag{2.71}$$

2.8.2 IPRM evolution equations

For weak deformations of homogeneous turbulence, when the time scale of the mean deformation is comparable to that of the turbulence, equations eq. (2.69) must be modified to account for the effects of the non-linear turbulence-turbulence interactions. Kassinos and Reynolds [24] argued that under weak mean deformation, when the turbulence has time to interact with itself, each particle sees an *effective gradient* due to the background action of the sea of large-scale eddies in addition to the mean velocity gradient. The same action provides an effective rotational randomization of the particles, much as mean or frame rotation tends to randomize the Fourier modes under RDT. Based on these arguments, Kassinos and Reynolds [24, 36] proposed the following form of the *Interacting Particle Representation Model* (IPRM) equations that are valid for general deformations of homogeneous turbulence

$$\begin{aligned} dN_i &= -G^n_{ki}N_k dt\,, && (2.72a)\\ dV_i &= -(G^v_{ik}+2\Omega^f_{ik})V_k dt + PN_i dt \underbrace{-C_1V_i dt - C_2V\epsilon_{ipq}dW_pn_q\,.}_{\text{rotational randomization}} && (2.72b) \end{aligned}$$

The effective gradients are given by

$$G^n_{ij} = G_{ij} + \frac{C_n}{\tau} r_{ik} d_{kj}\,, \quad G^v_{ij} = G_{ij} + \frac{C_v}{\tau} r_{ik} d_{kj}\,, \tag{2.73}$$

where τ is the turbulence time scale. The model constants C_n and C_v are chosen to be $C_n = 2.2\,C_v = 2.2$. The rotational randomization model is designed to leave the turbulent kinetic energy unaffected and it involves a Gaussian white-noise forcing dW_i, having the following properties when averaged

$$\overline{dW_i} = 0\,, \quad \overline{dW_i dW_j} = dt\delta_{ij}\,, \quad \overline{A_j dW_i} = 0\,, \tag{2.74}$$

where A_i is a stochastic vector. The pressure is again determined by the incompressibility condition $V_s N_s = 0$,

$$P = (G^v_{mk} + G^n_{mk} + 2\Omega^f_{mk})\frac{V_k N_m}{N^2}\,. \tag{2.75}$$

The model constants C_1 and C_2 are given by

$$\begin{aligned} C_1 = C_2^2 &= \frac{8.5}{\tau}\Omega^s f_{pq} n_p n_q, \quad \Omega^s = \sqrt{\Omega^s_q \Omega^s_q}, \quad \Omega^s_i = \epsilon_{ipq} r_{qk} d_{kp}\,. \\ C_n &= 2.2 C_v = 2.2\,, \\ \tau = \frac{\kappa}{\epsilon} &= \frac{2\kappa}{\epsilon} C_v r_{iq} d_{qs} r_{si}\,. \end{aligned} \tag{2.76}$$

For the evaluation of the time scale τ, the standard ϵ evolution equation with a correction in the presence of rotational effects is used,

$$\frac{d\epsilon}{dt} = -C_o \frac{\epsilon^2}{2\kappa} - C_s S_{pq} r_{qp} \epsilon - C_\Omega \sqrt{\Omega_n \Omega_m d_{nm}}\epsilon\,, \tag{2.77}$$

with

$$C_o = \frac{11.0}{6}, \quad C_s = 3.0, \quad C_\Omega = 0.01\,. \tag{2.78}$$

Note that with the use of effective gradients the governing equations retain under slow deformation the basic structure of the RDT equations, even though they now include nonlinearity through the effective gradients, as they should. Furthermore, using effective gradients means that one does not need to resort to traditional return-to-isotropy "slow" terms. This is important because there are known cases where return to isotropy does not apply under very weak deformation, such as the release of turbulence following a history of deformation under irrotational plane strain or axisymmetric expansion [3, 37, 38]. The effective gradients allow the IPRM to match the turbulence behavior shown in DNS and experiments for these atypical cases.

2.9 Structure Based Models (SBMs)

The PRM and IPRM fall within the SBM category of models. The main idea behind this category of models is that the structure of a turbulent field can be completely described by a set of tensors, called structure tensors. A phenomenological approach to introduce the structure tensors was proposed by Reynolds and Kassinos, which provides a promising route for devising improved RANS turbulence closures. The main difference between the structure-based model and the PRM stems on the methodology used for the formulation of the statistical quantities. In the PRM, the statistics are obtained by averaging over particles of fixed normal vectors n_i, while in the SBM model, averaging is performed on particles carrying the same eddy-axis vector a_i.

Kassinos and Reynolds [2] introduced the first SBM for flows subjected to rapid mean deformations, thus obeying to the RDT theory. This model succeeded in providing accurate modeling of the stresses under irrotational deformation, exact modeling of the RDT fixed points for all combinations of mean strain and mean rotation. Motivated by the success of the rapid model, Kassinos and Reynolds extended the model to account for weak deformation rates in homogeneous turbulence through the inclusion of stochastic terms [22], in a way that the realizability of the resulted transport equations is guaranteed.

Below a brief summary of the original model of Kassinos and Reynolds (KR) is given, starting from the basic conditional moments

$$R_{ij}^{|a} = \tilde{V}^2[\frac{(1-\phi)}{2}(\delta_{ij} - a_i a_j) + \phi a_i a_j + \frac{\gamma}{2}\frac{\Omega_k}{\Omega}(\epsilon_{iky} a_y a_j + \epsilon_{jky} a_y a_i)]\,, \tag{2.79a}$$

$$D_{ij}^{|a} = \frac{\tilde{V}^2}{2}(\delta_{ij} - a_i a_j)\,, \tag{2.79b}$$

where Ω_k is the mean vorticity vector. These tensors are then averaged over all particles to obtain

$$R_{ij} = q^2\left[\frac{(1-\phi)}{2}(\delta_{ij} - a_{ij}) + \phi a_{ij} + \frac{\gamma}{2}\frac{\Omega_k}{\Omega}(\epsilon_{iky} a_{yj} + \epsilon_{jky} a_{yi})\right]\,, \tag{2.80a}$$

$$d_{ij} = \frac{(\delta_{ij} - a_{ij})}{2}\,, \tag{2.80b}$$

where ϕ is the fraction of energy in the jetal mode, $(1-\phi)$ is the fraction of energy in the vortical mode and γ is the jetal-vortex correlation parameter. The normalized eddy-axis tensor a_{ij} describes the orientation of the eddies, given by

$$a_{ij} = \frac{\langle V^2 a_i a_j \rangle}{\langle V^2 \rangle}\,, \tag{2.81}$$

where a_i is a unit vector aligned with the axis of independence.

Eq. (2.80a) reveals a distinct discrepancy between the SBM approach and the conventional EVM. EVM are based on the Boussineq approximation, which states that the turbulent stress tensor has a proportional relation to the mean strain rate through the constitutive equation

$$R_{ij} = \frac{2\kappa}{3}\delta_{ij} - 2\nu_T S_{ij}, \quad \nu_T = C_\mu \kappa^2/\epsilon\,. \tag{2.82}$$

Instead, in structure-based modelling the Reynolds stress is related to a number of structure parameters and the mean vorticity vector Ω_i.

Based on the previous arguments, the stochastic differential of the energy-scaled eddy-axis vector $A_i = V a_i$ is given by

$$\begin{aligned} dA_i &= [G_{ik}A_k - G_{nm}a_n a_m A_i - G_{nm}v_n v_m A_i]dt \\ &\quad + C_1 A_i dt + C_2 dW_i + C_3 dW_p \Gamma_p A_i + C_4 \epsilon_{ipq} dW_p A_q\,. \end{aligned} \tag{2.83}$$

Starting from eq. (2.83), the transport equation for the eddy-axis tensor was found to be

$$\begin{aligned} \frac{da_{ij}}{dt} &= G_{ik}a_{kj} + G_{jk}a_{ki} - (3\phi+1)S_{km}Z^a_{kmij} + (3\phi-1)S_{nm}a_{mn}a_{ij} \\ &\quad - 2\gamma S_{nm}\frac{\Omega_k}{\Omega}\epsilon_{nkt}(Z^a_{tmij} - a_{tm}a_{ij}) \\ &\quad + \frac{1}{\tau}[C_r(1-\phi)(1-a^2)(\frac{\delta_{ij}}{3} - a_{ij}) + C_e\frac{\Omega_p}{\Omega}(\epsilon_{jpt}a_{ti} + \epsilon_{ipt}a_{tj})]\,, \end{aligned} \tag{2.84}$$

where Z^a_{ijpq} is a fully symmetric fourth order tensor, defined as

$$Z^a_{ijpq} = \frac{\langle V^2 a_i a_j a_p a_q \rangle}{\langle V^2 \rangle}\,. \tag{2.85}$$

The transport equations for the jetal and jetal-vortex correlation parameters ϕ and γ are given by

$$\frac{d\phi}{dt} = -2\phi S_{km}(a_{km} - r_{km}) + 2\gamma \frac{\Omega_k \Omega_z}{\Omega}(\delta_{kz} - a_{kz}) - \frac{C_\phi}{\tau}\phi \,, \tag{2.86}$$

and

$$\begin{aligned}
(\frac{d\gamma}{dt} + \zeta\Omega^*\gamma)[\frac{1}{2}\frac{\Omega_k\Omega_z}{\Omega^2}(\delta_{kz} - a_{kz})] &= (1 - 2\phi)\frac{\Omega_k\Omega_z}{\Omega^2}(\delta_{kz} - a_{kz}) \\
&+ \phi\frac{\Omega_z}{\Omega}\epsilon_{pzm}S_{mk}a_{kp} + \gamma\Big\{[S_{nm}r_{mn} - \frac{1}{4}S_{km}a_{mk}] \\
&+ \frac{\Omega_k\Omega_z}{\Omega^2}[S_{zm}a_{mk} + \frac{(1 - 6\phi)}{4}S_{nm}Z^a_{kzmn} - \frac{1}{2}\frac{\Omega_p\Omega_q}{\Omega^2}S_{qp}a_{kz} \\
&- \gamma S_{pq}\frac{\Omega_m}{\Omega}\epsilon_{qmt}Z^a_{tpkz}]\Big\} - \frac{C_\gamma}{\tau}\gamma \,,
\end{aligned} \tag{2.87}$$

where Ω^* is the *rms effective eddy rotation rate*

$$\Omega^* = \left[\frac{\Omega_n\Omega_m}{4}(\delta_{nm} - a_{nm}) + \Omega_z\epsilon_{zkr}S_{rp}a_{pk} + S_{km}S_{mz}a_{kz} - S_{kt}S_{pq}Z^a_{ktpq}\right]^{1/2} . \tag{2.88}$$

The model parameter ζ present in eq. (2.87) is taken as

$$\zeta = C_1\frac{\sqrt{II_\Omega}}{II_\Omega + C_2 II_S} + \zeta^* \,, \tag{2.89}$$

where

$$\zeta^* = \begin{cases} C_3\frac{|\Omega_i\Omega_j S_{ij}|}{4II_\Omega\sqrt{II_S}}, & \text{if } S^e > 0\,; \\ 0 & \text{if } S^e = 0\,; \\ C_4\frac{\Omega_i\Omega_j S_{ij}}{4II_\Omega\sqrt{II_S}}, & \text{if } S^e < 0\ . \end{cases}$$

ζ^* is the structure equilibrium parameter, which is modeled in terms of the mean structure strain-rate and the second invariants

$$S_e = S_{ij}a_{ji} \,, \tag{2.90a}$$

$$II_S = S_{ij}S_{ij}/2, \quad II_\Omega = -\Omega_{ij}\Omega_{ji}/2 \,. \tag{2.90b}$$

The standard κ-ϵ model is used for the evaluation of the time scale

$$\frac{d\kappa}{dt} = -S_{ij}R_{ji} - \epsilon\,, \tag{2.91a}$$

$$\frac{d\epsilon}{dt} = [-C_d S_{kk} - C_o\frac{\epsilon}{2\kappa} - C_s S_{pq}r_{qp} - C_\Omega\sqrt{\Omega_{ij}\Omega_{jk}a_{ik}}]\epsilon\,, \tag{2.91b}$$

with

$$C_d = \frac{4}{3}, \quad C_o = \frac{11}{6}, \quad C_s = 3.0, \quad C_\Omega = 0.01\,. \tag{2.92}$$

Lastly, the values of the model constants are chosen to be:

Rapid Model: $C_1 = 5.9$, $C_2 = 2.0$, $C_3 = 7.0$, $C_4 = 2.5$,

Slow Model: $C_r = 1.8$, $C_e = -0.35$, $C_\phi = 1.3$, $C_\gamma = 2.8$.

2.10 Algebraic Structure-Based Model.

The ASBM belongs to the family of structure-based Models (SBM) that are designed to include information about the morphology of the energy-containing turbulence eddies. ASBM has been built as an engineering simplification to more complex differential structure-based models, [4, 32] and requires two turbulence scales and the mean velocity gradients as inputs. Given these inputs, it uses algebraic relations to return the normalized structure tensors, including the Reynolds stresses, as output.

2.10.1 Structure parametrization

The fundamental idea behind the algebraic structure representation in ASBM is that any three-dimensional three-component (3D-3C) turbulent field can be constructed by the superposition of an ensemble of simpler 2D-3C fields representing individual eddies. Thus, individual eddies can be envisioned as building blocks that are used in ensembles to represent complex turbulence fields. Individual eddies can differ in character according to their componentality (C) and dimensionality (D). Averaging over an ensemble of eddies yields an algebraic constitutive equation that relates the normalized Reynolds stress tensor r_{ij} to the other structure parameters of the ensemble

$$
\begin{aligned}
r_{ij} &= \frac{1}{2}(1-\phi)(\delta_{ij}-a_{ij}) + \phi a_{ij} \\
&\quad + (1-\phi)\chi[\frac{e^-}{2}\delta_{ij} - \frac{e^+}{2}a_{ij} - b_{ij} + [ab]_{ij}] \\
&\quad - \gamma_k(\epsilon_{ipr}a_{pj} + \epsilon_{jpr}a_{pi})\{\frac{(1-\chi e^-)}{2}\delta_{kr} + \chi b_{kr} - \chi a_{kn}b_{nr}\}\,,
\end{aligned}
\tag{2.93}
$$

where we have used

$$
e^{\pm} = 1 \pm a_{nm}b_{mn}, \quad [ab]_{ij} = a_{in}b_{nj} + a_{jn}b_{ni}\,. \tag{2.94}
$$

To compute the Reynolds stress tensor one has to know the structure parameters that appear on the RHS of equation (2.93), namely the *eddy-axis tensor* a_{ij}, the *jetal parameter* ϕ, the Jetal-vortex correlation, also called *helical*, parameter γ, the *flattening tensor* b_{ij} and the *flattening scalar* χ. These are obtained through model functions that are based on the asymptotic states produced by the RDT of homogeneous turbulence and adjusted for the effects of weak deformation and wall-proximity, where appropriate. A brief description of these structure parameters and of the model functions used to compute them is given below and in greater detail in [5, 10].

2.10.1.1 Eddy-axis tensor

The unit eddy-axis vector a_i describes the orientation of individual eddies. The eddy-axis tensor a_{ij} is the energy-weighted, ensemble-averaged direction cosine tensor of the eddies, defined in eq. (2.81), where A_{ij} is related to the eddy-axis tensor the equation

$$
A_{ij} = q^2 a_{ij}\,. \tag{2.95}
$$

In differential SBM, the evolution of a_{ij} is based on the transport equation for a material line in homogeneous turbulence. In the ASBM, a_{ij} is obtained by following the weak-equilibrium procedure of Rodi [39], where it is assumed that variations in A_{ij} are due to variations in q^2 only, while variations in a_{ij} are neglected. Thus,

$$
\frac{dA_{ij}}{dt} \approx 2a_{ij}(\mathcal{P} - \epsilon)\,, \tag{2.96}
$$

where $\mathcal{P}$ and ϵ are the production and dissipation rates of the turbulent kinetic energy. Furthermore, the algebraic procedure is split into two steps, based on the assumption that the effects of irrotational mean deformation and mean rotation on the eddy axis tensor can be decomposed. This splitting is justified by the observation that the orientation of the eddy-axis must be computed in the analysis frame where the flow is in equilibrium or very close to it. This is typically a rotating frame. The eddy axis is computed with no reference to the frame rotation, as it is only kinematically rotated by it [2, 40]. The two evaluation steps are summarized next.

The irrotational contribution is calculated using the implicit algebraic expression

$$a_{ij}^s = \frac{\delta_{ij}}{3} + \tau \frac{S_{ik}^* a_{kj}^s + S_{jk}^* a_{ki}^s - \frac{2}{3}|Sa^s|\delta_{ij}}{a_o + 2\sqrt{a_1^2 + \tau^2 S_{kp}^* S_{kq}^* a_{pq}^s}} \,, \tag{2.97}$$

where τ is a turbulent time scale, $S_{ij}^* = S_{ij} - S_{kk}\delta_{ij}/3$ is the anisotropic part of the mean strain rate tensor S_{ij}, and $|Sa_s| = S_{pq}^* a_{qp}^s$. Here, a_o=1.4 and $a_1 = (2.1 - a_o)/2$ are "slow" parameters whose values were determined by considering the initial growth rate of the Reynolds stress anisotropy when $S\tau$ is very small. Moreover, these parameters were optimized simultaneously with other model constants to ensure the model satisfies a canonical boundary-layer state.

Next, mean rotation effects are included through a rotation operator H_{ij} that is applied to a_{ij}^s in order to yield the final homogeneous eddy-axis tensor

$$a_{ij} = H_{ik} H_{jm} a_{km}^s \,, \tag{2.98}$$

where H_{ij} is the rotational transformation tensor, given by

$$H_{ij} = \delta_{ij} + \alpha_1 \frac{\Omega_{ij}}{\sqrt{\Omega_{st}\Omega_{st}}} + \alpha_2 \frac{\Omega_{ip}\Omega_{pj}}{\Omega_{st}\Omega_{st}} \,. \tag{2.99}$$

Here, Ω_{ij} is the mean rotation tensor. The requirement that H_{ij} obeys the orthonormality conditions $H_{ip}H_{jp} = \delta_{ij}$ and $H_{pi}H_{pj} = \delta_{ij}$ enforces a dependence between the two coefficients α_1 and α_2, namely

$$\alpha_1 = \sqrt{2\alpha_2 - \alpha_2^2/2} \,. \tag{2.100}$$

Matching the RDT limiting states under the combined action of mean plane strain and rotation determines α_2,[40]

$$\alpha_2 = \begin{cases} 2 - 2\sqrt{\frac{1}{2}(1+\sqrt{1-r})} & \text{if } r \leq 1 \\ 2 - 2\sqrt{\frac{1}{2}(1-\sqrt{1-1/r})} & \text{if } r \geq 1\,, \end{cases}$$

where $r = (a_{pq}\Omega_{qr}S^*_{rp})/(S^*_{kn}S^*_{nm}a_{mk})$.

2.10.1.2 Jetal parameter

Motion around the eddy-axis is called vortical, whereas the motion aligned to it is called jetal. The eddy jetal parameter $0 \leq \phi \leq 1$ represents the fraction of the energy in the jetal mode. Of course, the energy fraction in the vortical mode is given by $1 - \phi$. In the ASBM, it is assumed that homogeneous isotropic turbulence is composed entirely of vortical eddies. The vortical character of the turbulence ($\phi = 0$) is preserved by rapid irrotational strain, but in the presence of mean rotation the jetal component is activated.

2.10.1.3 Helical parameter

Under rapid irrotational strain the turbulence is assumed to be vortical. Jetal turbulence results from the breaking of reflectional symmetry [2, 3] caused by mean or frame rotation. Furthermore, in the presence of mean shear, the vortical and jetal components of motion are correlated. In the ASBM, the correlation between the vortical and jetal components is related to the stropholysis vector γ_k. The stropholysis vector is zero for purely vortical or purely jetal turbulence, leading to

$$\gamma = \beta\sqrt{\frac{2\phi(1-\phi)}{1+\chi}}, \quad \gamma_k = \gamma\frac{\Omega^T_k}{\sqrt{\Omega^T_s\Omega^T_s}}\,, \tag{2.101}$$

where γ is the helical parameter, β is a parameter indicative of the degree of correlation between fluctuating velocities at different directions. Ω^T_k is the total rotation vector given by the sum of the frame and the mean rotation vector. χ is the eddy flattening parameter introduced next.

2.10.1.4 Eddy flattening

If the motion is not axisymmetric around the eddy, the eddy is called flattened. This asymmetry occurs when rotation is present and is incorporated in the model through a scalar, called flattening parameter χ, and a tensor, called the flattening tensor b_{ij}. The flattening tensor b_{ij} is modeled in terms of the mean and frame vorticity vectors Ω_i and Ω_i^f,

$$b_{ij} = \frac{\Omega_i^* \Omega_j^*}{|\Omega^{*2}|}, \quad \Omega_i^* = \Omega_i + C_b \Omega_i^f \, . \tag{2.102}$$

To capture the correct sign of the secondary shear stress for the case of shear with streamwise frame rotation, C_b is set equal to -1. Thus, b_{ij} is a frame-dependent parameter, sensitized to the particular frame choice.

2.10.2 Computation of the structure scalars

Completion of the homogeneous formulation of the ASBM requires the specification of the scalar structure parameters ϕ, β, γ and χ. In the general case, these are defined in a three-dimensional space in terms of

$$\eta_m = \sqrt{\frac{\hat{\Omega}_m^2}{\hat{S}^2}} \qquad \eta_f = \eta_m - \text{sign}(X)\sqrt{\frac{\hat{\Omega}_T^2}{\hat{S}^2}} \qquad a^2 = a_{ij}a_{ji} \, , \tag{2.103}$$

where, $\hat{\Omega}_m^2 = -a_{ij}\Omega_{ik}\Omega_{kj}$, $\hat{\Omega}_T^2 = -a_{ij}\Omega_{ik}^T\Omega_{kj}^T$, $\hat{S}^2 = a_{ij}S_{ik}^* S_{kj}^*$, and $X = a_{ij}\Omega_{ik}^T S_{kj}^*$. Functional forms for the scalar structure parameters, such as $\phi = \phi(\eta_m, \eta_f, a^2)$, $\beta = \beta(\eta_m, \eta_f, a^2)$ etc., are chosen with reference to RDT limiting states, while interpolation functions are chosen to bridge between these limiting RDT states and isotropy. The details of the functional forms can be found in [5].

2.10.3 Near-wall effects

In the ASBM, it is assumed that as a solid boundary is approached, the turbulence eddies are forced by wall blocking to become parallel to the plane of the wall, as shown in the diagram of Fig. 2.1. At the same time, the eddies become jetal because of the blocking on the wall-normal velocity component. As described below, the parametrization of the turbulence structure is adjusted for these wall-proximity effects through an elliptic blocking procedure.

Blocking parameter The blocking scalar parameter Φ provides a measure of the proximity to the wall. This parameter is computed through an elliptic relaxation equation

$$L^2 \Phi_{,jj} = \Phi, \quad L = 0.17 \max(\frac{\kappa^{3/2}}{\epsilon}, 80.0 \sqrt[4]{\frac{\nu^3}{\epsilon}}) \, , \tag{2.104}$$

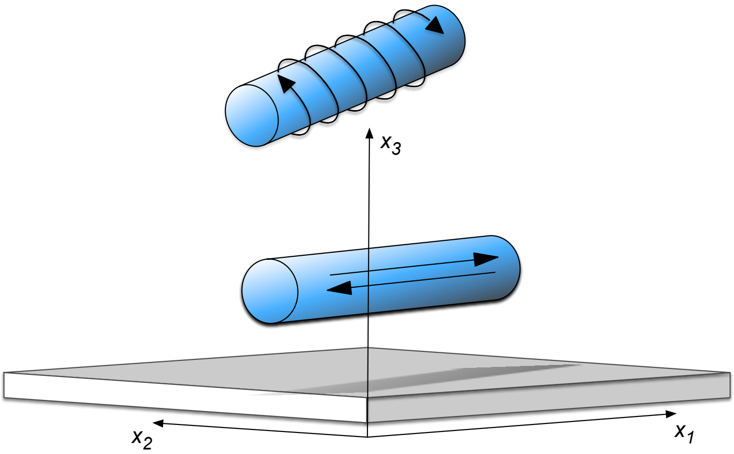

FIGURE 2.1: An eddy becomes jetalized due to the blocking effect of a solid boundary.

where κ, ϵ are the turbulent kinetic energy and the dissipation rate respectively.

Blockage tensor The blockage tensor is computed from the the scalar blocking parameter

$$B_{ij} = \begin{cases} \frac{\Phi_{,i}\Phi_{,j}}{\Phi_{,k}\Phi_{,k}}\Phi, & \text{if } \Phi_{,k}\Phi_{,k} > 0 \\ 0, & \text{if } \Phi_{,k}\Phi_{,k} = 0 \end{cases} \tag{2.105}$$

and gives the strength and the direction of the wall projection. Thus, depending on the distance from the wall as measured through Φ, the eddies are partially projected onto a plane parallel to the wall, through the operation

$$a_{ij} = P_{ik}P_{jl}a^h_{kl}\,, \tag{2.106}$$

where the eddy projection tensor P_{ij} is given by

$$P_{ik} = \frac{(\delta_{ik} - B_{ik})}{D_a}, \qquad D_a^2 = 1 - (2 - B_{kk})a^h_{mn}B_{nm}\,. \tag{2.107}$$

Note that the eddies are renormalized during the operation so that the eddy axis tensor is maintained as the energy-weighted direction cosine tensor of unit trace. The "jetalization" of the eddies due to the preferential blocking of the wall-normal velocity component is accomplished through the blocking of the jetal and helical scalar eddy parameters

$$\phi = 1 + (\phi^h - 1)(1 - B_{kk})^2, \qquad \gamma = \gamma^h(1 - B_{kk})\,. \tag{2.108}$$

Chapter 3

A structure-based model for the transport of passive scalars in homogeneous turbulent flows

3.1 Introduction

The transport of passive scalars is of great scientific interest since it plays a role in physical phenomena such as atmospheric dispersion and in engineering applications involving turbulent mixing. The term passive scalar refers to the simplified case where a scalar is present in such a low concentration that it does not influence the evolution of the fluid flow. Hence, the transport of passive scalars is also a convenient simplified starting point for the study of processes where one expects a more complex interaction between the scalar and the fluid flow, such as reacting flows with concentration gradients and heat release.

At sufficiently high Reynolds numbers, the predominant theory for the description of the velocity field statistics is based on Kolmogorov's [11] idea of local isotropy, which assumes that the small scales remain mostly isotropic, independently of the presence of any large-scale anisotropies. By analogy, similar arguments were extended by Obuknov [12] and Corrsin [13] to describe the statistics of a passive scalar in homogeneous and isotropic turbulent flow at high Reynolds and Peclet numbers. The assumption of local isotropy enables the drastic simplification of the governing transport equations and leads to similarity solutions for the passive scalar and velocity fields, even in the presence of mean scalar gradients [16]. The simplicity and elegance of such solutions has motivated a large amount of work in the literature. [14, 15]

Yet, deviation from small-scale isotropy has been observed experimentally by a number of workers. For example, Tong and Warhaft [41] considered the case of isotropic turbulence in the presence of a transverse mean scalar gradient, finding that $\overline{(\phi'_{,y})^2} \sim 1.4\overline{(\phi'_{,x})^2}$ where ϕ' denotes the fluctuating passive scalar and y is the direction of the mean gradient. A similar observation was published some years earlier by Sreenivasan et al. [42] for shear turbulence, again in the presence of transverse mean scalar gradient. The departure from isotropy for small-scale second-order statistics that was reported in these studies was relatively small. However, in the case of third order small-scale statistics, the assumption of small-scale isotropy breaks down entirely, as first reported by Stewart [43] for high Reynolds and Peclet number measurements in the atmospheric boundary layer. Stewart observed that the scalar-derivative skewness, defined as

$$S_{\phi'_{,x}} = \overline{(\phi'_{,x})^3}/[\overline{(\phi'_{,x})^2}]^{3/2}\,, \tag{3.1}$$

was of order one and not zero, as small-scale isotropy requires. Based on experimental observations, Sreenivasan and Tavoularis [44] argued that the skewness should vanish only when the mean shear and the mean scalar gradient are both zero. In all other cases, it was found that:

(a) $sgn(S_{\phi'_{,x}}) = -sgn(S)sgn(S_\phi)$[1] ,

(b) $|S_{\phi'_{,x}}|$ varies linearly with the magnitude of $\ell_0 S_\phi/(\overline{\phi'^2})^{1/2}$,

(c) $|S_{\phi'_{,x}}|$ depends on the history of S ,

where ℓ_0 is the characteristic lengthscale of the large eddies, S_ϕ is the magnitude of the mean scalar gradient and S is the magnitude of the mean velocity gradient, both imposed transverse to the mean flow direction. Clearly the three above observations show that scalar derivative skewness *is directly linked to both the mean field and the large-scale structure.*

The aforementioned efforts addressed passive scalar transport in non-rotating flows. Recently, however, significant effort has been directed to the study of passive scalar transport in shear flows in rotating frames as well. Brethouwer [46] performed a number of DNS computations at different frame rotation rates for the case of homogeneous shear flow in the presence of mean scalar gradient. Particularly, for the case of a transverse mean scalar gradient, he observed that scalar flux in the mean flow direction tends to become much larger compared to the flux in transverse direction. The DNS study of Kassinos et al., [47] provided additional supporting evidence for the strong dependency of the passive scalar transport on the relative strength of the frame rotation rate and the mean shear rate and emphasized the role played by the large-scale turbulence structure in determining passive scalar transport.

---

[1] also mentioned in [45]

3.1.1 General approach and objectives

The significant effect that the large-scale structures have on the evolution of the small-scale scalar statistics [48] has motivated us to construct a structure-based model (SBM) for passive scalar transport with the ability to account for these effects. Such an SBM for passive scalar transport could be based either on the Interacting Particle Representation Model (IPRM)[36] or a simplified engineering SBM such as the Algebraic Structure-Based Model (ASBM) [49]. In either case, the intent is to take advantage of the turbulence structure information carried in these models in order to provide improved predictions of scalar transport. In order to accomplish this in a self-consistent framework, we found it necessary to develop a set of transport equations for the scales of the passive scalar field that are sensitized to the structure of the large scales.

In Section 3.2, we give a brief summary of the one-point turbulence structure tensors and the IPRM framework. In Section 3.3, we develop an extension of the IPRM model to account for the passive-scalar statistics. In order to bring the extended IPRM model into a closed form, a set of structure-based scales for the passive scalar field is derived and discussed in Section 3.4 through Section 3.6. The validation of the complete structure-based model equations for a large number of test cases is carried out in Section 3.7, leading to encouraging results. In Section 3.8, we outline our future plans to adapt the current approach for use with the ASBM and show preliminary results that appear to be promising. A summary and conclusions are given in Section 3.9.

3.2 Mathematical background

3.2.1 The governing equations

The transport of a passive scalar ϕ in an incompressible fluid with no buoyancy effects is governed by the continuity, momentum and passive scalar transport equations,

$$u_{i,i} = 0, \tag{3.2a}$$

$$\partial_t u_i + u_j u_{i,j} = -\frac{1}{\rho} p_{,i} + \nu u_{i,jj}\,, \tag{3.2b}$$

$$\partial_t \phi + u_j \phi_{,j} = \gamma \phi_{,jj}\,, \tag{3.2c}$$

where ρ is the density of the fluid and u_i, p, ϕ are the instantaneous velocity, pressure and passive scalar fields respectively. The fluid viscosity and scalar diffusivity are denoted by ν and γ respectively. Hereafter, we are using index notation whereby repeated indexes imply summation and an index following a comma denotes differentiation with respect to the corresponding spatial coordinate. Applying Reynolds' decomposition of the flow variables,

$$u_i = \overline{u}_i + u'_i, \qquad p = \overline{p} + p', \qquad \phi = \overline{\phi} + \phi' \,, \tag{3.3}$$

to eq. (3.2) leads to the set of equations governing the transport of the turbulence fluctuations. For the case of homogeneous turbulence these take the form,

$$\begin{aligned} u'_{i,i} &= 0, && (3.4a)\\ \partial_t u'_i + \overline{u}_j u'_{i,j} &= -G_{ik}u'_k - u'_j u'_{i,j} - \frac{1}{\rho}p'_{,i} + \nu u'_{i,jj} \,, && (3.4b)\\ \partial_t \phi' + \overline{u}_j \phi'_{,j} &= -\Lambda_j u'_j - u'_j \phi'_{,j} + \gamma \phi'_{,jj} \,, && (3.4c) \end{aligned}$$

where $G_{ij} = \overline{u}_{i,j}$ and $\Lambda_i = \overline{\phi}_{,i}$ are the mean velocity gradient tensor and mean scalar gradient vector respectively.

3.2.2 The one-point turbulence structure tensors

In addition to the one-point structure tensors which were introduced in Chapter 2, we defined the structure dimensionality tensor for the scalar field as

$$D^s_{ij} = \overline{\xi'_{z,i}\xi'_{z,j}} \,, \qquad d^s_{ij} = D^s_{ij}/D^s_{kk} \,, \qquad \tilde{d}^s_{ij} = d^s_{ij} - \delta_{ij}/3 \,, \tag{3.5}$$

where ξ'_i is an irrotational vector field satisfying

$$\epsilon_{imk}\xi'_{k,m} = 0 \,, \qquad \xi'_{i,i} = \phi' \,, \qquad \xi'_{i,kk} = \phi'_{,i} \,. \tag{3.6}$$

Note, that as a result of the definition (3.6),

$$D^s_{ij} = \overline{\xi'_{z,i}\xi'_{z,j}} = \overline{\xi'_{i,z}\xi'_{j,z}} \,. \tag{3.7}$$

Hence, when the scalar field in organized in large-scale structures with a large extent in a particular direction, x_α, then $\phi'_{,\alpha} \to 0$ and as a result $d^s_{\alpha\alpha} \to 0$. In the opposite case, when the scalar field is organized in two-dimensional sheets normal to the the x_α direction, the only non-vanishing scalar gradients are $\phi'_{,a}$ and as result $d^s_{\alpha\alpha} \to 1$.

The fluctuating passive scalar quantity is represented into Fourier series as follow

$$\phi' = \sum_k \hat{\phi}(\mathbf{k}, t) e^{-ik_m x_m} \,. \tag{3.8}$$

Hence, the passive scalar spectrum is $E_\phi \sim \langle \hat{\phi}\hat{\phi}^* \rangle$. Furthermore, in the scope of the present work, which is restricted to homogeneous turbulence, the dimensionality tensor for the scalar turbulent field can be expressed in terms of an equivalent Fourier representation involving the following integrals,

$$D^s_{ij} = \int \frac{k_i k_j}{k^2} E^{\phi}(\mathbf{k}) d^3\mathbf{k}\,, \tag{3.9}$$

where $\hat{\phi}$ is the Fourier mode of the fluctuating passive scalar field and $E^\phi \sim \langle \hat{\phi}\hat{\phi}^* \rangle$ is the scalar variance spectrum tensor. Moreover, it is worth noting that the tensor trace D^s_{qq} is identical to the scalar variance $\overline{\phi'^2}$.

3.3 An Interacting particle representation model for passive scalar transport

In the present work, equations (2.72) are supplemented by the IPRM equation for the passive scalar,

$$\frac{d\Phi}{dt} = -\Lambda^{\Phi}_i V_i\,, \tag{3.10}$$

where Λ^ϕ_i is the effective gradient for the passive scalar

$$\Lambda^\phi_i = \Lambda_i + \Lambda^*_i = \overline{\phi}_{,i} + \Lambda^*_i\,. \tag{3.11}$$

Here, Λ^*_i is the non-linear contribution to the effective scalar gradient arising from the background turbulence-turbulence interactions. This is modeled as

$$\Lambda^*_i = \frac{C_v \langle V_q \Phi \rangle}{\tau_\phi q^2} r_{is} d_{sq}\,, \qquad q^2 = \langle V^2 \rangle\,, \tag{3.12}$$

with $q^2{=}2\kappa$ being the turbulent kinetic energy and τ_ϕ the characteristic time scale of the scalar field.

3.3.1 Conditionally averaged particle clusters

The algorithmic implementation of the IPRM involves the numerical solution of equations (2.72) and (3.10) along with appropriate evolution equations of the turbulence scales that appear in the effective gradients (see Sections 3.4 and 3.5). One also has to provide initial conditions, which amount to sprinkling a random or uniform distribution of particles on a unit $\mathbf{n}$ sphere. The initial condition has to be consistent with continuity, which in the IPRM context amounts to enforcing the initial orthogonality of the n_i, V_i and S_i vectors.

Numerical experiments have shown that instead of tracking a larger number of individual particles, one gains in numerical efficiency by tracking "clusters" of particles. Particle clusters amount to organized collections of particles that all have the same unit vector $n_i = N_i/N$. Thus, while an individual particle represents a 1D-1C field of turbulence, a cluster of particles represents a 1D-2C field. The gain in numerical efficiency results because the conditional averaging of the property evolution equations can be carried out analytically, yielding equations for the evolution of the cluster properties. As a result, converged one-point statistics can be obtained by tracking a much smaller number of clusters instead of large number of individual particles. Figures 3.1a and 3.1b show examples of the IPRM initializations corresponding to individual particles and conditional clusters respectively. In the case of individual particles (1D-1C fields), the n_i vectors (black) are sprinkled on the unit sphere; shown in the plane of each particle are the velocity (red) and streamfunction vectors (blue). In the case of clusters (1D-2C fields), the n_i vectors (black) are again sprinkled on the unit sphere, but shown in the plane of each particle are all the velocity vectors (red) that belong to the particular cluster.

Averaging over the particles of a given cluster yields the conditional statistics of the cluster. These include the conditional one-point structure-tensors tensors, given by

$$R_{ij}^{|n} = \langle V_i V_j | n \rangle \, , \quad D_{ij}^{|n} = \langle V^2 n_i n_j | n \rangle \, , \quad F_{ij}^{|n} = \langle V^2 s_i s_j | n \rangle \, . \tag{3.13}$$

where the superscript $^{|n}$ indicates moments obtained by averaging over all the particles belonging to a cluster with a common n_i. The cluster properties include the conditional scalar variance and the conditional scalar flux,

$$\Phi^{2|n} = \langle \Phi^2 | n \rangle \, , \quad Q_i^{|n} = \langle V_i \Phi | n \rangle \, . \tag{3.14}$$

For more details regarding the basic ideas and the fundamental formulation the reader should refer to [24, 36].

The conditionally averaged IPRM model, including the transport of a passive scalar can then be summarized as follows,

$$\begin{aligned} \frac{dR_{ij}^{|n}}{dt} = &- (G_{ik}^v + 2\Omega_{ik}^f) R_{kj}^{|n} - (G_{jk}^v + 2\Omega_{jk}^f) R_{ki}^{|n} + (G_{km}^v + G_{km}^n + 2\Omega_{km}^f) \times \\ &(R_{im}^{|n} n_k n_j + R_{jm}^{|n} n_k n_i) - \left[2C_1 R_{ij}^{|n} - C_2^2 R_{qq}^{|n} (\delta_{ij} - n_i n_j) \right] , \end{aligned} \tag{3.15}$$

where the rotational randomization parameters C_1, C_2 are modeled based on dimensional considerations and the requirement that the material indifference to rotation property is satisfied

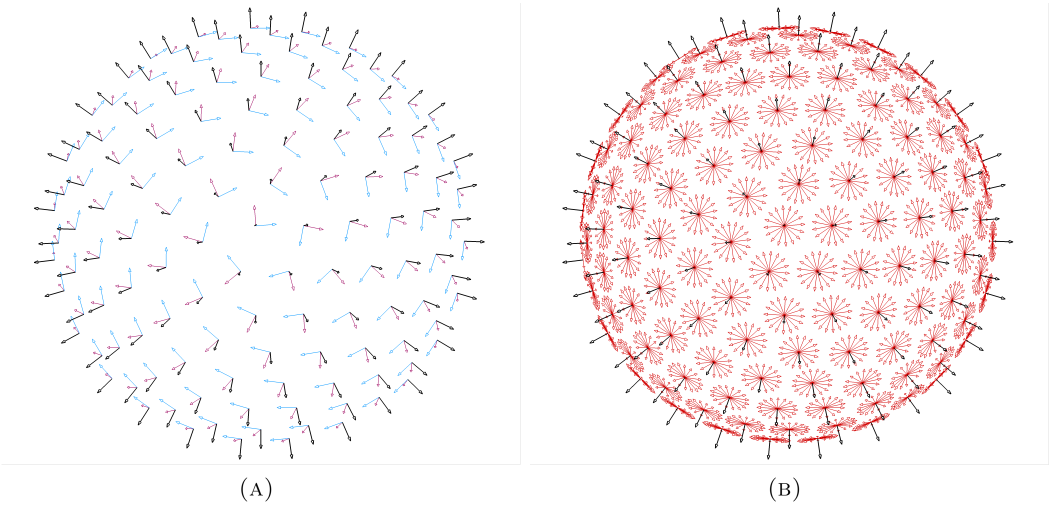
(A) (B)

Figure 3.1: Initialization of the IPRM model: (a) individual particles version; (b) conditional clusters version. In both cases, the unit gradient vectors (black) are sprinkled on the unit sphere. On the left, the velocity (red) and the streamfuction (blue) vectors are shown in the plane of each individual particle (1D-1C field). On the right, only the velocity vectors (red) belonging to each cluster (1D-2C field) are shown. In the conditional cluster version of the IPRM, one advances in time the evolution equations of the conditional moments of the cluster rather than equations for individual properties, thus gaining significantly in numerical efficiency.

$$C_1 = C_2^2 = \frac{8.5}{\tau}\Omega^* f_{pq} n_p n_q \,, \quad \Omega^* = \sqrt{\Omega_k^* \Omega_k^*} \,, \quad \Omega_i^* = \epsilon_{ipq} r_{qk} d_{kp} \,. \tag{3.16}$$

In order to bring the model into a closed form, the turbulence timescale is obtained through the following expression[24, 36]

$$\tau = \frac{C_v q^2}{\epsilon} r_{is} d_{sm} r_{mi} \,, \quad q^2 = \langle R_{kk} \rangle \,, \tag{3.17}$$

where the energy dissipation rate is evaluated from a transport model equation that will be introduced in the next section. The conditional evolution equations for the scalar properties are given by

$$\frac{d}{dt}\left(\frac{\Phi^{2|n}}{2}\right) = -Q_i^{|n} \Lambda_i^{\phi} \,, \tag{3.18}$$

and

$$\frac{d}{dt} Q_i^{|n} = -R_{ij}^{|n} \Lambda_j^{\phi} - (G_{ik}^v + 2\Omega_{ik}^f) Q_k^{|n} - C_1 Q_i^{|n} + (G_{mk}^v + G_{mk}^n + 2\Omega_{mk}^f) Q_k^{|n} n_m n_i \,. \tag{3.19}$$

The non-linear contribution to the passive-scalar effective gradients Λ_i^ϕ involves the passive-scalar time-scale τ_ϕ, defined by

$$\tau_\phi = C_v \frac{\langle \Phi^2 \rangle}{\epsilon_\phi} r_{ij} d_{js} r_{si} \,. \tag{3.20}$$

The elegance of eq. (3.20) is that τ_ϕ is determined without any further modeling assumptions, since it is automatically adjusts to the energy related model parameters.

Substituting for Λ_i^ϕ in equation (3.18) shows that the nonlinear contribution due to turbulence-turbulence interactions has the form

$$\langle V_q \Phi \rangle \langle V_i \Phi | n \rangle \frac{C_v}{\tau_\phi q^2} r_{is} d_{sq} \,. \tag{3.21}$$

Numerical experiments suggest that the approximation,

$$\langle V_q \Phi \rangle \langle V_i \Phi | n \rangle \frac{C_v}{\tau_\phi q^2} r_{is} d_{sj} \approx \langle V_i V_q | n \rangle \langle \Phi^2 \rangle \frac{C_v}{\tau_\phi q^2} r_{is} d_{sq} \,, \tag{3.22}$$

yields an improvement to the overall model behavior. Adopting this modification, the final form of the scalar variance equation is

$$\frac{d}{dt}\left(\frac{\Phi^{2|n}}{2} \right) = -Q_i^{|n} \Lambda_i - A_{ij} R_{ij}^{|n} \,, \tag{3.23}$$

where

$$A_{ij} = \frac{C_v \langle \Phi^2 \rangle}{\tau_\phi q^2} r_{is} d_{sj} \,. \tag{3.24}$$

The modeled expression (3.20) for τ_ϕ is derived such that the ratio of the timescales yields

$$\mathcal{R} \equiv \frac{\tau}{\tau_\phi} = \frac{\langle V^2 \rangle \epsilon_\phi}{\langle \Phi^2 \rangle \epsilon} \,. \tag{3.25}$$

Closure of the conditional IPRM requires determination of the dissipation rates for both the turbulent passive scalar and energy fields, a topic we consider in the following sections. Particularly, we consider the transport of two scalar scales, that of the scalar variance and the large-scale gradient variance, which subsequently are used to model the passive scalar dissipation rate ϵ_ϕ.

3.4 Turbulence scales in structure-based modeling

The Interacting Particle Representation model (IPRM) has been constructed with numerical efficiency in mind, as needed in engineering applications. Hence, in modeling nonlinear effects associated with the energy cascade process no attempt has been made to resolve different scales directly in the IPRM. This means that there is no internal determination of turbulence scales. For example, there is no internal length scale specification, as one caries the unit gradient vector n_i instead of N_i. Nevertheless, closure of the IPRM equations requires proper specification of the turbulent kinetic energy dissipation rate ϵ and scalar dissipation rate ϵ_ϕ in equations (3.17) and (3.20). Hence, model transport equations for the scales are required and must be externally supplied.

In the framework of two-equation structure-based modeling, Reynolds, Langer and Kassinos [50] (hereafter RLK02) have proposed the use of the Large-Scale-Enstrophy (LSE) equation to provide one of the turbulence scales. In the LSE equation, closure is achieved in terms of the one-point structure tensors, thus sensitizing the turbulence scales to the effects of the turbulence structure. The main idea behind the formulation of the large-scale enstrophy model is that the turbulent kinetic energy is transferred from large to small scales through a cascade mechanism that is determined by non-linear interactions between the large-scale coherent structures and the small scales. To bring this interaction between different scales to the foreground, RLK02 applied the triple decomposition scheme, described in Chapter 2.4, which is based on the idea that the large-scale eddies contain most of the turbulent energy and that these large-scale eddies determine the small-scale processes. Starting from this idea and using a simple model energy spectrum that varies as $k^{-5/3}$, RLK02 were able to relate the turbulent kinetic energy dissipation rate ϵ to the root-mean-square (rms) of the large-scale enstrophy,

$$\tilde{\omega} = \sqrt{\overline{\tilde{\omega}_i \tilde{\omega}_i}}\,. \tag{3.26}$$

In the case of homogeneous turbulence, the model transport equations for the turbulent kinetic energy κ and the rms large-scale enstrophy $\tilde{\omega}$ are given by

$$\frac{d\kappa}{dt} = -(2\kappa) r_{ij} S_{ji} - [F_\epsilon \kappa \tilde{\omega} + \nu \tilde{\omega}^2]\,, \tag{3.27a}$$

$$\frac{d\tilde{\omega}}{dt} = \tilde{\omega} f_{ij} S_{ji} - [C_{\tilde{\omega}^2_T} - \phi C_{\tilde{\omega}^2_P}]\tilde{\omega}^2 - \nu C_{\tilde{\omega}^2_\nu} \frac{\tilde{\omega}^3}{\kappa}\,, \tag{3.27b}$$

where the turbulent kinetic energy dissipation rate is determined by the following algebraic expression

$$\epsilon = F_\epsilon \kappa \tilde{\omega} + \nu \tilde{\omega}^2\,. \tag{3.28}$$

The first term in (3.28) refers to the cascade process, through which energy is transferred from larger towards smaller eddies. The viscous term is the exact representation of the dissipation rate by the large-scale motions; it is important only at low turbulence Reynolds numbers. Here, $S_{ij} = \frac{1}{2}(\bar{u}_{i,j} + \bar{u}_{j,i})$ is the strain rate tensor, while $F_\epsilon = C_\epsilon \chi$ and ϕ, χ are parameters of the large scale enstrophy model. Tables 3.1 and 3.2 summarizes all model parameters related to the turbulence scale equations as these were determined in RLK02, where further details can be found.

Spectrum	$C_{\tilde{\omega}_T^2}/C_E = C_{\tilde{a}_T^2}/C_E$	$C_{\tilde{\omega}_P^2}/C_E = C_{\tilde{a}_P^2}/C_E$	$C_{\tilde{\omega}_\nu^2} = C_{\tilde{a}_\gamma^2}$	C_E
k^2	$25/14$	$20/21$	$5/6$	0.3
k^4	$3/2$	$4/5$	$7/10$	0.5

TABLE 3.1: Values of the constants for the extended large-scale enstrophy (ELSE) model for different low wave-number spectra.

Spectrum	χ	ϕ	χ^ϕ	ϕ^ϕ
k^2	$3f_{ij}d_{ji}$	$9r_{ij}d_{jq}f_{qi}$	$9r_{iq}d^s_{qj}r_{ji}$	$9r_{iq}d^s_{qj}f_{ji}$
k^4	$3f_{ij}d_{ji}$	$9r_{ij}d_{jq}f_{qi}$	$9r_{iq}d^s_{qj}r_{ji}$	$9r_{iq}d^s_{qj}f_{ji}$

TABLE 3.2: Model parameters of the large-scale enstrophy model[7] and the extended large-scale enstrophy (ELSE) model for different low wave-number spectra.

Previous work by Kassinos and co-workers (unpublished) suggests that modeling the turbulent kinetic energy dissipation rate in terms of the large-scale enstrophy leads to improved predictions in the case of homogeneous shear in a rotating frame. Motivated by these observations, we have adopted the large-scale enstrophy equation in the new extension of the IPRM for passive scalars that we propose herein. Thus, in the framework of the current scheme, Eq. (3.28) is used in eq. (3.17) for the determination of τ, bringing the IPRM evolution of the velocity vector into a closed form. All subsequent validation tests utilize this model. However, to complete the model we also need to determine the scalar field scales. We turn to this task in the next section, again making use of the triple decomposition approach.

3.5 A set of structure-based scales for the passive scalar field

In this section, we adopt the passive-scalar variance and passive scalar gradient variance as the appropriate scales for the scalar field and we put forth a new model that properly accounts for the influence of the large-scale structural anisotropy on the evolution of these scales. Applying the triple decomposition scheme of the previous section to the governing equations (3.2) yields three transport equations; one for each of the three contributions to the instantaneous passive scalar field. In summary, these are

Mean passive scalar squared magnitude:

$$\begin{aligned}\underbrace{\partial_t(\frac{\bar{\phi}^2}{2}) + \bar{u}_j(\frac{\bar{\phi}^2}{2})_{,j}}_{\text{mean Lagrangian increase}} &= \underbrace{-(-\overline{\tilde{u}_i\tilde{\phi}})\bar{\phi}_{,i}}_{\substack{\text{transfer to}\\\text{large scales}}} - \underbrace{(-\overline{\langle u_i''\phi''\rangle})\bar{\phi}_{,i}}_{\substack{\text{transfer to}\\\text{small scales}}} \underbrace{-\gamma\bar{\phi}_{,i}\bar{\phi}_{,i}}_{\substack{\text{dissipation of}\\\text{mean field}}} \\ &\quad \underbrace{-\left[\bar{\phi}\,\overline{\langle u_i''\phi''\rangle} + \bar{\phi}\,\overline{\tilde{u}_i\tilde{\phi}} - \gamma(\frac{\bar{\phi}^2}{2})_{,i}\right]_{,i}}_{\text{spatial flux}},\end{aligned} \tag{3.29}$$

Large-Scale variance:

$$\begin{aligned}\underbrace{\partial_t(\frac{\overline{\tilde{\phi}^2}}{2}) + \bar{u}_j(\frac{\overline{\tilde{\phi}^2}}{2})_{,j}}_{\text{mean Lagrangian increase}} &= \underbrace{(-\overline{\tilde{u}_i\tilde{\phi}})\bar{\phi}_{,i}}_{\text{transfer from mean}} - \underbrace{(-\overline{\langle u_i''\phi''\rangle\tilde{\phi}_{,i}})}_{\substack{\text{transfer to}\\\text{small scales}}} \underbrace{-\gamma\overline{\tilde{\phi}_{,i}\tilde{\phi}_{,i}}}_{\substack{\text{dissipation by}\\\text{large scales}}} \\ &\quad \underbrace{-\left[\overline{\tilde{u}_i\frac{\tilde{\phi}^2}{2}} + \overline{\tilde{\phi}\langle u_i''\phi''\rangle} - \gamma(\frac{\overline{\tilde{\phi}^2}}{2})_{,i}\right]_{,i}}_{\text{spatial flux}},\end{aligned} \tag{3.30}$$

Small-Scale variance:

$$\begin{aligned}\underbrace{\partial_t(\frac{\overline{\phi''^2}}{2}) + \bar{u}_j(\frac{\overline{\phi''^2}}{2})_{,j}}_{\text{mean Lagrangian increase}} &= \underbrace{(-\overline{\langle u_i''\phi''\rangle})\bar{\phi}_{,i}}_{\text{transfer from mean}} + \underbrace{(-\overline{\langle u_i''\phi''\rangle\ \tilde{\phi}_{,i}})}_{\text{transfer from large scales}} - \underbrace{\gamma\overline{\langle\phi''_{,i}\phi''_{,i}\rangle}}_{\text{dissipation by small scales}} \\ &\quad \underbrace{-\left[\overline{\langle u_i''\frac{\phi''^2}{2}\rangle} + \overline{\tilde{u}_i\langle\frac{\phi''^2}{2}\rangle} - \gamma\overline{\langle\frac{\phi''^2}{2}\rangle}_{,i}\right]_{,i}}_{\text{spatial flux}}.\end{aligned} \tag{3.31}$$

Comparing the first two terms of the RHS of eq. (3.29) to the first term of the RHS of eq. (3.30) and eq. (3.31) respectively, we see that the mean field "feeds" the large and small scale fields through scalar variance transfer. Comparing the second terms of the fluctuating equations, we see that additional scalar variance transfer takes place from the large scales towards the small ones, revealing the importance of the cascade processes. Consequently, *the terms that are traditionally called production and dissipation of scalar variance are more accurately described as transfer terms representing exchanges between the scales, rather than source and sink terms.*

Spatial differentiation of eq. (3.2) yields the transport equation of passive scalar gradient vector

$$\partial_t a_i + u_j a_{i,j} = -a_j u_{j,i} + \gamma a_{i,jj}\,, \tag{3.32}$$

where we have introduced the shorthand notation

$$a_i \equiv \phi_{,i}\,. \tag{3.33}$$

The triple decomposition procedure yields the transport equations for the three contributors of the scalar-gradient variance.

Mean passive scalar-gradient magnitude squared:

$$\begin{aligned}
\underbrace{\partial_t(\bar{a}_i\bar{a}_i)+\bar{u}_j(\bar{a}_i\bar{a}_i)_{,j}}_{\text{mean Lagrangian increase}} = {} & \underbrace{-(-2\overline{\langle u''_m a''_i\rangle})\bar{a}_{i,m}}_{\substack{\text{transfer to}\\ \text{small scales}}}\underbrace{-(-2\overline{\tilde{u}_m\tilde{a}_i})\bar{a}_{i,m}}_{\substack{\text{transfer to}\\ \text{large scales}}}\underbrace{+(-2\bar{a}_i\bar{a}_j)\bar{u}_{j,i}}_{\substack{\text{production by}\\ \text{self stretching}}}\\
& \underbrace{-[2\bar{a}_i\overline{\langle a''_m u''_{m,i}\rangle}+2\bar{a}_i\overline{\tilde{a}_m\tilde{u}_{m,i}}]}_{\substack{\text{production by}\\ \text{cross}-\text{scale stretching}}}\quad\underbrace{-2\gamma\bar{a}_{i,m}\bar{a}_{i,m}}_{\text{dissipation from mean}}\\
& \underbrace{-\left[2\bar{a}_i\overline{\langle u''_m a''_i\rangle}+2\bar{a}_i\overline{\tilde{u}_m\tilde{a}_i}-\gamma(\bar{a}_i\bar{a}_i)_{,m}\right]_{,m}}_{\text{spatial flux}}\,,
\end{aligned} \tag{3.34}$$

Variance of large-scale passive scalar-gradient:

$$\begin{aligned}
\underbrace{\partial_t(\overline{\tilde{a}_m\tilde{a}_m})+\bar{u}_j(\overline{\tilde{a}_m\tilde{a}_m})_{,j}}_{\text{mean Lagrangian increase}} = {} & \underbrace{(-2\overline{\tilde{u}_i\tilde{a}_m})\bar{a}_{m,i}}_{\textit{transfer from mean}}\;-\;\underbrace{(-2\overline{\langle u''_i a''_m\rangle\tilde{a}_{m,i}})}_{\text{transfer to small scales}}\;+\underbrace{(-2\overline{\tilde{a}_m\tilde{a}_j})\bar{u}_{j,m}}_{\substack{\text{production by}\\ \text{mean stretching}}}\\
& \underbrace{+(-2\overline{\tilde{a}_i\tilde{a}_m\tilde{u}_{i,m}})}_{\text{production by self stretching}}\quad+\underbrace{(-2\bar{a}_i\overline{\tilde{a}_m\tilde{u}_{i,m}})+(-2\overline{\tilde{a}_m\langle u''_{i,m}a''_i\rangle})}_{\text{production by cross}-\text{scale stretching}}\\
& \underbrace{+(-2\gamma\overline{\tilde{a}_{m,i}\tilde{a}_{m,i}})}_{\text{dissipation by large scales}}\;\underbrace{-\left[2\overline{\langle u''_i a''_m\rangle\tilde{a}_m}+\overline{\tilde{a}_m\tilde{a}_m\tilde{u}_i}-\gamma(\overline{\tilde{a}_m\tilde{a}_m})_{,i}\right]_{,i}}_{\text{spatial flux}}\,,
\end{aligned} \tag{3.35}$$

Variance of small-scale passive scalar-gradient:

$$\begin{aligned}\underbrace{\frac{\partial}{\partial t}(\overline{a''_m a''_m}) + \bar{u}_j(\overline{a''_m a''_m})_{,j}}_{\text{mean Lagrangian increase}} = & \underbrace{+(-2\overline{\langle u''_i a''_m\rangle})\bar{a}_{m,i}}_{\text{transfer from mean}} + \underbrace{(-2\overline{\langle u''_i a''_m\rangle \tilde{a}_{m,i}})}_{\substack{\text{transfer from}\\ \text{large scale}}} \\ & + \underbrace{(-2\overline{\langle a''_m a''_j\rangle})\bar{u}_{j,m}}_{\substack{\text{production by}\\ \text{mean stretching}}} + \underbrace{(-2\overline{\langle a''_m a''_i u''_{i,m}\rangle})}_{\substack{\text{production by}\\ \text{self stretching}}} \underbrace{+(-2\overline{\langle a''_m a''_i\rangle \tilde{u}_{i,m}})}_{\substack{\text{production by}\\ \text{large}-\text{scale stretching}}} \\ & \underbrace{-[2\overline{\langle a''_m u''_{i,m}\rangle}\bar{a}_i + 2\overline{\tilde{a}_i\langle a''_m u''_{i,m}\rangle}]}_{\text{production by cross}-\text{scale stretching}} \quad \underbrace{-2\gamma\overline{\langle a''_{m,i} a''_{m,i}\rangle}}_{\text{dissipation by small scales}} \\ & \underbrace{-\left[\overline{\langle a''_m a''_m\rangle \tilde{u}_i} + \overline{\langle u''_i a''_m a''_m\rangle} - \gamma(\overline{\langle a''_m a''_m\rangle})_{,i}\right]_{,i}}_{\text{spatial flux}} \quad .\end{aligned} \tag{3.36}$$

Note that in addition to transfer between the scales, passive scalar gradient variance is also *produced* (not transferred) at all scales due to mean velocity gradient stretching. Note also that in the limit of homogeneous turbulence the mean scalar-gradient becomes uniform. Hence, the first term on the RHS of Eqs. (3.35) and (3.36), representing the transfer from the mean scalar gradient towards the fluctuating fields through the cascade process, vanishes.

In the current work, the two turbulence scales that are needed for modeling passive scalar transport are provided by the passive scalar variance and the large-scale passive scalar gradient variance, namely

$$\lambda = \overline{\phi'^2}/2\,, \tag{3.37a}$$

$$\tilde{a}^2 = \overline{\tilde{\phi}_{,i}\tilde{\phi}_{,i}}\,. \tag{3.37b}$$

In the homogeneous turbulence limit, the transport equations for λ and $\overline{\tilde{a}^2}/2$ reduce to

$$\frac{D\lambda}{Dt} = \underbrace{-\overline{u'_i\phi'}\Lambda_i}_{\text{production}} - \underbrace{(\gamma\overline{\phi'_{,i}\phi'_{,i}})}_{\text{dissipation}} = P_\phi - \epsilon_\phi\,, \tag{3.38}$$

and

$$\begin{aligned}\underbrace{\partial_t(\frac{\tilde{a}^2}{2}) + \bar{u}_j(\frac{\tilde{a}^2}{2})_{,j}}_{\text{mean Lagrangian increase}} \ = \ & \underbrace{-(-\overline{\langle u''_i a''_m\rangle \tilde{a}_{m,i}})}_{\text{transfer to small scales}} + \underbrace{(-\overline{\tilde{a}_m\tilde{a}_j})\bar{u}_{j,m}}_{\substack{\text{production by}\\ \text{mean stretching}}} \underbrace{+(-\overline{\tilde{a}_i\tilde{a}_m\tilde{u}_{i,m}})}_{\substack{\text{production by}\\ \text{self stretching}}} \\ & + \underbrace{(-\bar{a}_i\overline{\tilde{a}_m\tilde{u}_{i,m}}) + (-\overline{\tilde{a}_m\langle u''_{i,m}a''_i\rangle})}_{\substack{\text{production by}\\ \text{cross}-\text{scale stretching}}} \quad \underbrace{+(-\gamma\overline{\tilde{a}_{m,i}\tilde{a}_{m,i}})}_{\text{dissipation by large scales}} \quad .\end{aligned} \tag{3.39}$$

Equations (3.38) and (3.39) are complemented with the model equations of the turbulent kinetic energy κ and large-scale enstrophy $\tilde{\omega}^2$ of RLK02, thus providing all the scales needed by the extended IPRM. Note, however, that equations (3.38) and (3.39) contain unknown terms that must be modeled. In the next section, we provide closure in terms of the one-point structure tensors.

3.5.1 Modeling the fluctuating passive scalar variance equation

We express the λ equation (3.38) into an alternative form by decomposing the dissipation term into the large and small scale contributions, yielding

$$\frac{d\lambda}{dt} = -\overline{u_i'\phi'}\Lambda_i - [\gamma\overline{\langle\phi_{,i}''\phi_{,i}''\rangle} + \gamma\overline{\tilde{\phi}_{,i}\tilde{\phi}_{,i}}]\,. \tag{3.40}$$

Although mainly a small-scale quantity, scalar dissipation is directly linked to the large-scale eddies through the cascade mechanism. Based on Richardson's notion[51], we assume that the small-scale eddies are in dynamical equilibrium, since in this range, the timescales are small compared to the large-scale timescales. Thus, the small eddies can adapt quickly to maintain equilibrium with the scalar variance transferred by the large eddies. Hence, the scalar variance diffused is set to be approximately equal to the scalar variance that reaches the small scales via transfer from the large scales, such as

$$\left|\overline{\langle u_i''\phi''\rangle\tilde{\phi}_{,i}}\right| \approx \left|\gamma\overline{\langle\phi_{,i}''\phi_{,i}''\rangle}\right|. \tag{3.41}$$

The sum of the two terms inside the first bracket in eq. (3.40) equals the total dissipation term, thus

$$\frac{D\lambda}{Dt} = -\overline{u_i'\phi'}\Lambda_i - \epsilon_\phi\,, \tag{3.42}$$

yielding the following alternative expression for the scalar dissipation rate ϵ_ϕ

$$\epsilon_\phi = \underbrace{(-\overline{\langle u_i''\phi''\rangle)\tilde{\phi}_{,i}}}_{\text{transfer from large to small}} + \underbrace{\gamma\overline{\tilde{\phi}_{,i}\tilde{\phi}_{,i}}}_{\text{dissipation by large scales}}\,. \tag{3.43}$$

The first term at the RHS of eq. (3.42) is the source term associated to the mean scalar gradient, while the first term of eq. (3.43) refers to the rate at which passive-scalar variance is transferred from the large towards the small scales. The second term refers to diffusive loss of scalar variance; it becomes significant only at low Peclet numbers. Next we consider the closure of eq. (3.43).

Sreenivasan [52] and Warhaft [18] have shown that in isotropic turbulence at high Reynolds and Peclet numbers, with or without a mean-scalar gradient, the passive scalar spectrum varies close to $k^{-5/3}$ in the inertial sub-range regime. Based on their arguments, a simple model for the passive scalar spectrum function has been chosen, as shown in Fig. 3.2. The enstrophy $\overline{\omega'^2}$ and the passive scalar gradient variance $\overline{a'^2}$ are by definition small-scale quantities, thus the contribution of the large-scale motion to the Fourier integrals of these quantities becomes significant only in the final period of decay, during which the small and large scales become comparable. A standard model for the passive scalar dissipation rate that has appeared in many works is [18, 53]

$$\epsilon_\phi \sim \mathcal{R}\frac{\overline{\phi'^2}}{\tau} = 2\,\mathcal{R}\frac{\lambda}{\tau}\,. \tag{3.44}$$

where $\mathcal{R}$ is the ratio of integral time scale of turbulent velocity fluctuations to that of the scalar fluctuations and $\tau = 2\kappa/\epsilon$ is the turbulence time scale [53]. Substituting eq. (3.28) in the above definition at high Re_T leads to the expression for the passive scalar dissipation rate $\epsilon_\phi = F_\epsilon\mathcal{R}\,\lambda\tilde{\omega}$. Consequently, in the present framework, the large-scale enstrophy $\tilde{\omega}^2$ appears as the natural time scale to describe the transfer rate of scalar variance from large to small scales.

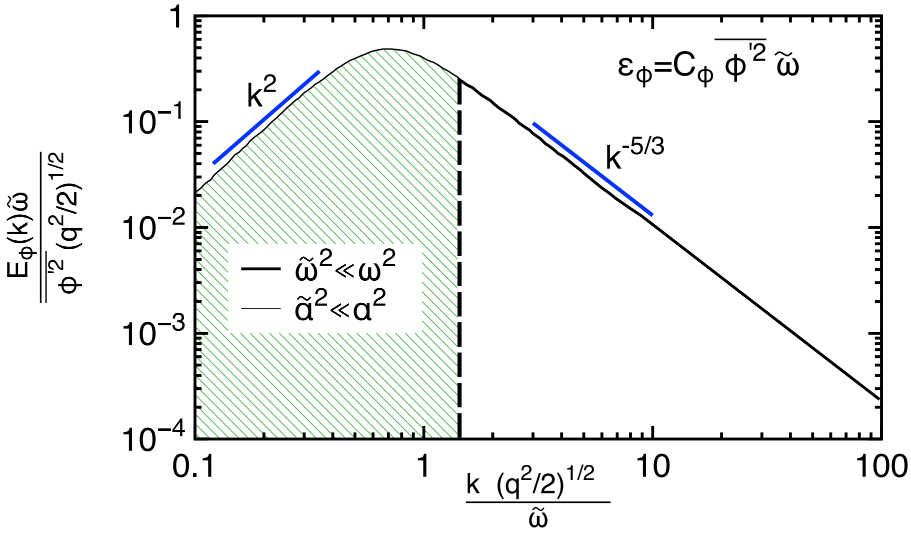

(A)

Figure 3.2: Standard model for passive-scalar spectrum at high Reynolds and Peclet numbers.

Based on the above considerations, the rate of scalar energy transfer to small-scale is modeled as follows

$$-\overline{\langle u_i''\phi''\rangle\tilde{\phi}_{,i}} = F_\phi \lambda \tilde{\omega}\,, \tag{3.45}$$

where F_ϕ is a dimensionless coefficient that depends on invariants of the turbulence structure tensors. Here, we set $F_\phi = C_\phi \chi^\phi$, where $\chi^\phi = 9\, r_{iq} d^s_{qj} r_{ji}$ and C_ϕ is a constant that will be determined later on. The functional form of χ^ϕ has been motivated by the work of Lesieur and Herring [54], who have shown that the passive scalar cascade is direct in the 2D-2C limit, mirroring the direct cascade of the enstrophy in this same limit. Furthermore, they showed that the scalar-fluctuation variance decays similar to the enstrophy, if the enstrophy spectrum is considered as a passive scalar. The chosen functional form of χ^ϕ is able to account for the presence of the direct cascade in the 2D-2C limit, while it becomes equal to unity for isotropic turbulence and vanishes in 2C-1D turbulence. Thus, we finally model the scalar dissipation rate ϵ_ϕ in the turbulent scalar variance equation by

$$\epsilon_\phi = F_\phi \lambda \tilde{\omega} + \gamma \tilde{a}^2 = C_\phi \chi^\phi \lambda \tilde{\omega} + \gamma \tilde{a}^2\,, \tag{3.46}$$

where C_ϕ remains to be determined.

3.5.2 Modeling the large-scale passive scalar-gradient variance equation

Next, we perform a term-by-term modeling of the $\tilde{a}^2$ equation. First, we model the dissipation term by

$$\gamma \overline{\tilde{a}_{m,i}\tilde{a}_{m,i}} = C_{\tilde{a}^2\gamma}\gamma \frac{\tilde{a}^4}{\overline{\phi'^2}}\,, \tag{3.47}$$

where $C_{\tilde{a}^2\gamma}$ will be defined in order to match decay rates at small turbulent Reynolds numbers (final period of decay).

As shown in the Appendix A.2, the relation that connects the scalar dimensionality tensor d^s_{ij} to the large-scale passive-scalar-gradient variance is analogous to the one that exists between the large-scale vorticity and the circulicity tensor F_{ij} (eq. A.25). Thus, we model the large-scale squared-magnitude-scalar-gradient correlation in the production term as

$$\overline{\tilde{a}_m \tilde{a}_j} = d^s_{mj}\tilde{a}^2\,. \tag{3.48}$$

Note that contracting d^s_{ij} yields the correct trace. Accordingly, the production by mean-stretching term can be modeled as

$$-\overline{\tilde{a}_m\tilde{a}_j}\bar{u}_{j,m} = -d^s_{mj}\tilde{a}^2\bar{u}_{j,m}\,. \tag{3.49}$$

We model the rate of transfer to small-scales in terms of the large-scale gradients by

$$-\overline{\langle u''_i a''_m\rangle\tilde{a}_{m,i}} = C_{\tilde{a}^2_T}\tilde{a}^2\tilde{\omega}\,, \tag{3.50}$$

where $C_{\tilde{a}^2_T}$ is a dimensionless coefficient that in general depends on invariants of the turbulence structure tensors.

Next, we turn to the modeling of the production terms. The first of the production terms due to cross-scale stretching involves the mean scalar gradient, $\bar{a}_m = \Lambda_m = \overline{\phi}_{,m}$, and is modeled on its own as,

$$-\bar{a}_i\overline{\tilde{a}_m\tilde{u}_{i,m}} = [C_{\tilde{a}^2_T} - \phi^\phi C_{\tilde{a}^2_P}]\Lambda\tilde{a}\tilde{\omega}\,, \tag{3.51}$$

where $\Lambda = \sqrt{\Lambda_k\Lambda_k}$ is the magnitude of the mean scalar gradient. The modeled expression has been chosen such that $\tilde{a}$ acquires the correct asymptotic behavior for decaying turbulence in the presence of mean scalar gradient (see Appendix A.3).

The second production term due to cross-scale stretching is modeled together with the term representing by production self-stretching. The term corresponding to production through self-stretching is composed entirely of large-scale quantities, and as can be easily shown, it vanishes in the limit of 1D-2C pancake turbulence (vortex sheets). To see this, one can assume without the loss of generality that x_3 is the axis of dependence. Then, $d_{33} \to 1$, while the velocity fluctuations in the x_3 direction (as well as the Reynolds stress component r_{33}) must vanish. Hence,

$$\tilde{a}_i\tilde{u}_{i,m} = \tilde{\phi}_{,i}\tilde{u}_{i,m} = \tilde{\phi}_{,3}\tilde{u}_{3,m} = 0\,. \tag{3.52}$$

Based on the above arguments, the modeled term is

$$\underbrace{-\overline{\tilde{a}_i\tilde{a}_m\tilde{u}_{i,m}}}_{\text{production by self stretching}} + \underbrace{(-\overline{\tilde{a}_m\langle u''_{i,m}a''_i\rangle})}_{\substack{\text{production by}\\ \text{cross}-\text{scale stretching}}} = F_{\tilde{a}^2_P}\tilde{a}^2\tilde{\omega}\,, \tag{3.53}$$

where $F_{\tilde{a}^2_P}$ is a dimensionless coefficient that will depend on invariants of the turbulence structure tensors. We use $F_{\tilde{a}^2_P} = C_{\tilde{a}^2_P}\phi^\phi$, where $C_{\tilde{a}^2_P}$ is a constant and $\phi^\phi = 9\,r_{iq}d^s_{qj}f_{ji}$. For isotropic turbulence $\phi^\phi = 1$, and for 2D-2C and 2C-1D turbulence $\phi^\phi = 0$.

Before we proceed to the evaluation of the model constants, we summarize the complete set of transport equations for the Extended Large-Scale Enstrophy model (ELSE) in their simplified form for homogeneous turbulence:

$$\frac{d\kappa}{dt} = -(2\kappa) r_{ij} S_{ji} - [F_\epsilon \kappa \tilde{\omega} + \nu \tilde{\omega}^2] \,, \tag{3.54a}$$

$$\frac{d\tilde{\omega}}{dt} = \tilde{\omega} f_{ij} S_{ji} - [C_{\tilde{\omega}^2_T} - \phi C_{\tilde{\omega}^2_P}] \tilde{\omega}^2 - \nu C_{\tilde{\omega}^2_\nu} \frac{\tilde{\omega}^3}{\kappa} \,, \tag{3.54b}$$

$$\frac{d\lambda}{dt} = -\overline{u'_i \phi'}\, \Lambda_i - [\gamma \tilde{a}^2 + C_\phi \chi^\phi \lambda \tilde{\omega}], \tag{3.54c}$$

$$\frac{d\tilde{a}}{dt} = -C_{\tilde{a}^2_\gamma} \gamma \frac{\tilde{a}^3}{\lambda} - d^s_{mj} S_{jm} \tilde{a} - [C_{\tilde{a}^2_T} - \phi^\phi C_{\tilde{a}^2_P}] \tilde{a} \tilde{\omega} + [C_{\tilde{a}^2_T} - \phi^\phi C_{\tilde{a}^2_P}] \Lambda \tilde{\omega} \,. \tag{3.54d}$$

The scalar-flux vector, the structure-tensors and their products are obtained from the IPRM model.

3.6 Evaluation of the model parameters in the ELSE scales model

The model parameters in the scale equations for the scalar are determined by matching the decay rates for the scalar variance and scalar dissipation rate in freely decay isotropic turbulence. Since the evolution of the passive scalar field is strongly affected by the velocity field as pointed out by Rogers et al. [55], we expect that the constants will depend also on the structure tensors and the turbulence scales related to the velocity field. Thus, for the evaluation of the constants we will utilize the complete set of transport equations, given by eq. (3.54).

First, we introduce a simplifying assumption by setting $[C_{\tilde{a}^2_T} - \phi^\phi C_{\tilde{a}^2_P}] = [C_{\tilde{\omega}^2_T} - \phi^\phi C_{\tilde{\omega}^2_P}]$. This assumption mainly stems from the fact that the constants $\{C_{\tilde{a}^2_T}, C_{\tilde{a}^2_P}\}$ and $\{C_{\tilde{\omega}^2_T}, C_{\tilde{\omega}^2_P}\}$ are used to model the non-linear terms appearing in the transport equation for $\tilde{a}^2$ and $\tilde{\omega}^2$ respectively, terms which are responsible for the cascade process. To illustrate this point, we considered the special case of freely decaying isotropic turbulence at high Re_T, $Pe = \frac{\nu}{\gamma}$, where the evolution of the turbulence is solely driven by these terms. Based on a similarity analysis, at large times $\tilde{a}^2$ and $\tilde{\omega}^2$ have the same decay rates, which moreover are independent of the form of the low wave-spectrum. The proposed substitution is consistent with this argument and has the additional advantage that it reduces by two the number of free model parameters that must be determined. Thus eq. (3.54d) is modified as follows

$$\frac{d\tilde{a}}{dt} = -C_{\tilde{a}^2_\gamma} \gamma \frac{\tilde{a}^3}{\lambda} - d^s_{mj} S_{jm} \tilde{a} - [C_{\tilde{\omega}^2_T} - \phi^\phi C_{\tilde{\omega}^2_P}] \tilde{a} \tilde{\omega} + [C_{\tilde{\omega}^2_T} - \phi^\phi C_{\tilde{\omega}^2_P}] \Lambda \tilde{\omega} \,. \tag{3.55}$$

Here, the kinetic energy and the passive-scalar variance spectra are denoted by being $E_\kappa(k,t)$ and $E_\phi(k,t)$ respectively. Expansions around $k=0$ yield the well-known expressions

$$E_\kappa(k,t) = 2\pi k^2 (B_o + B_2 k^2 + ...)\,, \tag{3.56a}$$

$$E_\phi(k,t) = 2\pi k^2 (C_o + C_2 k^2 + ...)\,, \tag{3.56b}$$

where B_n, C_n are the expansion coefficients. The current model is calibrated with respect to the two sets of low wave number spectra, $\{k^2, k^2\}$ and $\{k^4, k^4\}$, where the elements inside the curly brackets refer to the leading order of the expansion of the energy and passive scalar spectrum respectively.

3.6.1 High Re_T, Pe without mean scalar gradients.

In freely decaying isotropic turbulence at high Re_T and Pe numbers, direct viscous and diffusion effects occur at smaller scales than the ones containing most of the scalar variance. Thus, their contribution can be neglected and the system of equations simplifies to

$$\frac{d\kappa}{dt} = -C_\epsilon \chi \kappa \tilde{\omega}\,, \tag{3.57a}$$

$$\frac{d\tilde{\omega}}{dt} = -[C_{\tilde{\omega}^2_T} - \phi C_{\tilde{\omega}^2_P}]\tilde{\omega}^2\,, \tag{3.57b}$$

$$\frac{d\lambda}{dt} = -C_\phi \chi^\phi \lambda \tilde{\omega}\,, \tag{3.57c}$$

$$\frac{d\tilde{a}}{dt} = -[C_{\tilde{\omega}^2_T} - \phi^\phi C_{\tilde{\omega}^2_P}]\tilde{a}\tilde{\omega}\,. \tag{3.57d}$$

The solution of eq. (3.57) is given by

$$\frac{\kappa}{\kappa_o} = [1 + (C_{\tilde{\omega}^2_T} - \phi_{\text{iso}} C_{\tilde{\omega}^2_P})\tilde{\omega}_o t]^{-\chi_{\text{iso}} C_\epsilon / [C_{\tilde{\omega}^2_T} - \phi_{\text{iso}} C_{\tilde{\omega}^2_P}]}\,, \tag{3.58a}$$

$$\frac{\lambda}{\lambda_o} = [1 + (C_{\tilde{\omega}^2_T} - \phi_{\text{iso}} C_{\tilde{\omega}^2_P})\tilde{\omega}_o t]^{-\chi^\phi_{\text{iso}} C_\phi / [C_{\tilde{\omega}^2_T} - \phi_{\text{iso}} C_{\tilde{\omega}^2_P}]}\,, \tag{3.58b}$$

$$\frac{\tilde{\omega}}{\tilde{\omega}_o} = \frac{1}{1 + (C_{\tilde{\omega}^2_T} - \phi_{\text{iso}} C_{\tilde{\omega}^2_P})\tilde{\omega}_o t}\,, \tag{3.58c}$$

$$\frac{\tilde{a}}{\tilde{a}_o} = [1 + (C_{\tilde{\omega}^2_T} - \phi_{\text{iso}} C_{\tilde{\omega}^2_P})\tilde{\omega}_o t]^{-[C_{\tilde{\omega}^2_T} - \phi^\phi_{\text{iso}} C_{\tilde{\omega}^2_P}] / [C_{\tilde{\omega}^2_T} - \phi_{\text{iso}} C_{\tilde{\omega}^2_P}]}\,, \tag{3.58d}$$

where $\phi_{\text{iso}} = \phi_{\text{iso}}^{\phi} = 1$. At very large times, $(t \rightarrow \infty)$, the asymptotic behavior of the variables is given by

$$\frac{\kappa}{\kappa_o} \sim t^{-\chi_{\text{iso}} C_\epsilon / [C_{\tilde{\omega}_T^2} - C_{\tilde{\omega}_P^2}]}, \tag{3.59a}$$

$$\frac{\lambda}{\lambda_o} \sim t^{-\chi_{\text{iso}}^{\phi} C_\phi / [C_{\tilde{\omega}_T^2} - C_{\tilde{\omega}_P^2}]}, \tag{3.59b}$$

$$\frac{\tilde{\omega}}{\tilde{\omega}_o} \sim t^{-1}, \tag{3.59c}$$

$$\frac{\tilde{a}}{\tilde{a}_o} \sim t^{-1}. \tag{3.59d}$$

The ratio -$\chi_{\text{iso}}^{\phi} C_\phi / [C_{\tilde{\omega}_T^2} - C_{\tilde{\omega}_P^2}]$ defines the decay rate of the scalar variance in this case. This rate depends on the spectra of both the turbulent kinetic energy and the scalar. Assuming either a $\sim k^2$ or a $\sim k^4$ low-wavenumber behavior, Chasnov [16] used simple theoretical arguments in order to derive similarity states for both spectra in isotropic turbulence. These theoretical predictions were found to be in good agreement with LES simulations for cases with or without mean scalar gradient. We have extended this approach in order to take into account the decay rates of the enstrophy and of the mean squared magnitude of scalar gradient. The asymptotic states that have been obtained through this approach are summarized in Table 3.3, with additional details given in Appendix A.3. Compared to the theory, the model captures the correct decay rates for $\tilde{\omega}^2$ and $\tilde{a}^2$ for both the $\{k^2, k^2\}$, $\{k^4, k^4\}$ cases.

Spectra	κ	$\overline{\phi'^2}$	$\overline{\omega'^2}$	$\overline{a'^2}$
$\{k^2, k^2\}$	$B_o^{2/5} t^{-6/5}$	$C_o B_o^{-3/5} t^{-6/5}$	t^{-2}	$C_o B_o^{-1} t^{-2}$
$\{k^4, k^4\}$	$B_2^{2/7} t^{-10/7}$	$C_2 B_2^{-5/7} t^{-10/7}$	t^{-2}	$C_2 B_2^{-1} t^{-2}$
$\{k^2, k^4\}$	$B_o^{2/5} t^{-6/5}$	$C_2 B_2^{-1} t^{-2}$	t^{-2}	$C_2 B_o^{-7/5} t^{-14/5}$
$\{k^4, k^2\}$	$B_2^{2/7} t^{-10/7}$	$C_o B_2^{-3/7} t^{-6/7}$	t^{-2}	$C_o B_2^{-5/7} t^{-10/7}$

TABLE 3.3: Summary of the asymptotic expressions for the turbulent statistics using different combinations of low wave-spectra at high Re_T and Pe numbers, in freely decay turbulence.

In the absence of mean scalar gradients, the scalar variance evolves solely due to the presence of the advection term in its evolution equation. In this case, the scalar decay rate follows the decay rate of the turbulent kinetic energy. Assuming the $\{k^2, k^2\}$ low-wavenumber spectra yields,

$$\frac{\chi_{\text{iso}} C_\epsilon}{(C_{\tilde{\omega}_T^2} - C_{\tilde{\omega}_P^2})} = \frac{\chi_{\text{iso}}^{\phi} C_\phi}{(C_{\tilde{\omega}_T^2} - C_{\tilde{\omega}_P^2})} = \frac{6}{5}\,. \tag{3.60}$$

Recalling that $\chi_{\text{iso}} = \chi_{\text{iso}}^{\phi} = 1$, eq. (3.60) suggests that in this case

$$C_\epsilon = C_\phi\,. \tag{3.61}$$

Based on dimensional analysis, we have $\epsilon_\phi = \frac{d\lambda}{dt} \sim t^{-11/5}$. Applying the modeled expression for ϵ_ϕ leads to the same result, since $\epsilon_\phi^{model} = C_\phi \chi^\phi \lambda \tilde{\omega} \sim t^{-6/5} t^{-1} = t^{-11/5}$, thus providing support to our decision to model the scalar dissipation rate ϵ_ϕ as in eq. (3.46). Similarly, when a $\{k^4, k^4\}$ low-wavenumber behavior is assumed for the spectra, the model gives

$$\frac{\chi_{\text{iso}} C_\epsilon}{(C_{\tilde{\omega}_T^2} - C_{\tilde{\omega}_P^2})} = \frac{\chi_{\text{iso}}^\phi C_\phi}{(C_{\tilde{\omega}_T^2} - C_{\tilde{\omega}_P^2})} = \frac{10}{7} \quad \Rightarrow C_\epsilon = C_\phi \,. \tag{3.62}$$

Dimensional arguments suggest $\epsilon_\phi \sim t^{-17/7}$, which again coincides to the prediction of our model, since $\epsilon_\phi^{model} = C_\phi \chi^\phi \lambda \tilde{\omega} \sim t^{-10/7} t^{-1} = t^{-17/7}$. Based on these two cases, we take $C_\phi = C_\epsilon$ in general, thus reducing further the number of the model coefficients that needs to be determined. With this choice, the final form of the scalar dissipation becomes,

$$F_\phi = C_\epsilon \chi^\phi \quad \text{and} \quad \epsilon_\phi = F_\phi \lambda \tilde{\omega} + \gamma \tilde{a}^2 = C_\epsilon \chi^\phi \lambda \tilde{\omega} + \gamma \tilde{a}^2 \,. \tag{3.63}$$

Fig. 3.3 shows results for the evolution of the power law exponent of scalar variance in the absence of mean scalar gradients. Comparison is made between the predictions of the ELSE model and the LES results of Chasnov [16] for $\{k^2, k^2\}$ and $\{k^4, k^4\}$ spectra. In his paper, Chasnov points out that the decay exponent for the $\{k^2, k^2\}$ case is expected to be exact and that potential discrepancies can be attributed to error sources in the LES simulations, including a partial development of the flow due to the limited number of large-eddy turnover times available in the computations and inadequately resolved small scales. Even so, the predictions of the ELSE model agree quite well with LES results.

3.6.2 Low Re_T and Pe in the final period of decay.

Next, we consider the case of freely decaying isotropic turbulence at low Re_T and Pe. The final period of decay is dominated by diffusive effects, yielding a narrow range of large scales that contribute to the variance of the scalar field. In this regime, the nonlinear-interactions and consequently the energy transfer though the cascade process become negligible. As a result, the asymptotic state of the turbulence quantities depends solely on the low wavenumber part

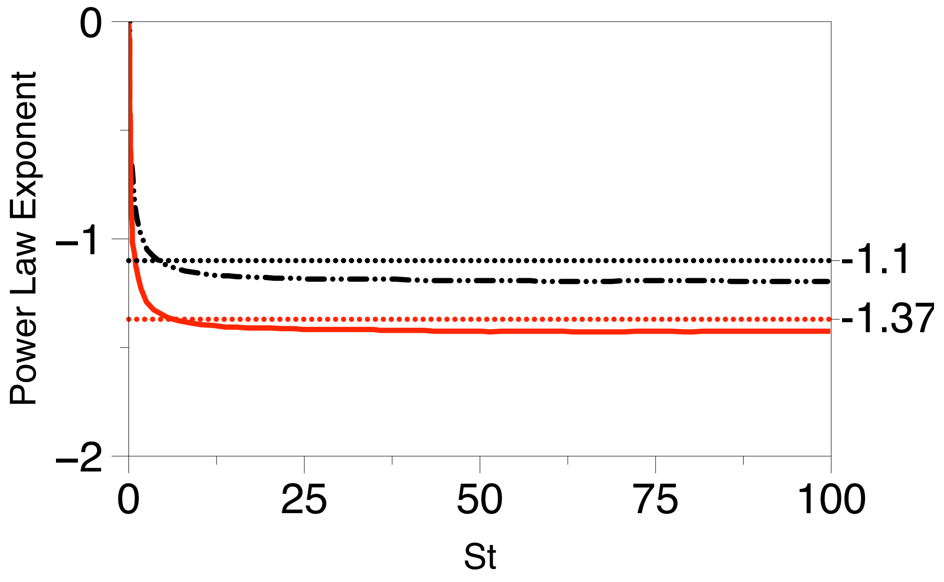

(a)

FIGURE 3.3: Predictions of the ELSE model for the time evolution of the power-law exponent of $\overline{\phi'^2}$ in the absence of mean scalar gradients. Double-dotted line (—··—) corresponds for $\{k^2, k^2\}$ low-wave number spectra, solid line (———) to $\{k^4, k^4\}$ spectra. Comparison is made with the asymptotic values of the LES predictions of Chasnov [16] (horizontal lines).

of the spectrum and the molecular diffusivity. In this case, the model equations simplify to

$$\frac{d\kappa}{dt} = -\nu\tilde{\omega}^2\,, \tag{3.64a}$$

$$\frac{d\tilde{\omega}}{dt} = -\nu C_{\tilde{\omega}^2_\nu}\frac{\tilde{\omega}^3}{\kappa}\,, \tag{3.64b}$$

$$\frac{d\lambda}{dt} = -\gamma\tilde{a}^2\,, \tag{3.64c}$$

$$\frac{d\tilde{a}}{dt} = -C_{\tilde{a}^2_\gamma}\gamma\frac{\tilde{a}^3}{\lambda}\,. \tag{3.64d}$$

The solution of eq. (3.64) is

$$(\frac{\tilde{\omega}}{\tilde{\omega}_o}) = (\frac{\kappa}{\kappa_o})^{C_{\tilde{\omega}^2_\nu}}\,, \tag{3.65a}$$

$$\frac{\kappa}{\kappa_o} = [1 + (2C_{\tilde{\omega}^2_\nu} - 1)\nu\frac{\tilde{\omega}^2_o}{\kappa_o}t]^{-1/[2C_{\tilde{\omega}^2_\nu}-1]}\,, \tag{3.65b}$$

$$(\frac{\tilde{a}}{\tilde{a}_o}) = (\frac{\lambda}{\lambda_o})^{C_{\tilde{a}^2_\gamma}}\,, \tag{3.65c}$$

$$\frac{\lambda}{\lambda_o} = [1 + (2C_{\tilde{a}^2_\gamma} - 1)\gamma\frac{\tilde{a}^2_o}{\lambda_o}t]^{-1/[2C_{\tilde{a}^2_\gamma}-1]}\,. \tag{3.65d}$$

At very large times, the solution for the passive scalar variables approaches the following asymptotic states

$$(\frac{\lambda}{\lambda_o}) \sim t^{-1/[2C_{\tilde{a}^2_\gamma}-1]}\,, \tag{3.66a}$$

$$(\frac{\tilde{a}}{\tilde{a}_o})^2 \sim t^{-2C_{\tilde{a}^2_\gamma}/[2C_{\tilde{a}^2_\gamma}-1]}\,. \tag{3.66b}$$

Table 3.4 summarizes the predictions for the asymptotic states of the turbulent variables using dimensional analysis and similarity arguments. The independence of the passive scalar quantities from the velocity spectrum is a consequence of the linearization of their transport equations for this case.

Spectra	κ	$\overline{\phi'^2}$	$\overline{\omega'^2}$	$\overline{a'^2}$
$\{k^2, k^2\}$	$B_o(\nu t)^{-3/2}$	$C_o(\gamma t)^{-3/2}$	$B_o(\nu t)^{-5/2}$	$C_o(\gamma t)^{-5/2}$
$\{k^4, k^4\}$	$B_2(\nu t)^{-5/2}$	$C_2(\gamma t)^{-5/2}$	$B_2(\nu t)^{-7/2}$	$C_2(\gamma t)^{-7/2}$
$\{k^2, k^4\}$	$B_o(\nu t)^{-3/2}$	$C_2(\gamma t)^{-5/2}$	$B_o(\nu t)^{-5/2}$	$C_2(\gamma t)^{-7/2}$
$\{k^4, k^2\}$	$B_2(\nu t)^{-5/2}$	$C_o(\gamma t)^{-3/2}$	$B_2(\nu t)^{-7/2}$	$C_o(\gamma t)^{-5/2}$

TABLE 3.4: Summary of the predictions for the asymptotic state of the turbulent statistics at the final period of freely decay turbulence for different combinations of low wave-spectra.

The model constant $C_{\tilde{a}^2_\gamma}$ can be determined by matching the asymptotic states predicted by the ELSE model to the corresponding predictions of dimensional analysis shown in Table 3.4. For a passive scalar spectrum with a k^2 low wavenumber behavior, this leads to

$$-\frac{1}{2C_{\tilde{a}^2_\gamma}-1} = -\frac{3}{2} \Rightarrow C_{\tilde{a}^2_\gamma} = 5/6\,. \tag{3.67}$$

If instead the low wave-number spectrum of the passive scalar varies as k^4, we have

$$-\frac{1}{2C_{\tilde{a}^2_\gamma}-1} = -\frac{5}{2} \Rightarrow C_{\tilde{a}^2_\gamma} = 7/10\,. \tag{3.68}$$

For a low wave-number spectrum that varies as k^2, setting $C_{\tilde{a}^2_\gamma} = 5/6$ in the asymptotic expression for $\tilde{a}^2$ yields $\tilde{a}^2 \sim t^{-5/2}$, which is consistent to the dimensional analysis. If instead the low wave-number spectrum varies as k^4, setting $C_{\tilde{a}^2_\gamma} = 7/10$ in the asymptotic expression for $\tilde{a}^2$ yielding $\tilde{a}^2 \sim t^{-7/2}$, which again agrees with the dimensional analysis.

3.6.3 Apriori testing

Having determined the model constants for the dissipation rates ϵ and ϵ_ϕ, we can perform an a priori test of the functional forms given in equations (3.28) and (3.46) by using available

DNS data. For example, when used with eq. (3.25), the two models yield the timescales ratio $\mathcal{R}$

$$\mathcal{R} \equiv \frac{\tau}{\tau_\phi} = \frac{3 r_{sq} d^s_{qm} r_{ms}}{f_{ij} d_{ji}} \, . \tag{3.69}$$

The form of Eq. (3.69) exhibits the expected dependence of $\mathcal{R}$ on the large-scale structure of the two fields, which is introduced through the structure tensors. For a priori test, we have used values for the structure tensor components given in the DNS work Kassinos et al. [47] for the case of homogeneous shear with a transverse scalar gradient, which yields the value $\mathcal{R} = 1.69$. While Kassinos et al. [47] did not report $\mathcal{R}$, their simulations results were in close agreement with those of Brethouwer [46] which reported a value of $\mathcal{R} = 1.71$. The good agreement between the two values provides an indication for the validity of the proposed models, since the ELSE model has not been calibrated for this case.

3.6.4 Validation of the scalar scales model: isotropic turbulence with imposed mean scalar gradient

Before we proceed to the full validation of the extended IPRM model, we consider a simple case where the ELSE model for the turbulence scales can be independently validated. In the presence of mean scalar gradient in isotropic turbulence at high Reynolds and Peclet number, the evolution of the passive scalar field is driven by the scalar-flux vector, which is present in the production term. The system of equations (3.54) then becomes

$$\frac{d\kappa}{dt} = -C_\epsilon \chi \kappa \tilde{\omega} \, , \tag{3.70a}$$

$$\frac{d\tilde{\omega}}{dt} = -[C_{\tilde{\omega}^2_T} - \phi C_{\tilde{\omega}^2_P}]\tilde{\omega}^2 \, , \tag{3.70b}$$

$$\frac{d\lambda}{dt} = -\overline{u'_i \phi'} \Lambda_i - C_\phi \chi^\phi \lambda \tilde{\omega} \, , \tag{3.70c}$$

$$\frac{d\tilde{a}}{dt} = -[C_{\tilde{\omega}^2_T} - \phi^\phi C_{\tilde{\omega}^2_P}]\tilde{a}\tilde{\omega} + [C_{\tilde{\omega}^2_T} - \phi^\phi C_{\tilde{\omega}^2_P}]\Lambda \tilde{\omega} \, . \tag{3.70d}$$

The simplicity of this test case (no mean velocity gradients) means that algebraic models of the scalar flux vector can be expected to produce reasonable results. Here, we use the explicit model of Younis et al. [56],

$$\begin{aligned} -\overline{u'_i \phi'} &= C_1 \frac{\kappa^2}{\epsilon} \Lambda_i + C_2 \frac{\kappa}{\epsilon} \overline{u'_i u'_j} \Lambda_j + C_3 \frac{\kappa^3}{\epsilon^2} \bar{u}_{i,j} \Lambda_j \\ &+ C_4 \frac{\kappa^2}{\epsilon^2} (\overline{u'_i u'_k} \bar{u}_{j,k} + \overline{u'_j u'_k} \bar{u}_{i,k}) \Lambda_j \, , \end{aligned} \tag{3.71}$$

which in the present case reduces to

$$-\overline{u_i'\phi'} = (C_1 + \frac{2}{3}C_2)\frac{\kappa^2}{\epsilon}\Lambda_i \, , \tag{3.72}$$

with standard values assigned to the model constants, namely, $C_1 = -4.55 \times 10^{-2}$ and $C_2 = 3.73 \times 10^{-1}$.

Fig. 3.4 shows a comparison of the predictions of the ELSE model for power law exponent for the scalar variance with the corresponding LES computations of Chasnov [16]. A good agreement is achieved. As shown in Fig. 3.5, a good agreement between the ELSE model and the LES of Chasnov[16] is also obtained for the scalar dissipation rate. Finally, Fig. 3.6 shows a comparison of model predictions for the ratio of the scalar-variance production to dissipation, $-\beta\overline{u_2'\phi'}/\epsilon_\phi$ to the corresponding LES results. For this comparison, β represents the magnitude of the mean scalar gradient. An excellent agreement is achieved, clearly showing that the model is sensitive to the choice of the different spectrum combinations.

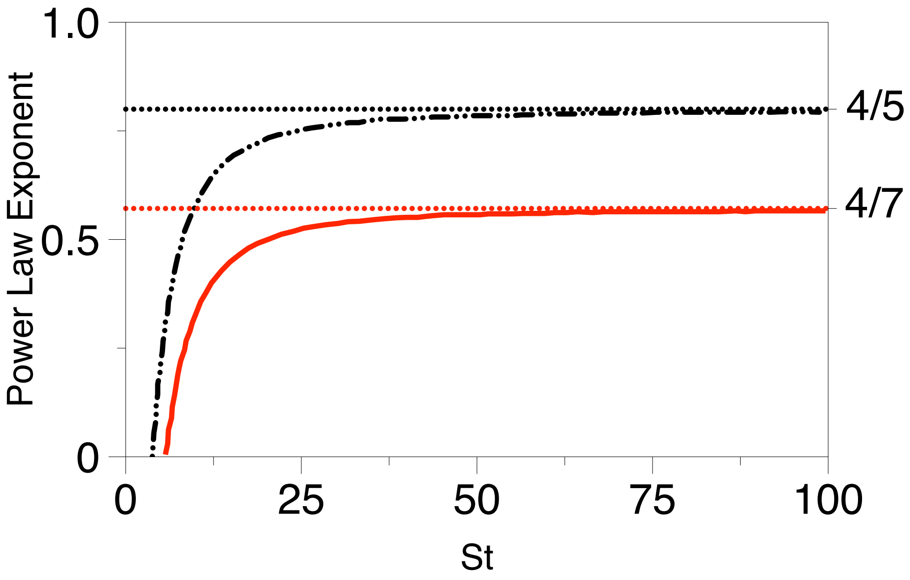

(A)

FIGURE 3.4: Predictions of the ELSE model for the time evolution of the power-law exponent of $\overline{\phi'^2}$ in the presence of mean scalar gradients. Double-dotted line (—··—) corresponds for $\{k^2, k^2\}$ low-wave number spectra, solid line (———) to $\{k^4, k^4\}$ spectra. Comparison is made with the asymptotic values of the LES predictions of Chasnov [16] (horizontal lines).

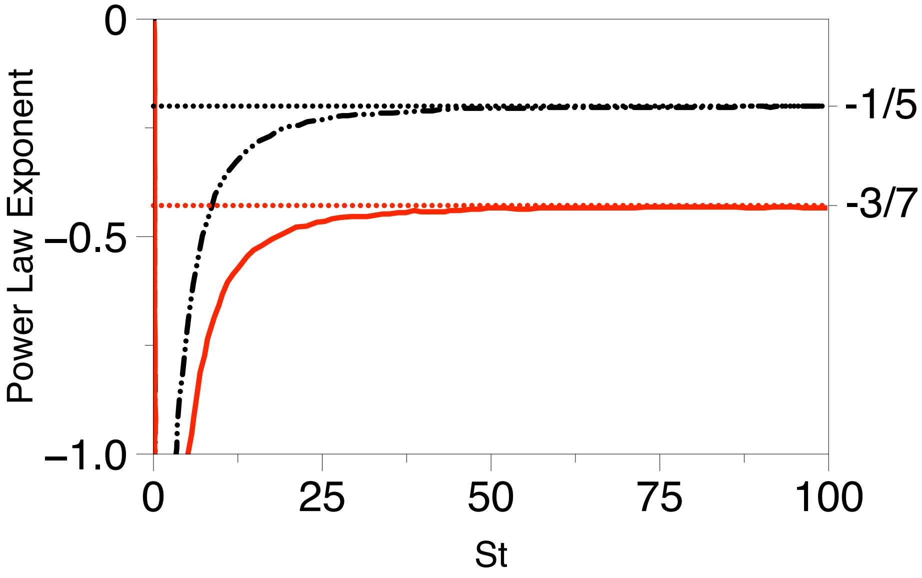

(A)

Figure 3.5: As in Fig. 3.4 but for the passive scalar dissipation rate ϵ_ϕ.

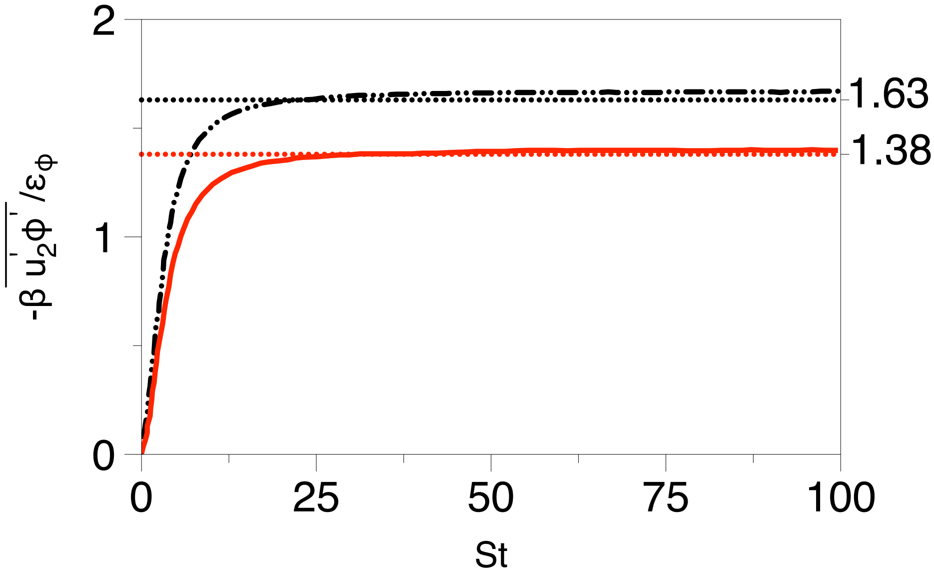

(A)

Figure 3.6: As in Fig. 3.4 but for the ratio of the scalar-variance production to passive scalar dissipation rate ϵ_ϕ.

3.7 Validation of the complete IPRM model for passive scalar transport

In this section, we present the validation of the complete IPRM model for passive scalar transport. For easy reference, the complete set of equations defining the model is summarized in Appendix A.1.

3.7.1 2D-2C isotropic decaying turbulence.

For 2D-2C isotropic turbulence at high Re_T and Pe, and in the absence of mean scalar or velocity gradients, eq. (3.54) reduces to

$$\frac{d\kappa}{dt} = 0\,, \tag{3.73a}$$

$$\frac{d\tilde{\omega}}{dt} = -C_{\tilde{\omega}_T^2}\tilde{\omega}^2\,, \tag{3.73b}$$

$$\frac{d\lambda}{dt} = -C_\phi \chi^\phi \lambda \tilde{\omega}\,, \tag{3.73c}$$

$$\frac{d\tilde{a}}{dt} = -C_{\tilde{\omega}_T^2}\tilde{a}\tilde{\omega}\,. \tag{3.73d}$$

The solution of eq. (3.73) is

$$\frac{\kappa}{\kappa_o} = 1\,, \tag{3.74a}$$

$$\frac{\tilde{\omega}^2}{\tilde{\omega}_o^2} = \frac{1}{[1 + C_{\tilde{\omega}_T^2}\tilde{\omega}_o t]^2}\,, \tag{3.74b}$$

$$\frac{\lambda}{\lambda_o} = [1 + C_{\tilde{\omega}_T^2}\tilde{\omega}_o t]^{-\chi^\phi C_\phi / C_{\tilde{\omega}_T^2}}\,, \tag{3.74c}$$

$$\frac{\tilde{a}^2}{\tilde{a}_o^2} = \frac{1}{[1 + C_{\tilde{\omega}_T^2}\tilde{\omega}_o t]^2}\,. \tag{3.74d}$$

At very large times, the power law exponent of λ tends to $-\chi^\phi C_\phi / C_{\tilde{\omega}_T^2}$. Furthermore, if we take the axis of independence to be x_3 without the loss of generality, the asymptotic limit of the structure tensors is

$$r_{ij} = d_{ij} = d^s_{ij} = \begin{pmatrix} 1/2 & 0 & 0 \\ 0 & 1/2 & 0 \\ 0 & 0 & 0 \end{pmatrix}, \quad f_{ij} = \begin{pmatrix} 0 & 0 & 0 \\ 0 & 0 & 0 \\ 0 & 0 & 1.0 \end{pmatrix},$$

yielding a value of $\chi^\phi = 9 r_{iq} d^s_{qj} r_{ji} = \frac{9}{4}$. Thus, the power law exponent becomes

$$\frac{\chi^\phi_{\text{2D-2C}} C_\phi}{C_{\tilde{\omega}_T^2}} = \frac{9}{4}\frac{C_\epsilon}{C_{\tilde{\omega}_T^2}} = \delta\,. \tag{3.75}$$

The value of parameter δ depends on the choice of the energy spectrum. It becomes 1.27 or 1.5 for $\{k^2, k^2\}$ or $\{k^4, k^4\}$ spectra respectively, while Lesieur [54] suggested a value around 2.0.

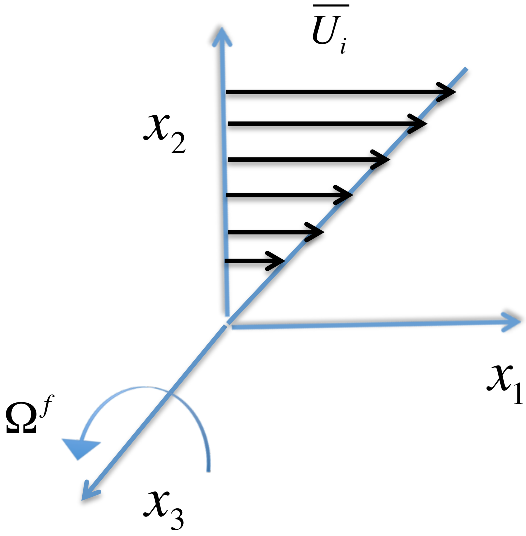

FIGURE 3.7: Sketch of the mean velocity profile, along with the frame rotation vector.

3.7.2 Homogeneous shear in fixed and rotating frames

Next, we consider the case of homogeneous shear in fixed and rotating frames at high Reynolds and Peclet numbers. Both transverse and streamwise mean scalar gradients are considered. These simple canonical cases are of particular interest because of their relevance to geophysical flows and industrial applications, such as turbomachinery flows. The configuration of the mean flow is given by

$$G_{ij} = S\delta_{i1}\delta_{j2}\,, \quad \Omega_i^f = \Omega^f\delta_{i3}\,, \quad \Lambda_i = S_\phi\delta_{i\alpha}\,, \tag{3.76}$$

where the no-summation (greek) index α denotes the direction of the mean scalar gradient, which can be either in the transverse or streamwise direction. S denotes the mean shear rate, S_ϕ is the magnitude of the mean scalar gradient, Ω_i^f is the frame-rotation vector, where $\Omega^f = -\Omega_{12}^f$, so that positive values of Ω^f corresponds to a frame counter-rotating with respect to the rotation sense of the mean shear S (see Figure 3.7).

During the validation process, a number of dimensionless parameters are computed and compared to the corresponding DNS and experimental data. The first of these, used to determine the initial conditions of each case, is the shear parameter ratio S^*, defined as

$$S^* = \frac{Sq^2}{\epsilon}\,, \tag{3.77}$$

which measures how "slow" or "rapid" the initial flow configuration is. Another important parameter is the ratio of the strengths of passive scalar and velocity fluctuations B, defined as

$$B = \frac{S\theta'}{S_\phi q'}\,, \quad \theta' = \sqrt{\overline{\phi'^2}}\,, \quad q' = \sqrt{q^2}\,. \tag{3.78}$$

In the presence of frame-rotation, another important parameter is the ratio of the frame rotation rate $\Omega^f = -\Omega^f_{12}$ to the mean shear rate S, given by

$$\eta_f = \frac{2\Omega^f}{S}\,. \tag{3.79}$$

The case $\eta_f = 0.5$ is of particular interest since it corresponds to the most unstable case, where the growth of turbulent kinetic energy is maximized, as shown in the bifurcation diagram in Fig. 3.8. Apart from this case, additional frame-rotating cases are considered ($\eta_f = -0.5$ and $\eta_f = 1.0$), along with the non-rotating case ($\eta_f = 0.0$).

A useful parameter in order to test the ability of the proposed model to capture the anisotropic nature of the turbulent field, is the inclination angle of turbulent scalar-flux vector α_ϕ. Since no scalar-flux is expected along the spanwise (x_3) direction, α_ϕ is defined relative to the streamwise direction (x_1) as

$$\alpha_\phi = \tan^{-1}\left(\frac{\overline{u'_2\phi'}}{\overline{u'_1\phi'}}\right). \tag{3.80}$$

Another parameter is the scalar-velocity correlation coefficient, denoted as ζ_i^α, which measures the degree of correlation between the scalar and velocity fields, defined as

$$\zeta_i^\alpha = \left(\frac{\overline{u'_i\phi'_\alpha}}{\sqrt{R_{ii}}\theta'_\alpha}\right), \tag{3.81}$$

where no-summation is performed on the indices. For example, ζ_1^2 refers to the turbulent flux of a scalar in the streamwise direction (x_1) in the presence of a transverse (x_2) mean scalar gradient. For zero values, the two fields are completely uncorrelated, whereas for large-values, a strong correlation is implied.

In all simulations involving homogeneous shear, the initial passive scalar field is zero, yielding an initial B parameter $B_0 = 0$, which subsequently evolves under the combined action of the turbulent velocity and the mean scalar fields respectively.

3.7.2.1 Homogeneous shear in the presence of transverse mean scalar gradient

We consider a transverse mean scalar gradient imposed under conditions that correspond to cases studied in the DNS work of Kassinos et al. [47]. First, we consider the case with an

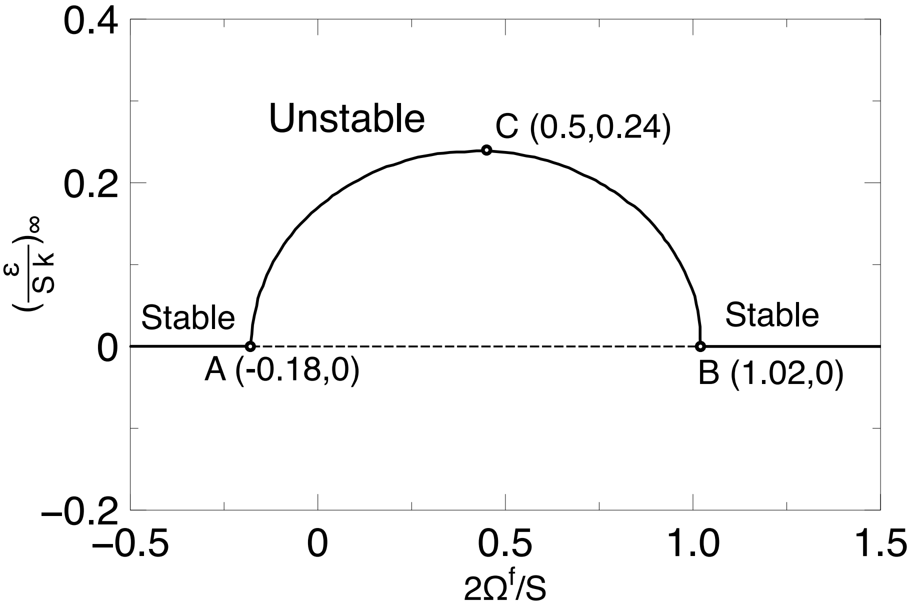

FIGURE 3.8: Bifurcation diagram for homogenous turbulence in rotating frames.

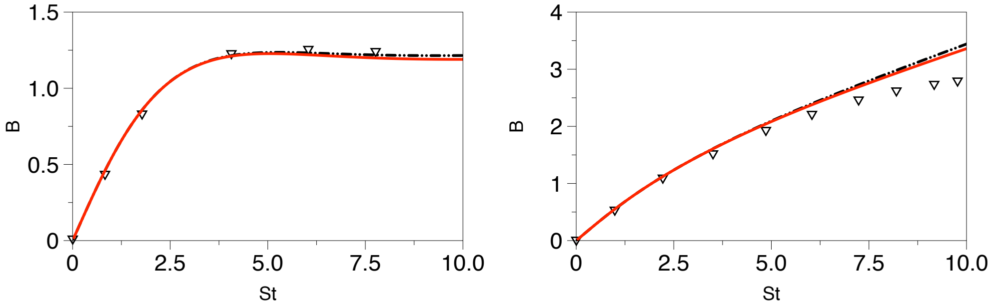

(A)

(B)

FIGURE 3.9: IPRM model predictions for the time evolution of relative strength of the scalar fluctuations B. Double-dotted lines (—··—) correspond to $\{k^2, k^2\}$ low-wave number case, solid lines (———) correspond to $\{k^4, k^4\}$ (———) low-wave number case. Comparison is made with DNS results (symbols) of Kassinos et al.[47] for homogeneous shear turbulence with transverse mean scalar-gradient at $Sq_o^2/\epsilon_o = 35.85$. Two different frame rotation rates are shown: (a) $\eta_f = 0.5$; (b) $\eta_f = 1.0$.

initial shear parameter $S_0^* = 35.85$, corresponding to case C0.2.0 in Kassinos et al.[47] In Fig. 3.9 we show predictions for the dimensionless ratio B for two different frame-rotation rates, particularly $\eta_f = 0.5$ and 1.0. Results are shown assuming either a $\{k^2, k^2\}$ or a $\{k^4, k^4\}$ spectra combination. The discrepancies between the two spectra choices are trivial, reaching up to 3% for large times. Thus, for the sake of space, we hereafter report results using only one spectra combination for each case.

In Fig. 3.10 IPRM predictions are compared to DNS results [47] for the time evolution of B using $\{k^4, k^4\}$ spectra combinations for four frame-rotation rates. Fair predictions for

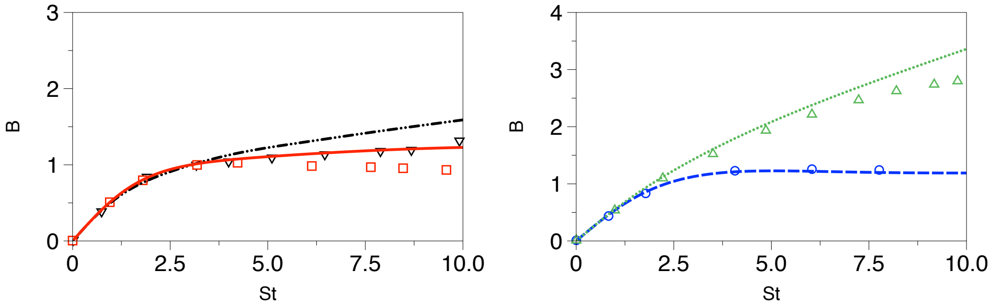

(A) (B)

FIGURE 3.10: IPRM model predictions (lines) for the time evolution of relative strength of the scalar fluctuations B using $\{k^4, k^4\}$ low wave-number spectra. Comparison is made with DNS results (symbols) of Kassinos et al.[47] for homogeneous shear turbulence with transverse mean scalar-gradient at $Sq_o^2/\epsilon_o = 35.85$. Four different frame rotation rates are shown: (a) (∇, —··—) $\eta_f = -0.5$; ($\square$, ———) $\eta_f = 0.0$; and (b) ($\bigcirc$, - - - -) $\eta_f = 0.5$; ($\triangle$, ··········) $\eta_f = 1.0$.

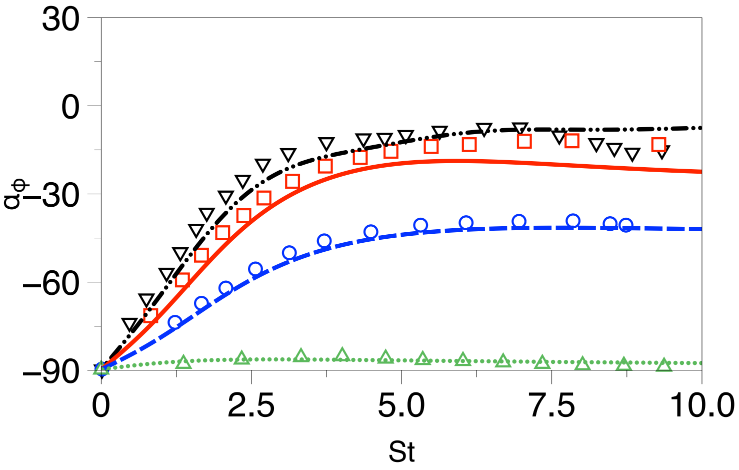

FIGURE 3.11: IPRM model predictions (lines) for the time evolution of the angle of the scalar flux vector α_ϕ using $\{k^4, k^4\}$ low wave-number spectra. Comparison is made with DNS results (symbols) of Kassinos et al.[47] for homogeneous shear turbulence with transverse mean scalar-gradient at $Sq_o^2/\epsilon_o = 35.85$. Four different frame rotation rates are shown: (∇, —··—) $\eta_f = -0.5$; ($\square$, ———) $\eta_f = 0.0$; ($\bigcirc$, - - - -) $\eta_f = 0.5$; ($\triangle$, ··········) $\eta_f = 1.0$.

the stationary frame and the co-rotating case ($\eta_f = -0.5$) are shown in Fig. 3.10a, while the closure captures quite well the remaining two cases, especially the most unstable case $\eta_f = 0.5$ (Fig. 3.10b).

The time advancement of the inclination angle α_ϕ is presented in Fig. 3.11, where the strong influence of the frame rotation is profound. A good agreement with the corresponding DNS data is achieved, especially for $\eta_f = 0.5$ and 1.0.

The evolution history of the scalar-velocity correlation coefficient ζ_i^α is shown in Fig. 3.12. For $\eta_f = -0.5$, model predictions are in very good agreement with the DNS values. For the

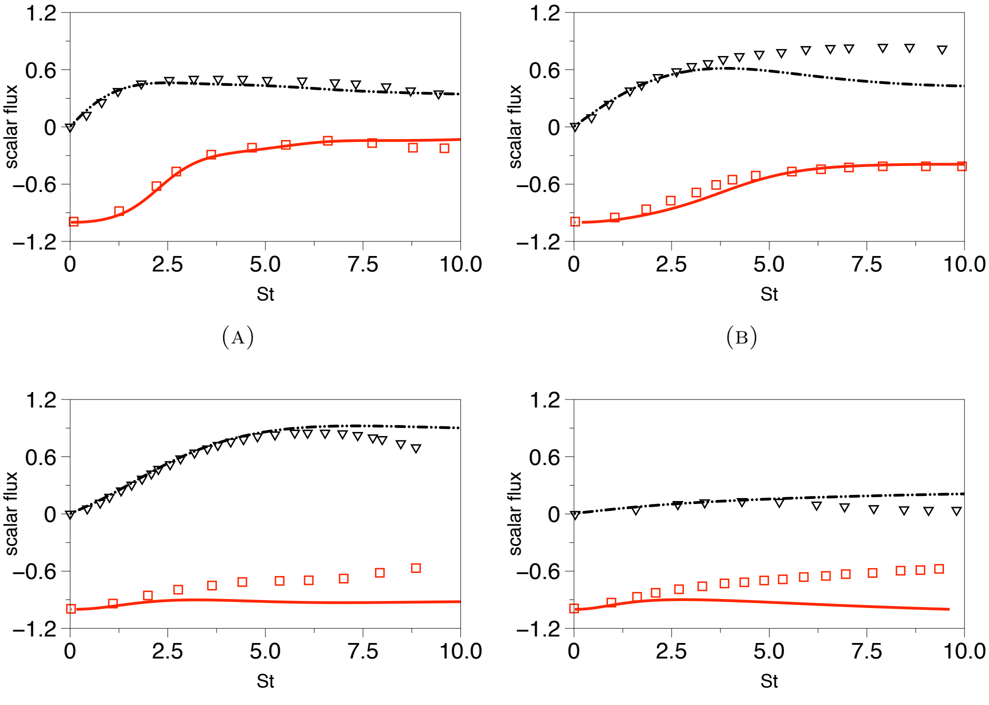

(A) (B)

(C) (D)

Figure 3.12: IPRM model predictions (lines) for the time evolution of the scalar flux coefficient ζ_i^α using $\{k^4, k^4\}$ low wave-number spectra. Comparison is made with DNS results (symbols) of Kassinos et al. [47] for homogeneous shear turbulence with transverse mean scalar-gradient at $Sq_o^2/\epsilon_o = 35.85$: (∇,—··—), ζ_1^2; (□,———), ζ_2^2. Four different frame rotation rates are shown: (a) $\eta_f = -0.5$; (b) $\eta_f = 0.0$; (c) $\eta_f = 0.5$; (d) $\eta_f = 1.0$.

fixed frame case, IPRM captures accurately ζ_2^2, whereas fair predictions are obtained for ζ_1^1. For $\eta_f = 0.5$ and $\eta_f = 1.0$, the closure agrees well with the DNS data for ζ_1^2 except at large times.

The initial shear parameter is $S_0^* = 35.85$ in this case, corresponding to a somewhat rapid mean deformation. Hence, the importance of the contribution of the effective gradients (non-linear terms) in the IPRM in the time evolution of the turbulent fields needs to investigated. Thus, we perform additional computations using the linear PRM model, which corresponds to exact RDT computations. Fig. 3.13 shows IPRM and PRM predictions for the parameter B. Comparison is made again to the DNS data of Kassinos et al. [47] for the C0.2.0. The improvement due to the inclusion of the effective gradients is significant for $\eta_f = 0.5$ and 1.0, whereas the predictions of the RPM (RDT) and IPRM models for the remaining two cases $\eta_f = -0.5$ and $\eta_f = 0.0$ are similar.

Next, we consider case C0.3.0 from the DNS work of Kassinos et al., [47] which is based on the same configuration, but for a much weaker mean shear rate, corresponding to an initial shear parameter $S_0^* = 3.58$. Fig. 3.14 shows the corresponding comparison between

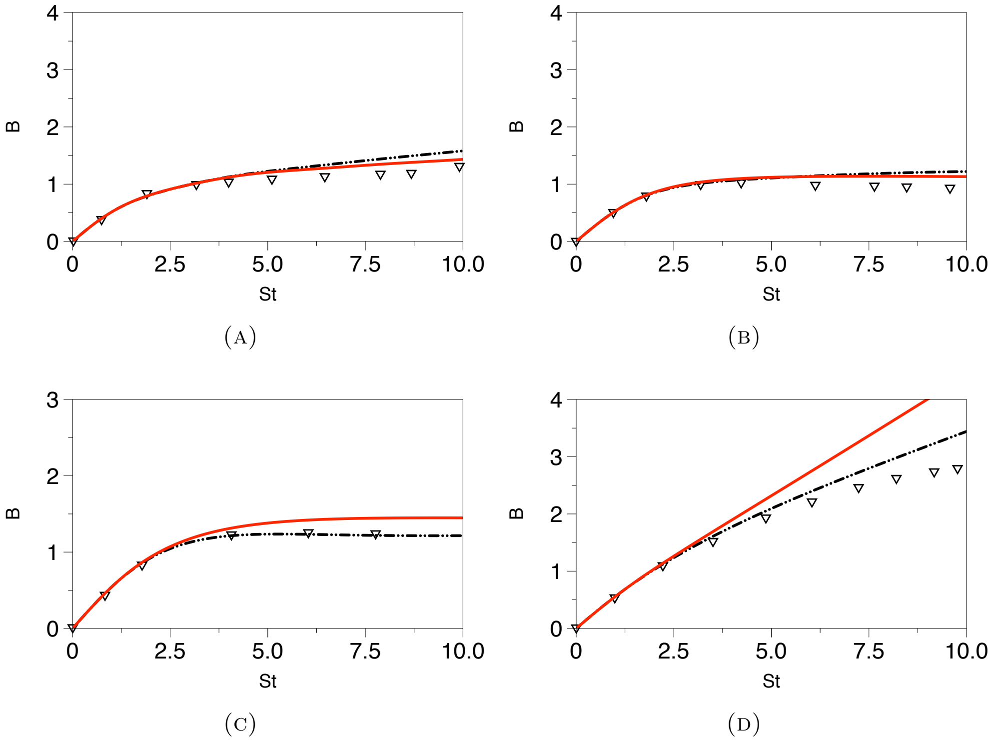

(a)

(b)

(c)

(d)

Figure 3.13: IPRM (—··—) and PRM (———) predictions using $\{k^2, k^2\}$ as the low wave-number spectra. Comparison is made with DNS results (symbols) of Kassinos et al. [47] for homogeneous shear turbulence with transverse mean scalar-gradient at $Sq_o^2/\epsilon_o = 35.85$. Four different frame rotation rates are shown: (a) $\eta_f = -0.5$; (b) $\eta_f = 0.0$; (c) $\eta_f = 0.5$; and (d) $\eta_f = 1.0$.

IPRM and PRM predictions for the parameter B, yielding similar behavior to the previous rapid case. Fig. 3.15 shows a comparison of the parameter B predictions of IPRM with the corresponding DNS predictions. As in the previous case, the model produces good results for $\eta_f = 0.5$ and 1.0, while when $\eta_f = -0.5$ and 0.0 it tends to overestimate B values at large total shear. The relative small differences between the IPRM and PRM predictions point to the fact that, even at this relative weak shear rate, linear effects play a significant role in the evolution of the turbulence fields, at least for the range of total shear shown.

Fig. 3.16 shows the corresponding comparison for the inclination angle α_ϕ. Overall, IPRM produces encouraging results, especially for $\eta_f = 0$ and $\eta_f = 0.5$, being able to capture satisfactory the DNS values at large times.

Next, we compare the predictions of IPRM model for the scalar-velocity correlation coefficient ζ_i^α with the DNS data (Fig. 3.17). IPRM achieves very good agreement with the DNS for $\eta_f = -0.5$ and 0.0 for both components ζ_1^2 and ζ_2^2. For $\eta_f = 0.5$ and 1.0, the IPRM provides fair predictions for ζ_1^2, while it underpredicts the value for ζ_2^2, a trend that was also observed in the C0.2.0 case.

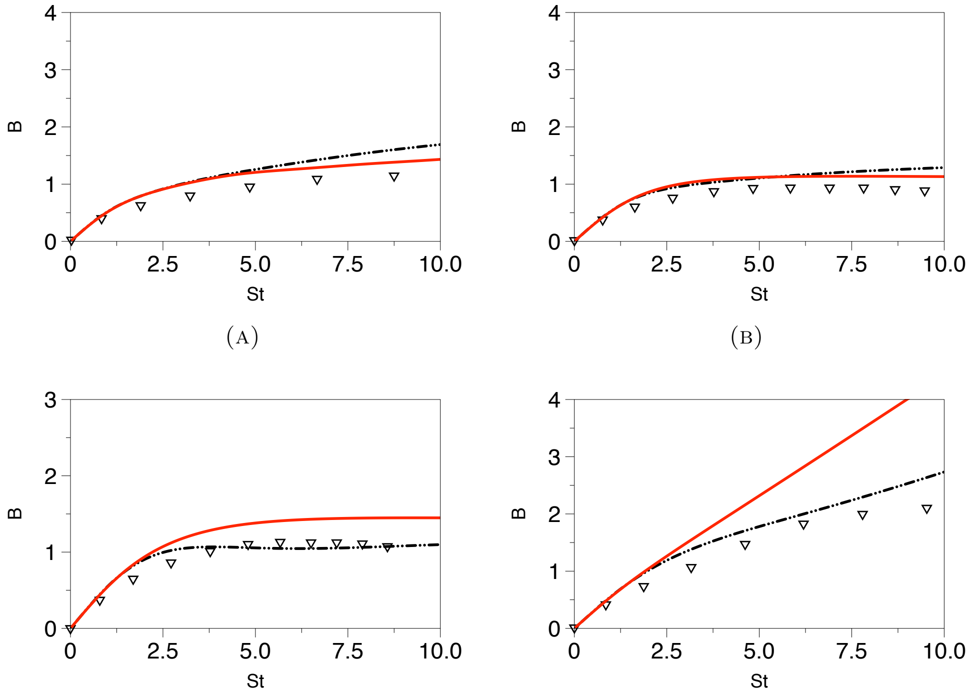

(A) (B)

(C) (D)

FIGURE 3.14: As in Fig. 3.13 but for $Sq_o^2/\epsilon_o = 3.58$.

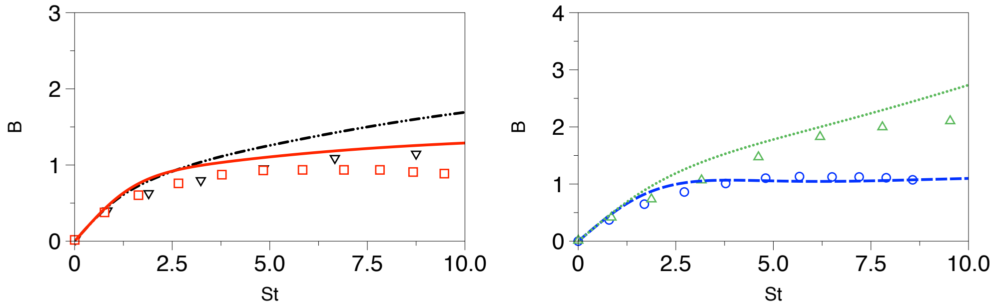

(A) (B)

FIGURE 3.15: As in Fig. 3.10 but for $Sq_o^2/\epsilon_o = 3.58$.

3.7.2.2 Homogeneous shear in the presence of streamwise mean scalar gradient

In this subsection, we consider homogeneous shear in the presence of streamwise mean scalar gradient. Computations are conducted for flow conditions that correspond to the DNS results of Brethouwer [46]. The initial shear parameter for all computations is set to be $S_0^* = 36.0$, while the initialization process for the passive-scalar field is similar to that used by Kassinos et al.[47], i.e. starting from a zero initial passive scalar field, corresponding to a zero value for the B parameter. As before, we perform computations for four frame rotation rates, $\eta_f = -0.5, 0, 0.5$ and 1.0. Fig. 3.18a shows results for the relative strength of the scalar fluctuations

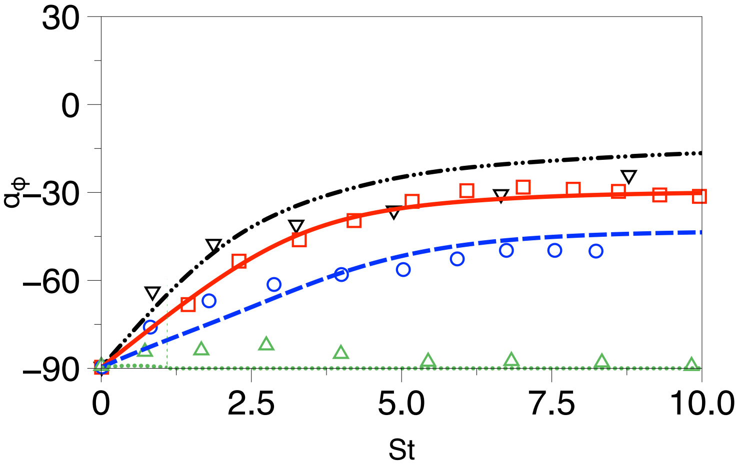

FIGURE 3.16: As in Fig. 3.11 but for $Sq_o^2/\epsilon_o = 3.58$.

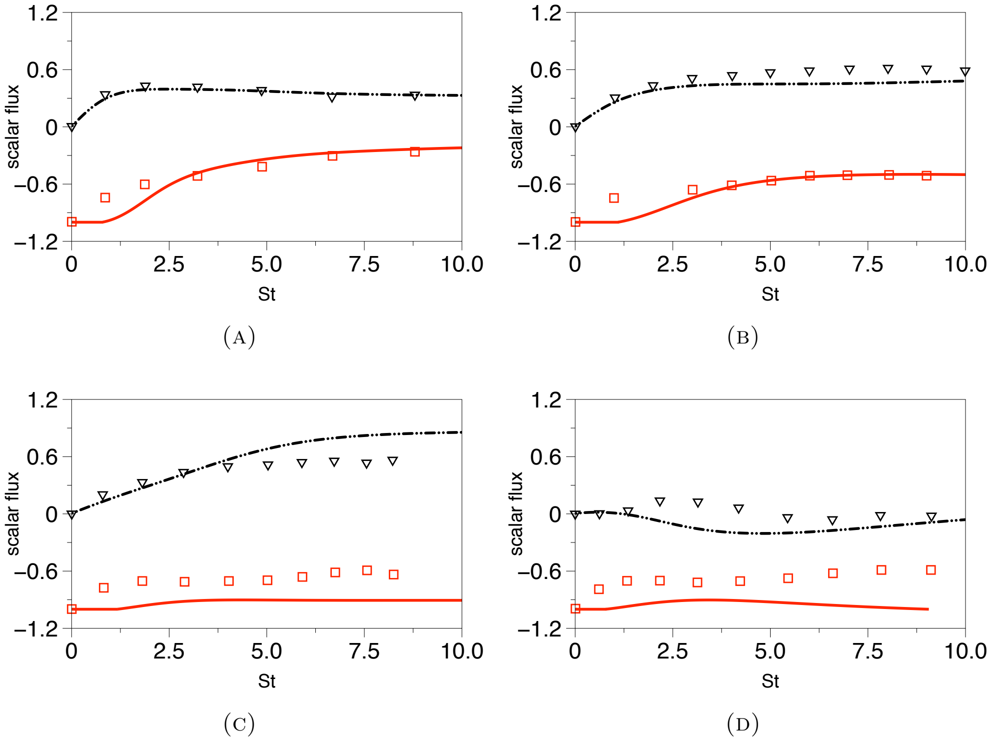

(A)

(B)

(C)

(D)

FIGURE 3.17: As in Fig. 3.12 but for $Sq_o^2/\epsilon_o = 3.58$.

B. In all cases, IPRM achieves excellent agreement with the DNS results, revealing its sensitivity to the direction of the mean scalar gradient. Fig. 3.18b shows the corresponding comparison for the inclination angle. As expected, IPRM predictions agree quite well with the DNS data for all cases. Especially for the co-rotating case $\eta_f = -0.5$, IPRM captures surprisingly well the shape of the profile during its transition from negative to positive values.

Fig. 3.19 shows the corresponding comparison for the scalar flux coefficient. In consistence

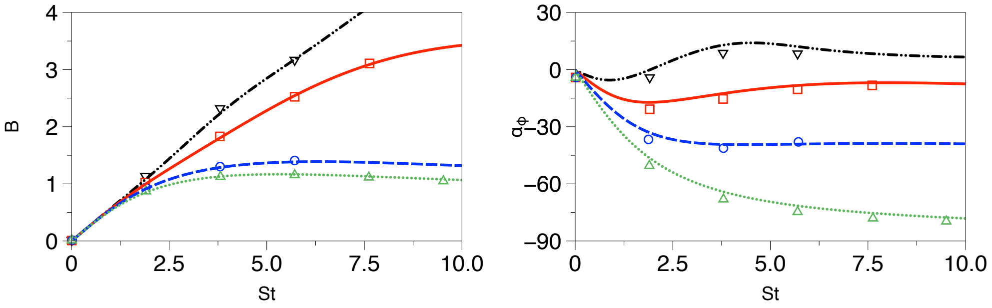

(A) (B)

FIGURE 3.18: IPRM model predictions (lines) for the time evolution of characteristics of the passive scalar field using $\{k^4, k^4\}$ low wave-number spectra. Shown on the left (a) is the relative strength of the scalar fluctuations B, and on the right (b) the angle of the scalar flux vector α_ϕ. Comparison is made with DNS results (symbols) of Brethouwer [46] for homogeneous shear turbulence with streamwise mean scalar-gradient at $Sq_o^2/\epsilon_o = 36.0$. Four different frame rotation rates are shown: (∇, —··—) $\eta_f = -0.5$; (□, ———) $\eta_f = 0.0$; (○, - - - -) $\eta_f = 0.5$; (△, ··········) $\eta_f = 1.0$.

with the results for α_ϕ, we see that IPRM captures accurately the time evolution of both ζ_1^1 and ζ_2^1 for $\eta_f = -0.5$. Good predictions are obtained for the remaining three cases, except for the predictions regarding ζ_1^1 at St larger than 5 for the cases $\eta_f = 0.0$ and $\eta_f = 1.0$., where the IPRM tends to underestimate its magnitude.

3.7.3 Irrotational axisymmetric contraction

Here, we consider the case of homogeneous turbulence deformed by irrotational axisymmetric contraction in the presence of a transverse mean scalar gradient at high Reynolds and Peclet numbers. Computations are conducted for conditions that correspond to the experimental work of Gylfason and Warhaft [57]. The initial shear parameter is $S_0^* \approx 5.0$, while the imposed initial passive scalar fluctuations correspond to an initial value for the B parameter of $B_0 = 1.0$. The flow configuration for the mean field is given by

$$G_{ij} = S\delta_{i1}\delta_{j1} - \frac{S}{2}\delta_{i2}\delta_{j2} - \frac{S}{2}\delta_{i3}\delta_{j3}\,, \quad \Lambda_i = S_\phi \delta_{i2}\,, \tag{3.82}$$

where $S > 0$. Fig. 3.20a shows results for the passive scalar dissipation rate ϵ_ϕ using both $\{k^2, k^2\}$ and $\{k^4, k^4\}$ low wavenumber spectra. We observe that the IPRM predictions are close to the experimental measurements for both spectra choices, with the results corresponding to $\{k^2, k^2\}$ being in better agreement, as expected, due to the flow configuration in the experiment. Fig. 3.20b shows the corresponding comparison for the passive scalar variance $\overline{\phi'^2}$. The IPRM model predicts that scalar variance remains practically unchangeable, in good agreement with the experiments [57].

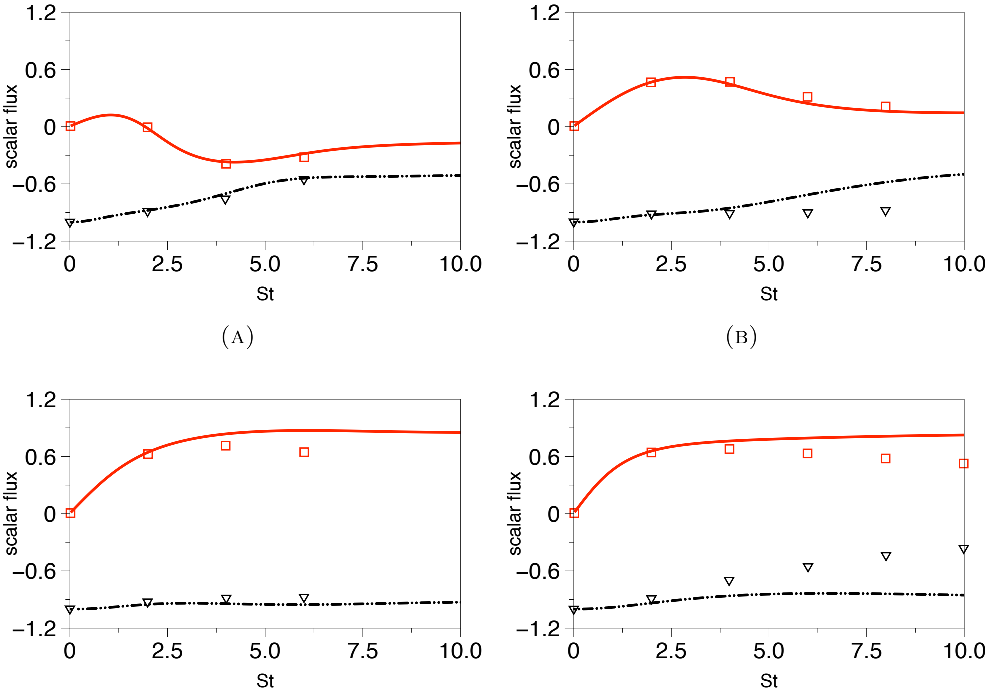

(A) (B) (C) (D)

Figure 3.19: IPRM model predictions (lines) for the time evolution of the scalar flux coefficient ζ_i^α using $\{k^4, k^4\}$ low wave-number spectra. Comparison is made with DNS results (symbols) of Brethouwer [46] for homogeneous shear turbulence with streamwise mean scalar-gradient at $Sq_o^2/\epsilon_o = 36.0$: (∇, —··—), ζ_1^1; ($\square$, ———), ζ_2^1. Four different frame rotation rates are shown: (a) $\eta_f = -0.5$; (b) $\eta_f = 0.0$; (c) $\eta_f = 0.5$; (d) $\eta_f = 1.0$.

3.8 Future plans for an algebraic four equation structure based model and initial results

In Section 3.5, we've used the triple decomposition approach to derive a set of model scale equations for the passive scalar field. These scale equations along with the corresponding scale equations for the velocity field, comprise the Extended Large-Scale Enstrophy (ELSE) turbulence scales model. The ELSE model has been formulated for use with structure-based models and it is therefore based on the assumption that information about the scalar flux vector and the one-point turbulence structure tensors is independently available. In the present work, the ESLE scales model was coupled with the IPRM, which provided all the necessary information.

We also plan to explore the coupling of the ELSE scales model with the the Algebraic Structure-Based Model (ASBM) [6, 49]. The ASBM is a one-point engineering model based on an equilibrium assumption that provides estimates of the equilibrium state of the one-point structure tensors for any given mean deformation mode. Currently, the ASBM does

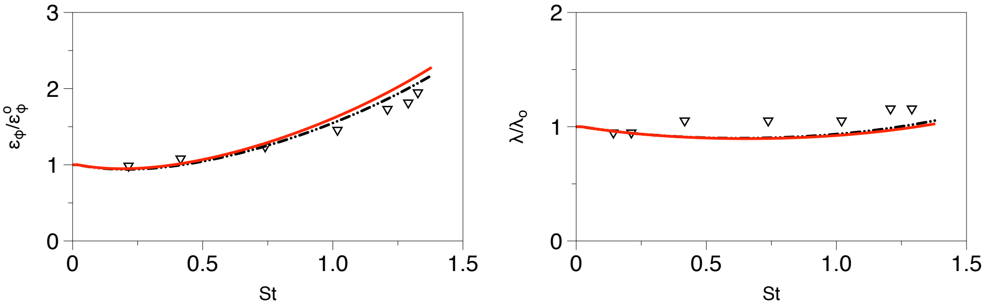

(A)

(B)

FIGURE 3.20: IPRM model predictions (lines) for the time evolution of characteristics of the passive scalar field using low wave-number spectra. Shown on the left (a) is the passive scalar dissipation rate ϵ_ϕ, and on the right (b) the passive scalar variance $\overline{\phi'^2}$. Comparison is made with the experimental measurements (symbols) of Gylfason and Warhaft [57] for homogeneous axisymmetric contraction with streamwise mean scalar-gradient at $Sq_o^2/\epsilon_o \approx 5.0$. Two different low-wave number spectra combinations are shown: (—··—) $\{k^2, k^2\}$; (———) $\{k^4, k^4\}$.

not provide estimates of the scalar dimensionality tensor d_{ij}^s, which is needed in the ELSE model. Numerical experiments that we have carried out using the Particle Representation Model (PRM) show that in the case of irrotational mean deformation, $d_{ij}^s \approx d_{ij}$ at large times, to a very good degree of approximation. This is a very attractive approximation because it affords closure of the model without the need to introduce another transport equation. While the PRM simulations show the approximation to be less accurate in the presence of mean rotation, we deemed it to be reasonable enough for use in the closure of the passive scalar model. The option to construct a more elaborate algebraic model for d_{ij}^s within the ASBM formalism, as done for d_{ij}, is not ruled out, but will only be attempted if it proves to be necessary during future evaluation of the model in complex turbulent flows. Using this approximation, the invariants that appear in the coefficients of the passive scalar model can be evaluated within the ASBM formalism, thus ensuring the self-consistency with the ELSE scales model.

In order to test the potential of incorporating the ASBM formalism in the complete model, we performed computations using two different approaches. In the first approach, the scalar-flux vector as well as the structure tensors and the associated tensor products and invariants are evaluated solely within the IPRM model, called the "pure IPRM" case. Alternatively, in the second approach named "ASBM case" only the scalar-flux vector is obtained using the IPRM model, whereas the ASBM provides all the data related to the structure tensors and their invariants. In Fig. 3.21 we show some preliminary results using both approaches for the time evolution of the B parameter for the homogeneous shear case in the presence of transverse mean scalar gradient. Two different frame-rotation rates are shown, $\eta_f = -0.5$ and 0.0, while comparison is made to DNS work of [47], particularly case C0.2.0. As we can see, the second

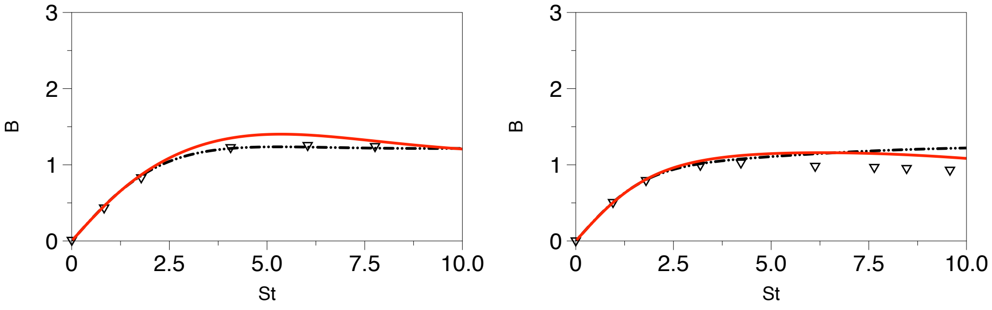

(A) (B)

FIGURE 3.21: Time evolution of the relative strength of the scalar fluctuations B using $\{k^2, k^2\}$ low wave-number spectra. Double-dotted lines (—··—) correspond for the "pure IPRM case", solid lines (———) to the case where ASBM is used to obtain the one-point structure-tensors ("ASBM case"). Comparison is made with DNS results (symbols) of Kassinos et al.[47] for homogeneous shear turbulence with transverse mean scalar-gradient at $Sq_o^2/\epsilon_o = 35.85$. Two different frame rotation rates are shown: (a) $\eta_f = -0.5$; (b) $\eta_f = 0.0$.

approach produces encouraging results, however more cases should be considered and further analysis regarding known issues related to the algebraic model should be resolved.

3.9 Conclusions

An extended IPRM model is proposed which, for the first time, provides predictions for the statistics of the passive-scalar fluctuations. A structure-based model is proposed in order to provide the turbulence scales based on a triple decomposition method of the exact passive scalar and velocity transport equations. Furthermore, we propose the use of the scalar variance and the large-scale scalar gradient variance as the two turbulence scales characterizing the scalar field. Due to the strong influence of the velocity field on the passive scalar statistics, the proposed model is coupled with the large-scale enstrophy model of RLK02. We have taken into account this fact by sensitizing the passive scalar model equations into products of the structure tensors and by modeling the dissipation rate in terms of the large-scale enstrophy.

The model parameters at high Re_T and Pe numbers were determined simply by matching the decay rates of the scalar variance in isotropic, unstrained turbulence and in the absence of mean scalar gradient. Model predictions exhibit very good agreement with similarity arguments for the decay rate of the scalar gradient variance and scalar dissipation rate. Additionally, the model has been tested in isotropic turbulence at high Re_T, Pe, this time in the presence of mean scalar gradient. The newly proposed model provided very good agreement with LES predictions and similarity arguments for the asymptotic decay rates of the scalar variance and of the ratio of the scalar variance production to scalar dissipation rate for different combinations of the low wave number spectra, showing its sensitivity in the choice of spectrum. For 2D-2C turbulence the model indicates correctly the presence of a direct cascade for the scalar variance, however it underpredicts the decay rate of the scalar variance. In order to further ascertain the performance of the model, the case of homogeneous shear flow in the presence either of transverse or streamwise mean scalar gradient at high Re_T, Pe, has also been considered. For each case, the model was tested in non-rotating and rotating frames, providing good predictions for a number of dimensionless parameters, such as the ratio of passive scalar intensities to velocity intensities, denoted as B, the inclination angle a_ϕ and the scalar-velocity correlation coefficient ζ_i^α. Especially for the case where a streamwise mean scalar gradient is imposed, the proposed model provides excellent predictions for B and α_ϕ, revealing its ability to adopt to the highly anisotropic nature of the passive-scalar field. Using structure tensors given by DNS fair predictions are obtained for the ratio of turbulence timescale to passive scalar timescale, denoted as $\mathcal{R}$. Additionally, the performance of the model was ascertained for one irrotational case, particularly for axisymmetric contraction in the presence of mean transverse gradient, yielding good predictions for the time evolution of the passive scalar variance $\overline{\phi'^2}$ and passive-scalar dissipation rate ϵ_ϕ. The satisfactory performance of the model at the limit of high Re_T and Pe supports the use of the large-scale enstrophy in the model expression of ϵ_ϕ. In order to complete the model, the constant associated with diffusion $C_{\tilde{a}^2_\gamma}$ is determined by examining the asymptotic behavior of the flow at low Re_T and Pe.

Preliminary computations were conducted in order to test the potential of incorporating ASBM to the complete model, showing encouraging results. All the above findings enforce our confidence for the validity of the passive scalar large scale model, which fits nicely with the $\kappa - \tilde{\omega}^2$ model. The overall agreement of the current model with the DNS simulations enforces our confidence that the proposed modeled expression for scalar dissipation rate is appropriate for the study of the turbulent passive scalar field. Our current efforts are focused on the construction of a model for the scalar dimensionality tensor d^s_{ij}, and the prospect of extending the model to more general flows.

Finally, it is useful to comment on the differences between the structure-based approach present herein and more common approaches such as those based on one-point Reynolds stress transport models. In this respect, two key features of the IPRM approach stand out. First is the inclusion of structure information via the one-point structure tensors in the scale equations, a feature that is not linked to the particle representation per se and thus can be expected to also carry over to one-point formulations, such as the ASBM. The sensitization of the turbulence scales to the structure of the turbulence can be expected to allow the model to reflect more accurately a number of limiting cases. An example of such an advantage that is directly related to the cases considered in this paper, comes from unpublished work by Kassinos. This work shows that using the large-scale enstrophy equation in place of the standard epsilon equation allows the IPRM (and ASBM) to capture the bifurcation diagram of homogeneous shear flow in a rotating frame much more accurately. The second characteristic is the extra information carried out in the particle representation that leads to an enhancement of realizability and robustness for the IPRM. These features provide enough evidence that further investigation of this approach might be both interesting and fruitful.

Chapter 4

A new stochastic Differential Structure-Based Model (D-SBM).

4.1 Introduction

The problems encountered in the original model have motivated us to re-consider the modeling procedure in order to extent its validity to weak irrotational deformations through the inclusion of additional physical information in the model equations. To achieve this, a number of objectives were defined, which are:

- Retain stochastic nature of the model.
- Revisit the R_{ij} constitutive equation (correlation) part.
- Obtain more sophisticated transports equations for the structural equations, which can produce non-zero values for ϕ and γ for irrotational flows, which is true only for flows that are subjected to slow deformations, while it will still provide zero values for rapid deformations.
- Validate the proposed structure-based model for a number of basic irrotational flows subjected to slow deformations.

Based on the above considerations, the constitutive equation was modified by substituting the mean rotation vector that appears in the jetal-vortex correlation part with the eddy effective rotation rate vector. The motivation behind this modification stems from the fact that under RDT, the jetal-vortex correlation is activated by mean or frame rotation. In slow irrotational deformations, we have an effective rotation (due to the action of the larger eddies on the smaller ones) that can also induce this correlation. In addition, the non-linear effects are expressed in terms of the effective gradients, an idea introduced by Kassinos et al. [24] who assumed that these turbulence-turbulence interactions provide a gradient acting on the eddies, in addition to the mean gradient. Furthermore, this modification maintains basic properties of 2D turbulence (e.g. material indifference).

4.1.1 Outline

Section 4.2 discuss the construction of a stochastic model which includes the concept of the effective gradients. It is devoted to the derivation of the evolution equations for the a_{ij} and the two structural parameters ϕ and gamma appearing in the constitutive equation for the Reynolds stresses . Section 4.3 is devoted to the construction of modified expressions for the one-point statistics and the evolution equations for a_{ij}, ϕ and γ based on the eddy-effective rotation rate vector. In addition, an evolution equation for the normalized dimensionality tensor d_{ij} is derived. In Section 4.5 we ascertain the performance of the newly proposed models for three basic irrotational cases, in the presence of either rapid or slow deformations. Comparison is made to the stochastic SBM model of Kassinos and Reynolds (KR) [22], briefly described in Chapter 2.9, and the DNS work of Lee and Reynolds [58].

4.2 Stochastic SBM based on effective gradients.

4.2.1 Evolution for a_{ij}.

4.2.1.1 Differential of a_i, V.

We start our analysis by modifying the differential of the normalized eddy-axis vector a_i to account for the additional non-linear effects

$$da_i = G^a_{ik} a_k dt - G^a_{ks} a_k a_s a_i dt \,, \tag{4.1}$$

where the model for the effective eddy deformation is incorporated inside the effective gradient tensor

$$G^a_{ij} = G_{ij} + \frac{C_a}{\tau} r_{iq} d_{qj} \,. \tag{4.2}$$

The constant C_a is determined through the orthogonality condition between a_i and n_i and is found to be equal to C_n. The values of the model constants C_v and C_n are chosen to be 1 and 2.2 respectively, as in Kassinos et al. [24]. Note that we have used the same tensor $r_{iq}d_{qj}$ to represent the eddy effective deformation rate as both n_i and v_i. In order to obtain the evolution equation for a_{ij}, an additional differential is needed, that of the velocity magnitude. Use of eq. (2.72) leads to the following expression

$$dV = \frac{1}{2V}[-2G^v_{ik}V_iV_k dt - 2C_1V^2dt + C_2^2V^2(dW_pdW_pn_sn_s - dW_sdW_qn_qn_s)]\,. \tag{4.3}$$

Note that we have kept only terms of order $O(t^2)$, since the remaining terms provide negligible contribution to the evolution of the velocity field.

4.2.1.2 Evolution equation for a_{ij}.

We combine eqs. (4.1) and (4.3) and apply averaging in order to obtain the evolution equation for the eddy-axis tensor

$$\frac{dA_{ij}}{dt} = G^a_{ik}A_{kj} + G^a_{jk}A_{ki} - 2G^a_{ks}q^2Z^a_{ijks} - 2G^v_{qk}\langle v_kv_qA_iA_j\rangle\,. \tag{4.4}$$

From the definition (2.81) it follows that the equation for the normalized eddy-axis tensor a_{ij} is given by

$$\frac{da_{ij}}{dt} = \frac{d}{dt}(\frac{A_{ij}}{A_{kk}}) = \frac{\dot{A}_{ij}}{A_{kk}} - \frac{A_{ij}}{A_{kk}}\frac{\dot{A}_{kk}}{A_{kk}} = \frac{\dot{A}_{ij}}{q^2} - a_{ij}\frac{\dot{A}_{kk}}{q^2}\,. \tag{4.5}$$

Using eq. (4.4) in eq. (4.5) one obtains the evolution equation for a_{ij}

$$\begin{aligned}\frac{da_{ij}}{dt} = &\underbrace{G_{ik}a_{kj} + G_{jk}a_{ki} - (3\phi+1)S_{qk}Z^a_{ijkq} + S_{qk}(3\phi-1)[a_{ij}a_{kq}] + 2\gamma\frac{\Omega_s}{\Omega}S_{qk}\epsilon_{ksy}[a_{yq}a_{ij} - Z^a_{yqij}]}_{\text{RDT term}}\\ &\underbrace{+\frac{C^v}{\tau}r_{qw}d_{wk}(3\phi-1)[a_{ij}a_{kq} - Z^a_{kqij}] + \gamma\frac{\Omega_s}{\Omega}\frac{C^v}{\tau}(r_{qw}d_{wk} + r_{kw}d_{wq})\epsilon_{kst}[a_{tq}a_{ij} - Z^a_{tqij}]}_{\text{slow term-velocity contribution}}\\ &+\underbrace{\frac{C^a}{\tau}d_{qk}[r_{iq}a_{kj} + r_{jq}a_{ki}] - \frac{2C^a}{\tau}r_{kq}d_{qs}Z^a_{ijks}}_{\text{slow term-eddy contribution}}\,.\end{aligned} \tag{4.6}$$

Eq. (4.6) is written in a form that clearly shows the influence of each field to the stochastic processes. We observe that the velocity field adds an additional contribution to both the stropholysis and jetal terms, while the eddy-contribution provides an effective rotational randomization of the a_{ij}.

4.2.2 Evolution for γ, ϕ.

In this subsection, we consider the evolution of the jetal parameter ϕ and the jetal-vortex correlation parameter γ. Details of the derivation of their evolution equations are given in Appendix C. As shown in the constitutive equation for the Reynolds stress, these structural parameters are responsible for the redistribution of the energy between the different modes, thus affecting the Reynolds stress components. First, we construct a suitable algebraic expression by multiplying eq. (2.79a) with $a_i a_j$, which yields the algebraic expression

$$\phi = R^{|a}_{ij} a_i a_j \,. \tag{4.7}$$

Taking the time-derivative of eq. (4.7) one finds

$$\frac{d\phi}{dt} = \frac{1}{q^2}[\langle \frac{dR^{|a}_{ij}}{dt} a_i a_j \rangle + \langle R^{|a}_{ij} \frac{d}{dt}(a_i a_j)\rangle - \frac{\langle R^{|a}_{ij} a_i a_j\rangle}{q^2}\langle \frac{dq^2}{dt}\rangle] \,. \tag{4.8}$$

Using eq. (2.79a) in eq. (4.8) produces the evolution equation for ϕ

$$\begin{aligned} \frac{d\phi}{dt} &= \underbrace{\gamma\frac{\Omega_s\Omega_t}{\Omega}[\delta_{st} - a_s a_t] + 2\phi S^v_{kq}[r_{qk} - a_{qk}]}_{\text{RDT term}} \\ &+ \underbrace{(1-2\phi)\frac{8.5\Omega^s}{2\tau}(1 - f_{pq}a_{qp}) + \gamma\frac{\Omega_k}{\Omega}\epsilon_{ikt}a_{ts}[\frac{C_a}{\tau} r_{iq} d_{qs} - \frac{C_v}{\tau} r_{sq} d_{qi}]}_{\text{slow term}} \,. \end{aligned} \tag{4.9}$$

For the construction of the correlation parameter γ we consider the contraction

$$\langle R^{|a}_{ij} \frac{\Omega_z}{\Omega} \epsilon_{izm} a_m a_j \rangle = \gamma \frac{\Omega_k \Omega_z}{\Omega^2}\frac{1}{2}(q^2\delta_{kz} - A_{kz}) \,. \tag{4.10}$$

Taking the time-derivative of eq. (4.10) yields

$$\begin{aligned} &\langle (\frac{dR^{|a}_{ij}}{dt})\frac{\Omega_z}{\Omega}\epsilon_{izm}a_m a_j\rangle + \langle R^{|a}_{ij}\frac{d}{dt}(\frac{\Omega_z}{\Omega})\epsilon_{izm}a_m a_j\rangle + \epsilon_{izm}\langle R^{|a}_{ij}\frac{\Omega_z}{\Omega}\frac{d}{dt}(a_m a_j)\rangle = \\ &(\frac{d\gamma}{dt})\frac{\Omega_k\Omega_z}{\Omega^2}\frac{1}{2}(q^2\delta_{kz} - A_{kz}) + \gamma\frac{d}{dt}(\frac{\Omega_k\Omega_z}{\Omega^2})\frac{1}{2}(q^2\delta_{kz} - A_{kz}) + \gamma\frac{\Omega_k\Omega_z}{2\Omega^2}\frac{d}{dt}(q^2\delta_{kz} - A_{kz}) \,. \end{aligned} \tag{4.11}$$

Using eq. (4.11) leads to the evolution equation for γ

$$
\begin{aligned}
&(\frac{d\gamma}{dt})\frac{\Omega_k\Omega_z}{\Omega^2}\frac{1}{2}(\delta_{kz}-a_{kz}) = \underbrace{-\frac{\gamma}{2}\frac{\Omega_k\Omega_z}{\Omega^2}(-S^a_{kq}a_{qz}+S^a_{pq}Z^a_{kzpq})+(1-3\phi)\epsilon_{izm}\frac{\Omega_z}{2\Omega}S^a_{iq}a_{qm}}_{\text{eddy contribution}} \\
&\underbrace{+\gamma\frac{8.5}{2\tau}\frac{\Omega_m\Omega_t}{\Omega^2}\Omega^s[(a_{tm}-\delta_{tm})+f_{pq}[\delta_{mt}a_{pq}-Z^a_{pqtm}]]}_{\text{pure slow term}} \\
&\underbrace{+\frac{\Omega_i\Omega_q}{2\Omega}(\delta_{iq}-a_{iq})[1-2\phi]+\frac{\gamma}{2}\frac{\Omega_m\Omega_r}{\Omega^2}a_{mt}(-\frac{\Omega_t\Omega_q}{\Omega^2}S_{qr}+S_{tr})}_{\text{pure vorticity contribution}} \\
&+\underbrace{S^n_{kq}\frac{\phi}{2}\frac{\Omega_z}{\Omega}\epsilon_{kzm}a_{mq}+\gamma[\frac{S^n_{qq}}{8}+\frac{S^n_{tz}}{4}(\frac{\Omega_m\Omega_z}{\Omega^2}a_{tm}+\frac{\Omega_m\Omega_t}{\Omega^2}a_{zm})-\frac{S^n_{sz}}{4}\frac{\Omega_s\Omega_z}{\Omega^2}-\frac{S^n_{qq}}{8}\frac{\Omega_m\Omega_t}{\Omega^2}a_{tm}}_{\text{gradient contribution}} \\
&\underbrace{-\frac{S^n_{kq}}{8}\frac{\Omega_s\Omega_t}{\Omega^2}Z^a_{tqsk}-\frac{S^n_{tm}}{8}a_{tm}]}_{\text{gradient contribution}} \\
&\underbrace{-\epsilon_{kzm}\frac{\Omega_z}{2\Omega}a_{mq}[\phi S^v_{kq}+(1-\phi)S^v_{qk}]}_{\text{velocity contribution}} \\
&\underbrace{+\gamma[S^v_{km}r_{mk}+S^v_{kk}\frac{\Omega_m\Omega_t}{8\Omega^2}a_{mt}(4\phi-1)+\frac{\Omega_k\Omega_z}{8\Omega^2}S^v_{qs}Z^a_{sqkz}(7-12\phi)-\frac{3}{8}S^v_{kk}-\frac{S^v_{tm}a_{tm}}{8}}_{\text{velocity contribution}} \\
&\underbrace{+S^v_{ik}\frac{\Omega_i\Omega_k}{4\Omega^2}-\frac{1}{4}S^v_{ik}(\frac{\Omega_m\Omega_k}{\Omega^2}a_{im}+\frac{\Omega_m\Omega_i}{\Omega^2}a_{mk})-\frac{\Omega_k\Omega_z}{2\Omega^2}\gamma\frac{\Omega_m}{\Omega}(\epsilon_{smt}Z^a_{tqkz}+\epsilon_{qmt}Z^a_{tskz})S^v_{qs}]}_{\text{velocity contribution}}\ .
\end{aligned}
\tag{4.12}
$$

Clearly the evolution equation for γ is the most complicated among all structural parameters, containing various terms. This equation is highly non-linear in terms of products among turbulent quantities. However, this expression is consistent to one of our objectives, which is to construct more sophisticated equations which would provide more accurate, and physically more meaningful results.

4.3 Extended Stochastic SBM including eddy effective rotation rate.

As already mentioned in the outline subsection of the current chapter, one of the main issues regarding the original model is that, for irrotational flows subjected to slow deformations, it predicts zero values for the ϕ and γ parameters. As this is true for flows subjected to rapid irrotational deformations, as explained in [22], in the presence of weak deformations the nolinear terms effectively redistribute the energy of an initially pure jetal mode ($\phi = 0$), resulting to the emergence of a vortical mode. These eddy-eddy interactions provide an effective eddy rotation acting on each individual eddy, allowing for non-zero values to be produced. As described in detail in Kasssinos & Reynolds (KR) [22], *" in order to capture these effects it is not enough to allow for non-zero ϕ and γ under irrotational strain "*. KR took a step forward and suggested the replacement of the mean vorticity of the Ω_i in eq. (2.79a) with the effective eddy rotation rate Θ_i, given by

$$\Theta_z = \epsilon_{zrp} G^a_{rk} a_p a_k \,. \tag{4.13}$$

This modification, in the presence of non-zero ϕ and γ can yield a contribution in the stropholysis part even in the absence of mean rotation. Motivated by their arguments, in this subsection we introduce a stochastic model, called Model 2, which combines the idea of the effective mean gradients in a similar manner as in Model 1, while modifying the constitutive equation as proposed by KR.

4.3.1 Constitutive relationship between r_{ij} and a_{ij}, ϕ, γ.

Substituting eq. (4.13) in eq. (2.79a) produces the constitutive equation for the normalized Reynolds stress

$$r_{ij} = \frac{R_{ij}}{q^2} = [\frac{(1-\phi)}{2}(\delta_{ij} - a_{ij}) + \phi a_{ij} + \frac{\gamma}{2\Omega^*}(2S^a_{tq} Z^a_{tqij} - G^a_{iq} a_{qj} - G^a_{jq} a_{qi})] \,, \tag{4.14}$$

where

$$\Omega^* = \sqrt{\langle \Theta_i \Theta_i \rangle} \,, \tag{4.15a}$$

$$\Omega^{*2} = \langle \Theta_i \Theta_i \rangle = G^a_{sk} G^a_{sq} a_{kq} - S^a_{tk} S^a_{pq} Z^a_{tkpq} \,, \tag{4.15b}$$

$$\langle \Theta_i \Theta_j \rangle = \delta_{ij}(G^a_{sk} G^a_{sq} a_{kq} - S^a_{tk} S^a_{pq} Z^a_{pqtk}) + S^a_{tk}(G^a_{iq} Z^a_{tkjq} + G^a_{jq} Z^a_{tkiq}) \tag{4.15c}$$

$$- G^a_{jk} G^a_{iq} a_{kq} - G^a_{sk} G^a_{sq} Z^a_{ijkq} \,. \tag{4.15d}$$

As expected, eqs. (4.15) contribute to the constitutive equation even for strained-only flows through the effective gradients. However, for strained-only flows in the RDT limit and for initially zero value for the jetal-vortex correlation γ, the stropholysis part of eq. (4.14) remains zero, in accordance to the RDT theory.

4.3.2 Modified expression for pressure strain rate tensor M_{ijpq}.

The fourth-rank pressure strain rate tensor is derived by the conditioned moment

$$M_{ijpq}^{|a} = \langle V_i V_j n_p n_q | a \rangle \, , \tag{4.16}$$

which consists of three distinct parts, namely

$$\begin{aligned}
\frac{M_{ijpq}^{v|a}}{q^2} &= \frac{(1-\phi)}{8} \epsilon_{irt}\epsilon_{jzs}[(\delta_{rz}\delta_{pq} + \delta_{rp}\delta_{zq} + \delta_{rq}\delta_{zp}) - \delta_{rz}a_p a_q]a_t a_s \, , && \text{(4.17a)} \\
\frac{M_{ijpq}^{j|a}}{q^2} &= \frac{\phi}{2}[\delta_{pq}a_i a_j - a_i a_j a_p a_q] \, , && \text{(4.17b)} \\
\frac{M_{ijpq}^{h|a}}{q^2} &= \frac{\gamma}{8}\frac{\Theta_k}{\Theta}(\epsilon_{irt}a_t a_j + \epsilon_{jrt}a_t a_i)[(\delta_{rk}\delta_{pq} + \delta_{rp}\delta_{kq} + \delta_{rq}\delta_{kp}) && \text{(4.17c)} \\
&\quad - (\delta_{rk}a_p a_q + \delta_{rp}a_k a_q + \delta_{rq}a_k a_p)] \, , && \text{(4.17d)}
\end{aligned}$$

where v,j and h refer to the vortical, jetal and helical components respectively. As shown in Appendix C, applying averaging on each component of the tensor produces the corresponding model expressions for the individual components of M_{ijpq}

$$\begin{aligned}
\frac{M_{ijpq}^{v}}{q^2} = \frac{(1-\phi)}{8}&[3\delta_{ij}(\delta_{pq} - a_{pq}) - 3\delta_{pq}a_{ij} + Z_{ijpq}^a + (a_{pj}\delta_{iq} + a_{qj}\delta_{ip}) \\
&+ (\delta_{jp}a_{iq} + \delta_{qj}a_{ip}) - (\delta_{jp}\delta_{iq} + \delta_{qj}\delta_{ip})] \, ,
\end{aligned} \tag{4.18}$$

$$\frac{M_{ijpq}^{j}}{q^2} = \frac{\phi}{2}(\delta_{pq}a_{ij} - Z_{ijpq}^a) \, , \tag{4.19}$$

and the helical part

$$\begin{aligned}
\frac{M_{ijpq}^{h}}{q^2} = \frac{\gamma}{8\Omega^*}&[6\delta_{pq}G_{rn}^a Z_{ijnr}^a - 2G_{rn}^a W_{ijpqnr} - 3\delta_{pq}(G_{in}^a a_{nj} + G_{jn}^a a_{ni}) \\
&+ 3(G_{in}^a Z_{pqnj}^a + G_{jn}^a Z_{pqni}^a) - G_{rn}^a(Z_{qnrj}^a\delta_{pi} + Z_{qnri}^a\delta_{pj}) + G_{pn}^a(a_{nj}\delta_{qi} + a_{ni}\delta_{qj}) \\
&- 2G_{pn}^a Z_{nqij}^a - 2G_{qn}^a Z_{ijnp}^a + G_{qn}^a(a_{nj}\delta_{pi} + a_{ni}\delta_{pj} - G_{rn}^a(Z_{pnrj}^a\delta_{qi} + Z_{pnri}^a\delta_{qj})] \, .
\end{aligned} \tag{4.20}$$

where the total pressure-strain rate tensor is given by

$$M_{ijpq} = M^v_{ijpq} + M^j_{ijpq} + M^h_{ijpq}\,. \tag{4.21}$$

4.3.3 Evolution for a_{ij}.

Following similar procedure as before, we found the evolution equation for the eddy-axis tensor to be

$$\frac{dA_{ij}}{dt} = G^a_{ik}A_{kj} + G^a_{jk}A_{ki} - 2S^a_{ks}q^2 Z^a_{ijks} - 2S^v_{qk}\langle v_k v_q A_i A_j\rangle\,. \tag{4.22}$$

The first three terms of the RHS of eq. (4.22) are identical to the ones presented in eq. (4.4), whereas the last term contains the strophOlysis part. This part will be modeled based on eddy effective rotation rate, in constrast to the analogous stropholysis part in eq. (4.4) which is modeled based on the stropholysis term of the conditional constitutive equation as given in eq. (2.79). Using eq. (4.22) in eq. (4.5) produces the evolution equation for a_{ij}

$$\begin{aligned}\frac{da_{ij}}{dt} &= S^a_{ik}a_{kj} + S^a_{jk}a_{ki} + (\Omega^a_{ik}a_{kj} + \Omega^a_{jk}a_{ki}) - 2S^a_{qk}Z^a_{ijkq} + (3\phi-1)S^v_{qk}[a_{kq}a_{ij} - Z^a_{kqij}]\\ &+ \frac{2\gamma}{\Omega^*}S^v_{qk}(S^a_{tp}Z^a_{tpkq}a_{ij} - G^a_{kp}a_{pq}a_{ij} - S^a_{tw}W_{twkqij} + G^a_{kw}Z^a_{wqij})\,.\end{aligned} \tag{4.23}$$

Note the presence of the sixth-order tensor W_{ijkmpq}, which is a fully-symmetric tensor defined as

$$W_{ijkmpq} = \frac{\langle V^2 a_i a_j a_k a_m a_p a_q\rangle}{\langle V^2\rangle}\,. \tag{4.24}$$

This tensor is modeled in terms of a_{ij} and its invariants as described in detail in [2], who constructed a fully realizable expression, which reduces to the modeling expression of Z^a_{ijpq}, when any two indices are contracted, e.g. when $k{=}m$.

4.3.4 Evolution for γ, ϕ.

In order to bring the modified model into a closed form, we need to obtain the evolution equations for ϕ and γ. The mathematical derivation for these expressions is considered in great detail in Appendix C. Starting from eq. (4.7) we obtain

$$\begin{aligned}\frac{d\phi}{dt} &= 2\phi S^v_{qk}(r_{kq} - a_{kq}) + (1-2\phi)\frac{8.5}{\tau}\Omega^s f_{pq} d_{qp} \\ &+ \frac{\gamma}{\Omega^*}\left[S^a_{tq}(S^a_{js} - S^v_{js})Z^a_{jstq} + (G^v_{si} - G^a_{is})G^a_{iq}a_{qs}\right],\end{aligned} \tag{4.25}$$

which coincides to eq. (2.86) for irrotational deformations in the RDT limit, in which γ value remains zero. The evolution equation for γ is given by the following expression

$$\begin{aligned}&(\frac{d\gamma}{dt})\frac{\langle\Theta_z\Theta_m\rangle}{2\Omega^{*2}}(\delta_{zm} - a_{zm}) = \frac{(3\phi-1)}{2\Omega^*}(G^a_{rq}G^a_{rk}a_{kq} - S^a_{pq}S^a_{ik}Z^a_{pqik}) \\ &+ \frac{1}{2\Omega^*}[-S^v_{pk}S^a_{mq}Z^a_{pkmq} + G^a_{rq}(\phi G^v_{rk} + (1-\phi)G^v_{kr})a_{qk}] \\ &+ \frac{\phi}{2\Omega^*}(S^n_{kq}S^a_{ms}Z^a_{mskq} - G^n_{kq}G^a_{ks}a_{sq}) - \frac{\gamma}{2}\frac{d}{dt}(\frac{\langle\Theta_z\Theta_m\rangle}{\Omega^{*2}})(\delta_{zm} - a_{zm}) \\ &+ \frac{\gamma}{2}\langle\frac{\Theta_s}{\Theta}\frac{d}{dt}(\frac{\Theta_z}{\Theta})\rangle(\delta_{sz} - a_{sz}) - \gamma\frac{8.5}{\tau}\Omega^s f_{pq}(d_{pq} - \frac{\langle\Theta_m\Theta_y\rangle}{\Omega^{*2}}\langle n_p n_q a_y a_m\rangle) \\ &+ \gamma[\frac{S^n_{kk}}{8} - \frac{S^n_{kk}}{8}\frac{\langle\Theta_t\Theta_m\rangle}{\Omega^{*2}}a_{mt} - S^n_{kq}\frac{\langle\Theta_q\Theta_k\rangle}{4\Omega^{*2}} - \frac{S^n_{kq}}{8}a_{qk} + S^n_{kq}\frac{\langle\Theta_q\Theta_m\rangle}{2\Omega^{*2}}a_{mk} \\ &- \frac{S^n_{kq}}{8}\frac{\langle\Theta_t\Theta_s\rangle}{\Omega^{*2}}Z^a_{sktq}] + \gamma\frac{\langle\Theta_z\Theta_m\rangle}{2\Omega^{*2}}(G^a_{zk}a_{km} - S^a_{pq}Z^a_{pqzm}) \\ &+ \gamma[S^v_{qk}r_{kq} - \frac{3}{8}S^v_{qq} + \frac{(4\phi-1)}{8}S^v_{qq}\frac{\langle\Theta_m\Theta_y\rangle}{\Omega^{*2}}a_{ym} + \frac{(7-12\phi)}{8}S^v_{jk}\frac{\langle\Theta_m\Theta_y\rangle}{\Omega^{*2}}Z^a_{ykmj} \\ &- S^v_{yz}\frac{\langle\Theta_z\Theta_m\rangle}{2\Omega^{*2}}a_{ym} + S^v_{sz}\frac{\langle\Theta_s\Theta_z\rangle}{4\Omega^{*2}} - \frac{S^v_{kq}}{8}a_{qk} \\ &- \gamma\frac{\langle\Theta_z\Theta_m\rangle}{\Omega^{*3}}(S^v_{qs}S^a_{tw}W_{sqtwmz} - S^v_{qs}G^a_{sw}Z^a_{wqmz})]\,.\end{aligned} \tag{4.26}$$

where the terms involving time derivatives are given by

$$\begin{aligned}\langle\Theta_i\frac{d\Theta_z}{dt}\rangle &= \delta_{iz}G^a_{rl}[G^a_{kw}(G^a_{rk}a_{wl} - G^a_{pk}Z^a_{plwr}) - 2S^a_{sw}(G^a_{rk}Z^a_{lswk} - G^a_{pk}W_{plsrwk})] \\ &+ G^a_{pl}[G^a_{kw}(G^a_{ik}Z^a_{zlwp} - G^a_{pk}Z^a_{wizl}) - 2S^a_{sw}(G^a_{ik}W_{zlspwk} - G^a_{pk}W_{zlsiwk})] \\ &+ G^a_{zl}[G^a_{kw}(G^a_{rk}Z^a_{wirl} - G^a_{ik}a_{wl}) - 2S^a_{sw}(G^a_{rk}W_{rlsiwk} - G^a_{ik}Z^a_{slwk})] \\ \frac{d}{dt}(\frac{\Theta_i}{\Theta}) &= \frac{1}{\Theta}\frac{d\Theta_i}{dt} - \frac{\Theta_i\Theta_j}{\Theta^3}\frac{d\Theta_j}{dt}, \\ \frac{d}{dt}(\frac{\Theta_i\Theta_j}{\Theta^2}) &= \frac{1}{\Theta^2}(\Theta_i\frac{d\Theta_j}{dt} + \Theta_j\frac{d\Theta_i}{dt}) - 2\frac{\Theta_k}{\Theta^2}\frac{\Theta_i\Theta_j}{\Theta^2}\frac{d\Theta_k}{dt}\,.\end{aligned} \tag{4.27}$$

The model constants that appear in the expressions for the effective gradients are now taken to be $C_v = 2.0$, $C_n = C_a = 2.2C_v$. If we take a closer look to eq. (4.26), we see that the first two terms are not zero even for irrotational flows with initially zero ϕ and γ, producing non-zero gamma values. Consequently, a non-zero stropholysis contribution appears in the constitutive equation, while a non-zero value for ϕ is achieved due to the activation of the stropholysis term of eq. (4.25).

4.3.5 Evolution for d_{ij}.

As mentioned above, the non-linear interactions are modeled in terms of products between the structure tensors r_{ij} and d_{ij}. While a lot of attention has been given to the construction of a suitable algebraic expression for r_{ij}, so far the normalized dimensionality tensor d_{ij} was estimated through the simple expression given by eq. (2.80b) through the use of axisymmetric assumption, an assumption that is not valid in the presence of weak deformations. Thus, we have proceeded to the construction of an evolution equation for d_{ij} which is consistent with the remaining model expressions.

We start with the differential of the normalized normal vector, given by

$$dn_i = G^n_{qk} n_k n_q - G^n_{ki} n_k \, . \tag{4.28}$$

Using eq. (4.28) and eq. (4.3) one finds

$$\begin{aligned} dD_i = d(Vn_i) = G^n_{ki} D_k dt + G^n_{qk} n_k n_q D_i dt - G^v_{pk} v_p v_k D_i dt - C_1 D_i dt \\ + \frac{C_2^2}{2} D_i (dW_p dW_p - dW_s dW_q n_q n_s) \, , \end{aligned} \tag{4.29}$$

where $D_i = Vn_i$. Starting from eq. (4.29), the evolution equation for the dimensionality tensor is found to be

$$\frac{dD_{ij}}{dt} = -G^n_{ki} D_{kj} - G^n_{kj} D_{ki} + 2G^n_{qk} \langle D_i D_j n_k n_q \rangle - 2G^v_{pk} \langle v_p v_k D_i D_j \rangle \, , \tag{4.30}$$

or

$$\frac{dD_{ij}}{dt} = -G^n_{ki} D_{kj} - G^n_{kj} D_{ki} + 2G^n_{qk} q^2 Z^n_{ijkq} - 2G^v_{pk} M_{pkij} \, , \tag{4.31}$$

where the fourth-moment Z^n_{ijkq} is defined by

$$Z^n_{ijkq} = \frac{\langle V^2 n_i n_j n_k n_q \rangle}{q^2}\,. \tag{4.32}$$

From the definition of the dimensionality tensor it follows that the evolution equation for the normalized dimensionality tensor is given by

$$\frac{dd_{ij}}{dt} = \frac{1}{q^2}\frac{dD_{ij}}{dt} - d_{ij}\frac{1}{q^2}\frac{dD_{kk}}{dt}\,. \tag{4.33}$$

Substituting eq. (4.31) in eq. (4.33) one obtains

$$\frac{dd_{ij}}{dt} = -G^n_{ki} d_{kj} - G^n_{kj} d_{ki} + 2G^n_{qk} Z^n_{ijkq} - 2\frac{G^v_{pk}}{q^2} M_{pkij} + 2S^v_{qk} r_{kq} d_{ij}\,. \tag{4.34}$$

4.4 Model synopsis.

Here we outline the basic equations and model parameters that comprise the proposed model. Details regarding these models are given in Sections 4.2 and 4.3.

Model 1

Model 1 is denoted as the stochastic model that uses effective gradients to model slow effects without the inclusion of the eddy effective rotation rate and is described by the following equations :

Constitutive equations:

$$r_{ij} = \Im_r(G_{ij}, a_{ij}, \phi, \gamma)\,, \tag{4.35a}$$

$$d_{ij} = \frac{1}{2}(\delta_{ij} - a_{ij})\,. \tag{4.35b}$$

Evolution Equations:

$$\begin{aligned}
\frac{da_{ij}}{dt} &= \Im_a(G^{v,n}_{ij}, a_{ij}, Z^a_{ijpq}, \phi, \gamma, \tau)\,,\\
\frac{d\phi}{dt} &= \Im_\phi(G^{v,n}_{ij}, a_{ij}, \phi, \gamma, \tau)\,,\\
\frac{d\gamma}{dt} &= \Im_\gamma(G^{v,n}_{ij}, a_{ij}, Z^a_{ijpq}, \phi, \gamma, \tau)\,,
\end{aligned} \tag{4.36}$$

Model 2

Model 2 takes into account the contribution of the eddy effective vector to the statistics of the homogeneous turbulence field and is summarized as follow:

Constitutive equations:

$$r_{ij} = \Im_r(G_{ij}^{v,n}, a_{ij}, Z_{ijpq}^a, \phi, \gamma, \Omega^*)\,. \tag{4.37}$$

Evolution Equations:

$$\begin{aligned} \frac{da_{ij}}{dt} &= \Im_a(G_{ij}^{v,n}, a_{ij}, Z_{ijpq}^a, W_{ijpqmn}, \phi, \gamma)\,, \\ \frac{d\phi}{dt} &= \Im_\phi(G_{ij}^{v,n}, a_{ij}, d_{ij}, Z_{ijpq}^a, \phi, \gamma, \tau, \Omega^*)\,, \\ \frac{d\gamma}{dt} &= \Im_\gamma(G_{ij}^{v,n}, a_{ij}, d_{ij}, Z_{ijpq}^a, W_{ijpqmn}, \phi, \gamma, \tau, \Omega^*)\,, \\ \frac{dd_{ij}}{dt} &= \Im_d(G_{ij}^{v,n}, d_{ij}, Z_{ijpq}^n, M_{ijpq})\,, \end{aligned} \tag{4.38}$$

Eqs. (2.91) and eq. (2.92) are used to determine the turbulence time scale in both models, whereas the model parameters C_1 and C_2 are the same with the ones used in the IPRM model, given in eq. (2.76).

4.5 Validation Results

In this section, the proposed models are tested for three independent irrotational homogeneous flows in a stationary frame ($\Omega_i^f = 0$), namely axisymmetric contraction (AXC), axisymmetric expansion (AXE) and plane strain (PL). The mean velocity tensor in axisymmetric turbulence is given by

$$S_{ij} = S\delta_{i1}\delta_{j1} - S/2\delta_{i2}\delta_{j2} - S/2\delta_{i3}\delta_{j3}\,, \quad \Omega_{ij} = 0\,, \tag{4.39}$$

with $S > 0$ for contraction and $S < 0$ for expansion. In the case of plane strain the mean strain tensor is defined as follows

$$S_{ij} = S\delta_{i1}\delta_{j1} - S\delta_{i2}\delta_{j2}\,, \quad \Omega_{ij} = 0\,. \tag{4.40}$$

The dimensionless total strain parameter is given by

$$C = \exp(\int_0^t |S_{max}(t^{'})| dt^{'}) \,, \tag{4.41}$$

and serves as the time coordinate in all figures, whereas $|S_{max}|$ is the magnitude of the maximum eigenvalue of the mean strain rate tensor. Comparison is made to the DNS values of Lee and Reynolds [58] for flows subjected to weak deformations and the PRM predictions for the analogous rapid distortion cases. Where meaningful, additional comparisons between the new structure-based models and the original stochastic model will be included. The data used for the comparison include the normalized anisotropic componentality (Reynolds stress) tensor $\tilde{r}_{ij}$, defined as $\tilde{r}_{ij} = r_{ij} - \frac{\delta_{ij}}{3}$ the normalized anisotropic dimensionality tensor $\tilde{d}_{ij} = d_{ij} - \frac{\delta_{ij}}{3}$, and the turbulence time-scale τ. Also, the time development of the structural parameters ϕ and γ is shown for the corresponding cases in order to discuss the physical behavior of Model 2. For all cases, we consider initially isotropic turbulence

$$\begin{aligned} & r_{ij} = \frac{\delta_{ij}}{3} \,, \quad d_{ij} = \frac{\delta_{ij}}{3} \,, \\ & \phi = \gamma = 0 \,. \end{aligned} \tag{4.42}$$

For the slow cases, we also set initial values for the turbulence scales in order to match the initial conditions of the DNS data

$$\begin{aligned} & \kappa = \kappa_0 \,, \quad \epsilon = \epsilon_0 \,, \\ & \tau = \tau_0 = \frac{\kappa_0}{\epsilon_0} \,. \end{aligned} \tag{4.43}$$

Model 1 and Model 2 are both constructed so that they coincide at the RDT limit. Thus we only need to consider the performance of Model 2 for homogeneous turbulence at the rapid distortion limit. Figure 4.1 shows a comparison between Model 2 predictions with the RDT results for the normalized Reynolds stress components $\tilde{r}_{ij}$ for the three irrotational cases. As expected, the proposed model is in excellent agreement with the RDT values.

The validity of the new structure-based models for the irrotational cases at the slow limit is now tested. We consider an initially isotropic state as specified in eqs. (4.42) and (4.43). The solution depends on these conditions through the non-dimensional parameter κ_0/ϵ_0. Models predictions are compared to the corresponding DNS results of Lee and Reynolds [58]. Figure 4.2a shows the evolution of the normalized Reynolds stress anisotropic tensor $\tilde{r}_{ij}$ for irrotational axisymmetric contraction with $S\kappa_0/\epsilon_0 = 0.56$. Both models are in very good

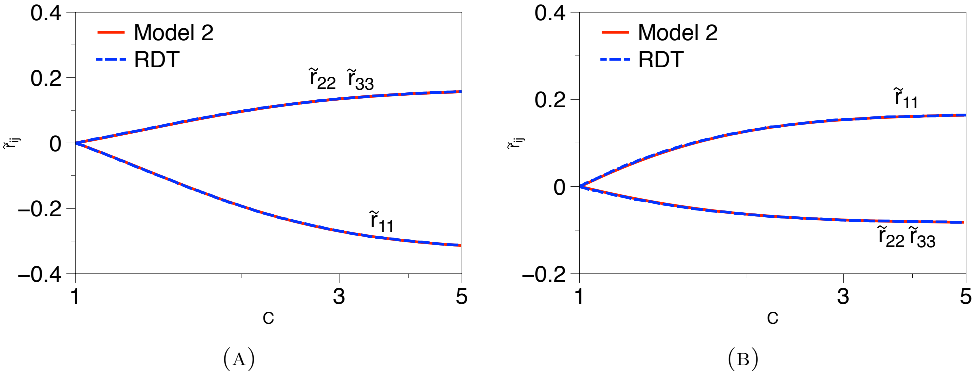

(A)

(B)

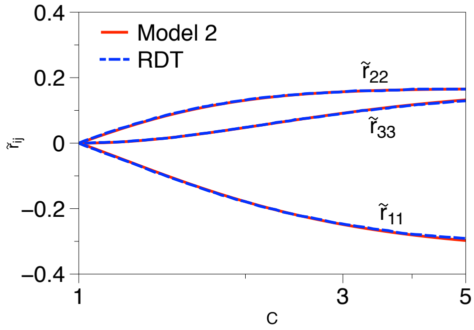

(C)

FIGURE 4.1: Comparison of the Model 2 predictions with the RDT results for the normalized Reynolds stress anisotropic tensor $\tilde{r}_{ij}$ for (a) irrotational axisymmetric contraction. (b) irrotational axisymmetric expansion. (c) plane strain.

agreement with the DNS values for the $\tilde{r}_{22}$, $\tilde{r}_{33}$ components, with Model 2 showing improved predictions for the $\tilde{r}_{11}$ component. Figure 4.2b shows the corresponding comparison for irrotational axisymmetric expansion with $S\kappa_0/\epsilon_0 = 0.41$. Both models significantly underpredict the level of anisotropy, even though Model 2 produces a slight increase of the components compared to Model 1 towards the DNS values. Figure 4.2c shows results for irrotational plane strain with $S\kappa_0/\epsilon_0 = 0.50$. Note that both models are accurate for small total strain and quickly degrade, particularly for $\tilde{r}_{22}$, $\tilde{r}_{33}$, while Model 2 provides a very good agreement with the DNS for the $\tilde{r}_{11}$.

Based on Figure 4.2, Model 2 provides an overall better agreement with the DNS than Model 1. Thus we consider only Model 2 predictions in the following figures. We now turn to the comparison of Model 2 and the original KR stochastic model with the DNS for the three irrotational cases having the same initial conditions as described before. The evolution of the Reynolds stress anisotropy for irrotational axisymmetric contraction is displayed in Figure 4.3a. Model 2 exhibits better agreement with DNS than KR Model for $\tilde{r}_{11}$, while for times larger than $C \approx 2$, KR Model provides more accurate predictions for the evolution of the normalized turbulent kinetic energy (Figure 4.3b).

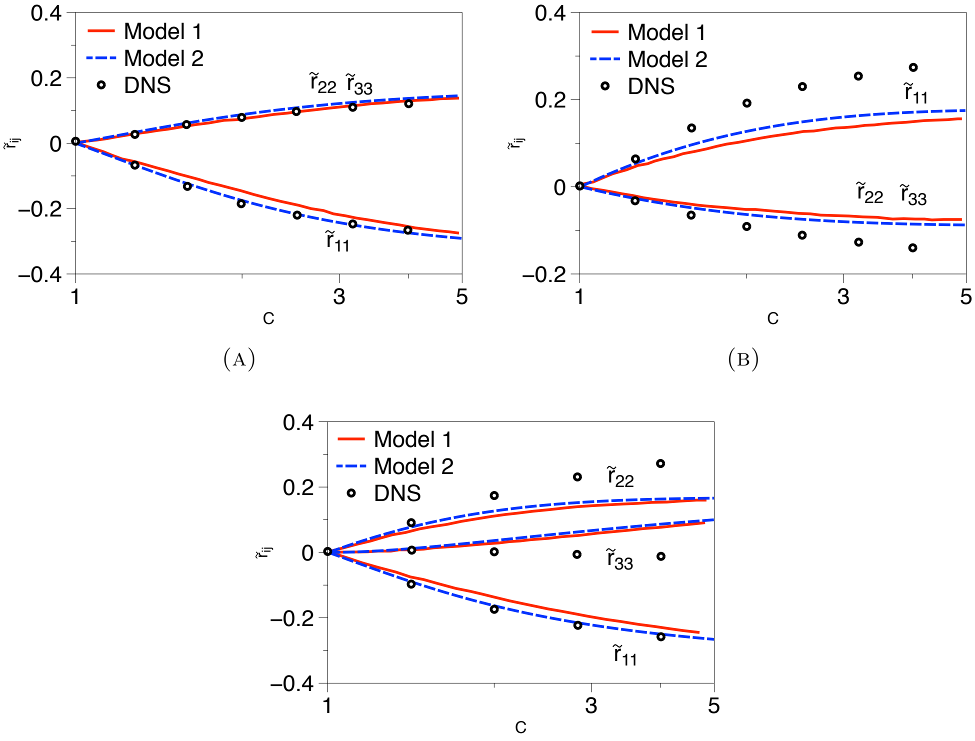

(A)

(B)

(C)

FIGURE 4.2: Model 1 and Model 2 predictions for the normalized Reynolds stress anisotropic tensor $\tilde{r}_{ij}$. (a) irrotational axisymmetric contraction with $S\kappa_0/\epsilon_0 = 0.56$. (b) irrotational axisymmetric expansion with $S\kappa_0/\epsilon_0 = 0.41$. (c) plane strain with $S\kappa_0/\epsilon_0 = 0.50$. Comparison is made to the DNS of Lee and Reynolds [58], shown as symbols.

Figure 4.4a shows the corresponding comparison for the evolution of the Reynolds stress anisotropic components for the irrotational axisymmetric expansion. Even though Model 2 significantly increases the level of anisotropy, eventually both models' predictions are proved deficient. Regarding the evolution of the turbulent kinetic energy, Model 2 remains accurate for larger times than KR model does, but eventually it also degrades (Figure 4.4b).

Next we turn to the analogous case for irrotational plane strain. Figure 4.5a demonstrates the time development of the Reynolds stress anisotropic components, showing the deficiency of both models to sufficiently capture the anisotropy magnitudes, despite the fact that Model 2 provides improved predictions, particularly for $\tilde{r}_{11}$. Regarding the evolution of the turbulent kinetic energy, shown in Figure 4.5b, we observe that Model 2 manages to remain accurate for the whole simulation, up to total strain $C = 5$, much longer than KR model.

Figure (4.6) shows Model 2 predictions for the time development of the jetal parameter ϕ and the stropholysis parameter γ for the three irrotational cases subjected to weak deformations. Starting from a purely vortical mode, Model 2 manages to produce non-zero values for both parameters, in contrast to Model 1 and KR models. The mechanism behind this deviation

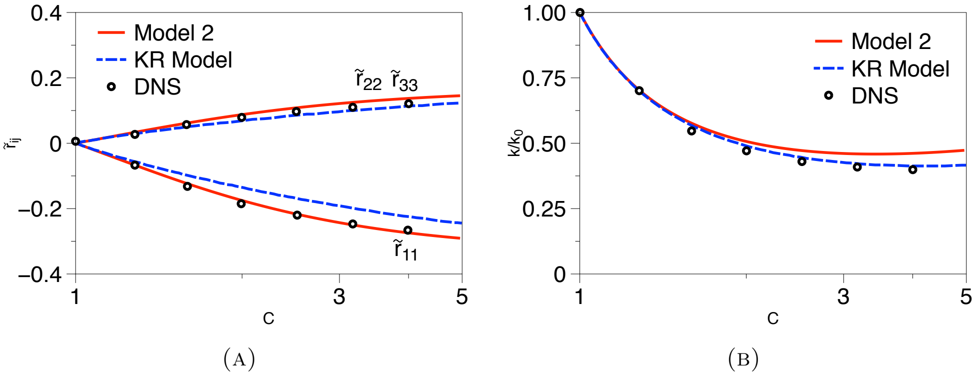

(A) (B)

FIGURE 4.3: Model 2 and KR model predictions for irrotational axisymmetric contraction with $S\kappa_0/\epsilon_0 = 0.56$. (a) Evolution of the normalized Reynolds stress anisotropic tensor $\tilde{r}_{ij}$. (b) Evolution of the normalized turbulent kinetic energy κ/κ_0. Comparison is made to the DNS of Lee and Reynolds [58], shown as symbols.

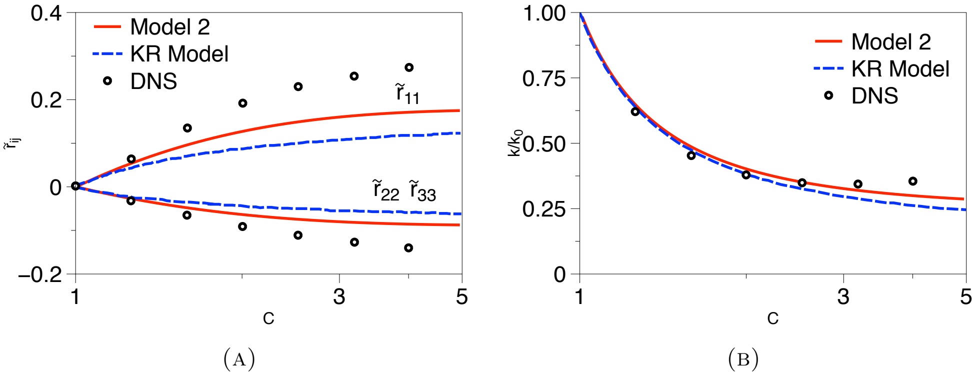

(A) (B)

FIGURE 4.4: Model 2 and KR model predictions for irrotational axisymmetric expansion with $S\kappa_0/\epsilon_0 = 0.41$. (a) Evolution of the normalized Reynolds stress anisotropic tensor $\tilde{r}_{ij}$. (b) Evolution of the normalized turbulent kinetic energy κ/κ_0. Comparison is made to the DNS of Lee and Reynolds [58], shown as symbols.

involves the initial non-zero contribution from the first two terms at the RHS of eq. (4.26), leading to a non-zero γ and consequently to a non-zero ϕ. Accordingly, the inclusion of the eddy-effective rotation rate in the constitutive equation lead to the activation of the stropholysis part, providing an additional contribution to the Reynolds stress in respect to the other models. After taking a closer look to the time evolution of the individual terms that are present in the transport equations, we concluded that even though the non-linear terms are the ones that "activated" the jetal mode, the evolution of the parameters is driven by the rapid terms. This argument is in compliance with the findings of Lee and Reynolds [58], enforced by Kassinos and Reynolds [22], who suggested that, even in the presence of an initially isotropic turbulent field, anisotropies could be triggered by unequal rates of return to isotropy for the two tensors r_{ij} and d_{ij}.

Additionally, we are interested on the evolution of the normalized dimensionality tensor d_{ij},

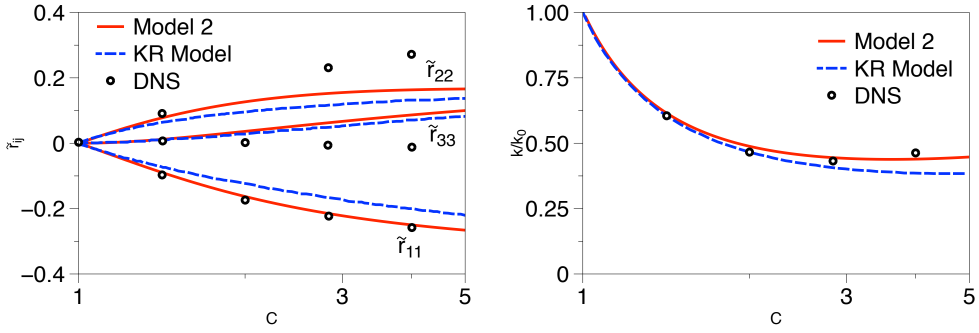

(A) (B)

FIGURE 4.5: Model 2 and KR model predictions for irrotational plane strain with $S\kappa_0/\epsilon_0 = 0.50$. (a) Evolution of the normalized Reynolds stress anisotropic tensor $\tilde{r}_{ij}$. (b) Evolution of the normalized turbulent kinetic energy κ/κ_0. Comparison is made to the DNS of Lee and Reynolds [58], shown as symbols.

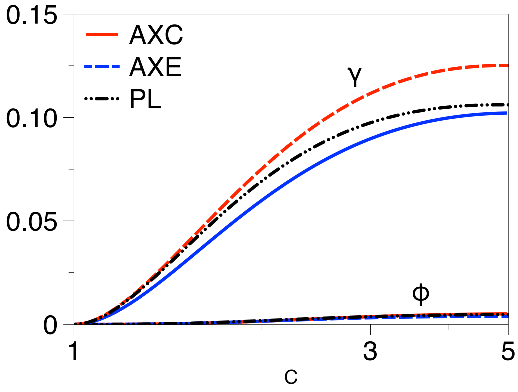

FIGURE 4.6: Model 2 predictions for the time evolution of the structural parameters ϕ and γ for irrotational axisymmetric contraction $(-)$; for irrotational axisymmetric expansion $(---)$; for irrotational plane strain $(\cdot\cdot-\cdot\cdot)$.

because this tensor is used to account for the non-linear effects through the model expressions for the effective gradients. In the following figures we ascertain the performance of Model 2 to predict the anisotropy of this tensor $\tilde{d}_{ij}$ for the three irrotational cases at the slow limit, defined as $\tilde{d}_{ij} = d_{ij} - \frac{\delta_{ij}}{3}$, either through the use of the algebraic expression in eq. (2.80b), or through its transport equation as expressed in eq. (4.34). For irrotational flows subjected to rapid deformations, eq. (2.80b) is shown to be exact, since the non-linear terms do not have time to disturb the random distribution of the eddy-axis vector at the plane of independence, thus the axisymmetric assumption remains valid. However, in the presence of slow deformations, non-linear eddy-eddy interactions provide an effective rotation acting on an individual eddy, leading to the breaking of the axisymmetry.

Figures 4.7a-4.8b show a comparison between Model 2 predictions and the corresponding DNS results using the two approaches. For all cases, the evaluation of d_{ij} through the transport

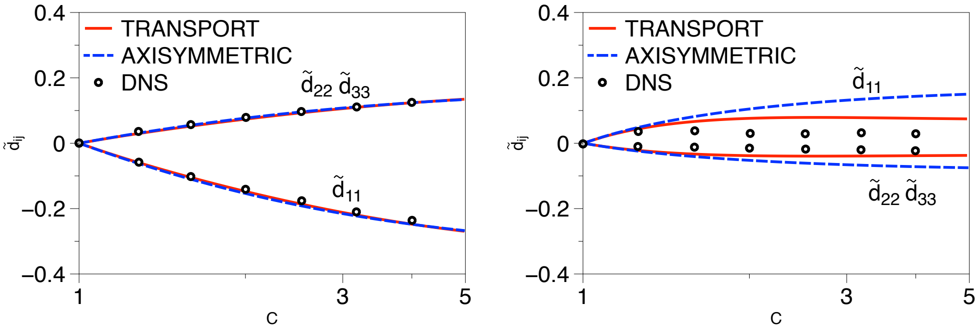

(A)

(B)

FIGURE 4.7: Model 2 predictions for the normalized anisotropic dimensionality tensor $\tilde{d}_{ij}$. Evaluation through eq. (2.80b) for axisymmetric assumption (−) and its transport evolution equation (− − −). (a) irrotational axisymmetric contraction with $S\kappa_0/\epsilon_0 = 0.56$. (b) irrotational axisymmetric expansion with $S\kappa_0/\epsilon_0 = 0.41$. Comparison is made to the DNS of Lee and Reynolds [58], shown as symbols.

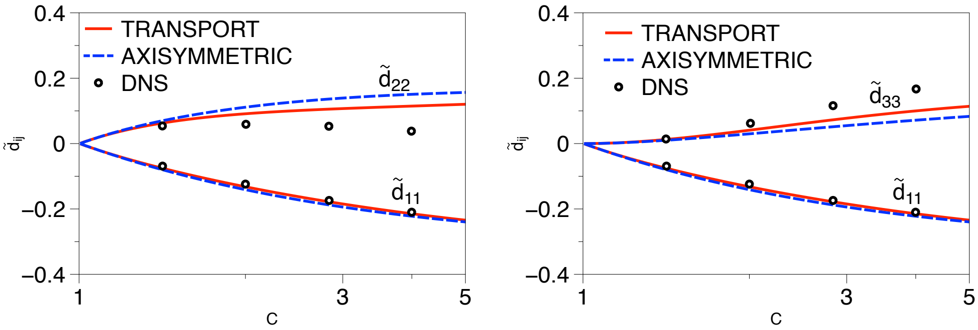

(A)

(B)

FIGURE 4.8: As in the previous figure for the irrotational plane strain. (a) $\tilde{d}_{11}$ and $\tilde{d}_{22}$ components. (a) $\tilde{d}_{11}$ and $\tilde{d}_{33}$ components.

equation produces more accurate predictions, particularly for axisymmetric expansion and plane strain, since for these cases the deviation from the axisymettric assumption is more profound. However, the replacement of the transport equation with the algebraic expression haven't lead to a noticeable improvement of the predictions for the axisymmetric expansion and plane strain cases, enforcing the argument that rapid terms are driving the evolution of the stresses.

4.6 Conclusions

The proposed structure-based models, denoted as Model 1 and Model 2, were validated for three fundamental irrotational cases, for rapid and weak deformations respectively. For the cases which correspond to rapid deformations, both Model 1 and Model 2 achieve excellent agreement with RDT, even at high levels of anisotropy. For irrotational axisymmetric contraction in the presence of weak deformations, both models are in good agreement with the DNS results for the Reynolds stress components. For the cases of irrotational axisymmetric expansion and plane strain, both models underpredict the magnitude of the $\tilde{r}_{22}$, $\tilde{r}_{33}$ anisotropic Reynolds stress components, providing however improved predictions in respect to the original stochastic model. Overall, the proposed models achieve better agreement with the DNS data than the KR model for all cases considered. Additionally, we replaced the simple algebraic expression for the dimensionality tensor with a suitable transport equation. The transport equation is constructed based on stochastic forcing terms such as to ensure realizability, yielding improved predictions for d_{ij}, without however any trivial changes on the Reynolds stresses. For initially isotropic turbulence, Model 2 is capable to produce non-zero values for the structural parameters, displaying a more meaningful physical behavior than the previous models, in consistence with previous works.

Chapter 5

Blending of the ASBM with the one-equation Spalart Allmaras model (ASBM-SA).

5.1 Introduction

Here we construct, for the first time, a new coupling of the ASBM with the one-equation SA model. The motivation is that the hybrid ASBM-SA model can potentially combine the numerical robustness and stability of the SA model along with the deeper physical content of the ASBM that ensures full realizability. Significant effort has been made for the development of a coupling which, except from providing improved results compared to the SA model, could be added to existing SA implementations with minimal additional effort. Such an approach could provide immediate access to ASBM technology in engineering codes. Thus, the main objectives of this work are (a) to describe the coupling of the ASBM and SA closures, (b) to outline the implementation of ASBM-SA model in our solver and evaluate its computational characteristics, such as numerical stability, speed of convergence etc., and (c) to evaluate the performance of the model in a number of standard benchmark cases.

5.1.1 Outline

Section 5.2 presents the details of the coupling of the ASBM closure with the SA model which yields the hybrid ASBM-SA model. This derivation is inspired by the work of Rahmann et al. [59], who derived a set of algebraic expressions from which the turbulence scales κ and ϵ can be extracted from one-equation turbulence models.

Section 5.3 is devoted to the validation of the proposed model in 2D standard benchmark cases. The computations include some simple cases where no flow separation occurrs, that of a fully developed channel flow and that of a turbulent boundary layer over a flat plate. Results for more advanced cases in the presence of moderate flow separation are shown also, such as a flow over a backward facing step, and a flow passing through an asymmetric diffuser. Finally, the performance of the hybrid model is ascertained in the challenging case of a turbulent flow over a 2D smooth bump in the shape of a "Modified Witch of Agnesi" hill, since it involves strong separation in the presence of both favorable/adverse pressure gradients .

5.2 Coupling with the SA model

The Spalart-Almaras (SA) closure is a one-equation turbulence model developed primarily for application in aerodynamics, but which has been successfully applied in a wider range of flows. The main limitation of SA (and any other one-equation model) is that it does not provide of a complete set of turbulence scales. On the other hand, the ASBM closure relies on the availability of suitable turbulence scales and this was the key stumbling block in trying to couple the ASBM and SA closures.

5.2.1 The Bradshaw Hypothesis

As early as the 1940's, a number of authors [60] had made the observation that in attached boundary layer flows the turbulent shear stress can be assumed to be approximately proportional to the turbulent kinetic energy and proposed simple models based on this approximation

$$|-\overline{uv}|/\kappa = a_1\,. \tag{5.1}$$

Later Bradshaw et al.[61] elaborated this approach further and used it as the basis for constructing a one-equation turbulence closure based on the assumption of a constant a_1, and as a result equation (5.1) is often referred to as 'the Bradshaw relation'. This relation is the starting point for coupling of the SA closure to the ASBM because it provides the framework for extracting the two turbulence scales needed by the ASBM from the SA closure.

Early attempts to use equation (5.1) for the construction of one-equation closures were based on the assumption of a constant a_1 throughout the flowfield. However, DNS and experimental data indicate that a_1 is not a constant in the near wall regime, neither in the viscous sublayer of the turbulent boundary layer, nor at the edge of the boundary layer, as indicated by Fares et al. [62] and Nagano et al. [63]. In their work, Nagano et al. provided a variable a_1 for the

Bradshaw relation through the use of Boussineq approximation,

$$\frac{|-\overline{uv}|}{\kappa} = a_1 = \frac{\nu_T}{\kappa}\frac{\partial u_t}{\partial y_n}\,, \tag{5.2}$$

where u_t is the tangential component of the mean velocity and y_n is the normal to the wall component of the local coordinate system, and where the turbulence structure parameter is assumed to have the functional form

$$a_1 = \sqrt{C_\mu f_a}\,. \tag{5.3}$$

Here, the role of the model function f_a is to account for the variation of a_1 in the viscous sublayer and the edge of the boundary layer.

5.2.2 Adaptation to the Spalart-Allmaras model

Traditionally, the Bradshaw hypothesis has been used as the starting point for transforming κ-ϵ closures to one equation models. Here, our objective is to use the same phenomenology in order to extract the turbulence scales (κ and ϵ) from the SA one-equation closure. Hence, we next require that the eddy viscosity as defined in the context of the SA closure[1],

$$\nu_T = f_{v1}\tilde{\nu}\,, \tag{5.4}$$

be consistent with the eddy viscosity arising in the low Reynolds number κ-ϵ model, namely

$$\nu_T = C_\mu f_\mu R, \qquad R = \frac{\kappa^2}{\epsilon}\,, \tag{5.5}$$

which yields the relation

$$f_{v1}\tilde{\nu} = C_\mu f_\mu R = \nu_T\,. \tag{5.6}$$

Using equations (5.3) and (5.6) in (5.2), allows the turbulent kinetic energy to be expressed in the form

$$\kappa = \tilde{\nu}\sqrt{\frac{f_{v1}}{C_\mu}}\, f_{\chi_{sa}}\, S\,, \qquad f_{\chi_{sa}} = \sqrt{\frac{f_{v1}}{f_a}}\,, \tag{5.7}$$

where the strain invariant $S = \sqrt{2S_{ij}S_{ij}}$ has been used in place of the velocity gradient $\partial u_t/\partial y_n$ for generality. The function $f_{\chi_{sa}}$ accounts for the variation of the turbulence structure parameter in both the viscous sublayer and the boundary layer edge and in general is a depended on the SA parameter χ_{sa} and on C_μ. Based on numerical optimizations the functional form

$$f_{\chi sa} = 1 + C_{\chi sa}^{0.8}, \quad C_{\chi sa} = \sqrt{C_\mu^2 + 1/(1+\chi_{sa})^2}, \quad C_\mu = 0.09\,, \tag{5.8}$$

has been adopted[59].

Specification of the effective strain contributions

Two important limitations of equation (5.7) is that it does not hold true in regions where S tends to zero and it does not adequately account for rotational effects. To overcome these limitations, and thus extend the range of applicability of the coupled closure, a modified strain rate $S_{\chi sa}$ is introduced in eq. (5.7), given by

$$S_{\chi sa} = \sqrt{\tilde{S}^2 + \tilde{S}_a^2}\,. \tag{5.9}$$

Here, $\tilde{S}$ represents an effective strain rate corrected for rotational effects, while $\tilde{S}_a$ provides an effective strain contribution in regions where S tends to zero.

Following the approach of Rahman et al.[59], the effective strain contributions are evaluated according to

$$\tilde{S} = f_k(S - \frac{|n_1| - n_1}{C_T})\,, \tag{5.10}$$

with

$$\begin{aligned} n_1 &= S - W\,, & f_k &= 1 - \frac{\tilde{f}_a}{C_T}\sqrt{\max(1 - Ra, 0)}\,, \\ Ra &= |W/S|\,, & \tilde{f}_a &= 1 - \exp(-\frac{\mu_T}{36\mu})\,, \end{aligned} \tag{5.11}$$

where $W = \sqrt{2\Omega_{ij}\Omega_{ij}}$ and $C_T = 2.0$. In eq. (5.10), the term inside the parenthesis considers the region where $Ra > 1$, such as in the vortex core, whereas function f_k accounts for $Ra < 1$ and ensures a smooth transition between the two regions. The second contribution to the modified strain rate, which provides a correction away from the wall, is given by

$$\tilde{S}_a = \frac{2C_{\chi sa}\tilde{f}_a}{3\nu}\left(\frac{\sqrt{\tilde{u}_i^2/2}}{1 + \mu_T/\mu}\right)^2, \tag{5.12}$$

where $C_{\chi sa}$ is given in equation (5.8) and $\tilde{u}_i$ is the mean velocity vector relative to the wall. Summarizing, κ is obtained from the equation

$$\kappa = \tilde{\nu} f_{\chi_{sa}} \sqrt{\frac{f_{v1}}{C_\mu}} \, S_{\chi_{sa}} \, , \tag{5.13}$$

along with the set of relations (5.8) through (5.12).

Consistent computation of the dissipation rate

In addition, a consistent evaluation of the dissipation rate ϵ is necessary in order to ensure realizable time and length scales. Following similar arguments as for the kinetic energy case[59], an algebraic expression for the reduced dissipation rate $\tilde{\epsilon}$ is adopted

$$\tilde{\epsilon} = f_{v1}^{1.3} \, \tilde{\nu} \, S_{\chi_{sa}}^2 \, , \tag{5.14}$$

where the exponent of f_{v1} is chosen through numerical optimizations.

Solid wall corrections

At a solid wall, both κ and $\tilde{\epsilon}$ tend to zero, but the vanishing of the reduced dissipation leads to numerical singularities and thus an additional correction is needed. The remedy is the addition of a term ϵ_w, which signifies the equality between the wall dissipation rate to the viscous-diffusion rate [59, 64], given by

$$\epsilon_w = 2 A_e \, \nu \, (\frac{\partial u_t}{\partial y_n})_w^2 \approx 2 A_e \, \nu \, S_{\chi_{sa}}^2 \, , \tag{5.15}$$

where ν is the kinematic viscosity of the fluid. Experimental and DNS data for channel flows and flow over a flat plate indicate a range for A_e between $0.05 < A_e < 0.11$. In the current computations, $A_e = C_\mu = 0.09$ is adopted.

Summing all parts that contribute to the dissipation rate yields the final modelling expression

$$\epsilon = \sqrt{\epsilon_w^2 + \tilde{\epsilon}^2} \, . \tag{5.16}$$

5.2.3 Determination of the ASBM time scale

The coupling of ASBM to the SA closure is completed by using equations (5.13) and (5.16) to obtain κ and ϵ respectively, which are then used for computing the turbulence time and length scales through the expressions [65],

$$\tau = \max\left(\frac{\kappa}{\epsilon}, C_T\sqrt{\frac{\nu}{\epsilon}}\right), \qquad L = C_L \max\left(\frac{\kappa^{3/2}}{\epsilon}, C_n(\frac{\nu^3}{\epsilon})^{1/4}\right), \tag{5.17}$$

where $C_L = 0.17$, $C_n = 80.0$, τ is the time scale and L is the characteristic length scale. For near-wall turbulence, a lower bound based on the Kolmogorov scales is imposed on the time and length scales. This procedure ensures proper near-wall behavior of the turbulence scales. Fig. 5.1 demonstrates a schematic description of the numerical procedure that was followed in the current work.

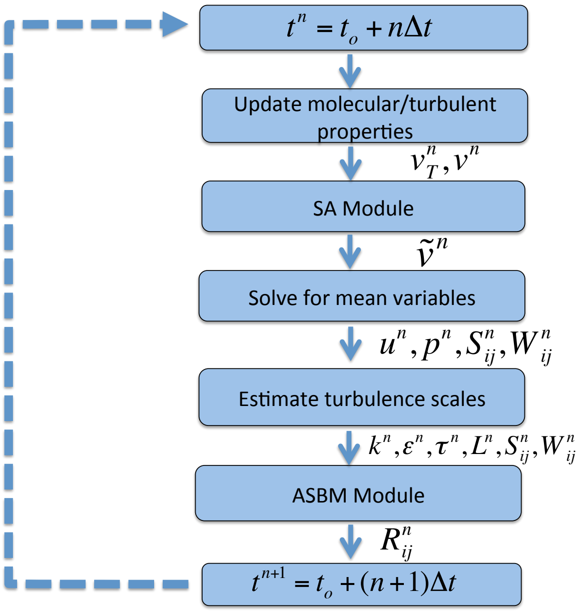

FIGURE 5.1: Schematic description of the structure of the coupling algorithm.

5.3 Computations

In order to test the efficiency and performance of the proposed ASBM-SA model, we consider a series of two-dimensional flows, namely a fully-developed channel flow, a turbulent boundary layer over a flat plate, a backward-facing step, an asymmetric diffuser and a smooth steep hill. The model is validated against DNS and experimental data and compared to the standard SA model. In all cases, the computations were repeated on progressivelly finer grids till a grid indepedent solution was achieved. An unstructured, nodal-based finite-volume code called CDP that has been developed at the Center of Turbulence Research (Stanford/NASA) is used as a general platform. For the discretization of the diffusive and advection terms in both the mean and turbulent transport equations, a second-order accurate centered-difference scheme with skewness corrections has been used. The coupling of the transport equations is done through a fractional-step method, while a Crank-Nicholson scheme is used for time integration. Details of the code have been described extensively in [66].

5.3.1 Fully-developed channel flow

Computations are carried out for fully-developed turbulent channel flow at a Reynolds numbers $Re_\tau = 180$, $Re_\tau = 550$ and $Re_\tau = 2000$, based on the channel half-height δ and friction velocity u_τ. The profiles are compared to the DNS data of Del Alamo and Jimenez [67] and Hoyas and Jimenez [68]. The flow is maintained by a uniform mean pressure gradient imposed along the streamwise direction x. No-slip boundary conditions are applied at the top and bottom walls and periodic conditions along the other two directions. Computations are carried on a 1x105x1 nonuniform grid based on the grid independence test and in order to ensure proper near-wall resolution, the first cells adjacent to the walls are placed at $y^+ < 1.0$. Results are non-dimensionalized using the friction velocity, as $U_x^+ = U_x/u_\tau$, $u_{rms} = \sqrt{R_{xx}}/u_\tau$, $v_{rms} = \sqrt{R_{yy}}/u_\tau$, $w_{rms} = \sqrt{R_{zz}}/u_\tau$ and $uv = -R_{xy}/u_\tau^2$.

Figures 5.2a - 5.2c show the mean velocity profile for the low ($Re_\tau = 180$), the intermediate ($Re_\tau = 550$) and the high ($Re_\tau = 2000$) Reynolds number cases, respectively. In all cases, the predictions of both the ASBM-SA and SA models agree well with the DNS data. As shown, in the buffer and log-layer regions ($30 < y^+ < 50$), the ASBM-SA coupling produces a marginal improvement relative to the SA predictions.

Corresponding profiles for the rms quantities are displayed in Figs. 5.3a - 5.3c, where again good agreement of the model predictions with the DNS data is noted. The SA closure cannot provide predictions for the rms turbulence quantities and thus the comparison is made only between the ASBM-SA closure and the DNS results.

5.3.2 Turbulent boundary layer

Next, we consider the case of a turbulent boundary layer flow over a flat plate, for which many experimental datasets are available. Here, we have chosen to validate the model against the experiments of Loureiro and Freire,[69] since these are related to the inlet conditions used later for the 'Witch of Agnesi' case. The Reynolds number is Re_δ=4772, based on freestream velocity u_δ and the boundary thickness δ, corresponding to a friction-velocity Reynolds number of $Re_\tau = 277$. At the inlet, Dirichlet boundary conditions are imposed for $\tilde{\nu}$ and U_i, while zero-flux is used for the other variables. For all flow variables, a penalty condition is applied at the outlet to ensure mass conservation and a zero-flux at the top free surface, while symmetry conditions are used in the spanwise direction. Finally, a no-slip

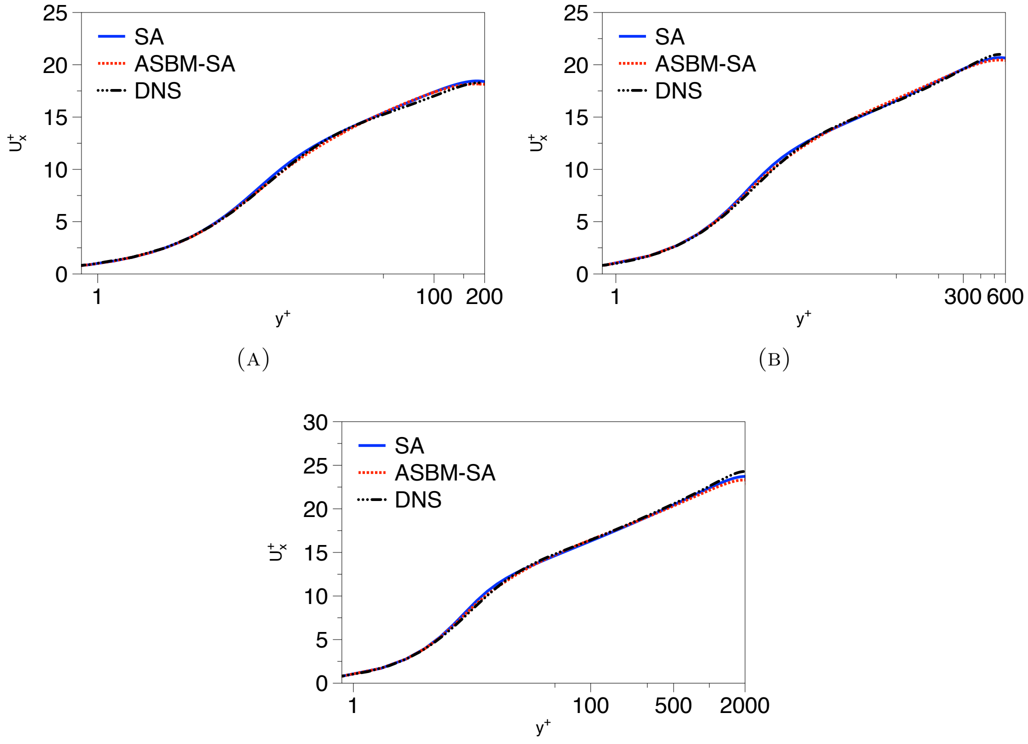

(A)

(B)

(C)

FIGURE 5.2: Fully-developed turbulent channel flow at (a) $Re_\tau = 180$ (b) $Re_\tau = 550$ and (c) $Re_\tau = 2000$. Model predictions (lines) for the streamwise mean velocity are compared to the DNS results (symbols) .[67, 68]

condition is used at the bottom wall. In order to ensure adequate resolution, the cells adjacent to the wall are placed within $y^+ < 0.9$. The computations are carried on a nonuniform grid of size 63x104x1 in the streamwise, wall-normal and spanwise directions, respectively. The grid is stretched along the wall-normal direction, but kept uniform along the streamwise. Finer grids were also considered, which all converged to the same solutions, indicating grid-independence for our results.

Figure 5.4a highlights the performance of the ASBM-SA closure. In the case of the mean velocity U_x^+, the predictions lie very close to those of the SA model and are in good agreement with the experiments. As shown in Fig. 5.4b, the ASBM-SA predictions for the rms turbulent fluctuations are in very good agreement with the experimental values for $y^+ > 10$.

5.3.3 Backward facing step

To ascertain the performance in separated flows, the proposed model is applied to the flow over a backward facing step. This is the simplest benchmark case with flow separation, since the separation point is fixed. Computations are conducted for flow conditions that correspond to

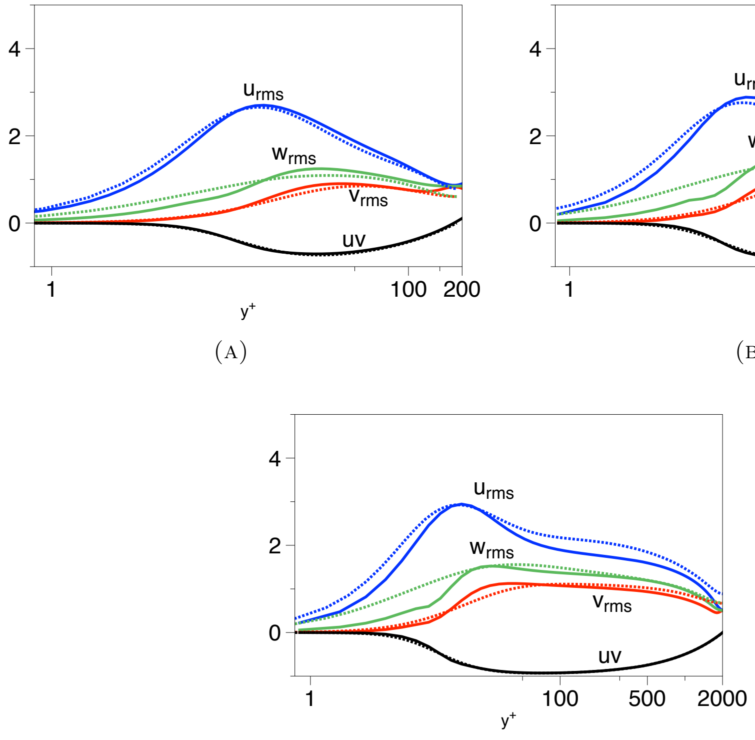

(A)

(B)

(C)

FIGURE 5.3: Fully-developed turbulent channel flow at (a) $Re_\tau = 180$ (b) $Re_\tau = 550$ and (c) $Re_\tau = 2000$. The predictions of the ASBM-SA model (solid lines) for the streamwise intensities are compared to the DNS results (dashed lines).[67, 68]

the experiment performed by Jovic and Driver[70] and the DNS computations by Le et al.[71]. At the inlet, a zero-pressure-gradient (ZPG) boundary layer profile is imposed, corresponding to a Reynolds number $Re_h = 5100$ based on the step size h and the freestream velocity u_o, and taken from an SA computation of a ZPG boundary layer. The same (SA based) inlet profile was used for both the SA and the ASBM-SA computations in order to make the comparison more meaningful. The ratio between the inlet height and the step height is 4. In the current computations, the grid is arranged in two blocks. The upper block (the area above the step) contains a 160x91x1 nonuniform grid, while the lower one contains a 134x31x1 nonuniform grid respectively. Both grids are stretched in both the streamwise and the crossflow directions. The grid independence of our results was verified by computing the flow on a finer grid containing an upper block of 161x153x1 and a lower one of 134x63x1 and demonstraing that the solution remained unaffected. The maximum distance between the first grid cell and the wall is kept within $y^+ \leq 0.75$. Details of the flow geometry and grid design are shown in Fig. 5.18.

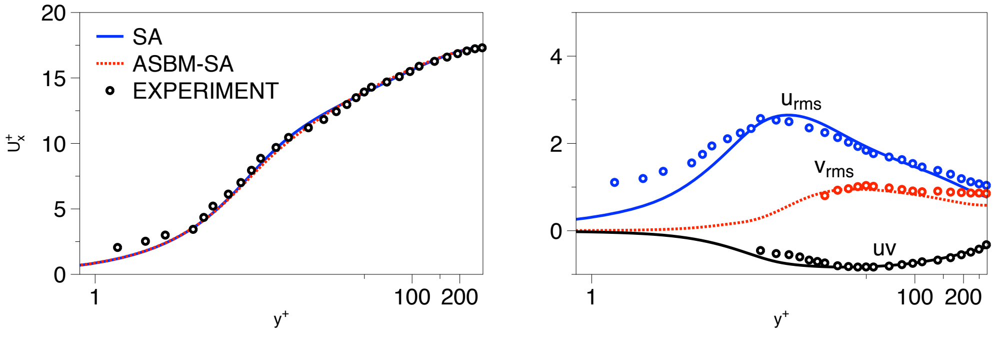

(A) (B)

FIGURE 5.4: Turbulent boundary layer at Re_δ=4772. SA and ASBM-SA model predictions (lines) for (a) the streamwise mean velocity and ASBM-SA model predictions (lines) for (b) the rms and shear stresses. Comparison is made to the experimental values of Loureiro and Freire[69], shown as symbols.

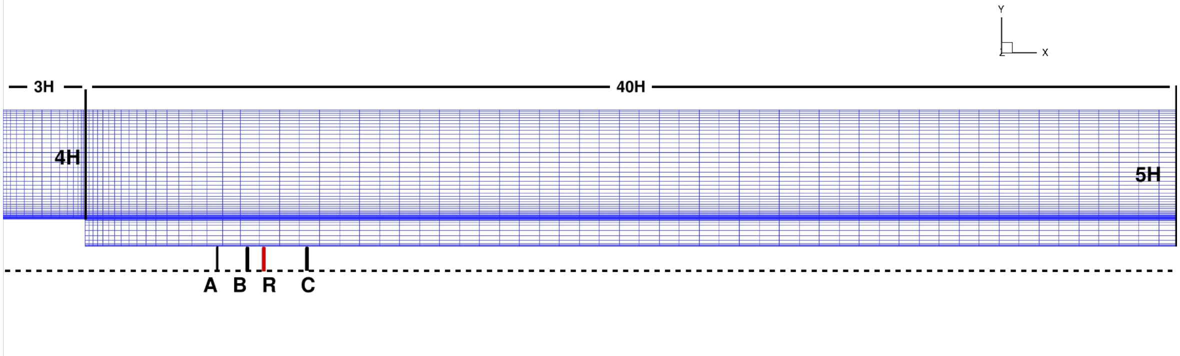

FIGURE 5.5: Geometry and grid design for RANS computations of turbulent flow over a backward facing step at inlet Re_h = 5100. The domain inlet is located at a distance of 3H upstream of the step corner, while the outlet is at a distance 40H downstream the corner. The ratio between inlet-step height is 4. Data is extracted at two stations located within the re-circulation region (A,B) and one station located at the recovery region (C). The location of the experimental reattachment point (R) is also shown.

The inlet conditions are specified at a distance of $3h$ upstream of the corner, whereas the outlet boundary conditions are imposed at 40h downstream of the corner. The imposed boundary conditions correspond to slip conditions at the top surface of the domain, no-slip conditions at the bottom wall, and periodic conditions in the spanwise direction. All the quantities reported are normalized by the step size h and the reference freestream velocity u_o. The distance x/h is measured exactly from the step corner. The streamwise mean velocity profiles at three representative positions are shown in Figs. 5.6a, 5.6b and 5.6c. The first two positions, x/h=4 and x/h=6 are located inside the recirculation region, whereas the third, x/h=10, is within the recovery region. As shown, both the SA and ASBM-SA models capture accurately the profiles in the separation region. In the recovery region, a slight underestimation of the freestream value is observed.

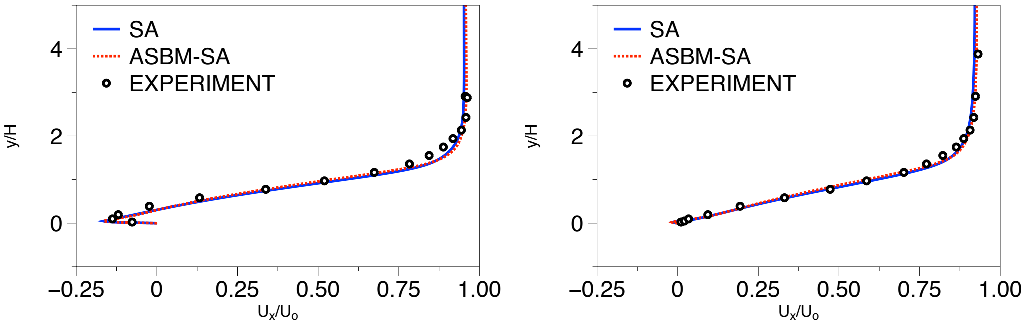

(A) $x/H = 4$ (B) $x/H = 6$

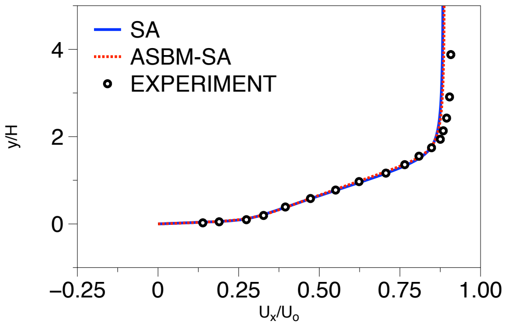

(C) $x/H = 10$

FIGURE 5.6: Turbulent flow over a backward facing step at $Re_h = 5100$. Model predictions for the streamwise mean velocity at streamwise locations: (a) x/h =4, (b) x/h=6 and (c) x/h=10. Comparison is made to the experiments of Jovic & Driver, [70] shown as symbols.

Comparisons for the distributions of Reynolds stress components at the three reference locations are shown in Figs. 5.7, 5.8 and 5.9. The ASBM-SA closure provides encouraging results in both the recirculation and recovery regions. It captures both the peak magnitudes and the freestream values, proving its sensitivity to the anisotropic nature of this flow.

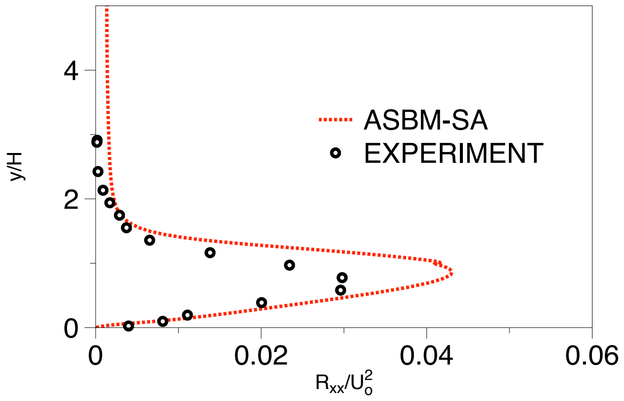

(A) $x/H = 4$

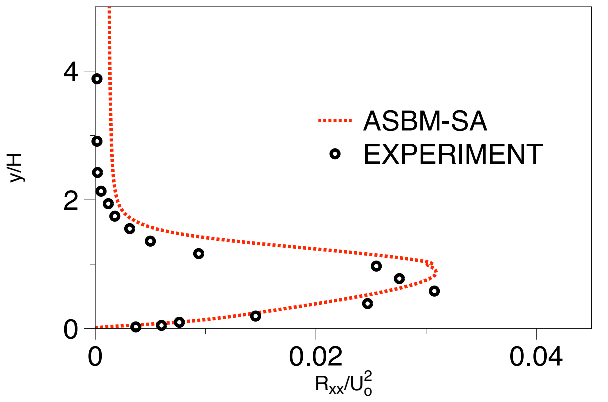

(B) $x/H = 6$

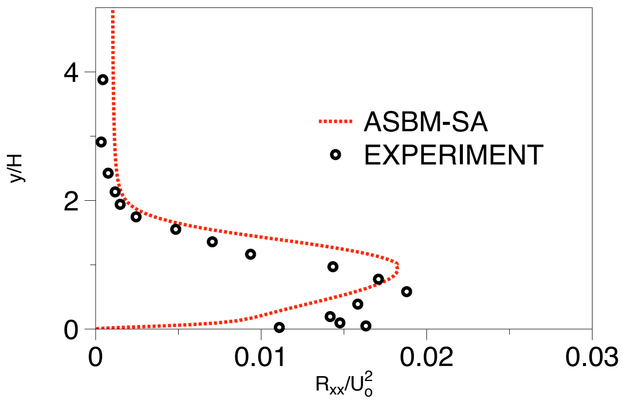

(C) $x/H = 10$

FIGURE 5.7: Turbulent flow over a backward facing step at $Re_h = 5100$. ASBM-SA model predictions for the normalized streamwise Reynolds stress (R_{xx}/U_o^2) at different streamwise locations: (a) x/h =4, (b) x/h=6 and (c)x/h=10. Comparison is made to the experiments of Jovic & Driver, [70] shown as symbols.

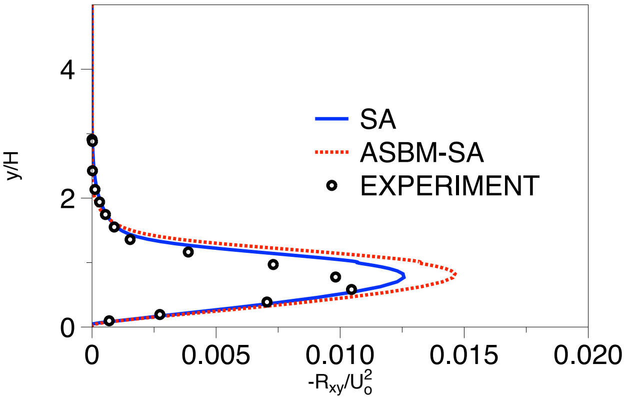

(A) $x/H = 4$

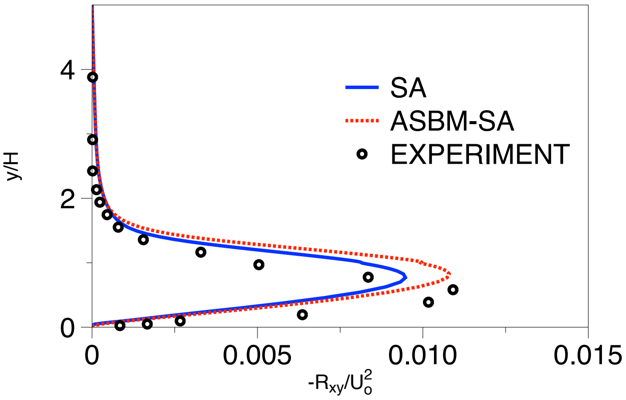

(B) $x/H = 6$

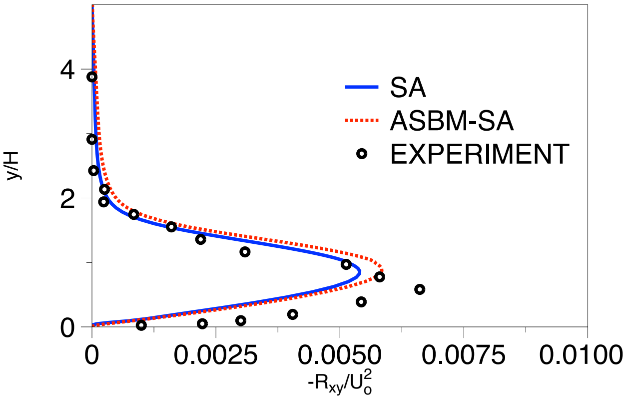

(C) $x/H = 10$

FIGURE 5.8: Turbulent flow over a backward facing step at $Re_h = 5100$. SA and ASBM-SA predictions for the normalized turbulent shear stress $(-R_{xy}/U_o^2)$ at three x-stations: (a) x/h =4, (b) x/h=6 and (c)x/h=10. Comparison is made to the experiments of Jovic & Driver [70], shown as symbols.

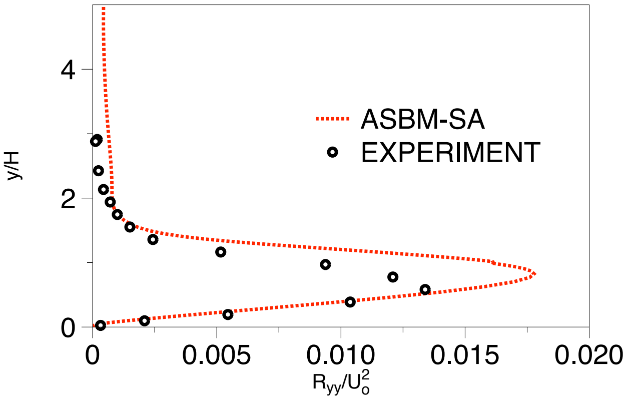

(A) $x/H = 4$

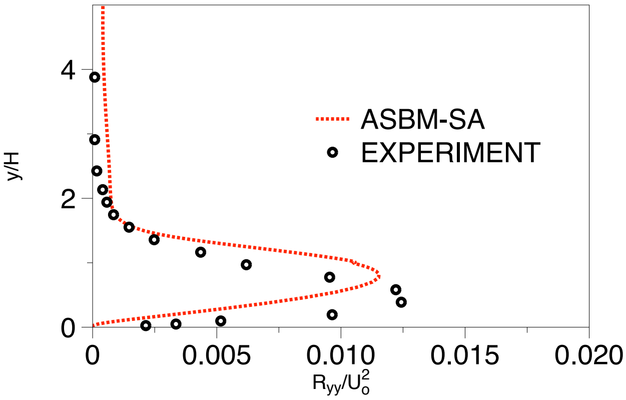

(B) $x/H = 6$

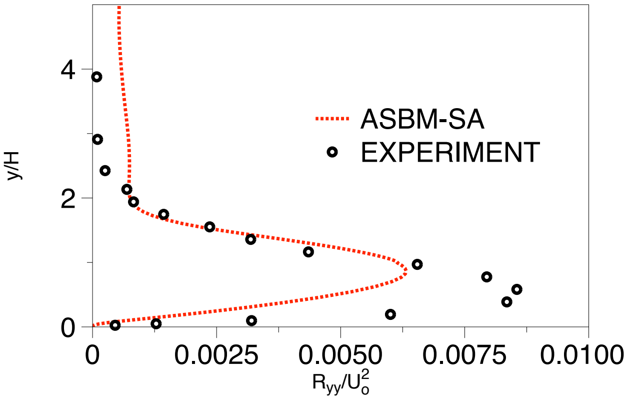

(C) $x/H = 10$

FIGURE 5.9: Turbulent flow over a backward facing step at $Re_h = 5100$. ASBM-SA predictions for the transverse Reynolds stress (R_{yy}/U_o^2) at three x-stations: (a) x/h =4, (b) x/h=6 and (c) x/h=10. Comparison is made to the experiments of Jovic & Driver, [70] shown as symbols.

The re-attachment length X_r predicted by DNS is $X_r = 6.39$ in step-height units. Both SA and ASBM-SA predict the same $X_r = 6.51$.

The variation of the skin-friction coefficient C_f with streamwise distance along the bottom wall is shown in Fig. 5.10. Both the SA and ASBM-SA closures are in reasonable agreement with the experimental and DNS results, but the ASBM-SA produces slightly improved C_f levels in the recirculation bubble and after reattachment.

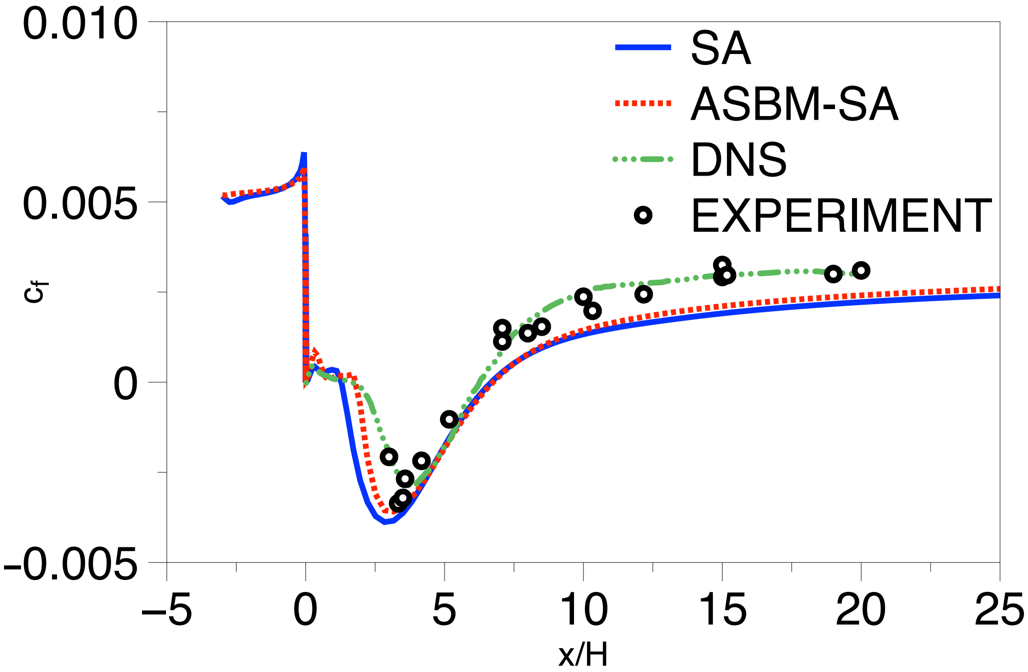

FIGURE 5.10: SA and ASBM-SA model predictions for the skin-friction coefficient at the bottom wall. Comparison is made to experiments of Jovic & Driver [70] and the DNS of Le et al.[71].

5.3.4 Asymmetric diffuser

Steady flow in a two dimensional asymmetric diffuser is considered next. In this type of flow, adverse pressure gradients are generated leading to a large recirculation bubble. The flow conditions are chosen to correspond to the reliable and detailed experimental database of Obi et at. [72] The profile specified at the inlet is obtained from an SA solution for a fully-developed channel flow corresponding to a Reynolds number of Re =20,000 based on the channel height and the centerline velocity. At the bottom and top walls a no-slip condition is applied, whereas periodic conditions are used in the spanwise direction. Finally, a penalty condition is used at the outlet, ensuring mass conservation. A 148x68x1 non-uniform grid is used, stretched along the transverse direction so that the $y^+ < 1$ of all grid points adjacent to the walls. Fig. 5.11 shows details of the computational grid, where the stations marked with letters A through D correspond to the positions $x/h = 6$, $x/h = 16$, $x/h = 24$ and $x/h = 29$ respectively, which are all located inside the recirculation region. Station A roughly corresponds to the experimental flow separation point. Finally, station R corresponds to the location of the experimental re-attachment point, which was located approximately at $x/h = 30$. Comparisons between model predictions and experimental results are done at these locations.

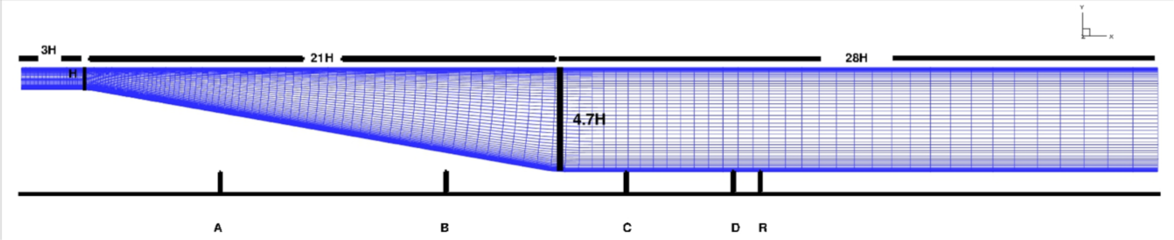

FIGURE 5.11: Geometry and mesh details for RANS computations of turbulent flow in an asymmetry diffuser. The domain inlet is located at a distance of 3H upstream the point at the beginning of the expansion region, while the outlet is at a distance 49H downstream that point. The expansion domain is 21H long at the streamwise direction, yielding an expansion ratio of 4.7. Data is extracted at four stations located within the re-circulation region. The re-attachment point(R) is also shown.

Fig. 5.12 demonstrates the time development of the maximum velocity residual, ensuring that fully converged, steady solutions are reached. The residual is normalized by its initial value and is given by

$$Res = max\left[\frac{V \ \times \Delta U/\Delta t}{(V \ \times \Delta U/\Delta t)_o}\right], \qquad \Delta U = U^{n+1} - U^n\,, \tag{5.18}$$

where n is the number of iteration, Δt is the uniform time step, U is the streamwise mean velocity and V is the volume of the corresponding cell. As shown in Fig. 5.12, the ASBM-SA model achieves the same final residual levels as the SA closure, an observation that applies to all cases considered in this work.

Both mean and turbulent quantities are normalized by the channel height H and the reference bulk velocity U_o, obtained from the channel simulation. The origin of the x coordinate ($x/h = 0$) is located at the beginning of the expansion section.

Figure 5.13 showcases the predictions of the ASBM-SA and SA models for the wall static-pressure coefficient $C_p = (p - p_o)/\frac{1}{2}\rho U_o^2$ and the skin-friction coefficient C_f along the bottom wall. The ASBM-SA closure yields a significant improvement in the prediction of C_p relative to SA, especially after reattachment (see Fig. 5.13a). The ASBM-SA model correctly predicts both the drop and the subsequent recovery of the pressure, with only a slight overestimation of the C_p near the outlet. This difference between experiments and predictions has also been

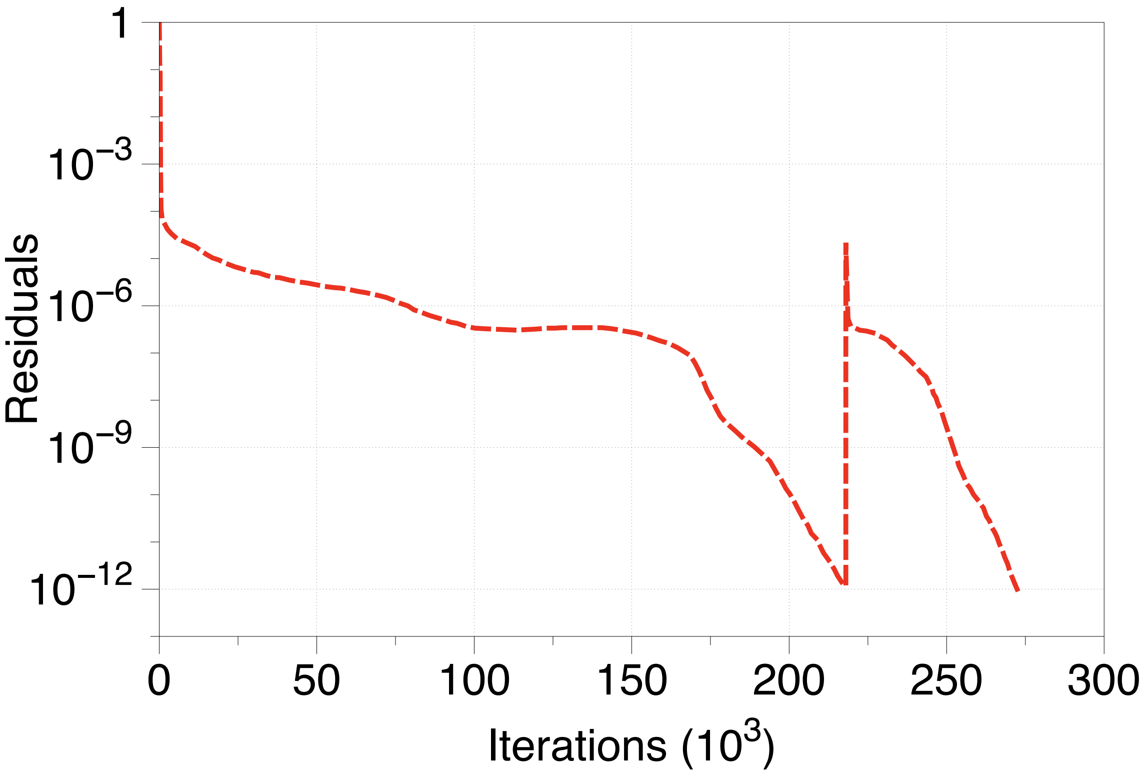

FIGURE 5.12: Time history of the mean velocity residual for the ASBM-SA. The instantaneous jump in the residual levels, indicates the point where the ASBM coupling is turned on.

observed in the LES results of Kaltenbach et al.[73] The two models produce similar C_f predictions that are in good agreement with the experiments. Based on these skin-friction results, the separation and re-attachment points are predicted by both the SA and ASBM-SA models to be approximately at $x/h = 3.6$ and $x/h = 33.5$ respectively. Thus, both models over-predict the size of the recirculation bubble. These results are consistent with those of DalBello et al.[74] who has also computed the same case using the SA model. A slight C_f oscillation is observed in the solution of both models at $x/h \approx 20$. This wiggle in the C_f profile is located around the point $x/H = 21$, which is the point where the geometry exhibits a sharp change (end of expansion region). Thus, these oscillations in the C_f profile seem to be associated with the sudden change of the geometry and are most likely caused by the recirculating flow encountering the inclined wall. These disturbances in the C_f profile are also known to be exhibited in the solutions of other RANS models[74].

Fig. 5.14 shows the predictions for the mean streamwise velocities at the reference stations. As shown, the ASBM-SA predictions are in better agreement with the experiments than the SA predictions at all stations, except at the last one that is located at the edge of the recirculation region.

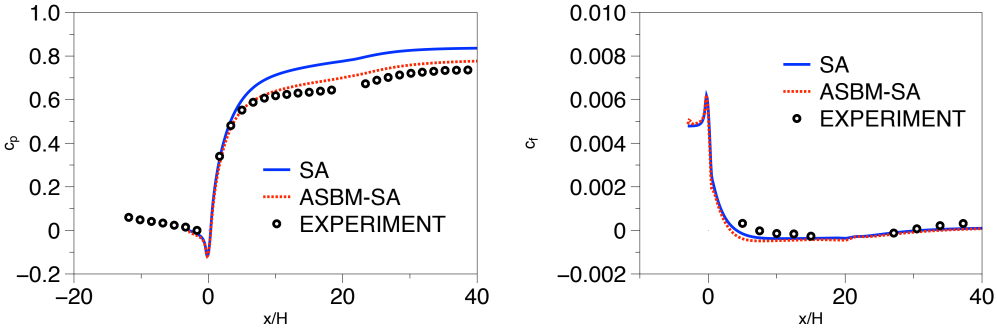

(A) (B)

FIGURE 5.13: SA and ASBM-SA model predictions at the bottom wall for (a) the wall static-pressure coefficient and (b) the wall skin-friction coefficient . Comparison is made to the experimental values of Obi et al.[72]

Comparisons between the ASBM-SA predictions and the experiments for the diagonal R_{xx} and R_{yy} Reynolds stress components are shown in Figs. 5.15 and 5.16 respectively. The closure is in fair agreement with the experiments, capturing the peak levels and saddle points in the profiles. Fig. 5.17 shows comparison between ASBM-SA predictions and SA for the

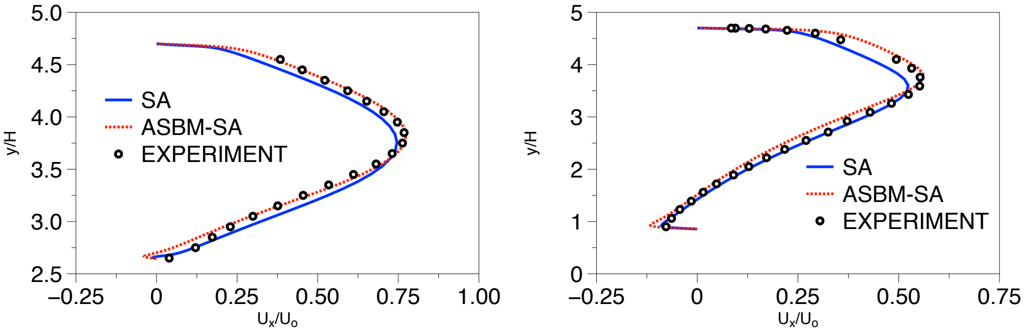

(A) station A, $x/h = 6.0$ (B) station B, $x/h = 16.0$

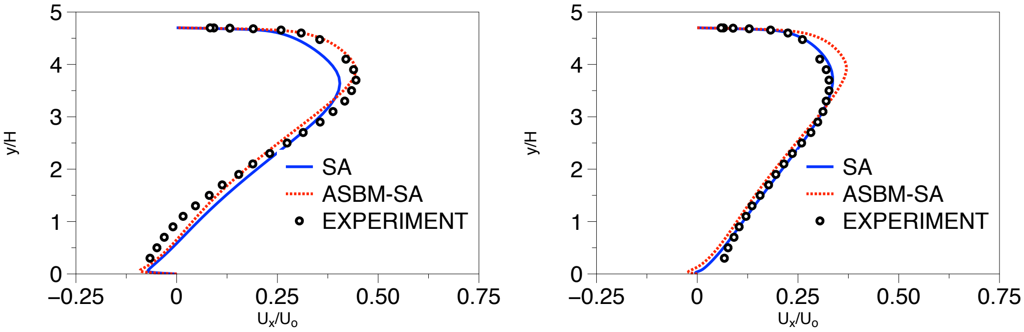

(C) station C, $x/h = 24.0$ (D) station D, $x/h = 29$

FIGURE 5.14: Turbulent flow over the asymmetry diffuser. Model predictions for the streamwise mean velocity U_x at various x-stations for SA and ASBM-SA closures. Comparison is made to the experimental values of Obi et al.[72].

shear stress component R_{xy}. At the first two stations, ASBM-SA overestimates the near wall peak magnitude at the bottom wall, whereas SA captures the correct magnitudes. At the last two-stations however, the closure recovers and provides better agreement with experiments than the SA closure.

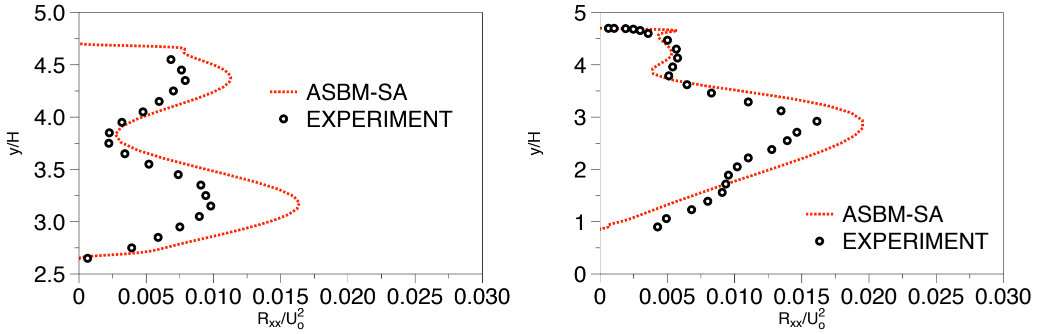

(A) station A, $x/h = 6.0$ (B) station B, $x/h = 16.0$

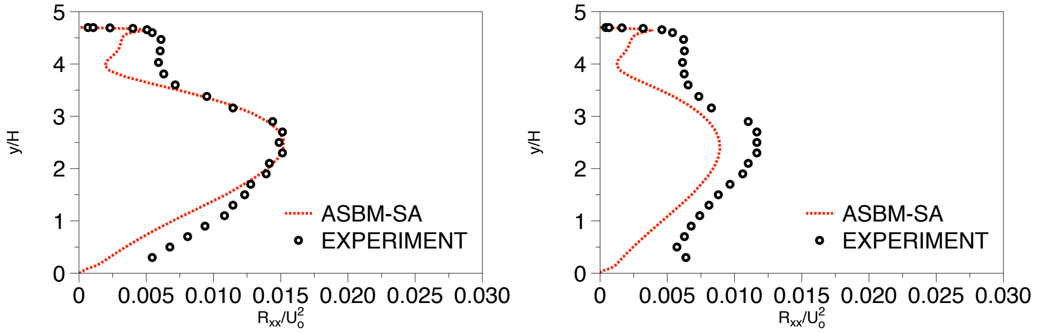

(C) station C, $x/h = 24.0$ (D) station D, $x/h = 29$

FIGURE 5.15: Model predictions for the streamwise components R_{xx} at various x-stations for SA and ASBM-SA closures. Comparison is made to the experimental values of Obi et al.[72]

5.3.5 Smooth hill

To further evaluate the model performance in configurations involving flow separation, we consider next a case in which the separation point is not fixed. Thus, the ASBM-SA and SA models are applied to a model complex terrain, specifically to flow over a steep smooth hill. The shape of the hill is defined using a modified 'Witch of Agnesi' profile. Detailed near-wall experimental data [69] provide a good data set for model validation. For the sake of comparison, additional computations for the same case were performed using ASBM couplings with other EVM, which were implemented by us in the same code. Based on our findings, we have chosen ASBM-BSL closure for our following discussion because it had shown that among ASBM couplings it is the one that produces the most reliable results for this case.

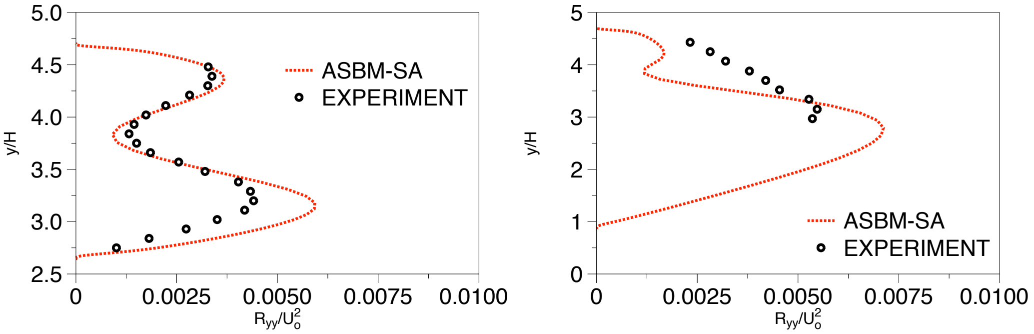

(A) station A, $x/h = 6.0$ (B) station B, $x/h = 16.0$

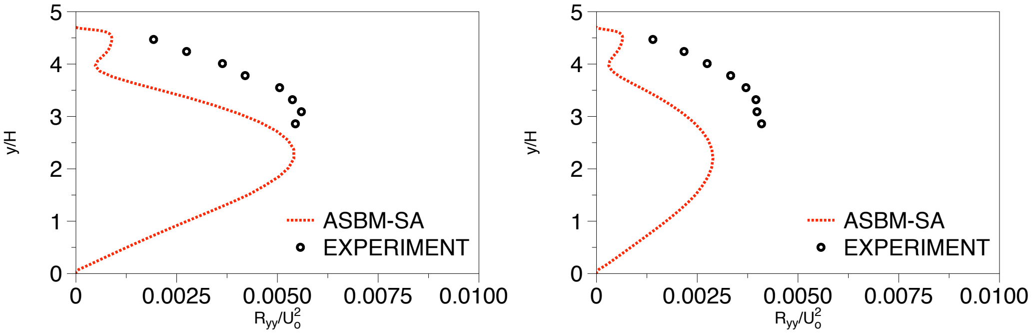

(C) station C, $x/h = 24.0$ (D) station D, $x/h = 29$

FIGURE 5.16: Model predictions for the streamwise components R_{yy} at various x-stations for SA and ASBM-SA closures. Comparison is made to the experimental values of Obi et al.[72]

The computational domain and its mesh details are shown in Fig 5.18. Domain dimensions are expressed in terms of the hill height H. Thus, the domain has a total height and length of $4H$ and $27.73H$, respectively, and is divided into three sections. First form left to right is the inlet section that has a length of $7.5H$ and contains 64x119x1 grid cells. A second section with a length of $10H$ encloses the hill and contains 169x119x1 cells, and finally the outlet block is $10.23H$ in length and contains 74x119x1 cells.A grid sensitivity analysis was used in order to ensure grid independence of the solution. For this purpose, additional computations on both a coarser (with blocks of 50x100x1, 120x100x1 and 60x100x1) and a finer grid (with blocks 97x125x1, 331x125x1 and 158x125x1) were performed. It was confirmed that the same solution was obtained when using the two finer grids, thus verifying that our solutions are grid converged.

At the inlet, the height of the cell adjacent to the wall is placed at a $y^+ \approx 0.25$. The inlet profile is extracted from a flat-plate boundary layer simulation at $Re_\delta = 4772$, where the Reynolds number is based on the freestream velocity u_δ and the boundary layer thickness δ. An outflow penalty condition was used at the outlet, a no-slip condition at the bottom wall,

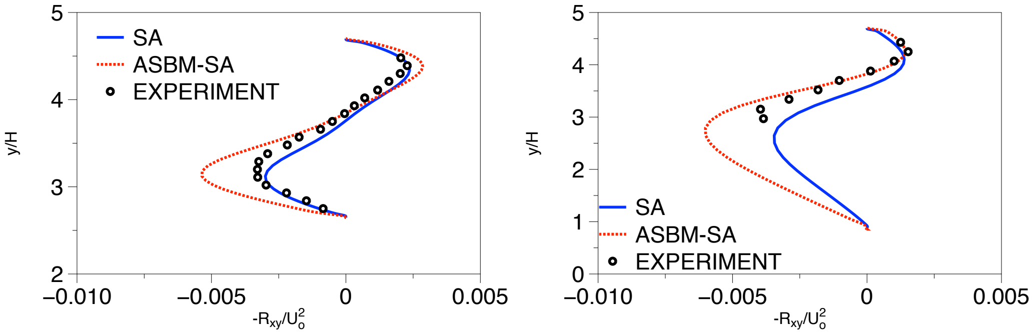

(A) station A, $x/h = 6.0$ (B) station B, $x/h = 16.0$

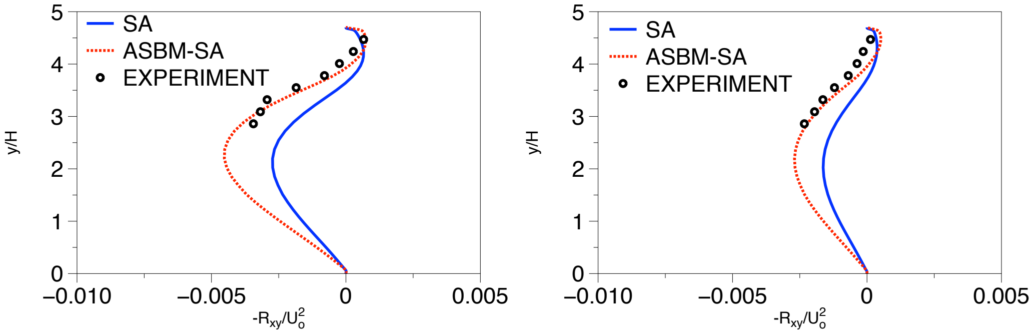

(C) station C, $x/h = 24.0$ (D) station D, $x/h = 29$

FIGURE 5.17: Model predictions for the shear stress component R_{xy} at various x-stations for SA and ASBM-SA closures. Comparison is made to the experimental values of Obi et al.[72]

a slip condition at the top free surface, and periodic conditions were imposed in the spanwise direction.

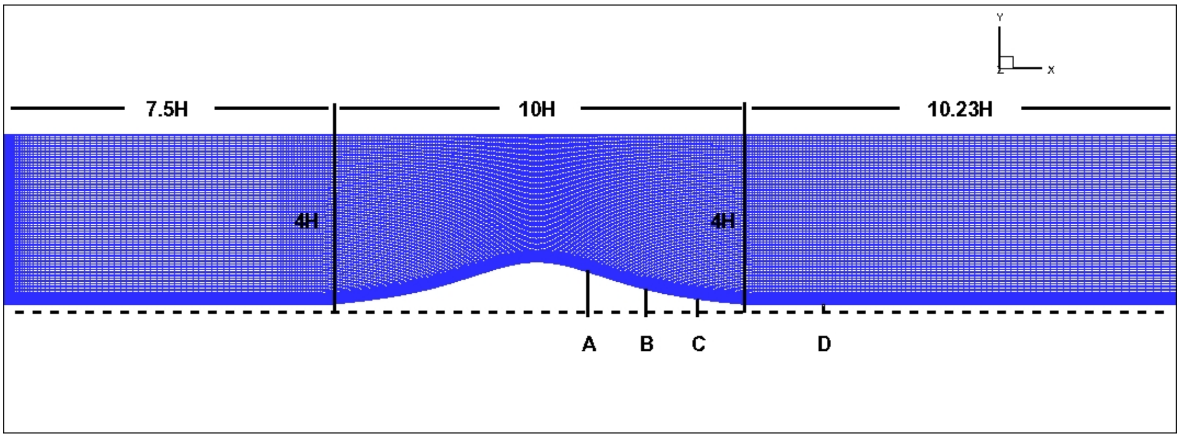

FIGURE 5.18: Geometry and grid design for RANS computations of turbulent flow over the 'Witch of Agnesi Hill' at inlet $Re_\delta = 4772$. The domain inlet is located at a distance of 12.5H from the hilltop, while the outlet is at 15.23H. The domain height is 4H. Data is extracted at three stations located within the re-circulation region (A,B,C) and one station located near the experimental re-attachment point.

Firstly we report on how the prediction for the recirculation region and the profiles of the turbulent intensities is affected by the choice of carrier closure. We report results for both the uncoupled and ASBM-coupled models. In particular, we focus on the extent of the predicted recirculation region and the profiles of the turbulent intensities and the turbulent shear stress at different stations along the streamwise direction.

Table 5.1 shows model predictions related to the recirculation zone. As shown, the uncoupled BSL model gives better results than the rest of the models, followed closely by the SA model. However, the ASBM-BSL also seems to be more sensitive to the coupling than ASBM-SA. After comparing all models, we concluded that the BSL and SA models produce the best predictions, in both the uncoupled and the ASBM-coupled case.

Turbulence Closure	Separation Point(x/H)	Re-attachment Point(x/H)	L_s/H
Uncoupled Case			
v^2-f	0.26	9.18	8.92
BSL	0.33	6.67	6.34
SST	0.27	8.08	7.81
Wilcox	0.27	9.67	9.40
SA	0.27	7.84	7.57
Coupled with ASBM			
ASBM-v^2-f	0.23	9.70	9.47
ASBM-BSL	0.27	7.80	7.53
ASBM-SST	0.27	9.1	8.83
ASBM-Wilcox	0.27	10.1	9.83
ASBM-SA	0.27	8.32	8.05
Experiments	0.50	6.67	6.17

TABLE 5.1: Recirculation zone data

Next, we investigated the stability and robustness of all the ASBM-coupled two-equation models. To achieve this we have used the following procedure: for each different ASBM coupling, we first run the carrier model alone (without the ASBM coupling) until a converged solution was obtained. Then, we have used that solution as an initial guess for the coupled run, where the same carrier model was now coupled to ASBM. The convergence results for this procedure are shown in Figure 5.20. On the horizontal axis we show the number of iterations, while on the vertical one we show the maximum velocity residual, normalized by its initial value. This is given by eq. (5.18).

As already mentioned in previous studies, the original ASBM-v^2-f resulted in spurious undulations in the contour plots of the mean velocity in the recirculation region, as shown in Figure 5.19a. The first important finding from this effort is that all the ASBM-coupled versions of the new carrier models (ASBM-SST, ASBM-BSL, ASBM-Wilcox, ASBM-SA) are completely free of these numerical artifacts. For example, Figure 5.19b shows contours of the streamwise mean velocity as obtained with the ASBM-SA coupled model, but similar results have been obtained with all the other new couplings of the ASBM. Thus, the artifacts in the original solution were not related to the ASBM, but were peculiar to v^2-f or at least to the ASBM-v^2-$f-$ coupling. Based on these findings, we have decided that this issue has been closed and at this stage there is no reason to revisit the ASBM formulation for this purpose.

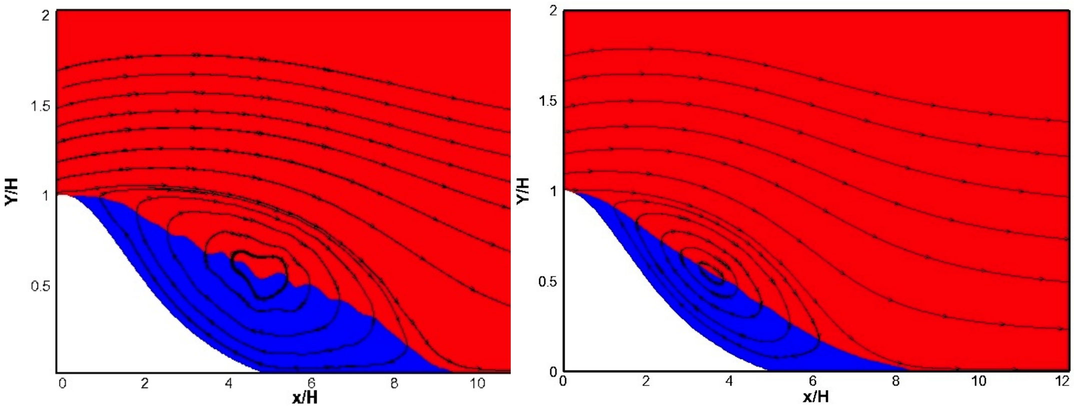

(A) ASBM-v^2-f (B) ASBM-SA

FIGURE 5.19: Contour predictions of the streamwise mean velocity profile for (a) ASBM-SA and (b) ASBM-v^2-f models on the leeward side of the hill.

As expected, all the κ-ω models exhibited very similar behavior, thus in Figure 5.20 we show only a comparison between the BSL-ASBM and SA-ASBM models. The main plot in Figure 5.20 shows the residuals during the final stages of convergence with the ASBM coupling turned on. In each time history, the instantaneous jump of the residual indicates the iteration at which the ASBM coupling was activated. The insert on the top right of the figure, shows the time history of the residuals for both stages of the simulations, i.e. including both the uncoupled and the coupled phases. As shown, in the uncoupled stage, the SA model achieves lower residuals than the BSL model, indicating the better convergence of the SA closure. Once the ASBM coupling is activated, we find that the amplitude of the residual's oscillations about the mean value is much smaller for SA-ASBM than for BSL-ASBM (by approximately four times). This indicates the superior robustness of the SA-ASBM coupling, a conclusion that we have reached repeatedly during the various tests that we have been carrying out over the last couple of months. Based on these results we plan to direct most of our future efforts in further developing the SA-ASBM coupling, since as it will be shown, its performance is otherwise comparable to or better than that of the κ-ω family of couplings.

In the figures that follow, all quantities are normalized using the hill height H and the reference inlet freestream velocity u_δ. Measuring streamwise distance x/h from the top of

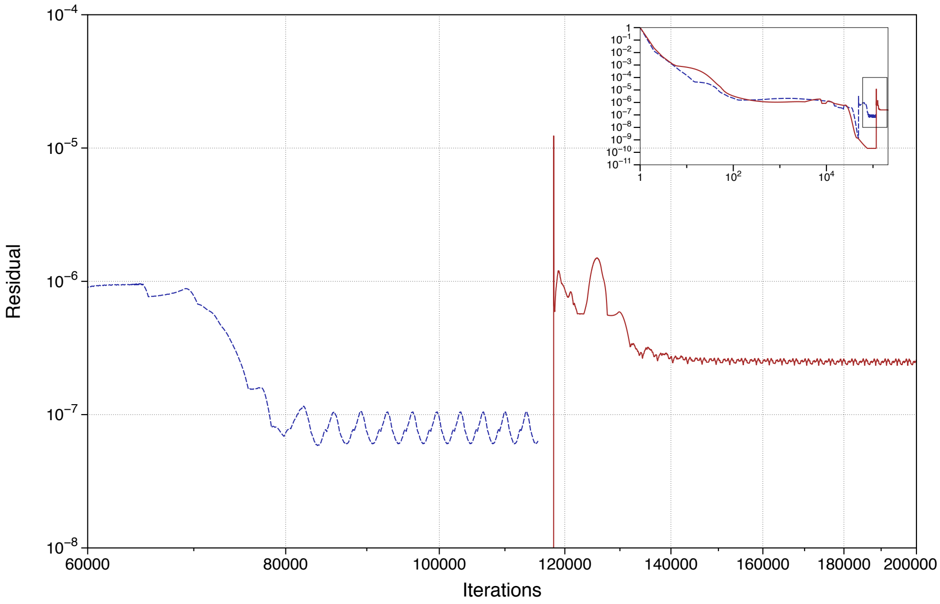

FIGURE 5.20: Time history of the mean velocity residual for the ASBM-BSL (blue dashed line) and ASBM-SA models (red solid line). The main figure shows only the final stages of convergence for the coupled models, while the insert shows the evolution of the residuals for the entire simulation range, including both the uncoupled and coupled runs. The instantaneous jumps in the residual levels, indicate the points where the ASBM coupling is turned on.

the hill, profiles are extracted at four different stations inside the recirculation region (from x/h=1.25 up to x/h=6.67), where the most notable discrepancies between the models are expected to occur. The four stations A, B, C, and D correspond to $x/h = 1.15$, 2.5, 3.75 and 6.67 respectively.

Figure 6.13 shows results for the mean streamwise velocity U_x. In all cases, comparison is made to experimental measurements and the predictions of the ASBM-BSL model. As shown, the predictions of all three closures are comparable.

Figure 5.22 shows the corresponding comparison for the case of the wall-normal mean velocity, U_y. Again, the predictions of the the three closures are comparable, but overall the ASBM-SA and ASBM-BSL closures seem to provide somewhat improved predictions in the recirculation zone relative to the SA model.

Next, we compare the predictions of the ASBM-SA model for the turbulent intensities with experimental measurements and the corresponding predictions of the ASBM-BSL model. The SA model is not included in this comparison because it cannot predict the turbulent intensities. Figures 5.23 and 5.24 show the streamwise (R_{xx}) and wall-normal (R_{yy}) Reynolds stress components respectively. In the case of R_{xx}, the ASBM-SA closure provides slightly better agreement with the experiments than the ASBM-BSL model throughout the recirculation zone. For example, at the first station A inside the recirculation region, the ASBM-SA is

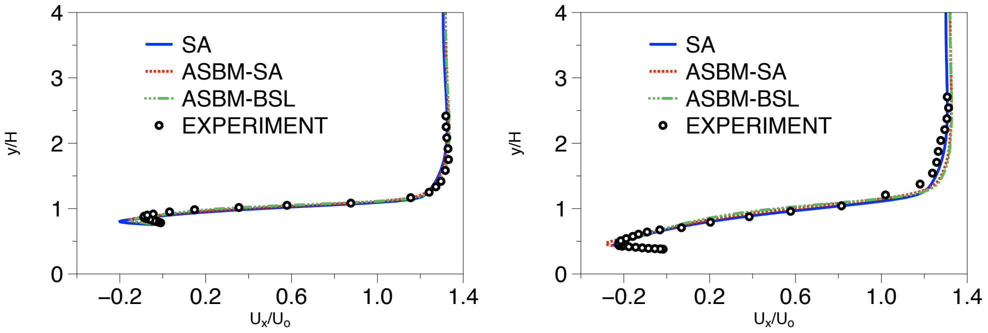

(A) station A, $x/h = 1.25$

(B) station B, $x/h = 2.5$

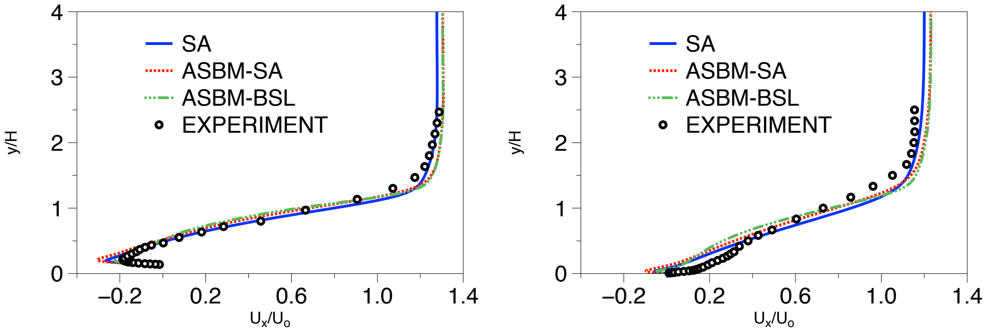

(C) station C, $x/h = 3.75$

(D) station D, $x/h = 6.67$

FIGURE 5.21: Turbulent flow over the 'witch of Agnesi' smooth hill. Model predictions for the streamwise mean velocity U_x at various x-stations for SA and ASBM-SA closures. Comparison is made to experimental values[69] and the predictions of ASBM-BSL model.

able to capture more satisfactorily the near-wall peak in R_{xx}, while at the last station D it slight improves the predicted R_{xx} profile. Overall, the ASBM-SA closure exhibits satisfactory agreement with experiments.

Figure 5.25 shows a comparison of the shear stress predictions of ASBM-SA with the corresponding experimental measurements and the predictions of the SA and ASBM-BSL closures. In the middle of the recirculation zone (stations B and C), the hybrid closures ASBM-SA and ASBM-BSL are able to capture the peak of the shear stress more accurately than SA, but they overpredict the peak at station D, which coincides with the experimental re-attachment point. Overall, the predictions of the two hybird closures are comparable and they are both able to capture the near-wall peak in the shear stress reasonably well. However, as shown in Figure 5.25e, at the top of the hill (station $x/h = 0$), we notice a problem with both model predictions, where positive magnitudes for the shear stress are predicted which might be related to the local nature of the ASBM closure and the lack of memory effects. Figure 5.26 shows the the variation of the skin-friction cofficient along the hill surface. The hybrid ASBM-SA and ASBM-BSL closures give comparable results that are in reasonable

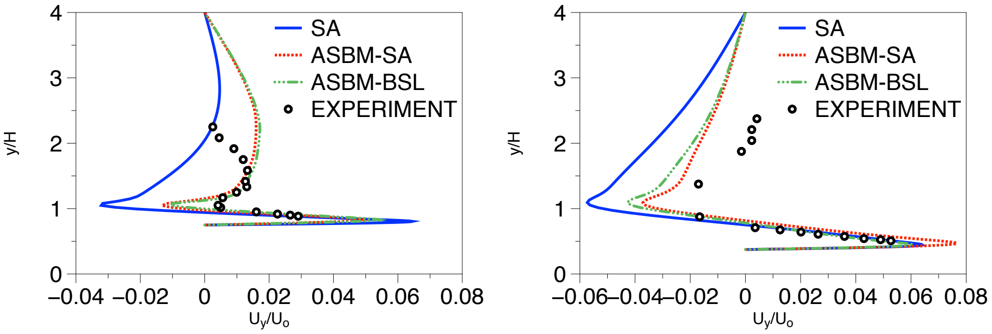

(A) station A, $x/h = 1.25$

(B) station B, $x/h = 2.5$

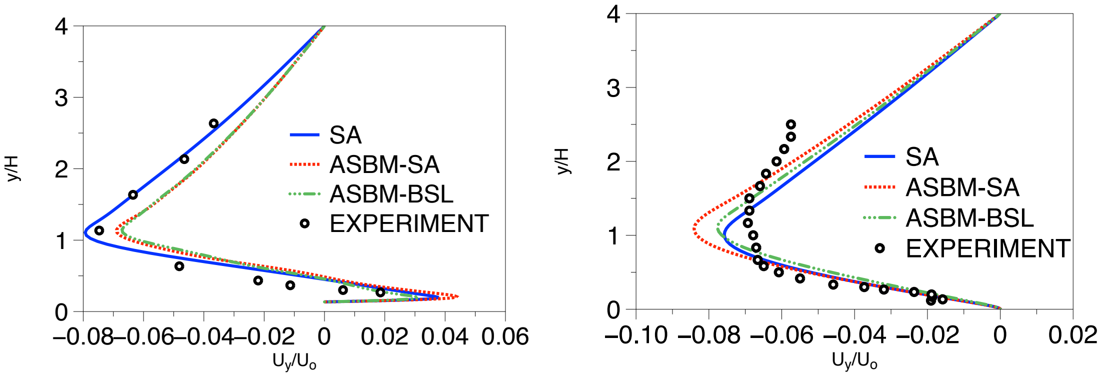

(C) station C, $x/h = 3.75$

(D) station D, $x/h = 6.67$

Figure 5.22: Model predictions for the streamwise mean velocity U_y at various x-stations for SA and ASBM-SA closure. Comparison is made to experimental values and the predictions of ASBM-BSL model.

agreement with experiments. It is worth noting that in the recirculation zone, the hybrid closures are in better agreement with experiments than the SA closure.

Overall the ASBM-SA closure provides comparable or slightly improved predictions relative to the ASBM-BSL closure. On the other hand, one has to take into account that ASBM-SA is a one-equation model and as such exhibits some computational performance advantages relative to the two-equation ASBM-BSL.

5.4 Conclusions

A new coupling between ASBM and the SA one-equation model was presented. To implement the coupling, consistent profiles for the turbulence scales were extracted from the SA predictions and fed to ASBM through a set of algebraic expressions[59], applicable for a large range of turbulent flows. The ASBM-SA closure preserves (not shown here) the full realizability enjoyed by the ASBM closure and exhibits improved numerical robustness and speed of convergence relative to other couplings such as the ASBM$-v^2$-f and even the ASBM-BSL.

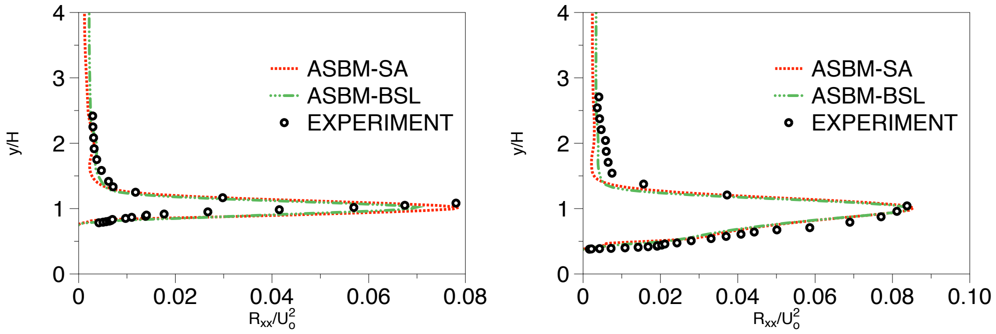

(A) station A, $x/h = 1.25$

(B) station B, $x/h = 2.5$

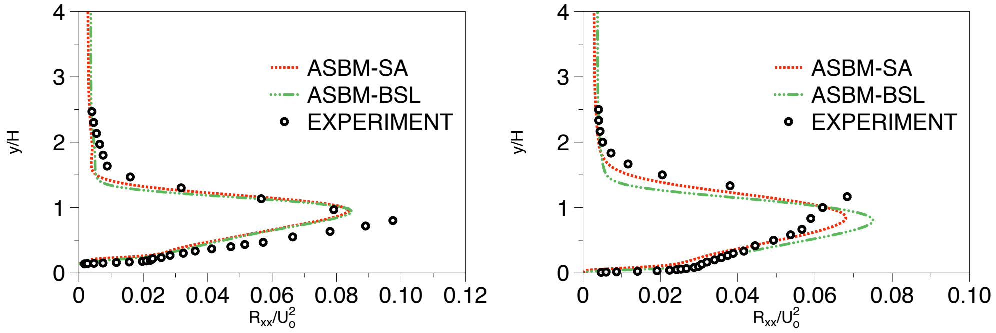

(C) station C, $x/h = 3.75$

(D) station D, $x/h = 6.67$

FIGURE 5.23: Model predictions for the streamwise Reynolds stress R_{xx} at various x-stations for SA and ASBM-SA closure. Comparison is made to experimental values and the predictions of ASBM-BSL model.

The performance of the hybrid model was evaluated in several standard benchmark cases. First, a fully-developed turbulent channel flow was considered, for which model predictions have shown satisfactory agreement with the experimental data for both mean and fluctuating quantities. Then a boundary layer simulation was performed, revealing good matching between CFD and experiment measurements for rms and shear correlations, especially for $y^+ > 10$. Then the simplest case of separated flow, that of a backward facing step, was examined. The coupled model managed to capture both peak magnitudes and freestream values of the mean and fluctuating variables, both in and out the recirculation region, exhibiting its sensitivity in anisotropic features. The ASBM-SA model was also evaluated for a case of turbulent flow in a planar asymmetric diffuser, where its predictions were found to be in fair agreement with experiments. Predictions for the static-pressure and skin-friction coefficients were within 4% of the experimental values. Finally, the model was challenged in a more difficult case involving separation, that of flow over a steep hill. Again, an overall good agreement between model and experimental predictions was achieved.

Concluding, the new coupling preserves the superior robustness of the SA closure, providing

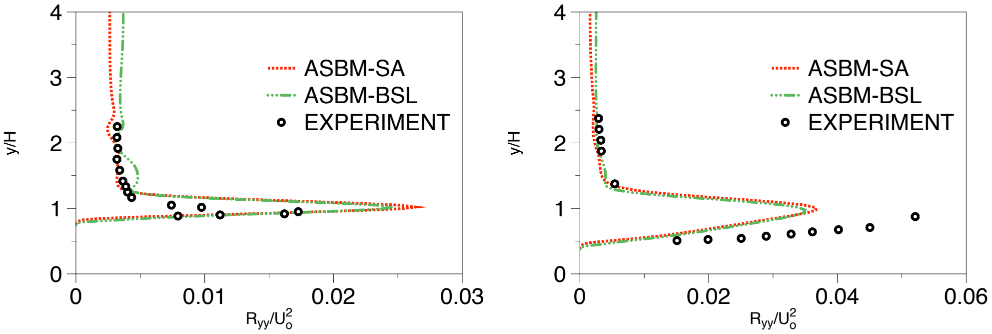

(A) station A, $x/h = 1.25$ (B) station B, $x/h = 2.5$

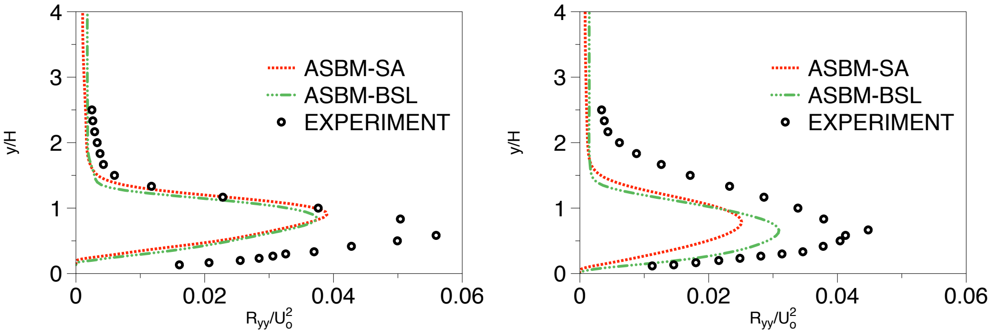

(C) station C, $x/h = 3.75$ (D) station D, $x/h = 6.67$

FIGURE 5.24: Model predictions for the transverse Reynolds stress R_{yy} at various x-stations for SA and ASBM-SA closure. Comparison is made to experimental values and the predictions of ASBM-BSL model.

smooth converged solutions with a good convergence rate. At the same time, the hybrid closure has been able to capture effectively the turbulence anisotropy in all the flows considered as a result of the ASBM contribution. Future work will focus on testing the coupling over two-dimensional airfoil surfaces and three-dimensional smooth hills.

A Fortran-90 module containing our implementation of the ASBM is being made available online[75]. Researchers interested in implementing the ASBM-SA closure in their own CFD codes can contact the authors for assistance.

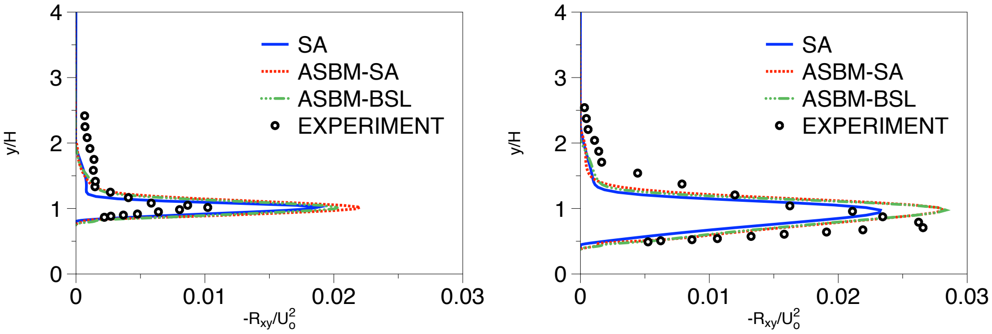

(A) station A, $x/h = 1.25$ (B) station B, $x/h = 2.5$

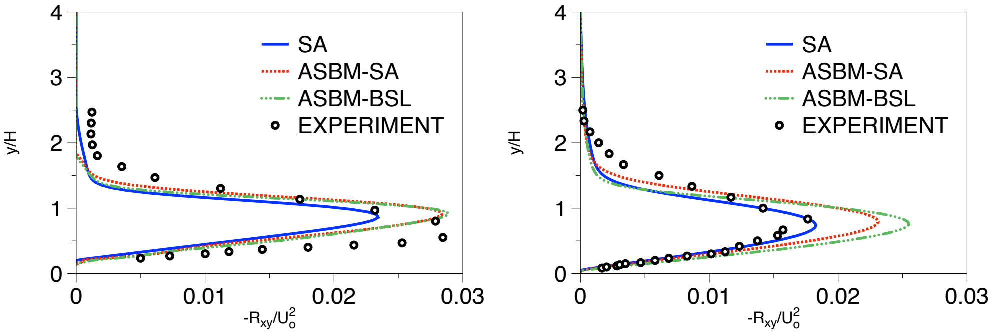

(C) station C, $x/h = 3.75$ (D) station D, $x/h = 6.67$

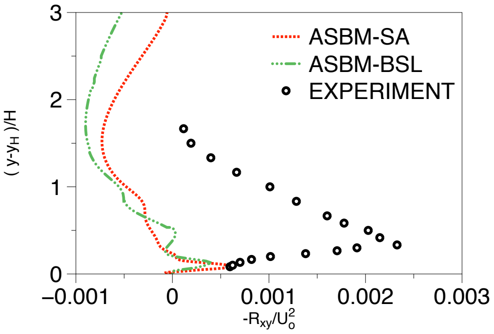

(E) station D, $x/h = 0$

FIGURE 5.25: Model predictions for the shear stress at various x-stations for SA and ASBM-SA closure. Comparison is made to experimental values and the predictions of ASBM-BSL model.

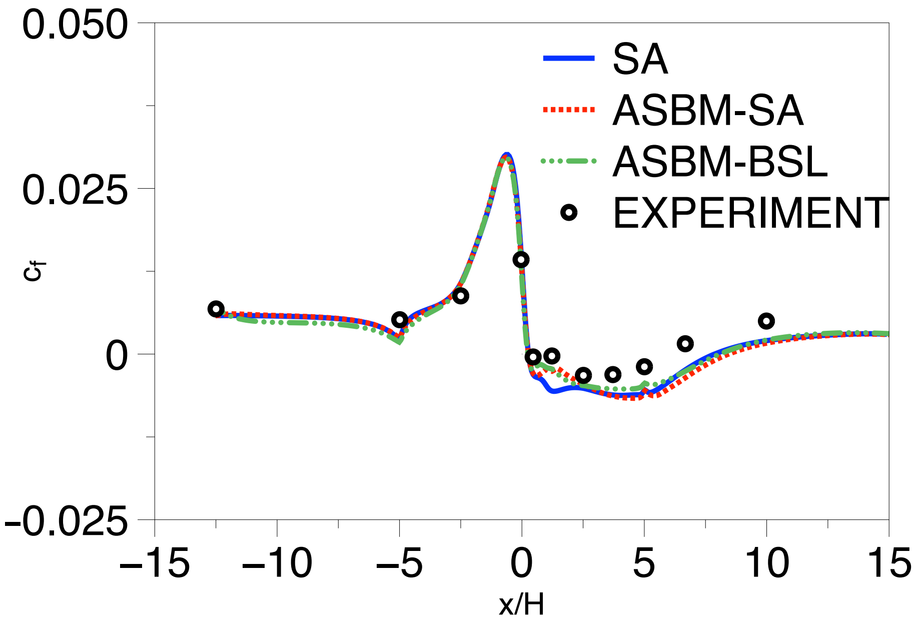

(a)

Figure 5.26: SA and ASBM-SA model predictions for the skin-friction coefficient. Comparison is made to experimental values and the predictions of ASBM-BSL model.

Chapter 6

Application of the ASBM-SA closure in a case of active-controlled flow separation

6.1 Introduction

In this chapter, we consider the application of the ASBM-SA closure to the case of turbulent flow over a 2D hill with and without separation control. In particular, we have considered the case of no-flow control, as well as the case where active-control is applied via steady-suction. During the CFDVAL2004 Workshop[76], these two cases were considered extensively in an effort to assess the performance of the current engineering turbulence models in strongly separated flows subjected to favorable/adverse pressure gradients.

Experiments have been conducted in the NASA Langley Transonic Cryogenic Tunnel by Greenblatt et al. [77]. The shape of the hump is that of a “Modified Glauert-Goldschmied” hill, similar to the one used by Seifert and Pack [78]. The experiments are nominally two-dimensional (2D), despite the presence of three dimensional (3D) effects near the side end-plates. The scenarios involved both uncontrolled and controlled flow (steady suction) for Reynolds numbers (Re) ranging from 0.37 up to 1.1 million, corresponding to Mach numbers (M) ranging from 0.04 up to 0.12. One no-flow control case and one active-control case were selected for the extraction of detailed experimental measurements.

Figure 6.1 shows the geometry of the whole domain, including a detailed view of the flow control lot. The chord length of the hump is denoted as c, the height of the domain H is 90% the chord length, while the maximum height of the hump is approximately 0.13 c. The slot is located near $x/c \approx 0.65$, where the slot width h is 0.00187 c. Detailed information regarding the geometry, computational grids and the relevant experiments can be found in [79].

One of the conclusions reached during the CFDVAL2004 Workshop is that blockage effects stemming from the presence of side plates need to be accounted for in simulations, otherwise the computed pressure coefficients levels exhibit significant discrepancy relative to the experiments, especially over the hump. Thus, the top tunnel surface around hump location is modified so as to reflect the change in the tunnel cross-sectional area due to the presence of the side-plates, as described in [79].

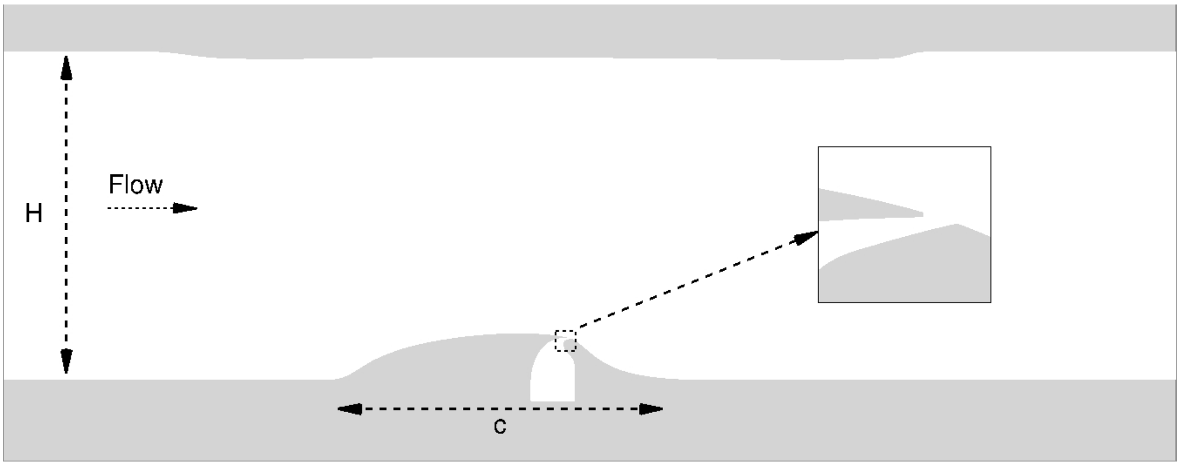

Figure 6.1: Sketch of the geometry, with a modification along the top-surface such as to account for the side-plate effects, as described in [79].

6.2 Validation results

Initially, we considered the case of a turbulent boundary layer over a flat plate, which is needed to provide the inlet profile for the two cases of the wall-mounted “Modified Glauert-Goldschmied” hill. Subsequently, we performed a series of computations regarding the no-flow control and steady-suction cases respectively. In all cases conisdered, we first run simulations using the SA closure until a time-converged solution was reached. Then, we performed additional runs starting from the SA converged solutions as an initial map in order to obtain the predictions of the ASBM-SA closure. The predictions of the ASBM-SA hybrid model and the standard SA model were then compared to the available experimental data. For each case, we have conducted grid-convergence analysis, starting from coarser and moving towards finer grids, in order to provide grid-independent solutions. In order to ensure that the grids were sufficiently resolved, the cells adjacent to the wall were placed within $y^+ < 1$, except inside the recirculation region where y^+ becomes slightly bigger, reaching values up to 1.4 for the SA closure and up to 1.2 for the ASBM-SA closure. Here, y^+ represents wall-normal spacing in wall units yu_τ/ν. Also, all solutions are assumed to become time-converged after achieving sufficiently small residuals, as discussed later.

Unstructured computational grids were generated using the ICEM-CFD mesh generator for all cases considered. Using these meshes the numerical solution was advanced using an unstructured, nodal-based finite-volume code called CDP, developed at the Center of Turbulence Research (Stanford/NASA), and which is used in our group as a general platform for the study of the incompressible flows. The diffusive and advection terms in both the mean and turbulent transport equations are discretized through a second-order accurate centered-difference scheme, while skewness corrections has been employed. The coupling of the transport equations is done through a time-splitting method, while for the time-advancement a Crank-Nicholson scheme is used. More details regarding the solver and its various options are given in [80].

6.2.1 Turbulent boundary-layer.

Initially, we simulated a spatially developing boundary layer flow over a flat plate, so as to match the experimental data of Greenblatt et al.[77]. These results were then used as the inlet boundary conditions for the cases involving the 2D hump. The desired Reynolds number is $Re_\delta \approx 68,200$, based on the freestream velocity U_o and the boundary layer thickness $\delta \approx 0.074\ c$. At the inlet, Dirichlet boundary conditions are imposed for the mean and turbulent variables, such as $\tilde{\nu}_\infty/\nu \approx 3$ and $U_o = 0.1\ M$, yielding a freestream Reynolds number $Re_\infty = 929,000$, based on the chord length c of the hump, and the freestream velocity U_o. At the outlet, a penalty condition is imposed to prevent the occurrence of reflectional effects while ensuring mass conservation. A slip condition was imposed at the top surface, a no-slip condition at the bottom wall surface and periodic conditions along the spanwise direction. In order to obtain grid-independent solutions, three different meshes of increasing resolution were considered. For each mesh, geometric functions were used to define the normal distribution of the nodes, while uniform spacing has been adopted along the streamwise direction. Grid 1 contains a non-uniform mesh of size 120 x 90 x 1 along the streamwise, wall-normal and spanwise directions respectively. The corresponding size for Grid 2 is 130 x 120 x 1 and for Grid 3 is 140 x 150 x 1. The finest grid yields a value of y^+ around 0.5 for the wall-adjacent cell at the location of the extracted data. Figures 6.2a-b show predictions using the SA closure for the streamwise mean velocity and pseudo-viscosity respectively. In Figure 6.3 we show a comparison between the predictions of the SA model using Grid 3 as the baseline grid, and the experimental data for the streamwise mean velocity U_x, yielding a good agreement.

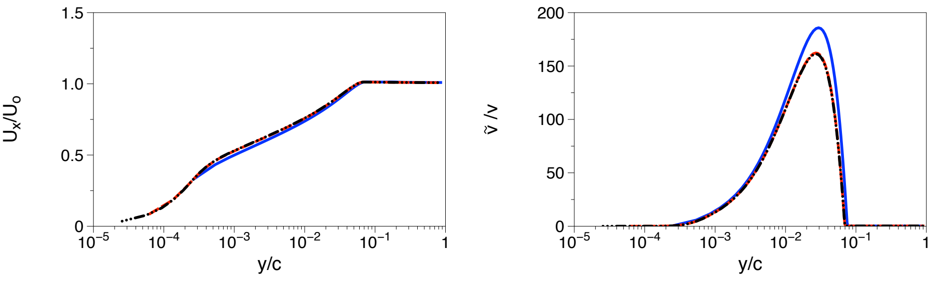

(A) (B)

FIGURE 6.2: Grid-convergence analysis for a spatially developing turbulent boundary layer at $Re_\delta \approx 68,200$. SA model predictions for (a) the streamwise mean velocity and (b) the pseudo-viscosity. Comparison is made among three different grids: Grid 1 (———) ; Grid 2 (- - - -) ; Grid 3 (—···—).

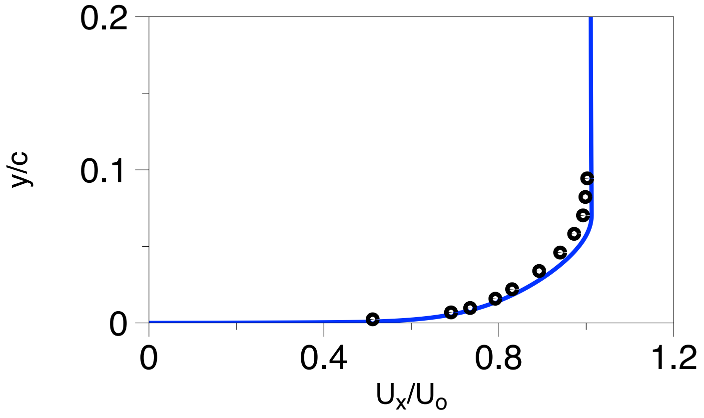

FIGURE 6.3: SA model predictions (lines) for the streamwise mean velocity. Comparison is made to the experiments (symbols) of Greenblatt et al. [77].

6.2.2 No-flow control

The case of flow over a hump having the shape of "Modified Glauert" hill is considered next. This case was originally conceived for testing the ability of active control to reduce the size of the existing recirculation bubble. However, from a turbulence modeling perspective, even the uncontrolled case is interesting due to the presence of strong separation, which proves to be challenging to turbulence engineering models. Thus, in our numerical experiments, we considered first the uncontrolled case of flow.

Simulations have been performed using SA and ASBM-SA models, which are compared to the experimental work of Greenblatt et al. [77] At the inlet surface, profiles for the variables are obtained from the SA solution for the turbulent boundary layer corresponding to $Re_\delta \approx 68200$ as described in the previous subsection. At the floor surface, as well as at the wall surfaces inside the cavity, solid wall (no-slip) boundary conditions were applied. A penalty condition is imposed at the outlet surface to ensure that mass flow exit the domain properly, while slip conditions are used at the top surface and periodic conditions for the spanwise direction. A grid-sensitivity analysis was conducted where two grid were considered. The coarser grid contains approximately 103,000 grid points, whereas the finer grid posses approximately 160,000 grid points. Mesh details are shown in Figure 6.4, with a zoomed view of the cavity region.

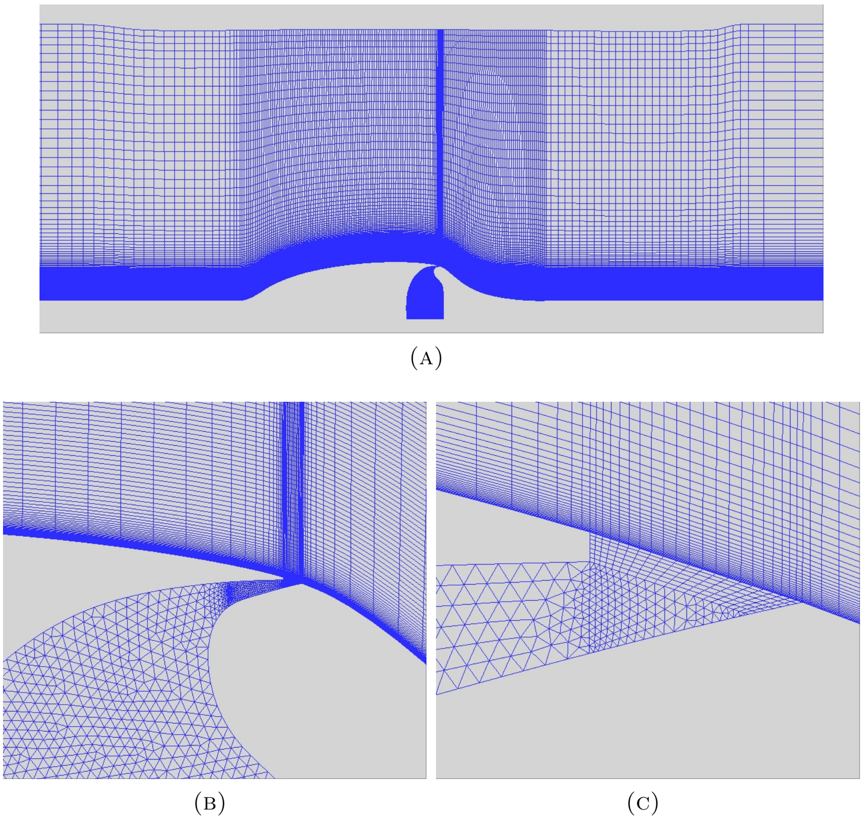
(A)

(B) (C)

FIGURE 6.4: Unstructured computational grid with details of the slot region.

Figures 6.5a-b show SA model predictions for the wall-static pressure coefficient $c_p = (p - p_0)/\frac{1}{2}\rho U_o^2$ and skin-friction coefficient $c_f = \tau_w/\frac{1}{2}\rho U_o^2$ respectively. Based on these results, the coarser grid is shown to be fine enough for the current case.

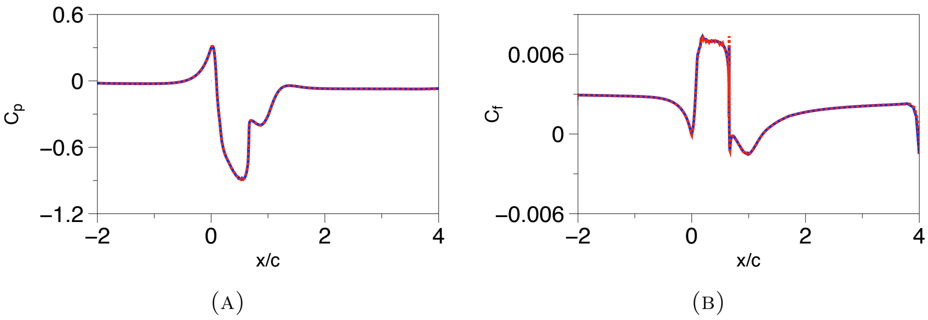

(A)

(B)

Figure 6.5: Effect of grid on SA model predictions for the uncontrolled case, for (a) the wall-static pressure coefficient and (b) the skin-friction coefficient. Two grids are shown: coarse grid (———) ; fine grid (- - - -).

Due to the algebraic nature of the ASBM closure, numerical difficulties are encountered for the cases where strongly separated flows are considered, as the present ones. During previous works, a filtering scheme was applied in order to obtain smooth solution, improving that way the numerical stability of the solution. However, use of the scheme in the current case yielded a mismatch between SA and ASBM-SA predictions for the skin-friction coefficients in regions where a good agreement was expected, such as upstream of the leading edge of the hill and downstream the recirculation region. This problem was resolved by separating the domain into two zones, one prior the leading edge where the filtering scheme is not active, and the region downstream the leading edge where the scheme is switched on (Fig. 6.6). Fig. 6.7 shows a comparison between SA and ASBM-SA predictions using both approaches for the filtering scheme, revealing the significant role the filtering details play on the skin-friction distribution all along the bottom surface. In contrast, the pressure coefficient remains unaffected by the choice of filtering scheme.

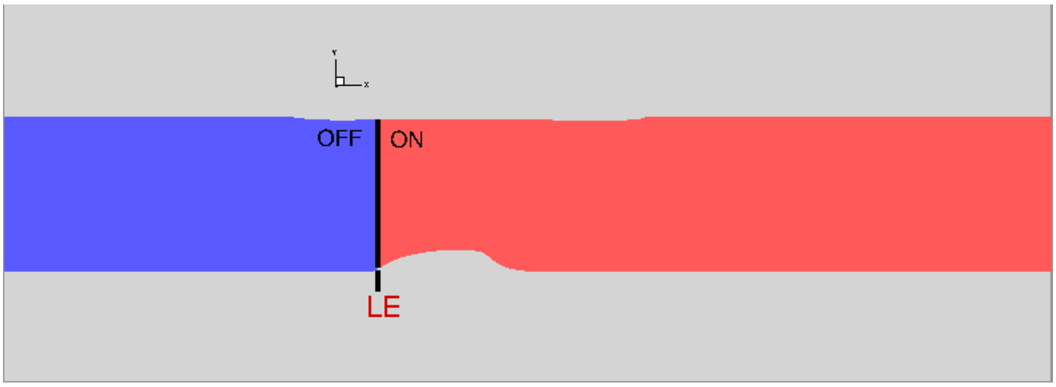

Figure 6.6: Separation zones showing where the filtering scheme is active (on) or not (off).

Figure 6.8 displays the evolution of the maximum mean streamwise velocity residual. The residual is divided by its initial value and is defined by

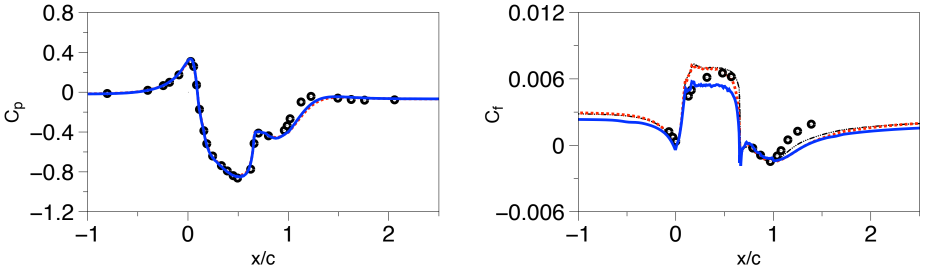

(A)

(B)

Figure 6.7: Effect of zonal filtering on (a) the wall static-pressure coefficient and (b) the wall skin-friction coefficient for the no-flow control case. SA (----) and ASBM-SA (—···—) are compared to the ASBM-SA predictions when filtering is active in the entire domain (———) and the experimenal values (symbols) of [77].

$$\text{Residual} \; = \max\left[\frac{V\times\Delta U_x/\Delta t}{(V\times\Delta U_x\Delta t)_0}\right], \quad \Delta U_x = U_x^{n+1} - U_x^{n}\,, \tag{6.1}$$

where n refers to the n-th iteration, Δt to the current time step and V is the volume of the corresponding cell. For both SA and ASBM-SA models, a drop of at least 5 orders of magnitude for the residuals compared to the initial field is achieved, which is believed to be sufficient to provide time-converged solutions.

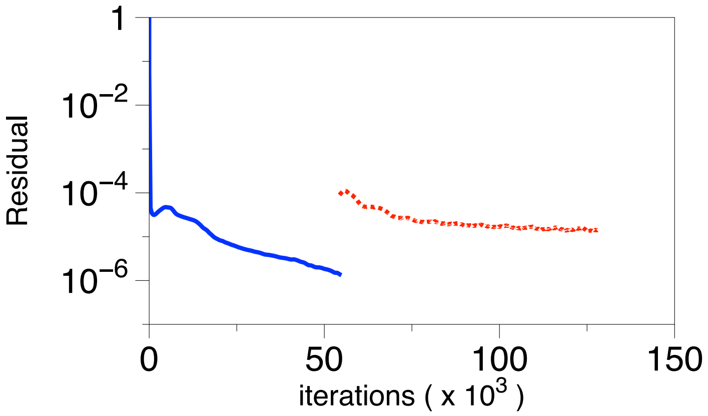

Figure 6.8: Time history of the streamwise mean velocity residual for the uncontrolled case. The sudden jump in the residual levels indicates the point where the ASBM coupling is switched on.

In order to both accelerate our simulations and overcome some stability issues related to the ASBM-SA computations inside the cavity in the case of no-suction, additional computations using similar meshes but without the presence of the cavity were conducted. Instead, we impose a solid-wall condition along the slot exit. Figures 6.9a-b show SA predictions for the mean velocity streamlines at the vicinity of the hump in the presence and absence of the cavity respectively, demonstrating the trivial discrepancies between the two approaches.

Figure 6.10 shows the corresponding comparison for the wall-static pressure coefficient, which again reveals the negligible effect on the results of the cavity absence when the flow control is inactive (no suction).

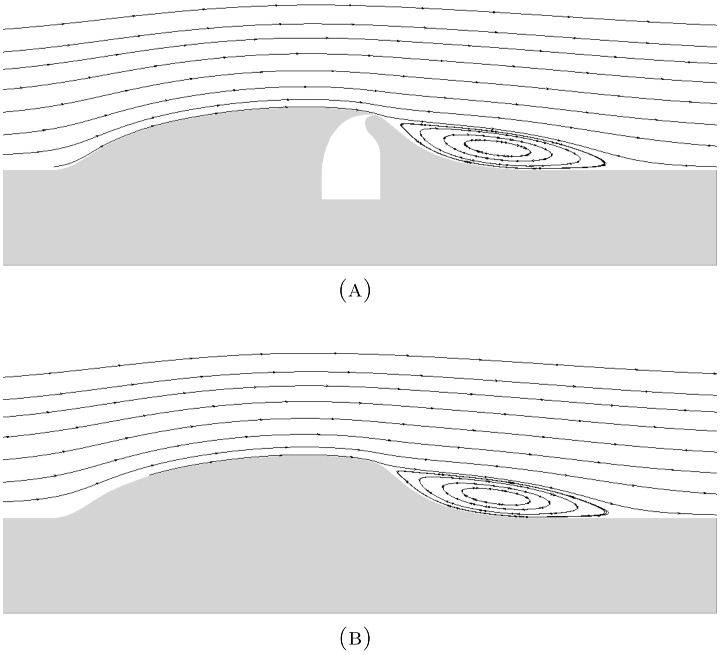

FIGURE 6.9: SA model predictions for the streamlines of the mean flow approaching the hump (a) in the presence of the cavity and (b) in the absence of the cavity.

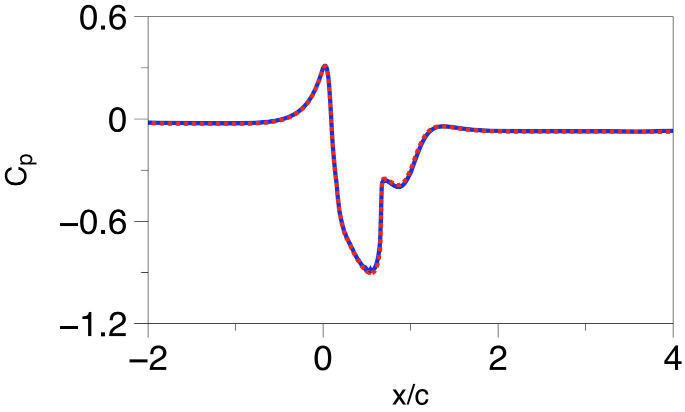

FIGURE 6.10: SA model predictions in the presence (———) or absence (- - - -) of the cavity for the wall-static pressure coefficient .

In the following figures, all turbulent and mean quantities (except c_f, c_p) are normalized based on the chord length c and the reference inlet freestream velocity U_o. Setting the leading edge of the hump as the origin of the streamwise distance ($x/c = 0$), profiles are extracted at three different stations inside the recirculation bubble as measured by the experiments ($x/c = 0.66,\ 0.8,\ 1.0$) and one station at the recovery region ($x/c = 1.2$), denoted as stations $A,\ B,\ C,\ D$ respectively (Figure 6.11).

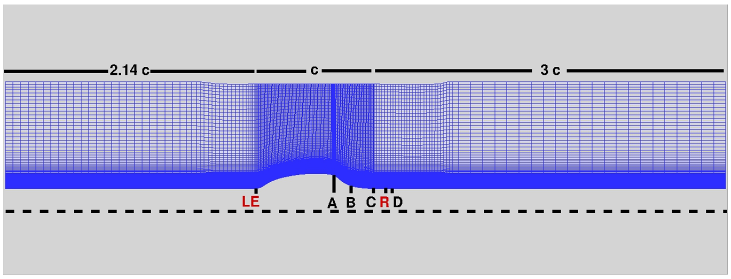

FIGURE 6.11: Geometrical and mesh details in the absence of cavity. Data is extracted in four stations, denoted as A, B, C and D. The leading-edge point (LE) and the re-attachment point (R) are also shown.

Figure 6.12 shows the predictions of the ASBM-SA and SA closures for the variation of the pressure (C_p) and skin friction (C_f) coefficients along the wall surface. Comparison is made to experimental measurements. The ASBM-SA model captures accurately the peak magnitude of the pressure coefficient around $x/c \approx 0.57$. In the range $-1 \leq x/c \leq 1.1$, that is from the inlet up to about the re-attachment point, the ASBM-SA provides slightly improved C_p predictions when compared to SA. Right after re-attachment, the ASBM-SA predicts a slightly delayed recovery of C_p as compared to the experiments (and the SA closure). The two models produce comparable agreement with the experiments for the skin-friction coefficient. ASBM-SA provides an improvement right after the upstream edge of the hill ($x/c \approx 0.2$), while SA predicts correctly the magnitude near the sharp geometry change that occurs around $x/c \approx 0.65$. Based on Table 6.1, both models overpredict the recirculation bubble, with ASBM having the tendency to delay the re-attachment of the flow further downstream, an observation which is in agreement with previous cases in which separated flows over 2D hills were considered, such as the “Witch of Agnesi” hump, as described in detail in [49].

Figure 6.13 shows results for the streamwise mean velocity U_x at the four stations. As shown in Figures 6.13a-b, at the first two stations ASBM-SA provides slightly improved predictions relative to the SA model, while SA is in better agreement with the experimental data at the next two stations, mostly due to the greater delay of re-attachment in the ASBM-SA predictions.

Next, we consider the performance of the ASBM-SA closure for the turbulent intensities and the fluctuating shear stress with respect to experimental results. The SA model is included only in the comparison for the fluctuating shear stress component, since it cannot provide predictions for the turbulent intensities. Figure 6.14 displays the streamwise Reynolds stress components R_{xx}. At station A, ASBM-SA captures the near-wall peak magnitude, yielding a reasonable predictions for R_{xx}. At the remaining three stations ($x/c = 0.8, 1.0, 1.2$), ASBM-SA is able to capture satisfactorily the peak magnitude. We note that the wiggles near $y/c = 0.2$ at station A (Fig. 6.14a) originate from the algebraic expressions for the estimation

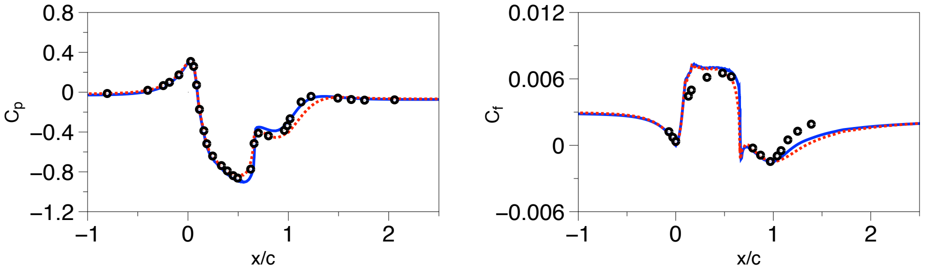

(A)
(B)

Figure 6.12: SA (———) and ASBM-SA (- - - -) model predictions for the no-flow control case for (a) the wall static-pressure coefficient and (b) the wall skin-friction coefficient. Comparison is made to experimental values (symbols) of[77].

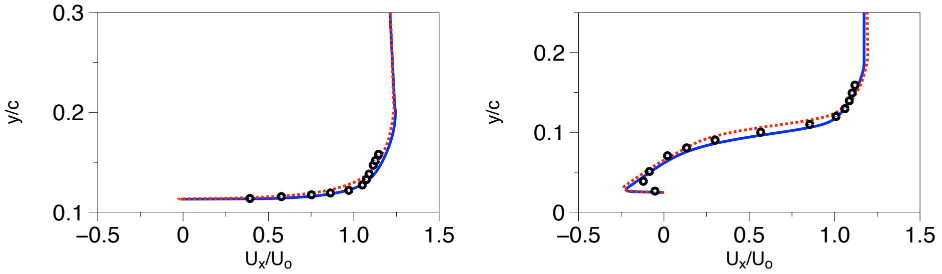

(A) station A, $x/c = 0.66$
(B) station B, $x/c = 0.8$

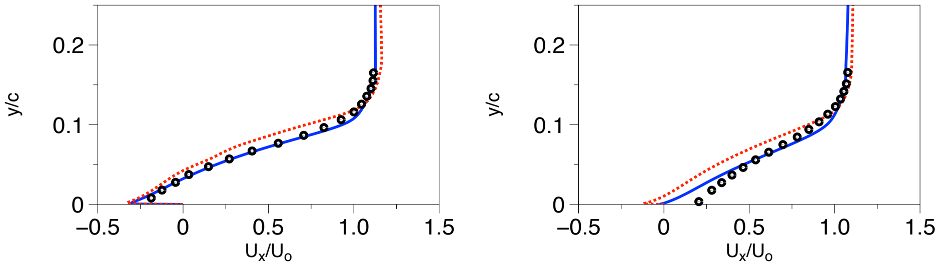

(C) station C, $x/c = 1.0$
(D) station D, $x/c = 1.2$

Figure 6.13: Turbulent flow over the “Glauert-Goldschmied” 2D hill for the no-flow control case. Model predictions for the streamwise mean velocity U_x at various x-stations for SA (———) and ASBM-SA (- - - -) closures. Comparison is made to experimental values of Greenblatt et al.[77].

of the turbulent kinetic energy (not shown here). Following term by term the algebraic procedure for the calculation of kinetic energy, we found that this issue is mostly likely related to the local mean velocity gradients. These wiggles are also present in previous works [49], for which similar findings were deduced. Also, the location $y/c = 0.2$ where the wiggles appear is close to the interface between two grid blocks. Overall, we believe that this is a localized effect which does not affect the quality of the solution.

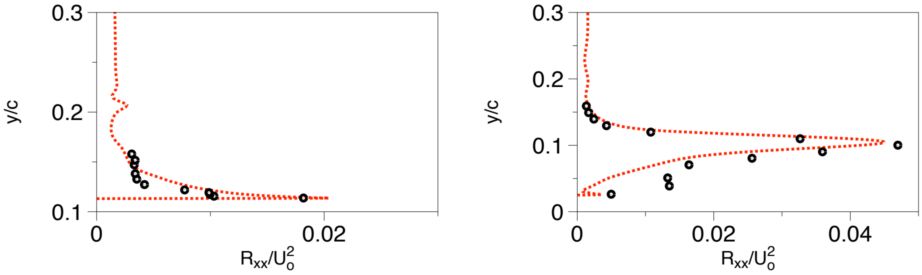

(A) station A, $x/c = 0.66$

(B) station B, $x/c = 0.8$

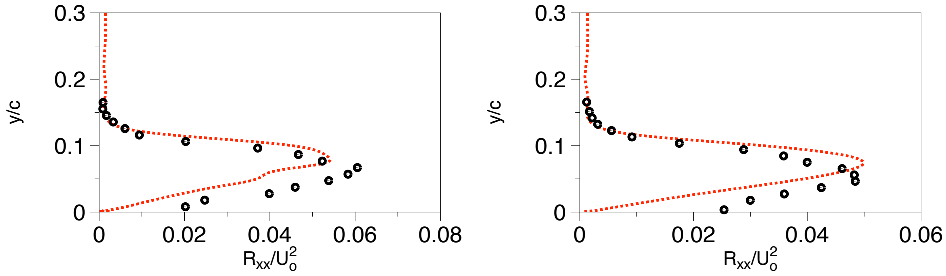

,

(C) station C, $x/c = 1.0$

(D) station D, $x/c = 1.2$

FIGURE 6.14: Turbulent flow over the ”Glauert-Goldschmied” 2D hill for the no-flow control case. ASBM-SA model predictions (lines) for the streamwise Reynolds stress component R_{xx} at various x-stations are shown. Comparison is made to experimental values (symbols) [77].

Figure 6.15 depicts the corresponding predictions for the transverse Reynolds stress component R_{yy}. ASBM-SA closure strongly overpredicts the near-wall magnitude at station A, while a fair agreement with the experiments is achieved at the remaining stations.

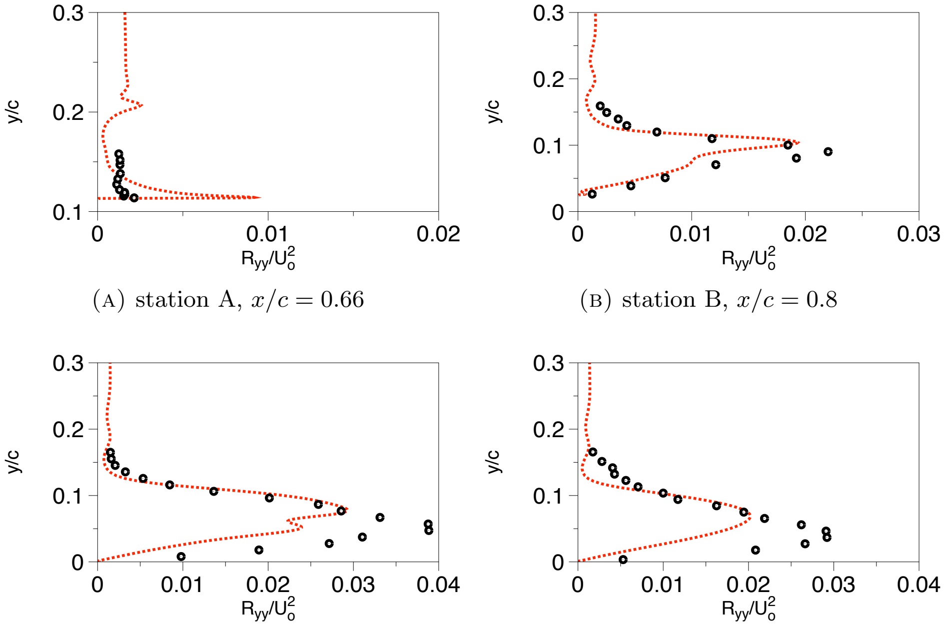

(A) station A, $x/c = 0.66$

(B) station B, $x/c = 0.8$

(C) station C, $x/c = 1.0$

(D) station D, $x/c = 1.2$

Figure 6.15: Turbulent flow over the "Glauert-Goldschmied" 2D hill for the no-flow control case. ASBM-SA model predictions (lines) for the transverse Reynolds stress component R_{yy} at various x-stations are shown. Comparison is made to experimental values (symbols) [77].

Figure 6.16 shows SA and ASBM-SA predictions for the fluctuating shear stress component. At the first station, ASBM-SA exhibits a similar behavior as for the transverse Reynolds stress component. At the remaining three stations, ASBM-SA provides noticable improvement relative to the SA model, in both the near-wall and freestream regions. This improvement is evident in the whole range of the recirculation bubble, suggesting a satisfactory response of the hybrid model to the strong anisotropic effects that characterize this region.

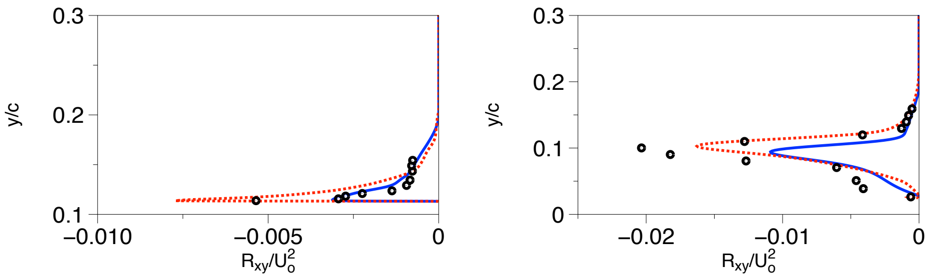

(A) station A, $x/c = 0.66$

(B) station B, $x/c = 0.8$

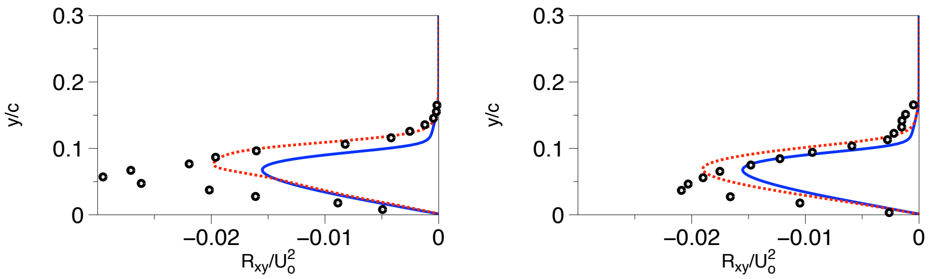

(C) station C, $x/c = 1.0$

(D) station D, $x/c = 1.2$

FIGURE 6.16: Turbulent flow over the "Glauert-Goldschmied" hill for the no-flow control case. Model predictions for the shear stress component R_{xy} at various x-stations for SA and ASBM-SA closures. Comparison is made to experimental values [77].

6.2.3 Steady suction

Even though we perform URANS computations, we consider essentially steady cases, thus we define the steady mass transfer momentum coefficient

$$c_\mu = \frac{\rho h U_{jet}^2}{1/2 c \rho U_o^2}\,, \tag{6.2}$$

where U_{jet} is the total jet velocity. For the current case, c_μ is set equal to 0.241%, corresponding to a constant mass flow rate of $\dot{m} = 0.01518\ kg/s$ being sucked through the slot, in order to match the experimental conditions of Greenblatt et al. [77]. Figure 6.17 shows ASBM-SA model predictions for the wall-normal spacing along the floor surface for the uncontrolled and controlled cases, needed to ensure that our solutions are obtained in sufficiently resolved grids. As expected, a sharp increase in y^+ levels occurs at the location of the slot exit where no-wall is present.

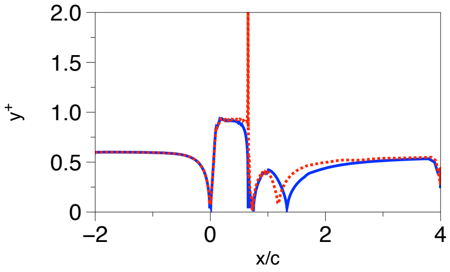

FIGURE 6.17: ASBM-SA model predictions for the streamwise variation at the bottom surface for the normal spacing at the wall normalized in wall-units. Results are shown for both the no-flow control (———) and the steady-suction (- - - -) cases.

Results for the wall-static pressure coefficient are shown in Figure 6.18, where she the predictions of the SA and ASBM-SA models are compared to the experimental data of Greenblatt et al.[77]. The ASBM-SA closure manages to capture accurately the magnitude and the location of the first sharp change right after the slot, located around $x/c \approx 0.67$, followed by a small recovery delay, as compared to the SA model, till the trailing edge of the hill ($x/c = 1$) where the two models coincide again.

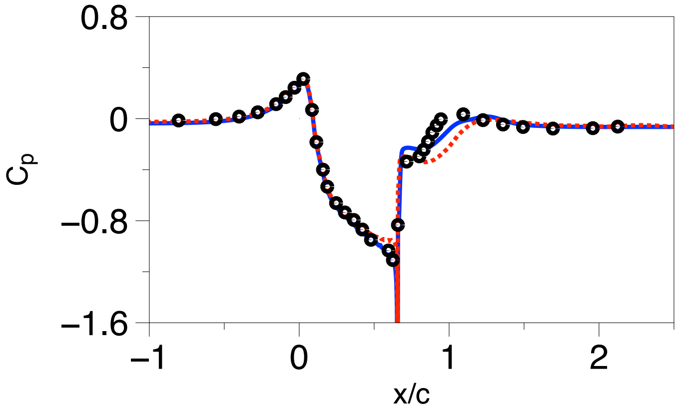

(A)

FIGURE 6.18: SA (———) and ASBM-SA (- - - -) model predictions for the steady-suction case for the wall static-pressure coefficient. Comparison is made to experimental values [77].

Figure 6.19 displays results for the streamwise mean velocity U_x at the four stations. As shown, SA provides slightly better agreement with the experiments than the ASBM-SA model. In figure 6.20 we see the corresponding comparison for the transverse mean velocity U_y. In general, SA predictions are in better agreement with the experimental data compared to ASBM-SA model.

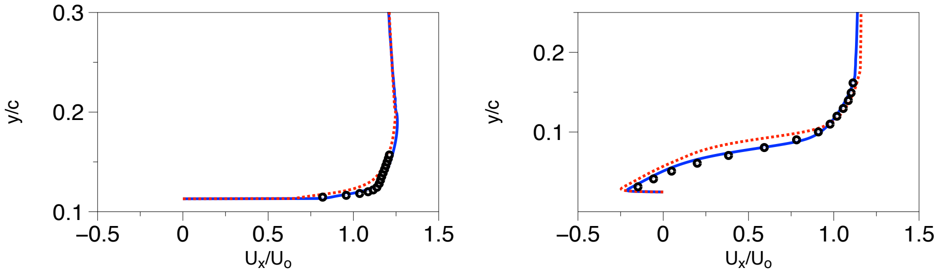

(A) station A, $x/c = 0.66$ (B) station B, $x/c = 0.8$

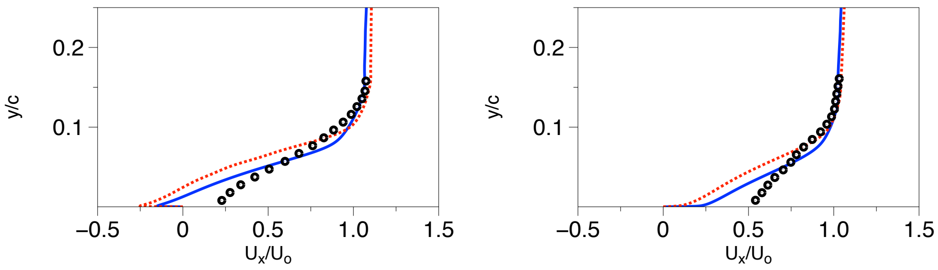

(C) station C, $x/c = 1.0$ (D) station D, $x/c = 1.2$

FIGURE 6.19: Turbulent flow over the "Glauert-Goldschmied" hill for the steady-suction case. Model predictions for the streamwise mean velocity U_x at various x-stations for SA and ASBM-SA closures. Comparison is made to experimental values [77].

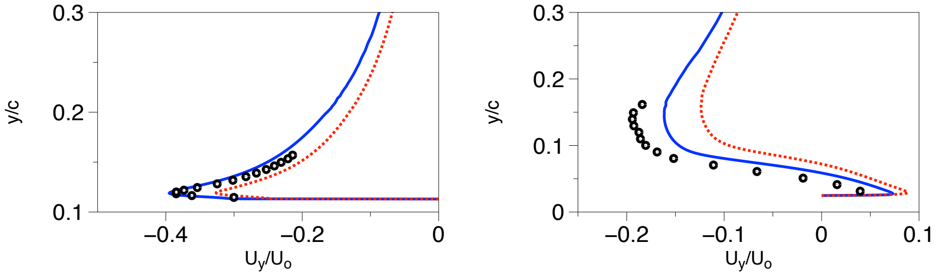

(A) station A, $x/c = 0.66$ (B) station B, $x/c = 0.8$

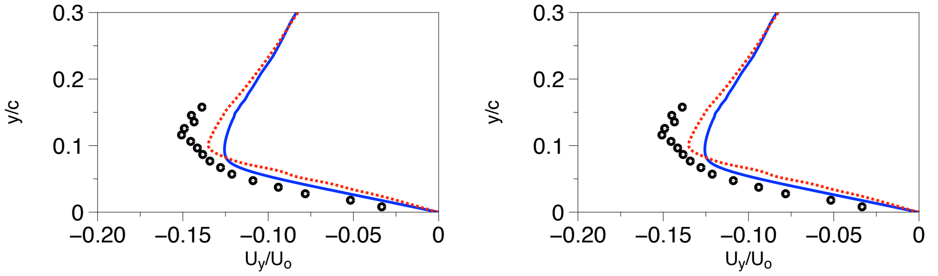

(C) station C, $x/c = 1.0$ (D) station D, $x/c = 1.2$

FIGURE 6.20: Turbulent flow over the "Glauert-Goldschmied" hill for the steady-suction case. Model predictions for the transverse mean velocity U_y at various x-stations for SA and ASBM-SA closures. Comparison is made to experimental values [77].

Table 6.1 shows details regarding the recirculation region. SA predicts more accurately the re-attachment point for both cases, providing an indication why SA closure obtains better results than the hybrid model for the mean statistics.

Table 6.1: Details of SA and ASBM-SA model predictions regarding the recirculation bubble for each case. Comparison is made to the experimental work of Greenblatt et al.[77].

Case	Model	sep.loc. experiment	sep.loc. CFD	Error (%)	reatt.loc. experiment	reatt.loc. CFD	Error (%)
no-flow control	SA	≈ 0.67	0.663	1.0	1.11 ± 0.003	1.235	11.3
no-flow control	ASBM-SA	≈ 0.67	0.656	2.1	1.11 ± 0.003	1.330	19.8
steady suction	SA	≈ 0.68	0.676	0.6	0.94 ± 0.005	1.113	18.4
steady suction	ASBM-SA	≈ 0.68	0.665	2.2	0.94 ± 0.005	1.180	25.5

Figure 6.21 shows the corresponding comparison for the streamwise Reynolds stress component R_{xx}. At three of the four stations, ASBM-SA correctly predicts the near-wall peak magnitude and the freestream values, yielding a fair agreement with the experiments.

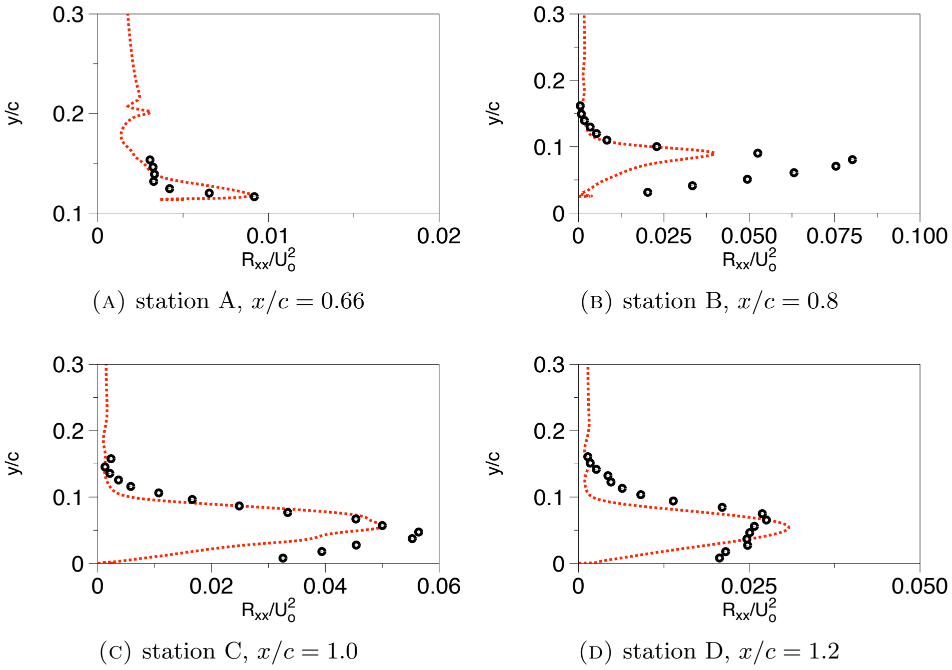

(a) station A, $x/c = 0.66$ (b) station B, $x/c = 0.8$

(c) station C, $x/c = 1.0$ (d) station D, $x/c = 1.2$

Figure 6.21: Turbulent flow over the "Glauert-Goldschmied" hill for the steady-suction case. Model predictions for the streamwise Reynolds stress component R_{xx} at various x-stations for SA and ASBM-SA closures. Comparison is made to experimental values [77].

In Figure 6.22, the agreement is qualitative between the ASBM-SA predictions and the experimental measurements for the transverse Reynolds stress component R_{yy}. Combining these results with the analogous ones for R_{xx} reveals the sensitivity of the algebraic model to the anisotropic nature of the flow.

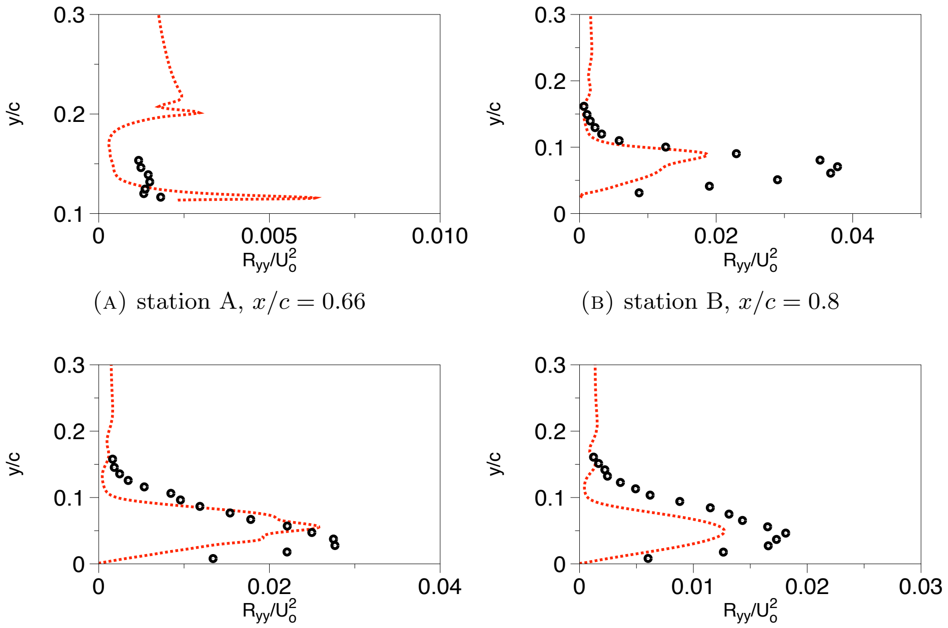

(a) station A, $x/c = 0.66$ (b) station B, $x/c = 0.8$

(c) station C, $x/c = 1.0$ (d) station D, $x/c = 1.2$

Figure 6.22: Turbulent flow over the "Glauert-Goldschmied" hill for the steady-suction case. Model predictions for the transverse Reynolds stress component R_{yy} at various x-stations for SA and ASBM-SA closures. Comparison is made to experimental values [77].

Results for the for the fluctuating shear stress component R_{xy} are shown in Figure 6.23. As shown, the hybrid ASBM-SA model is able to provide significantly improved predictions compared to the SA closure in the whole range of the recirculation region. Overall, ASBM-SA provides a satisfactory agreement with experiments.

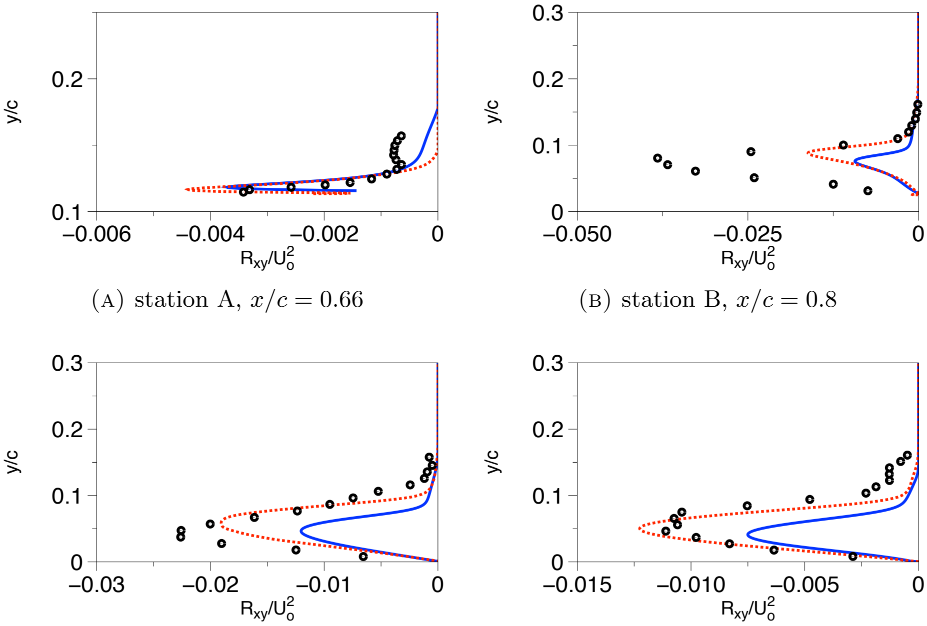

(A) station A, $x/c = 0.66$ (B) station B, $x/c = 0.8$

(C) station C, $x/c = 1.0$ (D) station D, $x/c = 1.2$

FIGURE 6.23: Turbulent flow over the “Glauert-Goldschmied” hill for the steady-suction case. Model predictions for the fluctuating shear stress component R_{xy} at various x-stations for SA and ASBM-SA closures. Comparison is made to experimental values [77].

The active control effect on the recirculation bubble is visualized in Figure 6.24. ASBM-SA model predictions for the streamlines of the mean velocity for both cases are shown, revealing a noticeable reduction of the bubble size.

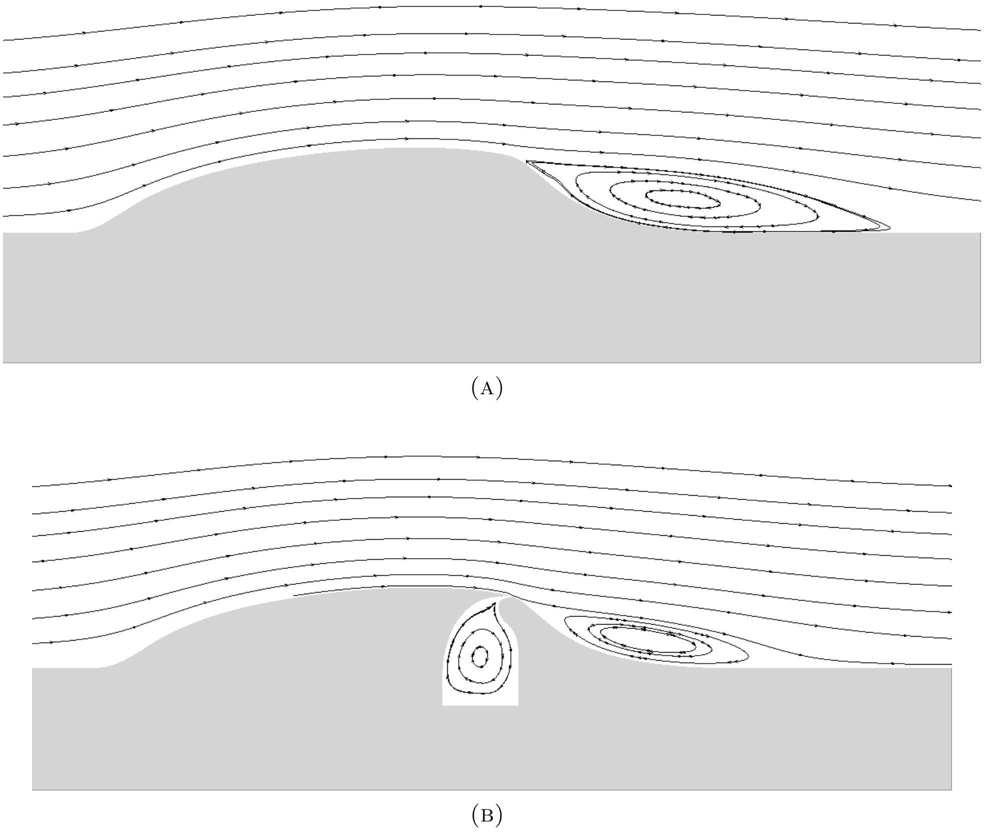
(A)

(B)

FIGURE 6.24: ASBM-SA model predictions for the streamlines of the mean velocity for (a) the uncontrolled case and (b) the controlled case .

6.2.4 An alternative expression for the turbulence lengthscale.

Until now, a standard expression is adopted in the current version of the ASBM-SA model in order to obtain the turbulence lengthscale L, as given by

$$L = C_L \max\left(\frac{\kappa^{3/2}}{\epsilon}, C_n(\frac{\nu^3}{\epsilon})^{1/4}\right), \tag{6.3}$$

where κ is the turbulent kinetic energy, ϵ is the dissipation rate, ν is the kinematic viscosity. The main disadvantage of expression (6.3) is that it contains limited physical information regarding the structure of the local flow field, since it is based solely on the turbulent variables κ and ϵ. Furthermore, this expression is calibrated from previous works [6] for cases where the ASBM is coupled with the four-equation v^2-f model. All the above make the applicability of expression (6.3) to the ASBM-SA closure questionable.

6.2.4.1 Details of the Rahmann's lengthscale expression.

The model coefficient C_μ is determined by the following expressions

$$C_\mu = \frac{\alpha_1}{1 - \frac{2}{3}\eta^2 + 2\xi^2}\,, \qquad \eta = \alpha_2 T_t S\,, \qquad \xi = \alpha_3 T_t W\,, \tag{6.4}$$

where T_t is a turbulence timescale, and W, S are the invariants of the mean strain rate and vorticity tensor respectively, defined by

$$S = \sqrt{2 S_{ij} S_{ji}}\,, \qquad W = \sqrt{2 \Omega_{ij} \Omega_{ji}}\,. \tag{6.5}$$

The alpha model coefficients are defined by

$$\alpha_1 = g\left(\frac{1}{4} + \frac{2}{3}\Pi_b^{1/2}\right), \qquad \alpha_2 = \frac{3g}{8\sqrt{2}}\,, \qquad \alpha_3 = \frac{3\alpha_2}{\sqrt{2}}\,, \qquad g = \left(1 + 2\frac{P_k}{\epsilon}\right)^{-1}, \tag{6.6}$$

where P_k/ϵ is the relative strength between the production and the dissipation rate and Π_b is an invariant of the Reynolds stress tensor. These parameters are modeled as

$$\Pi_b = C_v \frac{P_k}{\epsilon}\,, \qquad \frac{P_k}{\epsilon} = C_v \zeta^2\,, \qquad C_v = \frac{1}{2(1 + T_t S\sqrt{1 + \Re^2})}\,, \qquad \zeta = T_t S \max(1, \Re)\,, \tag{6.7}$$

where $\Re = |W/S|$ is a dimensionless parameter. Finally, the turbulence lengthscale is estimated by

$$L^2 = \zeta(9.0 + C_\mu Re_T)\sqrt{\frac{\nu^3}{\epsilon}}\,, \qquad Re_T = \frac{\kappa^2}{\nu\epsilon}\,. \tag{6.8}$$

Detailed analysis of the model is given in [81].

6.2.4.2 Validation

Consequently, we repeat our computations for the uncontrolled case, this time using an expression for the lengthscale as described in Rahmann et al. [81]. The elegance of this choice stems from the fact that it is constructed for use in another one-equation model, the Baldwin-Barth (BB) model [82], and from the fact that it is sensitized to both vorticity and shear dominated flows that are far from equilibrium. Figs. 6.25 show a comparison between ASBM-SA results using both expressions with the SA predictions and the experiments for the pressure and wall-static skin-friction coefficients. The choice of algebraic expression is shown to have trivial effect on the results for the specific case, while the numerical stability of the algorithm remained also unaffected.

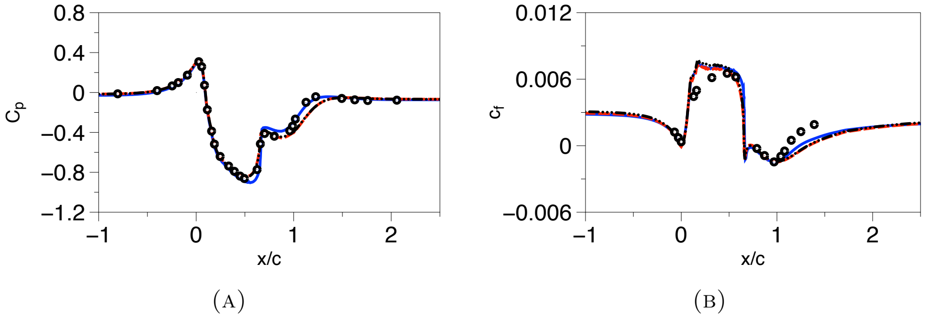

(A)

(B)

FIGURE 6.25: ASBM-SA model predictions when the new (—···—) and the old (- - - -) lengthscale expression is used for the no-flow control case for (a) the wall static-pressure coefficient and (b) the skin-friction coefficient. Comparison is made to SA model predictions (———) and the experimental values (symbols) [77].

Fig 6.26 shows the corresponding ASBM-SA predictions at station A for the fluctuating intensities and fluctuating shear stress. Choosing the new lengthscale expression resulted in improved predictions for the near-wall peak magnitude for all statistical correlations, while similar results are produced at the remaining stations.

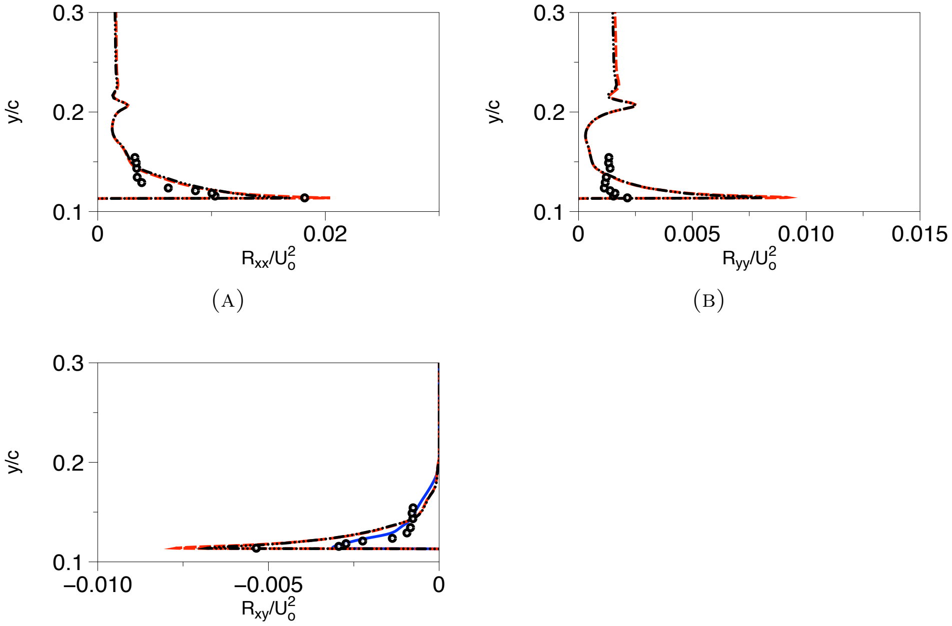

(A) (B)

(C)

FIGURE 6.26: ASBM-SA predictions using the new (—···—) and the old (----) lengthscale expression at station A for the no-flow control case. Comparison is made to the SA predictions (———) and the experimental values (symbols) [77] for (a) the streamwise Reynolds stress component R_{xx}, (b) the transverse Reynolds stress component R_{yy} and (c) the fluctuating shear stress component R_{xy}.

6.2.5 Conclusions

The ASBM-SA closure has been tested for the case of a flow over a two-dimensional smooth hill in the shape of a "Modified Glauert-Goldschmied" hump both in the presence and absence of separation control. For both cases considered, the ASBM-SA model produced satisfactory predictions for the streamwise Reynolds stress component R_{xx}, while a qualitative agreement with the experiments was achieved for the transverse component R_{yy}. ASBM-SA closure provided improved predictions compared to SA for the shear stress in the entire domain. Regarding the mean quantities, the predictions of both closures are comparable, providing fair agreement with the experiments. Overall, the hybrid model managed to capture satisfactory the traits of these highly anisotropic flows, while maintaining the high robustness of the SA model, at a good convergence rate. A new expression for the estimation of the turbulence lengthscale, suitable for flows far from equillibrium, is adopted and tested for the no-flow controlled case. This choice led to improved predictions for the near-wall peak magnitudes of the statistical correlations, while exhibiting similar robustness to the previous choice. Use of separated zones for the activation of the filtering scheme resulted to smoother mean velocity profiles in the recirculation region, and more meaningful skin-friction profiles upstream and downstream the separated region.

As part of future work we intend to ascertain the performance of the hybrid model over challenging two-dimensional flows, such as turbulent flows around a wall-mounted cube and plane wall jets, while an extension to three-dimensional smooth hills will be attempted. Regarding the refinement issues encountered in the current and previous works, further consideration is needed to understand why ASBM-SA delays further the re-attachment compared to SA for all validation cases considered until now, even though it gives better predictions for the shear stress over the entire region of the recirculation. We have already started developing more advanced filtering schemes, suitable for highly deformed meshes, since we believe that the choice of filtering scheme plays a role on the delay of flow's re-attachment, and contributes to yielding larger recirculation bubbles.

Chapter 7

2D airfoil simulations using the ASBM-SST hybrid model.

7.1 Introduction

In this chapter the main objective was to obtain converged smooth solutions with the full ASBM closure for flow over the VR7 rotorcraft airfoil in a wide range of flow parameters. Another objective was to further investigate the performance of the ASBM model for the flow over the symmetric NACA-0015 airfoil, since this type of NACA airfoil is thicker than the VR7 airfoil. Particularly, we focus on testing the response of the algebraic structure-based model to compressibility effects which are encountered in compressible flows, for Mach numbers ranging from 0.06 up to 0.3. In order to achieve that, we used a compressible solver, called SUmb, as the platform for coupling the ASBM closure to the SST model, leading to the ASBM-SST hybrid model. Due to the complexity of this solver, we have spent considerable time in order to incorporate the ASBM module in the solver in such a way that it is elegant for others to use it. Additionally, due to the highly nonlinear algebraic nature of the ASBM closure, we have developed a number of numerical improvements which enabled us to perform, for the first time, successful computations for these type of flows. Particularly, new smoothing expressions were constructed that are suitable for deformed meshes in order to improve the convergence and stability characteristics of the ASBM computations. Also, we developed an extended blending methodology that is applicable in compressible flow solvers which enabled model refinements.

7.1.1 Outline

Section 7.2 shows details related to three independent techniques that are developed in order to encounter the stability issues stemming from the non-linear nature of the ASBM closure. Particularly, it contains proper smoothing expressions for two-dimensional (2D) and three dimensional (3D) highly stretched meshes, blending expressions for the mean transport equations, whilst it introduces the concept of zonal separation, in which the computational domain is divided in two zones. Sections 7.3 and 7.4 discuss the performance of the ASBM-SST hybrid model for a number of 2D static cases over two types of airfoils, namely VR-7 and NACA-0015 respectively. In Sections 7.5 and 7.6, 2D pitching runs are performed in order to further ascertain the performance of the closure at different freestream Mach and Reynolds numbers, again for flows over two types of airfoils, VR-7 and NACA-0015 respectively. SST and ASBM-SST model predictions for a number of integrated mean quantities, such as lift, drag and pressure coefficients, are then compared to detailed experimental measurements.

7.2 Computational Formulation

The use of a suitable smoothing expression is motivated by the nonlinear algebraic nature of the ASBM closure, combined with the need for highly deformed meshes surrounding the airfoil surfaces. Smoothing is typically utilized in ASBM implementations to provide improved convergence and stability characteristics. The final smoothing expression that we have reached takes into account the volumes of the nodes, and satisfies the limiting case of completely uniform grids (cube volumes). The expression is applicable to 3D grids, even though in this work it has been applied only to 2D grids.

7.2.0.1 Smoothing expression

In order to construct a suitable smoothing of a variable Φ, we divide the nodes in three categories named A,B,C, in respect to their distance from the reference node (referenced with index 0). The expression takes into account the volume which encloses each node. The equations satisfy the limiting state of uniform grids. The 2D expression is given by

$$\begin{aligned} \bar{\Phi} &= \frac{\Phi_0}{4} + \frac{3}{4}\Phi^{ave}_{rest}\,, \\ \bar{\Phi}^{ave}_{rest} &= \frac{\sum_{i=1}^{4}(\frac{\Phi_i}{2V_i})^A + \sum_{i=1}^{4}(\frac{\Phi_i}{4V_i})^B}{\sum_{i=1}^{4}(\frac{1}{2V_i})^A + \sum_{i=1}^{4}(\frac{1}{4V_i})^B}\,, \end{aligned} \tag{7.1}$$

whereas the 3D expression is given by

$$
\begin{aligned}
\bar{\Phi} &= \frac{\Phi_0}{8} + \frac{7}{8}\Phi^{ave}_{rest}\,, \\
\bar{\Phi}^{ave}_{rest} &= \frac{\sum_{i=1}^{6}(\frac{\Phi_i}{2V_i})^A + \sum_{i=1}^{12}(\frac{\Phi_i}{4V_i})^B + \sum_{i=1}^{8}(\frac{\Phi_i}{8V_i})^C}{\sum_{i=1}^{6}(\frac{1}{2V_i})^A + \sum_{i=1}^{12}(\frac{1}{4V_i})^B + \sum_{i=1}^{8}(\frac{1}{8V_i})^C}\,.
\end{aligned}
\tag{7.2}
$$

Figure 7.1 shows how neighboring nodes are distributed around reference node 0. Nodes of type A are the closest to the reference node, type B are the middle ones and C are the most distant ones. For a grid consisting of hexaedrons, as it is the case in SUmb, the total number of neighboring nodes is 26.

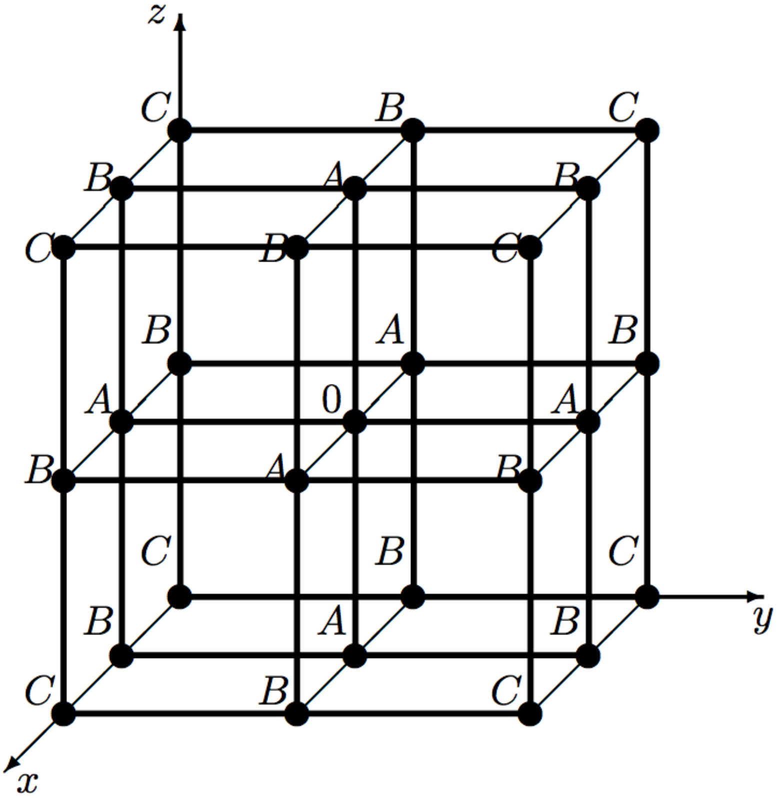

FIGURE 7.1: The distribution of neighbor nodes around the reference node with index 0.

7.2.0.2 Blending expressions

This concept, originally introduced by O'Sullivan et al (2010) for incompressible flows, has been extended to account for compressibility effects in the mean momentum and mean energy equations. The extended mean momentum equations are given by

$$\begin{aligned}
&\frac{\partial(\rho u_i)}{\partial t} + \frac{\partial(\rho u_i u_j)}{\partial x_j} + \frac{\partial}{\partial x_j}[p + \frac{2}{3}\rho\kappa(1-\alpha)]\delta_{ij} = \\
&-\alpha\frac{\partial}{\partial x_j}[\rho R_{ij}] + \frac{\partial}{\partial x_j}\left[\mu(\frac{\partial u_i}{\partial x_j} + \frac{\partial u_j}{\partial x_i} - \frac{2}{3}\frac{\partial u_k}{\partial x_k}\delta_{ij})\right. \\
&\left. + (1-\alpha)\mu_T(\frac{\partial u_i}{\partial x_j} + \frac{\partial u_j}{\partial x_i} - \frac{2}{3}\frac{\partial u_k}{\partial x_k}\delta_{ij})\right],
\end{aligned} \tag{7.3}$$

and the energy equation is given by

$$\begin{aligned}
\frac{\partial(\rho e)}{\partial t} + \frac{\partial(\rho u_i e\delta_{ij})}{\partial x_j} + \frac{\partial}{\partial x_j}[u_i(p + \frac{2}{3}\rho\kappa(1-\alpha))\delta_{ij}]& \\
= -\alpha\frac{\partial}{\partial x_i}[u_j\rho R_{ij}] + \frac{\partial}{\partial x_i}\left[u_j\mu(\frac{\partial u_i}{\partial x_j} + \frac{\partial u_j}{\partial x_i}\right.& \\
- \frac{2}{3}\frac{\partial u_k}{\partial x_k}\delta_{ij}) + (1-\alpha)u_j\mu_T(\frac{\partial u_i}{\partial x_j}& \\
\left. + \frac{\partial u_j}{\partial x_i} - \frac{2}{3}\frac{\partial u_k}{\partial x_k}\delta_{ij}) + q_j^{tot}\delta_{ij}\right],&
\end{aligned} \tag{7.4}$$

where κ is the turbulent kinetic energy, u_i, p, e denote the mean parts of the velocity, pressure and total internal energy fields respectively, whilst α is the blending factor, which represents the fraction of Reynolds stress contribution coming from the ASBM closure,

$$R_{ij} = \overline{u_i' u_j'} = \alpha R_{ij}^{ASBM} + (1-\alpha)R_{ij}^{BOUS}\,. \tag{7.5}$$

For $\alpha = 0$, eqs. (7.3)-(7.4) reduce to a pure EVM formulation, whereas for $\alpha = 1$ they correspond to a pure ASBM scheme. Additionally, q_j^{tot} is the total heat flux loss, given by

$$q_j^{tot} = \frac{1}{\gamma - 1}(\frac{\mu}{Pr} + \frac{\mu_T}{Pr^T})\frac{\partial C_s^2}{\partial x_j}\,. \tag{7.6}$$

Here, C_s is the sound speed, Pr is the dimensionless Prandtl number and γ is the heat capacity ratio.

7.2.0.3 Zonal Separation

During our computations, ASBM incurred numerical failures at the wake region at the vicinity the airfoil. These were handled by separating the domain into two distinct regions based on a reference point. The reference point had coordinates (0,c), which coincides with the trailing edge point at zero angle of attack and it remained fixed during all simulations. Upstream of this point, ASBM was active, whereas downstream of the point pure SST model was used instead. Fig 7.2 shows the "active" zonal region for an airfoil when stall is already present and separated flow is encountered. Clearly, a significant portion of the recirculation region lies inside the active region, enforcing ASBM influence on the computations. As shown in Fig 7.2, the solutions obtained are smooth and continuous across the zonal boundary. The continuity and smoothness of the solution extends to turbulence quantities such as the turbulent kinetic energy (not shown here).

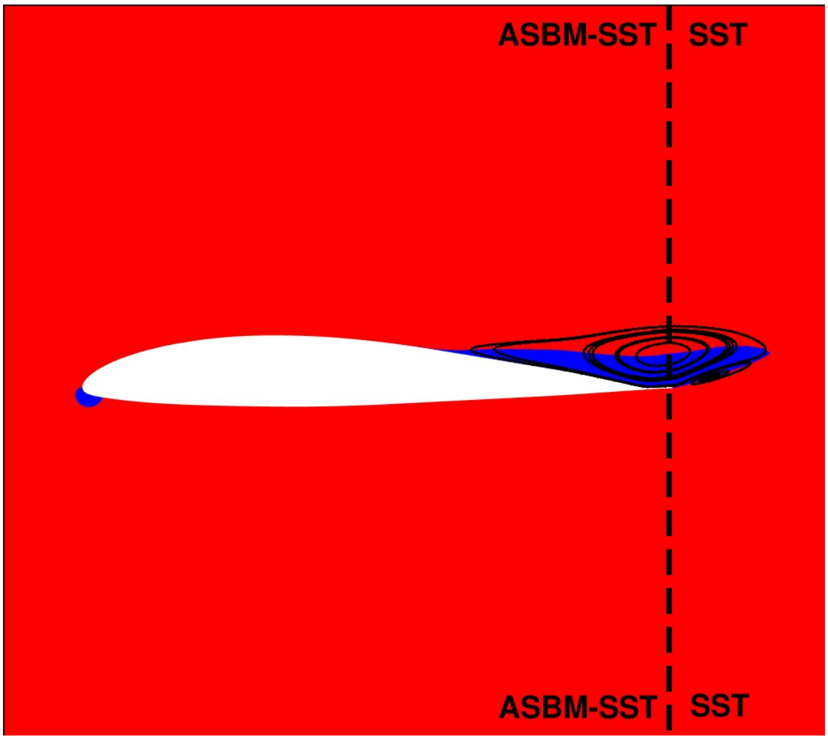

Figure 7.2: Separation zones which determine where ASBM is active or not at $a = 13.0^o$ angle of attacks.

7.2.1 SUmb compressible solver.

SUmb is a multi-block structured flow solver developed in the Stanford University. It solves the compressible Euler, laminar Navier-Stokes and Reynolds-Averaged Navier-Stokes equations. It has been developed as a completely general solver and it is therefore applicable to a variety of other types of problems, including external aerodynamic flows. SUmb is a parallel code, suited for running on massively parallel platforms. For more details regarding this platform, see [83].

7.2.2 General guidelines for the validation cases

In all simulations considered, static or dynamic, the maximum height of the cells adjacent to the airfoil surface ranged from $y^+ \approx 1.0$ to $y^+ \approx 2.5$, depending on the case, in order to ensure that the boundary layer was sufficiently resolved. For all computations, the value of the freestream turbulence intensity Tu was set to 0.001, and the freestream eddy viscosity ratio ER was set to 0.01, where

$$Tu = \left. \frac{(2\kappa/3)^{1/2}}{U_{ref}} \right|_{\infty}, \tag{7.7a}$$

$$ER = \left. \frac{\mu_T}{\mu_{ref}} \right|_{\infty}, \tag{7.7b}$$

where the subscript ref refers to the reference values. The reference Reynolds averaged velocity U_{ref} is defined by the farfield Mach number, whilst the reference kinematic velocity is defined using both the Reynolds and Mach numbers respectively. Consequently, farfield values for the remaining independent variables used in the model can be set. A constant specific heat ratio γ equal to 1.4 and a Prandtl number equal to 0.72 were assumed, with the freestream temperature $T_\infty = 288.15$ K, corresponding to a speed of sound value of $C_{s,\infty}$ of 340 m/s. Also, the dynamic laminar viscosity μ was calculated using Sutherland's equation. The above reference values were used to non-dimensionalize the transport equations. On the airfoil's surface, a viscous wall (no-slip) boundary condition was imposed, while a far-field boundary condition was set by applying freestream values to all variables at the corresponding sub-faces. In the spanwise direction, symmetry conditions were imposed.

Results and comparisons are made for the lift, drag, moment and pressure coefficients , defined by

$$C_L = \frac{L}{\frac{1}{2}\rho U_\infty^2 c}, \tag{7.8a}$$

$$C_D = \frac{D}{\frac{1}{2}\rho U_\infty^2 c}, \tag{7.8b}$$

$$C_M = \frac{M}{\frac{1}{2}\rho U_\infty^2 c}, \tag{7.8c}$$

$$C_p = \frac{(p - p_\infty)}{\frac{1}{2}\rho U_\infty^2 c}, \tag{7.8d}$$

where L, D, M are the lift, drag and moment per unit span and U_∞ the freestream mean velocity.

Converged solutions for all pure SST runs were obtained first. Subsequently, starting from the SST converged solution, predictions for a blending factor $\alpha = 0.5$ were obtained. Using the converged solution for $\alpha = 0.5$ as an initial guess, the converged solution for the pure ASBM computation ($\alpha = 1$) was then obtained. This methodology remained unchanged during all simulations, both static and dynamic.

7.3 Static Runs for VR-7 airfoil.

Firstly, we consider a turbulent flow over a VR-7 rotorcraft airfoil, at at freestream Mach numbers of $M_\infty = 0.184$, $M_\infty = 0.25$ and $M_\infty = 0.30$ for a series of fixed angles of attack, ranging from 0^o to 15^o. The converged, steady model predictions for the current and following cases are compared with the static experimental data of [84].

In order to ascertain the performance of the closure at the linear regime, the relative errors associated with the lift curve slope (LCS) and the zero-lift angle (ZLA) are introduced, given by

$$\begin{aligned} \sigma_1 &= |\frac{C^e_{L,1} - C^c_{L,1}}{C^e_{L,1}}| \times 100 \ , \\ \sigma_o &= |\frac{ZLA^e - ZLA^c}{ZLA^e}| \times 100 \, , \end{aligned} \tag{7.9}$$

where superscripts e and c refer to the experimental and computational values respectively.

7.3.1 M_∞=0.3 with tab.

Firstly we consider the unsteady case at freestream Mach Number of $M_\infty = 0.30$, yielding to a Prandtl-Glauert factor equal to $\beta = 0.9539$. A fixed time step equal to 0.0058 s was chosen, whilst at each time step, 30 Newton-Raphson sub-iterations were imposed, a number which proved to be large enough in all static cases.

Table 7.1 shows the linear expressions and the associated relative errors for the lift-curve slope. Clearly, ASBM improves the slope estimation almost 100 percent relative to the pure SST results , revealing its sensitivity to the pressure changes. Zero-lift angle remains practically unaffected.

Case	LCS	σ_1	ZLA	σ_o
Exp	0.1227	-	-1.56	-
SST	0.1036	15.5	-2.13	36.5
ASBM	0.1145	6.7	-2.22	41.0

Table 7.1: Linear expressions and zero-lift angle based on least-squares methods, accompanying with their relative errors.

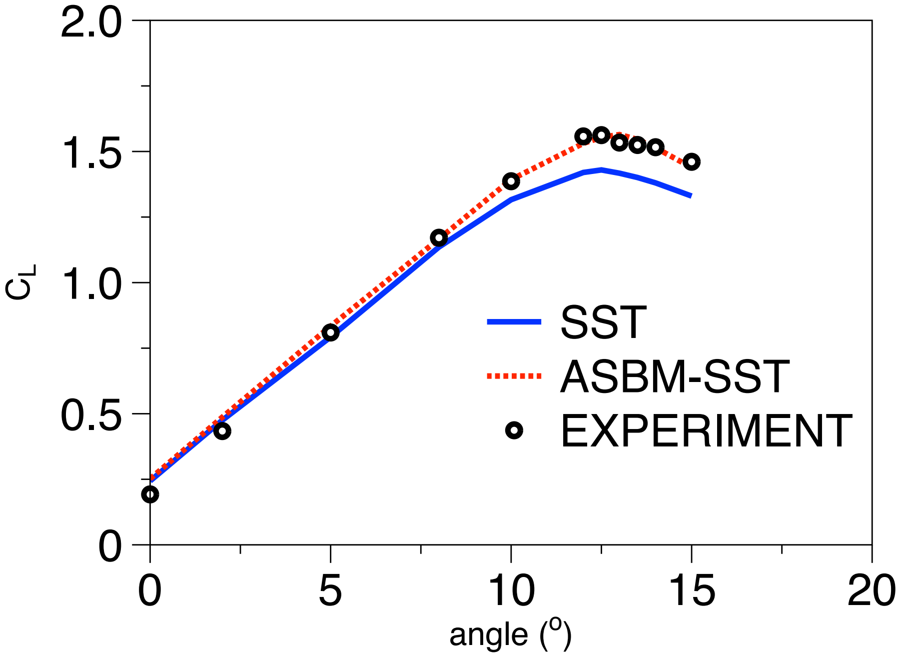

Figure 7.3: Lift coefficient C_L as a function of angle of attack for $M_\infty = 0.3$ and $Re_c = 4.25 \times 10^6$. Predictions of the ASBM-SST (dashed line) and SST (solid line) closures are compared to the experiments of McCroskey et al. [84], shown as symbols.

Fig 7.3 shows a comparison of model predictions and experimental results for the lift coefficient. ASBM closure provides a much better agreement to the experiments relative to the SST computation, although a slight delay of the onset of stall is noted.

Fig. 7.4 shows model and experimental predictions for the drag coefficient. Again, we see negligible changes at small angle of attacks. After the dynamic stall, the ASBM closure tends to underpredict the C_D value by a larger amount than the SST closure, however the deviations are inside error limits, especially near and after stall region where high uncertainties due to different effects are encountered, as described by Moulton et al (2010).

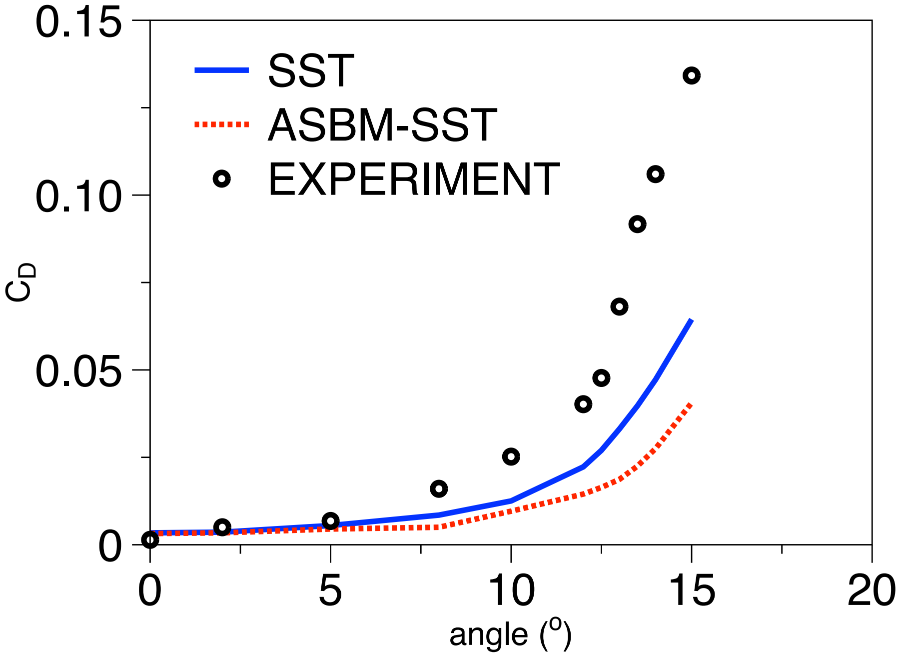

FIGURE 7.4: Pressure part of the coefficient of drag C_D as a function of angle of attack for $M_\infty = 0.3$ and $Re_c = 4.25 \times 10^6$. Predictions of the ASBM-SST (dashed line) and SST (solid line) closures are compared to the experiments of McCroskey et al. [84], shown as symbols.

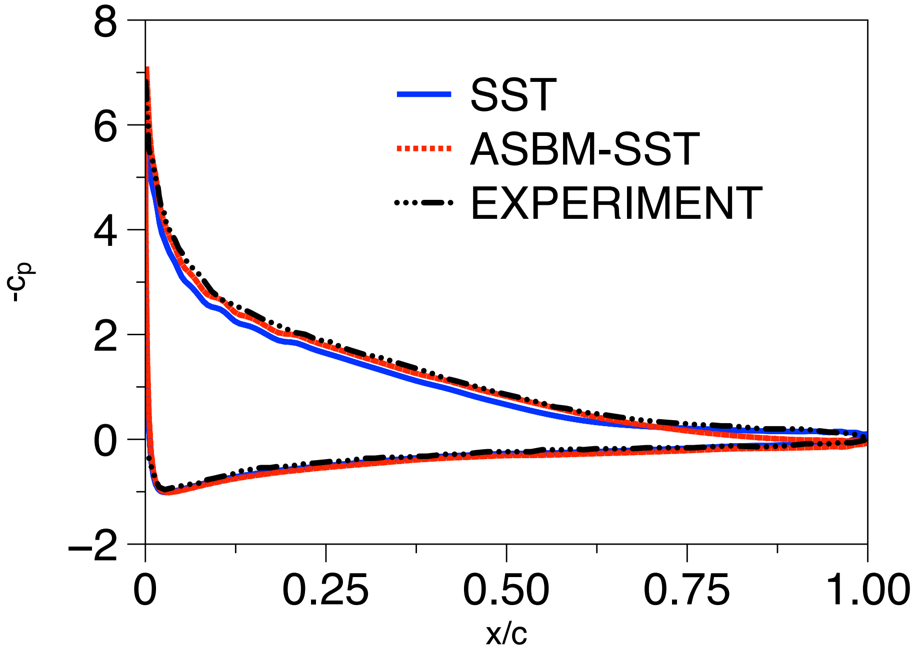

FIGURE 7.5: Pressure coefficient of lift C_P as a function of angle of attack for $M_\infty = 0.3$ and $Re_c = 4.25 \times 10^6$. Predictions of the ASBM-SST (dashed line) and SST (solid line) closures are compared to the experiments of McCroskey et al. [84], shown as symbols.

Since the lift coefficient attains much larger values than the drag coefficient, based on the above results for C_L it's reasonable to anticipate improvement of the pressure distribution along airfoil's surface, even though the C_D predictions are not improved. Fig. 7.5 advocates this argument. The pressure distribution at the suction side, shows a noticeable improvement, starting from the leading edge and extending downstream until $(x/c) \approx 0.8$. Near the trailing edge, the SST closure produces slightly better predictions, however the trailing edge region has the smallest contribution to the lift integration. This is why the overall coefficient predictions dramatically improved.

7.3.2 M_∞=0.25 with tab.

In order to further assess the performance of the closure, the unsteady case at freestream Mach Number of $M_\infty = 0.25$ was considered at $\beta = 0.9682$.

Table 7.2 shows an improvement of the slope close to 50% when ASBM is fully active ($\alpha = 1$), whereas the marginal effects to the zero-lift angle estimation are again confirmed.

Case	LCS	σ_1	ZLA	σ_o
Exp	0.1235	-	-1.526	-
SST	0.1096	11.26	-2.215	45.14
ASBM	0.1135	7.80	-2.218	45.32

Table 7.2: Linear expressions and zero-lift angle based on least-squares methods, accompanying with their relative errors.

Figure 7.6 presents both model and experimental calculations for the lift coefficient, displaying the notable ability of the ASBM closure to accurately capture C_L profile. In the case of the drag coefficient, C_D, Fig 7.7 shows again the trivial changes at small angle of attacks and the tendency of the closure to further under-predict the coefficient in the high angle of attack regime.

Figure 7.8 shows that, as previously observed, the pure ASBM produces an improved pressure distribution on the upper side. Again, in the vicinity of the trailing edge SST gives better predictions than ASBM, but this does not affect the overall advantage of ASBM because of the small contribution of the trailing edge region to C_L.

7.3.3 M_∞=0.184 with tab.

In order to further test the performance of the closure at lower Reynolds numbers, we performed unsteady computations at freestream Mach Number of $M_\infty = 0.184$, following a similar methodology as in the previous cases.

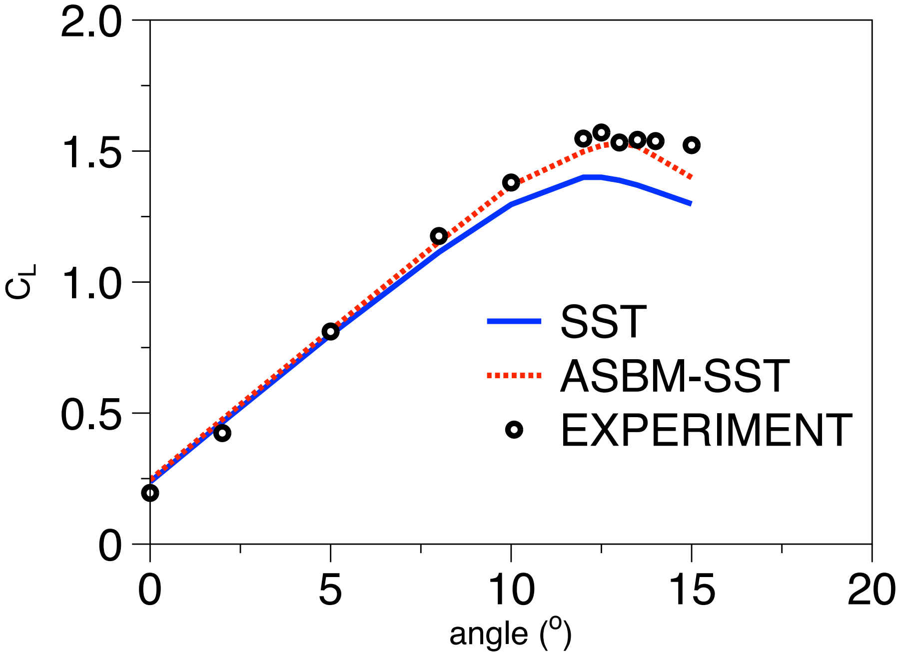

FIGURE 7.6: Same as Fig. 7.3, but for $M_\infty = 0.25$ and $Re_c = 3.55 \times 10^6$.

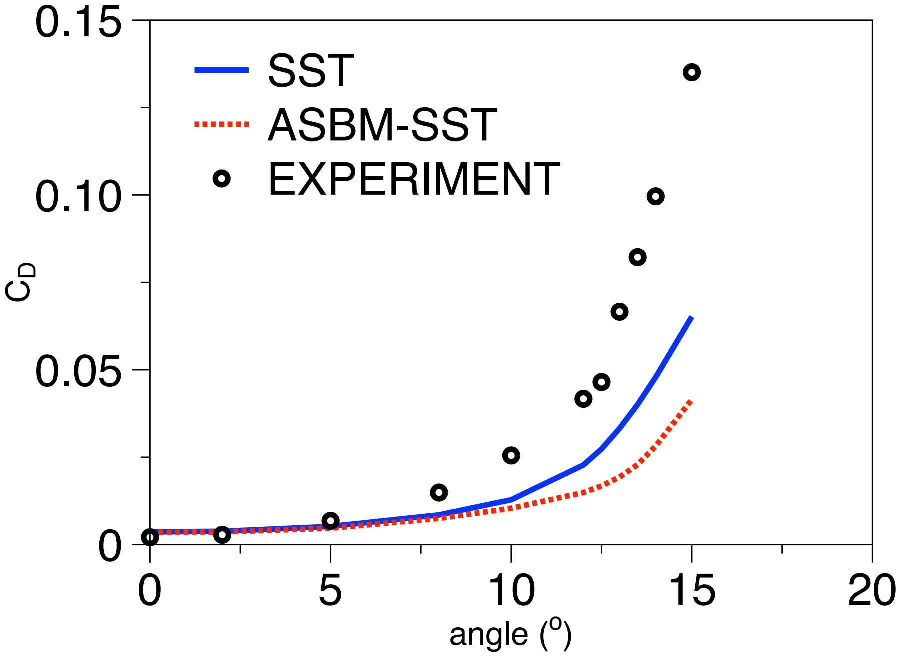

FIGURE 7.7: Same as Fig. 7.4, but for $M_\infty = 0.25$ and $Re_c = 3.55 \times 10^6$.

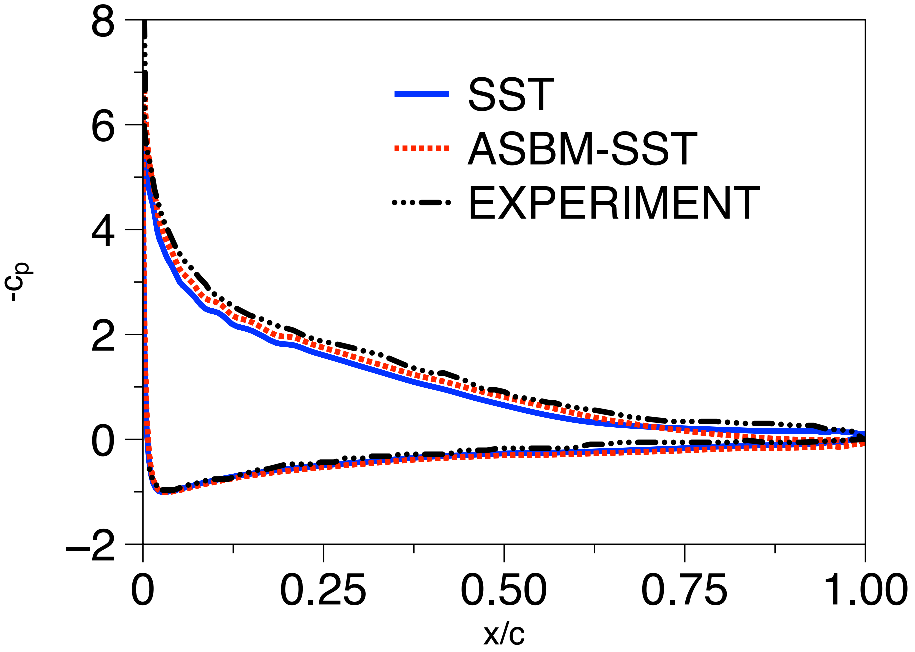

FIGURE 7.8: Same as Fig. 7.5, but for $M_\infty = 0.25$ and $Re_c = 3.55 \times 10^6$.

Table 7.3 shows the linear expressions and the relative errors for the lift-curve slope, revealing an improvement of the slope prediction close to 100% when ASBM is fully active (relative to the SST $\alpha = 0$ computation).

Case	LCS	σ_1	ZLA	σ_o
Exp	0.1185	-	-1.573	-
SST	0.1072	9.50	-2.170	37.95
ASBM	0.1117	5.74	-2.119	34.71

TABLE 7.3: Linear expressions and zero-lift angle based on least-squares methods, accompanying with their relative errors.

Fig 7.9 displaying again the superior accurancy of ASBM closure. In Fig. 7.10, we find the same trends for C_D as in the former cases.

7.3.3.1 Pressure tab interpolation.

To further establish the validity of the comparison between CFD and experiments, we adopt an additional integration method via the Trapezium rule, in accordance to McCroskey et al. [84]. At the trailing edge point, an interpolation of values between the nearest points to the edge from the upper and lower surface is utilized. The computational data were linearly interpolated between computational node locations at the experimental tap locations.Figs. 7.11 graphically represents the small deviations between the two approaches.

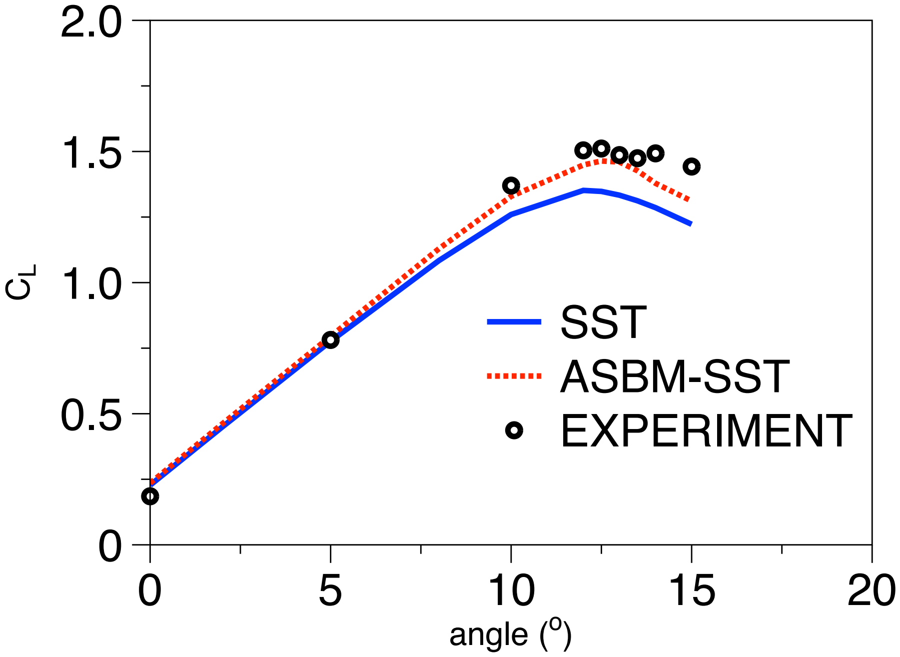

FIGURE 7.9: Same as Fig. 7.3, but for $M_\infty = 0.184$ and $Re_c = 2.6 \times 10^6$.

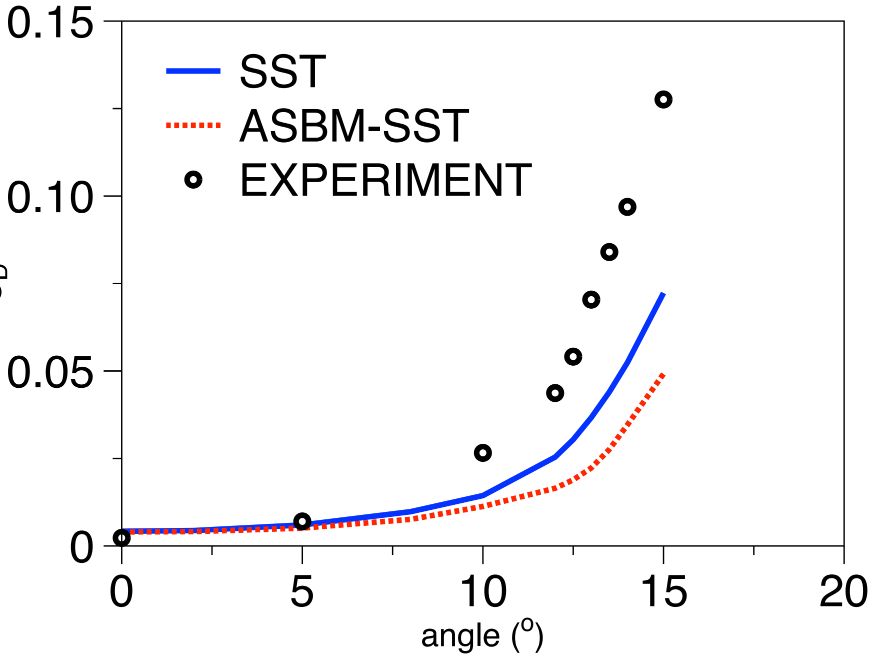

FIGURE 7.10: Same as Fig. 7.4, but for $M_\infty = 0.184$ and $Re_c = 2.6 \times 10^6$.

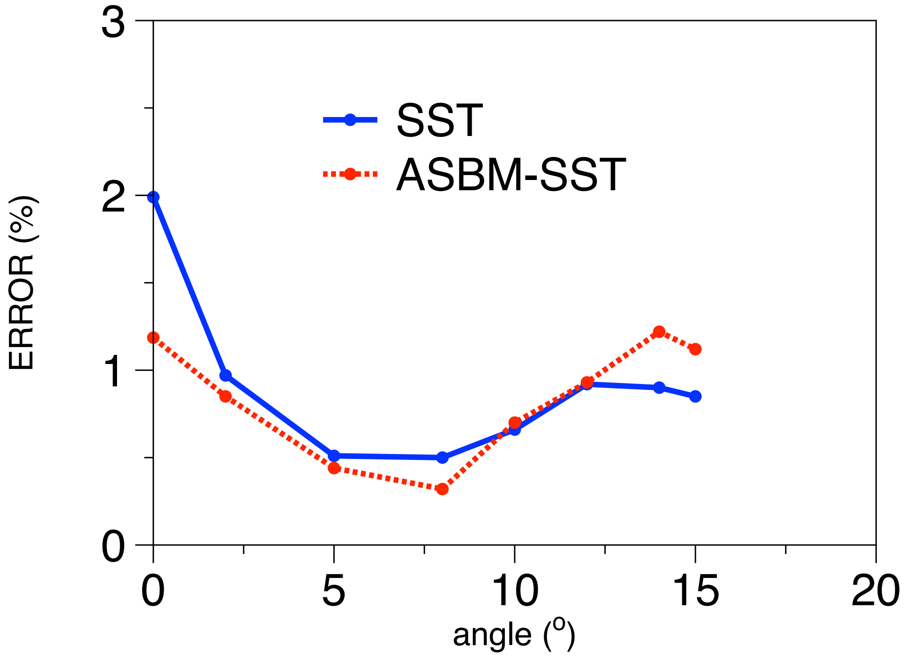

FIGURE 7.11: Absolute relative errors when integrating with CFD nodes and the experimental pressure tabs using the Menter κ-ω SST as a carrier model at $M_\infty = 0.25$, $Re_c = 3.55{\times}10^6$.

7.3.4 VR7 computations without tab.

As mentioned above, convergence issues made necessary the use of zonal decomposition in order to achieve fully converged ASBM solutions at high angles of attack. During our computations, we concluded that the main source of the instabilities is located in the vicinity of the trailing edge tab. Based on pure SST runs with and without the trailing edge tab, we have conlcuded that at higher angles of attack the effect of the tab presence on the computed integral coefficients (C_L, C_D, and C_M) is less than 2%. Hence, we proceeded to obtain full ASBM solutions over the entire domain (i.e. without zonal separation). The geometry modifications were applied to the airfoil's tail region for which the x-coordinate ranges between 0.98c and 1.00c. Additional points were added as needed to ensure a smooth geometry in the vicinity of the trailing edge. The case we have considered is again for the flow over the VR7 airfoil at freestream Mach Number of $M_\infty = 0.25$ and chord length based $Re_c = 3.55 \times 10^6$ at fixed angles of attack. Again, the SST closure is chosen as a carrier model and the angle of attack ranges from 0^o to 15^o.

Fig.7.13 depicts SST and ASBM predictions for the distribution of the pressure coefficient along the cross section of the airfoil. No experimental data is available for this angle, however we clearly see smooth profiles obtained for both closures.

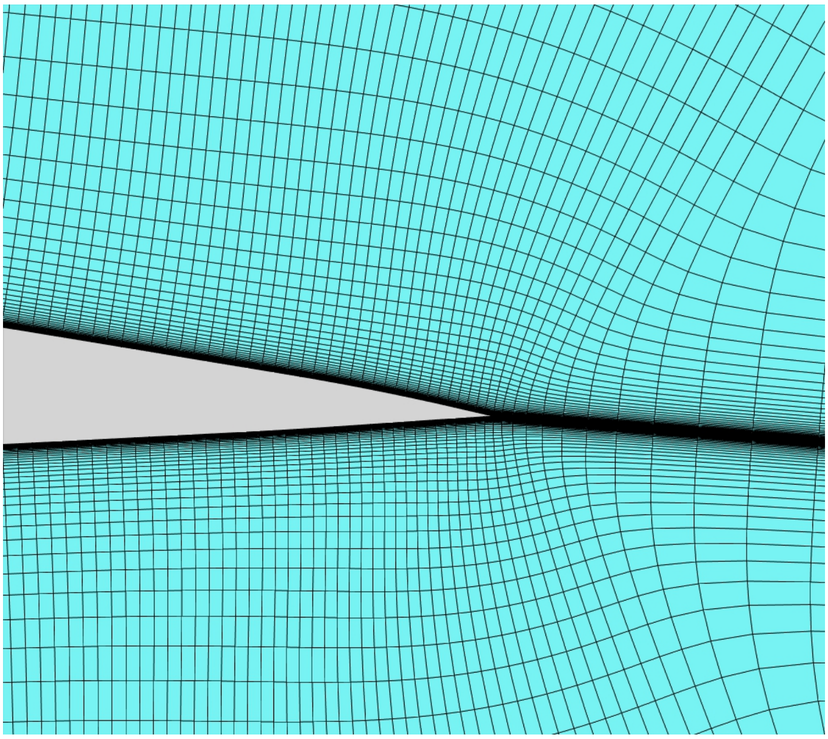

FIGURE 7.12: Details of the VR7 mesh design focused in the vicinity of the airfoil trailing edge.

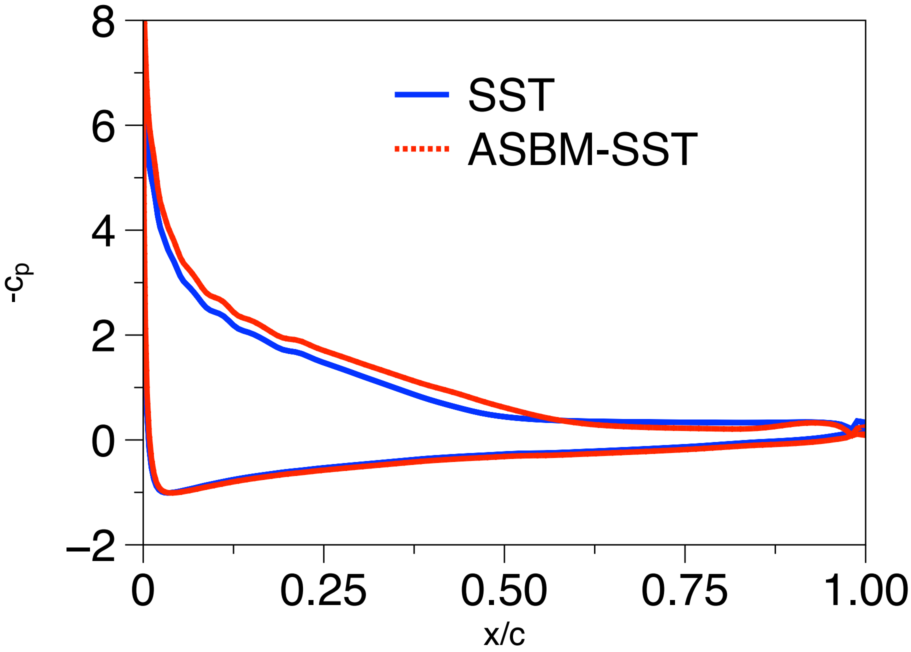

FIGURE 7.13: VR7 Computations at M_∞=0.25, at $Re_c = 3.55 \times 10^6$. Model predictions for the pressure coefficient at an angle of attack of $\alpha = 15^o$.

7.4 Static Runs for NACA-0015 airfoil.

Next, we examined the standard case of a turbulent flow over a symmetric NACA type airfoil with camber thickness 15% its chord length, denoted as NACA-0015. This scenario is interesting because NACA-0015 airfoil is thicker than the VR-7, which has camber thickness 12% its chord length instead. Firstly we conducted static runs for fixed angles from 0^o up to 20^o, at a constant freestream mach number of $M_\infty = 0.062$ and two different freestream Reynolds numbers, $Re_c = 6.55 \times 10^5$, 1.27×10^6, where Re_c is based on the chord length c and freestream mean velocity U_{ref}.

7.4.1 M_∞=0.062 and $Re_c = 6.55 \times 10^5$, no trip.

First, we considered the unsteady case at freestream Mach Number of $M_\infty = 0.062$ and $Re_c = 6.55 \times 10^5$ for a series of fixed angles of attack. The SST closure was chosen as a carrier model and the angle of attack was varied from 0^o to 20^o. The converged steady predictions of the model for the current and following cases are compared with the static experimental data of Eastman [85]. Based on the above Mach number, the value of the Prandtl-Glauert factor is $\beta = \sqrt{1 - M_\infty^2} = 0.9981$.

Initially, we explored the effect of the far-field boundary placement (domain size) on the integrated quantities. For this purpose, we computed the same baseline case (M_∞=0.062 and $Re_c = 6.55 \times 10^5$) using three different domains with a far-field extent of 25c, 35c and 55c respectively, and in all cases the same number (297x97) of grid nodes. As shown in Fig. 7.14a, the lift coefficient predictions are insensitive to the different domain sizes (0.44% maximum relative error), whereas as shown in Fig. 7.14b, the predictions for the drag coefficient display a stronger dependency with relative errors around 4.5%. However, as discussed in detail in previous reports on VR-7 computations, the drag coefficient predictions already suffer from significant uncertainties emerging from a number of effects, such as geometrical, blocking, and even the method used to numerical integration yielding the integral force coefficients [86]. Consequently, we believe that the uncertainty associated with the far field extent is of the same order as the uncertainties already present in the C_D values. Based on the above, we have chosen 25c as the baseline far field extent in order to accelerate the simulations.

Next, we performed grid-convergence analysis in order to determine the proper grid resolution. We have used three different grids at a fixed domain extent of 25c, for which different trailing edge streamwise spacings Δx_{TE} were adopted. The connection between the total number of cells adjacent to the airfoil surface N_a and the streamwise trailing edge spacing is given by

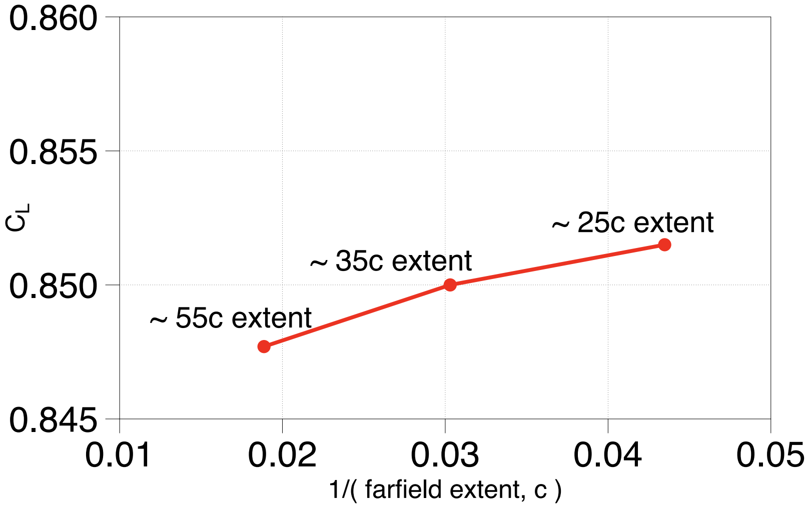

(a)

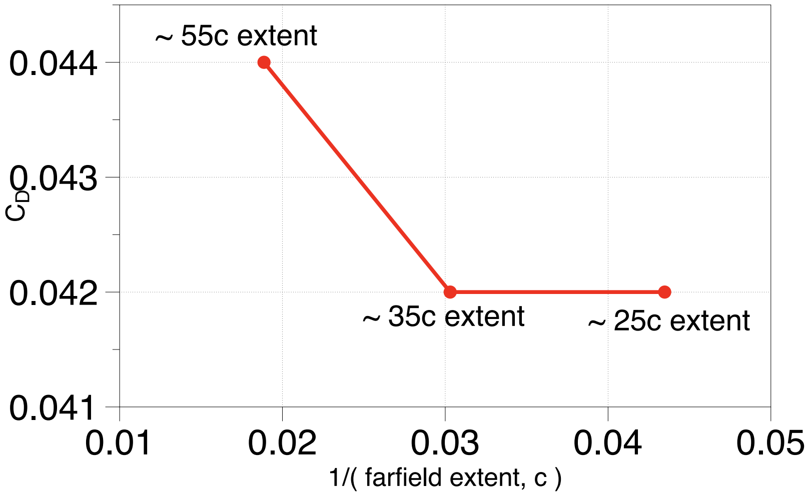

(b)

Figure 7.14: Static computations on a 297 x 97 baseline grid using the SST closure for the NACA 0015 airfoil with $M_\infty = 0.062$ and $Re_c = 6.55 \times 10^5$ and at $\alpha = 11^o$. Effect of far-field extent on: (a) Lift coefficient C_L; (b) Drag coefficient C_D.

$$\Delta x_{TE} = \frac{c}{N_a + 1} \,. \tag{7.10}$$

Fig. 7.15 shows the predictions of the SST closure for the lift coefficient C_L as a function of $1/N^{1/2}$, where N is the total number of grid cells. The discrepancy between the two most resolved grids is negligible (around 1 %), suggesting that the choice 297 x 97 provides an adequately resolved grid and this has been adopted for all subsequent computations for this case. Based on the findings of previous workers who dealt a similar case, such as Consul[87], we consider the results to be sufficiently converged, when the change in C_L is smaller than

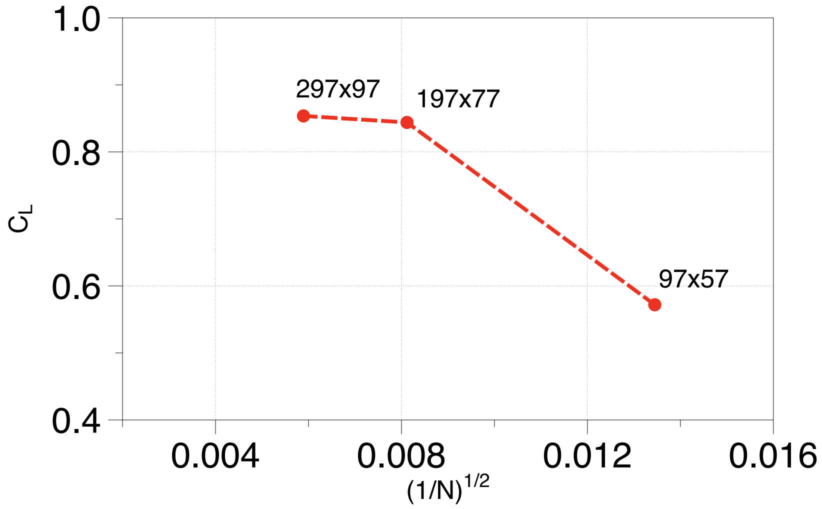

FIGURE 7.15: Static computations on a 25c farfield extent baseline grid using the SST closure for the NACA0015 airfoil with $M_\infty = 0.062$ and $Re_c = 6.55 \times 10^5$ at $\alpha = 11^o$. Effect of grid resolution on the lift coefficient C_L.

about 1% and the change in C_D smaller than 5%, as .

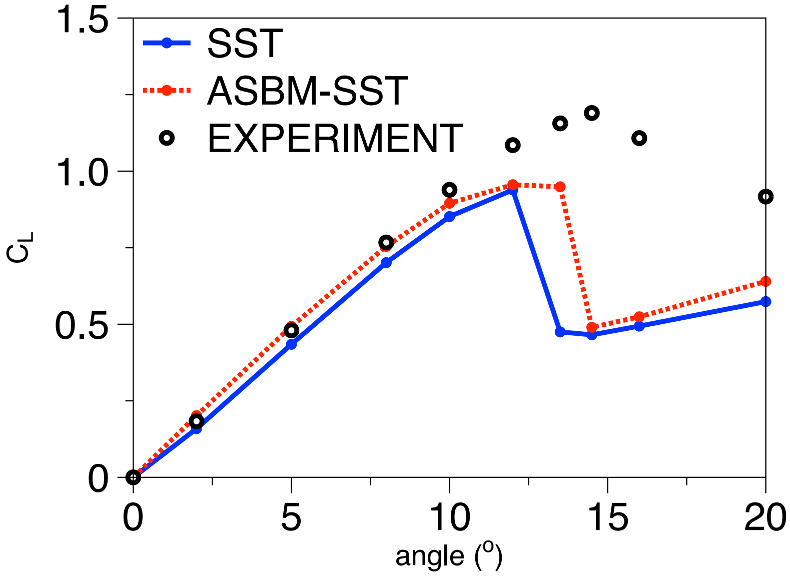

FIGURE 7.16: Static computations for the lift coefficient C_L as a function of angle of attack using the ASBM-SST (dashed line) and SST (solid line) closures with $M_\infty = 0.062$ and $Re_c = 6.55 \times 10^5$. Comparison is made to the experiments of Eastman et al. (1939), shown as symbols.

Fig. 7.16 shows model and experimental predictions for the lift coefficient. In the linear regime, ASBM tends to increase the lift coefficient values towards the experimental values, whereas a delay of the onset of stall to a higher angle of attack (which again is in better agreement with the experiments) yields improved results relative to the SST predictions. Fig. 7.17 shows the corresponding predictions for lift coefficient C_L as a function of drag coefficient C_D. Again ASBM exhibits a small but noteworthy improvement, especially in the linear regime. At high angles, we see the occurrence of a short drop in lift for both closures. This can be explained by the sudden spread of the recirculation bubble, which also leads to a sharp increase in drag, whilst its growth rate and its effect on lift depends on the Reynolds number, as discussed in Sharpe [88].

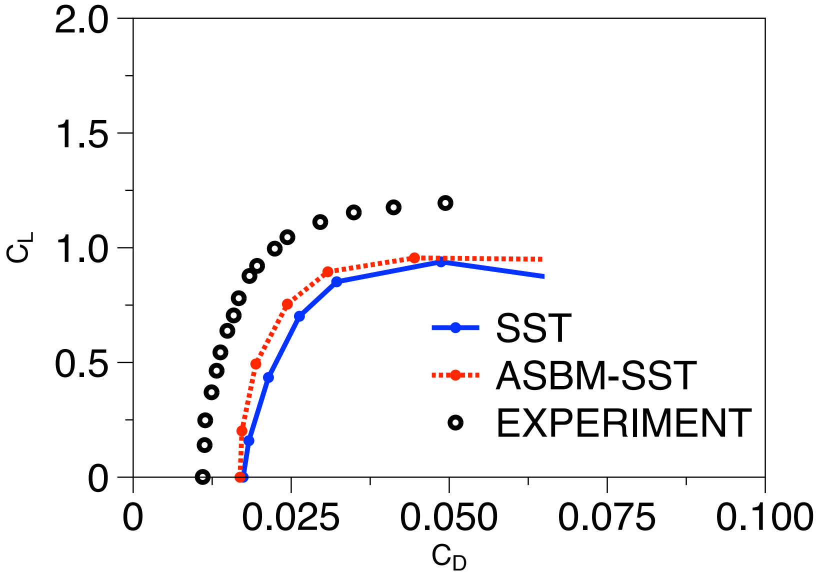

FIGURE 7.17: Static computations for the lift coefficient C_L as a function of the drag coefficient C_D using the ASBM-SST (dashed line) and SST (solid line) closures with $M_\infty = 0.062$ and $Re_c = 6.55 \times 10^5$. Comparison is made to the experiments of Eastman et al. (1939), shown as symbols.

7.4.2 M_∞=0.062 and $Re_c = 1.27 \times 10^6$, no trip.

In order to further assess the performance of the ASBM closure, the unsteady case at freestream Mach Number of $M_\infty = 0.062$ and $Re_c = 1.27 \times 10^6$ was considered. Again the angle of attack varies from 0^o to 20^o and the same Prandtl-Glauert factor as before is used ($\beta = 0.9981$).

The methodology used for the evaluation of the results was the same as before, keeping all model parameters unchanged during all simulations. Based on the findings from the previous case, we adopted a fixed domain extent of 25c, without any further investigation. Furthermore, grid-convergence analysis regarding lift coefficient predictions suggested that a 297 x 97 grid was sufficient for our purposes due to the marginal relative errors (around 0.5 %), as shown in Fig. 7.18.

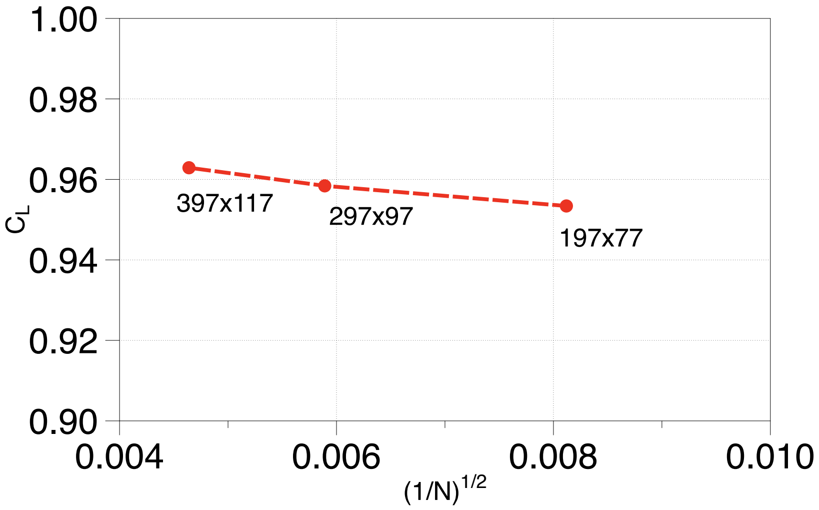

FIGURE 7.18: Static computations on a 25c farfield extent baseline grid using the SST closure for the NACA 0015 airfoil with $M_\infty = 0.062$ and $Re_c = 1.27 \times 10^6$ at $\alpha = 11^o$. Effect of grid resolution on the lift coefficient C_L.

Fig. 7.19 shows results for the lift coefficient C_L as a function of the angle of attack. As in the previous case, ASBM is found to improve the C_L predictions relative to the SST over the entire range of angles of attack. The ASBM also captures more accurately the stall angle. The moderate improvement brought about by ASBM is also evident in Fig. 7.20, where C_L is shown as a function of C_D.

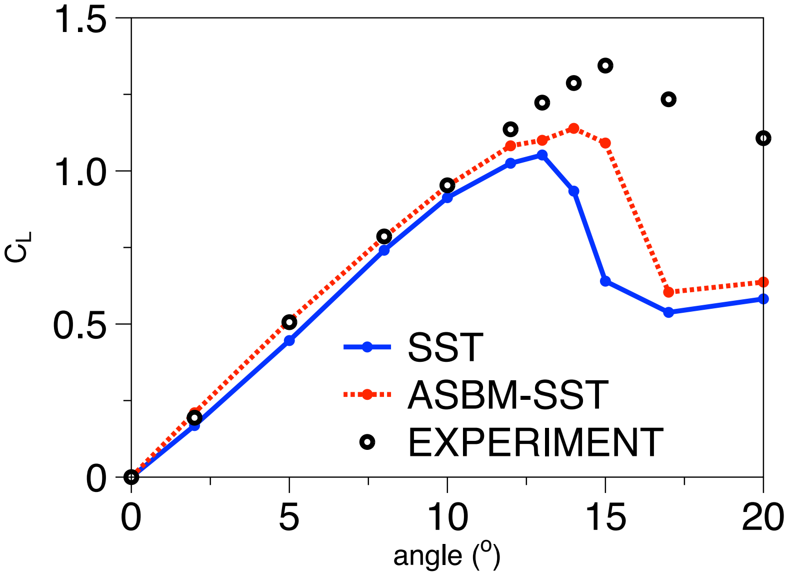

FIGURE 7.19: Static computations for the lift coefficient C_L as a function of angle of attack using the ASBM-SST (dashed line) and SST (solid line) closures with $M_\infty = 0.062$ and $Re_c = 1.27 \times 10^6$. Comparison is made to the experiments of Eastman et al. (1939), shown as symbols.

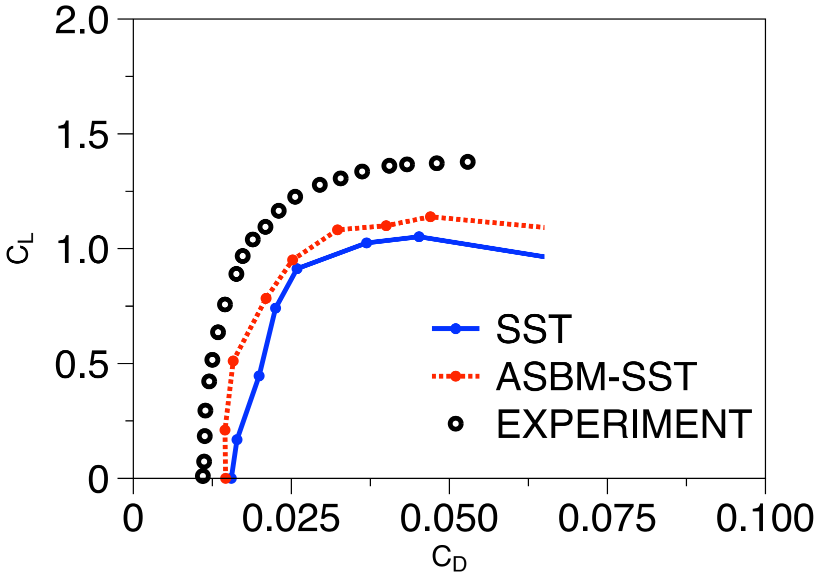

FIGURE 7.20: Static computations for the lift coefficient C_L as a function of the drag coefficient C_D using the ASBM-SST (dashed line) and SST (solid line) closures with $M_\infty = 0.062$ and $Re_c = 1.27 \times 10^6$. Comparison is made to the experiments of Eastman et al. (1939), shown as symbols.

7.5 Pitching Runs for NACA0015

Next, we examine the performance of the ASBM closure for a turbulent flow over a VR-7 rotorcraft airfoil undergoing pitching motions. We consider three cases at different parameters, described in Table 7.5, whilst model predictions are compared with the experimental data of [89]. Converged solutions for all pure SST runs were obtained after approximately 190 time steps, using a fixed time step equal to 0.03189s. At each time step, 30 Newton-Raphson sub-iterations were imposed, a number which proved to be adequate in all cases.

7.5.1 Grid-sensitivity analysis at M_∞=0.1235 and $Re_c = 1.48 \times 10^6$.

First, we conducted a grid analysis at a freestream Mach Number of $M_\infty = 0.1235$ and $Re_c = 1.48 \times 10^6$ for a fixed angle of attack of $\alpha = 11^o$ using the SST closure. The angle of attack was chosen to correspond to the higher end of the pitching angles, where the largest discrepancies during the pitching motion in both drag and lift coefficient are expected to occur. Based on the above Mach number, the value of the Prandtl-Glauert factor is $\beta = \sqrt{1 - M_\infty^2} = 0.9923$. We computed the same baseline case for four different meshes, starting from the coarsest grid (197x77) and moving towards the finest mesh (397x117). Fig. 7.21 shows the predictions of the SST closure for the lift coefficient C_L and the pressure part of the drag coefficient $C_{D,p}$ as a function of $1/N^{1/2}$, where N is the total number of grid cells. The discrepancy between the three most resolved grids is negligible for both coefficients, less than 1% and 3% for the lift and drag coefficients respectively, suggesting that the choice 237 x 97 provides an adequately resolved grid.

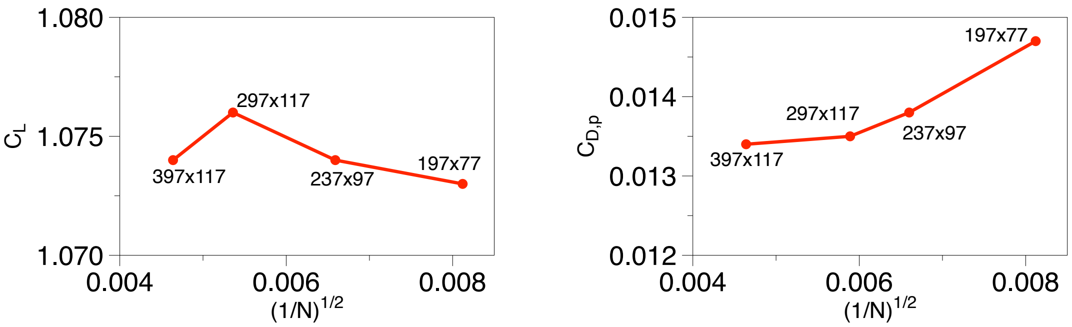

FIGURE 7.21: Static computations on a 25c farfield extent baseline grid using the SST closure for the NACA0015 airfoil with $M_\infty = 0.1235$ and $Re_c = 1.48 \times 10^6$ at $\alpha = 11^o$. Effect of grid resolution on (a) the lift coefficient and (b) the pressure-part of the drag coefficient.

Based on a grid-convergence analysis, we have adopted a 237x97 baseline grid with a 25c far-field extent for all NACA0015 pitching cases considered. The details of the various parameters for each case are shown in Table 7.5, where k is the reduced frequency, ω is the angular velocity of the pitching. For all cases considered, the freestream Mach number M_∞ equals to 0.1235.

Case	Mean (^{o}/rad)	Amplitude (^{o}/rad)	Osc.Freq (Hz)	ω (rad/s)	Re (10^6)	k
1	0 /0.0000	5.4 /0.0942	0.488	3.06619	1.49	0.02
2	3 /0.0524	8 /0.1396	0.612	3.84531	1.48	0.026
3	4 /0.0698	8 /0.1396	0.245	1.53938	1.48	0.01

TABLE 7.4: Details regarding the various parameters used for the pitching computations as described in Green and Giuni [89].

7.5.2 Case 1.

We first consider the case where the NACA0015 airfoil undergoes pitching motions about the quarter chord ($c/4$), described by

$$\begin{aligned} \alpha &= 0.0 + 5.4\sin(\omega t), \quad k = 0.02\,, \\ k &= \frac{\omega c}{2U_\infty}\,, \end{aligned} \tag{7.11}$$

where U_∞ is the far-field air speed and t is the actual computational time. We consider the case with $Re_c = 1.49 \times 10^6$, with a mean angle of 0° and a pitch oscillation amplitude

$\Delta\alpha = 5.4^o$. In all cases, we have run the simulation for almost 3 periods T, where $T = \frac{2\pi}{\omega}$, allowing the airfoil to settle into a periodic state (closed loop). In order to ensure that our results are time-converged, we have first performed a time convergence analysis using the SST closure. Fig. 7.22 illustrates that 250 sub-iterations per time step are adequate to obtain fully time converged solutions. We have adopted this number of sub-iterations for the ASBM run as well (currently without any further investigation).

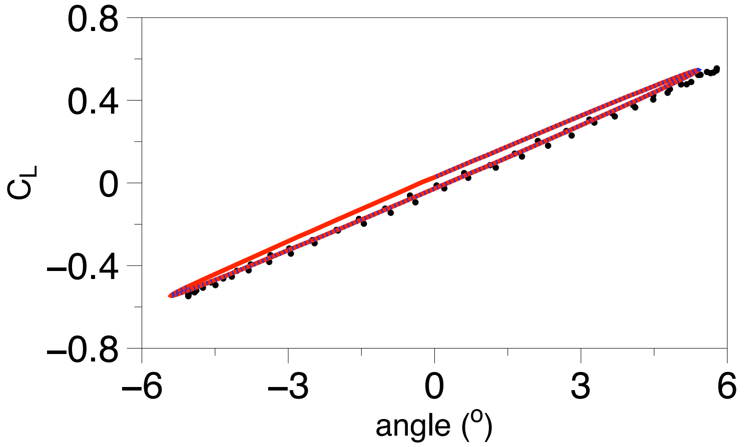

FIGURE 7.22: SST predictions for the evolution of the lift coefficient C_L when 250 sub-iterations (solid lines) and 350 sub-iterations (dashed lines) per time step are chosen for pitching computations over NACA 0015 airfoil on a 237×97 baseline grid with $M_\infty = 0.1235$, $Re_c = 1.49 \times 10^6$ and $k = 0.02$. Comparison is made to experiments of Green and Giuni [89], shown as symbols.

Fig. 7.23a shows model predictions and experimental results for the lift coefficient. The ASBM-SST closure tends to increase the width of the pitching loop by over-predicting the separation in C_L during the upswing and downswing motions. The ASBM-SST also tends to overpredict the level of C_L relative to experiments near the positive extremum of the pitching angles and to underpredict it near the negative extremum. SST seems to provide better agreement with the experiments relative to ASBM-SST. In the case of the drag coefficient (fig. 7.23b), ASBM-SST provides improved predictions for pitching angles below approximately 3°, while SST predictions are closer to the experiments than ASBM-SST for angles above 3°. Both closures miss the peak in $C_{D,p}$ near the positive extremum of the pitching motion.

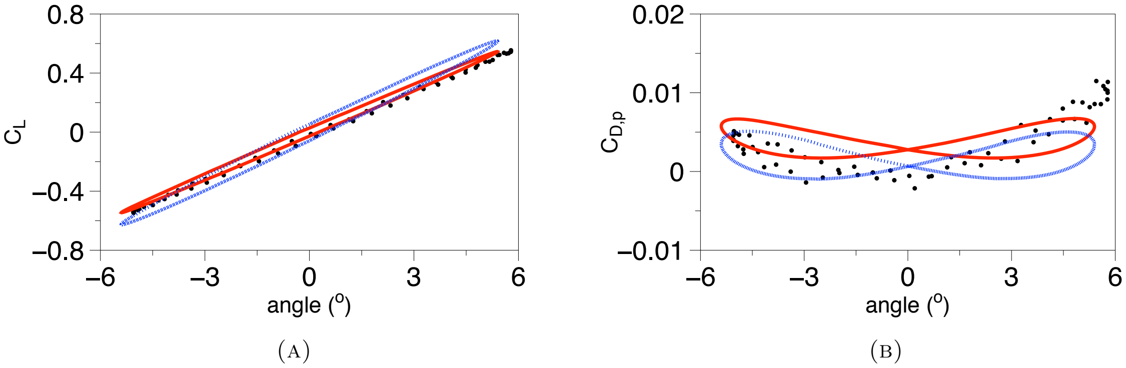

Figure 7.23: Pitching computations for the NACA 0015 airfoil with $M_\infty = 0.1235$, $Re_c = 1.49 \times 10^6$ and $k = 0.02$ for (a) the lift coefficient C_L and (b) the pressure part of the drag coefficient $C_{D,p}$, as a function of the angle of attack using ASBM-SST (dashed blue line) and SST (solid red line) closures. Comparison is made to the experiments of Green and Giuni [89], shown as symbols.

7.5.3 Case 2.

Next,we consider a case where the NACA 0015 airfoil undergoes pitching motions about the quarter chord ($c/4$), described by

$$\begin{aligned} \alpha &= 3.0 + 8.0\sin(\omega t), \quad k = 0.026\,, \\ k &= \frac{\omega c}{2U_\infty}\,. \end{aligned} \tag{7.12}$$

Fig 7.24 shows the time convergence analysis for this case, which suggests that a number of 250 sub-iterations is sufficient to obtain fully time-converged results.

Fig. 7.25a shows the comparison of the SST and ASBM-SST predictions for the lift coefficient in this case. Again the SST captures more accurately the profile of the pitching loop over the entire angle of attack range. As before, ASBM-SST tends to increase the separation between the C_L magnitudes during the upswing and downswing motions and to overpredict the magnitude of C_L near the positive extremum of the cycle. This increase becomes more profound as we move towards higher angles, closer to the dynamic stall. As shown in Fig. 7.25b, the SST predictions are also in better agreement with the experiments than the ASBM-SST predictions for the drag coefficient in the positive angle region, while ASBM-SST provides more accurate results in the negative range.

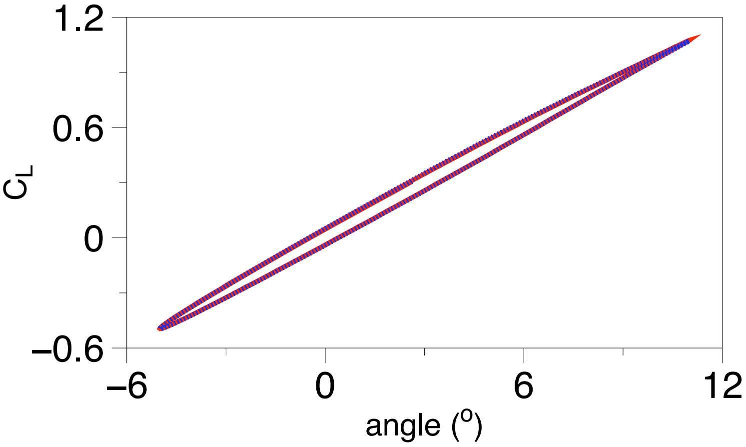

FIGURE 7.24: Pitching computations for the NACA 0015 airfoil on a 237 × 97 baseline grid using the SST closure with $M_\infty = 0.1235$, $Re_c = 1.48 \times 10^6$ and $k = 0.026$. Effect of number of sub-iterations per time step on the evolution of the lift coefficient C_L: 250 sub-iterations (solid lines) and 350 sub-iterations (dashed lines) per time step.

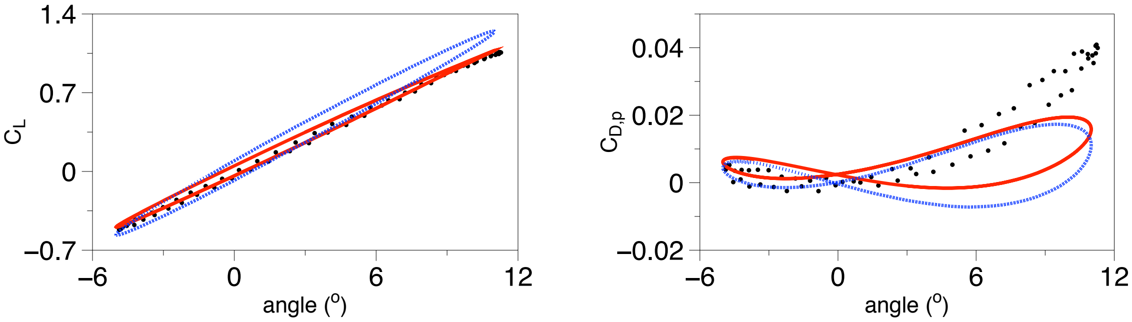

(A)

(B)

FIGURE 7.25: Pitching computations for the NACA 0015 airfoil with $M_\infty = 0.1235$, $Re_c = 1.48 \times 10^6$ and $k = 0.026$ for (a) the lift coefficient C_L and (b) the pressure part of the drag coefficient $C_{D,p}$, as a function of the angle of attack using ASBM-SST (dashed line) and SST (solid line) closures. Comparison is made to the experiments of Green and Giuni [89], shown as symbols.

7.5.4 Case 3

In the last NACA0015 case considered, the evolution of the angle of attack is described by

$$\begin{aligned} \alpha &= 4.0 + 8.0\sin(\omega t), \quad k = 0.01\,, \\ k &= \frac{\omega c}{2U_\infty}\,. \end{aligned} \tag{7.13}$$

Fig. 7.26a shows again the tendency of ASBM-SST to over-estimate the lift magnitude over most of the angle-of-attack range and particularly in the positive extremum. In the case of the drag coefficient $C_{D,p}$ ASBM-SST again provides better estimates than SST for negative angles. For positive angles, both closures under-predict $C_{D,p}$ relative to the experiments, but during the airfoil downswing phase of the pitching motion, the under-prediction by ASBM-SST is more pronounced.

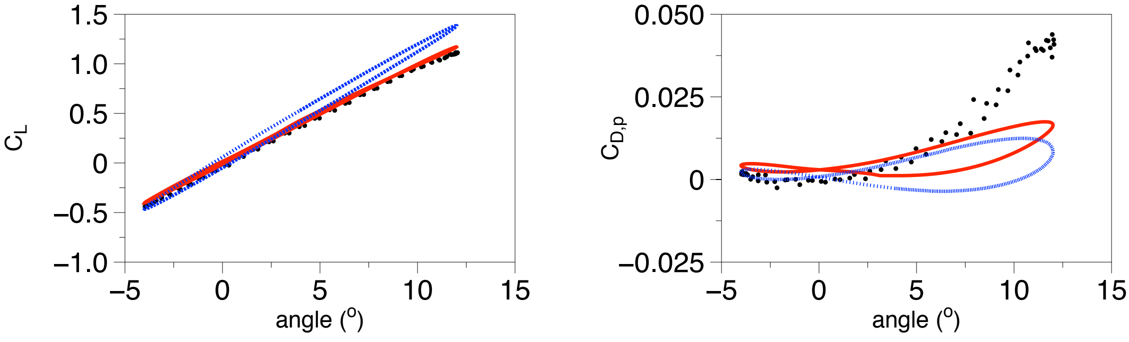

(A)

(B)

FIGURE 7.26: Pitching computations for the NACA 0015 airfoil with $M_\infty = 0.1235$, $Re_c = 1.48 \times 10^6$ and $k = 0.01$ for (a) the lift coefficient C_L and (b) the pressure part of the drag coefficient $C_{D,p}$, as a function of the angle of attack using ASBM-SST (dashed line) and SST (solid line) closures. Comparison is made to the experiments of Green and Giuni [89], shown as symbols.

7.6 Pitching Runs for VR7

Next, we proceed to examine the performance of the ASBM-SST closure for turbulent flow over a VR7 airfoil undergoing pitching motions, for which experimental data is available[84]. In order to reduce the factors that potentially affect the numerical stability of our computations, we have chosen two cases for which the reduced frequency k is similar to the ones adopted for the NACA cases. In contrast to the previous runs, the range of the angle of attack extends above the stalling angle, thus strong hysteresis effects are expected, making the study of these two cases a more interesting task. Also, we note that the maximum thickness of the VR7 airfoil is 11.4% of the chord length c, which is lower than the corresponding parameter for the NACA0015 (15%).

First, we have performed unsteady computations at a fixed angle $\alpha = 11^o$ with $M_\infty = 0.30$ and $Re_c = 4.25 \times 10^6$ in order to ensure that our results are grid-independent. Four different grids were considered, starting from the coarsest grid which contained $197 \times 77 \times 1$ grid nodes and moving towards the finest grid which contained $397 \times 117 \times 1$ nodes. Fig. 7.27 shows SST predictions for the integrated coefficients $\{C_L, C_{D,p}\}$ as a function of the number of nodes.

Based on these results, we have chosen 297 × 97 × 1 as the baseline grid for the pitching computations.

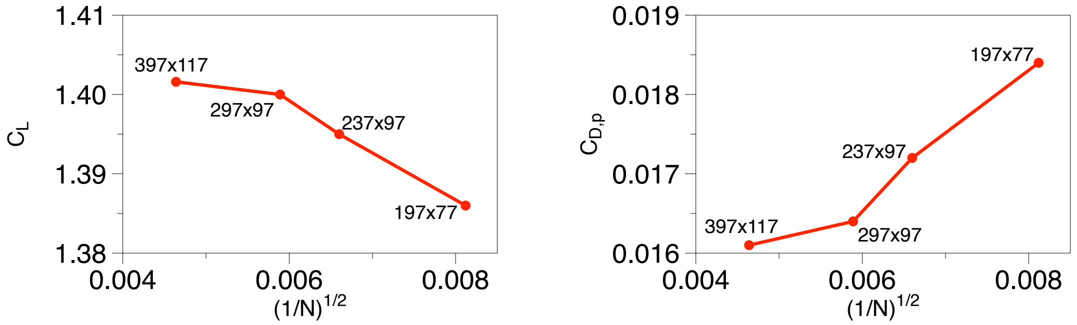

FIGURE 7.27: Computations on a 25c farfield extent baseline grid using the SST closure for the VR7 airfoil with $M_\infty = 0.30$ and $Re_c = 4.25 \times 10^6$ at $\alpha = 11^o$. Effect of grid resolution on (a) lift coefficient and (b) pressure-part of the drag coefficient.

Table 7.5 gives details for the parameters as they were imposed during the subsequent simulations.

Case	Mean (^{o}/rad)	Amplitude (^{o}/rad)	Osc.Freq (Hz)	ω (rad/s)	Re (10^6)	k
1	4.1 /0.07156	10 /0.1745	1.3307	8.3612	4.25	0.025
2	4.1 /0.07156	10 /0.1745	2.6614	16.722	4.25	0.050

TABLE 7.5: Details regarding the various parameters used for the pitching computations as described in McCroskey et al [84].

7.6.1 Case 1

The evolution of the angle of attack is described by

$$\begin{aligned} &\alpha = 4.1 + 10.0\sin(\omega t), \quad k = 0.025\,, \\ &k = \frac{\omega c}{2U_\infty}\,. \end{aligned} \tag{7.14}$$

Fig. 7.28 shows SST and ASBM-SST predictions for the lift and drag coefficients. At low angles of attack ($\alpha < 7$), both closures produce similar results. As the stalling angle is approached and the hysteresis effects become significant, SST predictions are in better agreement with the experiments than the ASBM-SST ones. The ASBM-SST closure tends to shift the cross over of the C_L loop towards higher angles, while it under-predicts the magnitude of the drag coefficient $C_{D,p}$ during the downwash motion.

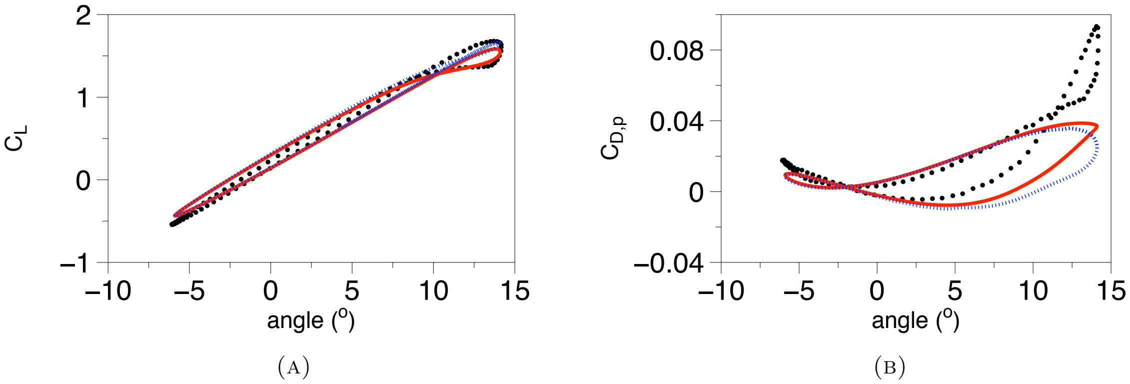

(A) (B)

FIGURE 7.28: Pitching computations for the VR7 airfoil with $M_\infty = 0.30$, $Re_c = 4.25 \times 10^6$ and $k = 0.025$ for (a) the lift coefficient C_L and (b) the pressure part of the drag coefficient $C_{D,p}$, as a function of the angle of attack using ASBM-SST (dashed line) and SST (solid line) closures. Comparison is made to the experiments of McCroskey et al.[84], shown as symbols.

7.6.2 Case 2

The angle of attack is evolved according to the following expression

$$\begin{aligned} \alpha &= 4.1 + 10.0\sin(\omega t), \quad k = 0.05\,, \\ k &= \frac{\omega c}{2U_\infty}\,. \end{aligned} \tag{7.15}$$

Fig. 7.29 shows again the tendency of the ASBM-SST closure to delay the appearance of the crossover in the lift coefficient C_L values till more positive angles of attack and to underestimate the pressure part of the drag coefficient during the downswing of the airfoil motion. These consistent behaviour points to the need to understand better the response of the ASBM-SST closure to hysteresis effects, since at angles far from the stalling angle, both closures provide comparable results.

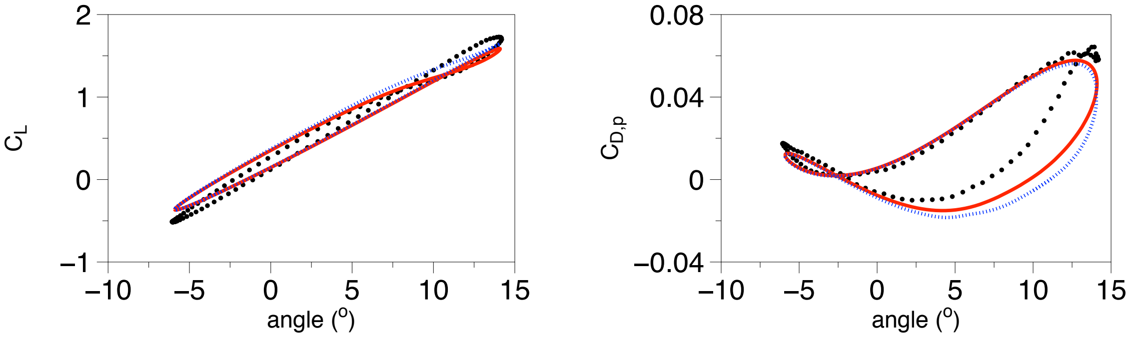

(A)

(B)

FIGURE 7.29: Pitching computations for the VR7 airfoil with $M_\infty = 0.30$, $Re_c = 4.25 \times 10^6$ and $k = 0.050$ for (a) the lift coefficient C_L and (b) the pressure part of the drag coefficient $C_{D,p}$, as a function of the angle of attack using ASBM-SST (dashed line) and SST (solid line) closures. Comparison is made to the experiments of McCroskey et al. [84], shown as symbols.

7.7 Conclusions

We have performed both static and dynamic computations for a number of different freestream parameters. For the static cases, we have been able, for the first time, to obtain full ASBM solutions, from 0^o up to 20^o for the NACA-0015 cases and from 0^o up to 15^o for the VR-7 cases, achieving 2-3 orders of magnitude reductions in the L2 norm of the mean and turbulent variables. For all the static cases considered, ASBM augmented the lift coefficient magnitude towards the experimental values. The ASBM also predicts a delay on the onset of stall onset till higher angles of attack, which is in better agreement with the experimental results. Thus, overall the ASBM predictions are providing better agreement with the experimental results when compared to the results obtained with SST closure. These results have been verified to be fully converged and free of boundary effects through a series of grid and far-field boundary extent convergence analyses.

Regarding the dynamic cases, we have been able for the first time to to obtain full ASBM solutions for all cases, achieving 2-3 orders of magnitude reductions in the L2 norm of the mean and turbulent variables. Zonal separation was necessary only for the pitching computations where VR-7 airfoil was used. We have performed a total of five different pitching computations, three for the symmetric NACA0015 airfoil and two for the VR7 airfoil. Comparable values for the freestream parameters were used in both sets of computations. In all the cases considered, SST provided better agreement than ASBM-SST to the experimental values for the lift coefficient, due to the tendency of ASBM to overpredict the lift coefficient magnitude. The ASBM-SST closure decreases the drag coefficient magnitude achieving better agreement with experimental data for negative values of the angle of attack. For positive angles of attack near the dynamic stall, ASBM-SST experiences more intensively the hysteresis effect compared to SST, yielding a faster decrease of the drag coefficient than it should. As was done for the static case, we ensured that these results are fully converged and free of boundary effects through a series of grid and far-field boundary extent convergence analyses.

We are currently exploring ways to obtain full ASBM solutions without resorting to zonal-separation for the case of pitching airfoils. We also plan to focus on understanding why the ASBM-SST closure seems to magnify unrealistically the hysteresis effect near the positive extremum of the pitching cycle, despite the fact that ASBM-SST was found to perform better than SST during dynamic stall without pitching.

Chapter 8

Conclusions.

8.1 Structure-based model for passive scalar transport.

At the conclusion of this thesis, we have managed to develope, for the first time, a structure-based model which accounts for the statistics of a passive-scalar field. In order to achieve that, we have derived a set of transport equations using the triple-decomposition scheme. After performing a term by term modelling based on physical considerations, we evaluated the model so that it matches asymptotic rates for simple decaying cases. The model is constructed so that it is sensitive to the choice of low-wave spectrum.

The performance of the model was tested in a large number of cases, exhibiting encouraging results. The model responds adequately in the presence of frame rotation effects for homogeneous shear turbulence in the presence of mean passive scalar gradient. Also, the model provided good predictions for one irrotational case, particularly that of an Axisymmetric Contraction for which experimental data was availiable for comparison.

Motivated by the success of the proposed structure based model for passive scalar transport, we have set a number of objectives for the near future. Currently, a transport model for the passive scalar dissipation rate is being developed, stemming directly from the large-scale model equations. This modeled equation will accompany the passive scalar variance equation. In addition, we are exploring the potential of using ASBM instead of the extended IPRM model for the estimation of the structure tensors and their products. However, in order to achieve closure in this case, an algebraic expression for the scalar-flux is needed, suitable for rotating frames. Thus, we are in a process of extending the explicit scalar-flux model of Younis as described in [56] to account for frame-rotation effects.

Also, we work intensively towards the extension of the proposed model to stably-stratified flows. This effort requires the inclusion of additional terms in the IPRM conditional expressions for the Reynolds stress and the modeling of the buoyancy-related terms that appear in the transport equations for the turbulent kinetic energy κ and large-scale enstrophy $\tilde{\omega}^2$. The model parameters related to the additional terms were evaluated so that the model matches the correct decay rates for the simple case of decaying buoyancy-generated turbulence at high Re and Pe numbers.

The extended model is currently validated in a number of stably-stratified flows for Richardson number ranging from zero to unity, showing very promising results. Moreover, the model is shown to be sensitive on the relative angle between the mean velocity gradient and the mean passive scalar gradient, for angles ranging from 0^o (parallel) up to 90^o (perpendicular).

8.2 Coupling of the ASBM with EVMs.

We have accumulated a significant understanding about the behaviour, strengths and weaknesses of ASBM for applications in aerodynamics. Our own assessment is that ASBM remains a promising contestant for adoption in aerodynamics, but we have also identified a few important weaknesses that must be addressed if the model is to achieve its full potential. We also believe that the experience with ASBM provides sufficient grounds for optimism with regards to the potential of other classes of Structure-Based Models, such as the Interacting Particle Representation Model (IPRM). These issues are analysed in greater detail below in a discussion organized along the two main tracks of work carried out over the last four years, namely the the ASBM-SA and ASBM-SST closures.

8.2.1 ASBM-SA hybrid model

8.2.1.1 Main Accomplishments:

- We have managed to couple, for the first time, the ASBM closure with one-equation Eddy Viscosity Models (EVM), most notably the Spallart-Allamaras (SA) model. We have used suitable algebraic expressions for the extraction of the turbulence scales, as described in Rahmnan et al. [59, 81].

- Successful validation of the performance of the ASBM-SA model over a wider range of test cases than what had been accomplished with previous couplings (e.g. with v^2-f and Menter's κ-ω.). Overall, ASBM-SA obtained good predictions for the turbulent correlations (intensities, shear stress) for all test cases.

- With ASBM-SA we have achieved superior numerical stability compared to previous couplings, while also achieving good convergence rate. Additionally, the improved numerical stability leads to the elimination of artificial spurious strikes occurring in the recirculation regions of strongly separated flows (such as smooth hills) when other couplings are used (such as v^2-f).

8.2.1.2 Weaknesses-Limitations:

- Overestimation of the size of the recirculation region in separated flows, as already observed in all previous ASBM couplings.
- Numerically unstable for certain 3D flows (e.g. square duct flow), a weakness which we believe is related to the physical content of the ASBM model.
- Unrealizable shear-stress predictions at the top of smooth hills. We believe this deficiency is related to the physical content of the ASBM closure. In particular, we believe that the RDT state map needs to be revised or completely replaced with an improved scheme.
- Use of a filtering/smoothing scheme, needed to improve the stability of the model, significantly influences the wall-shear stress profile (e.g. on NASA hump case). The current schemes are constructed for uniform grids, however more advanced schemes should be developed for the cases where highly stretched grids are present, such as in complex flows (e.g. separated flows). Currently, we believe that this deficiency is partly responsible for the overestimation of the recirculation bubble.

8.2.2 ASBM-SST hybrid model

8.2.2.1 Main Accomplishments:

- A series of static computations for a wide range of angle of attacks and freestream parameters were performed in order to ascertain the performance of the ASBM-SST hybrid model, for a flow over two types of airfoils, NACA0015 and VR7.
- In order to obtain smooth, fully converged solutions, we developed advanced filtering schemes suitable for both 2D and 3D highly stretched grids. Currently, these schemes are suitable for structured-grids, however efforts are focused on extending them on unstructured grids.
- For the VR7 computations, additional stability techniques were developed, needed to obtain converged solutions, such as zonal separation and blending methods.

- We successfully performed, for the first time, computations for a flow over an airfoil undergoing pitching motions. Initially we considered three different cases of pitching computations over a NACA0015 airfoil, for which the ranges of angle of attacks were chosen to be below the stall angle. Neither zonal separation nor blending approach were used. Next, two different cases of pitching computations over a VR7 airfoil were considered, for which the same angle of attack was chosen. This time, the range of angle of attacks included the stall angle, but computations utilised the stability techniques mentioned above.
- For all static computations, ASBM-SST provided improved predictions for the lift and pressure coefficient respectively.

8.2.2.2 Weaknesses-Limitations:

- In all pitching computations, ASBM-SST showed a strong tendency to overestimate the lift coefficient around the stall angle, yielding a faster decrease of the drag coefficient than it should. We believe that this deficiency is somehow related to the existence of hysteresis effects, thus further analysis of the impact these effects have on ASBM-SST is needed.
- In the case of the VR7 computation with pitching, resorting to zonal separation remains necessary, something we deem to be undesirable. As part of future work we will seek ways to improve the numerical stability of the ASBM-SST closure in order overcome the need to use of this technique.
- We believe that modifications on the fundamental formulation of the ASBM closure are required in order to improve the ability of the closure to capture complex effects such as the ones encountered in pitching motions.

Appendix A

Details on the large-scale passive scalar model.

A.1 The complete IPRM model for passive scalar transport

The evolution equation for the normal vector n_i and the conditional Reynolds stress are given by

$$\frac{dn_i}{dt} = -G_{ki}n_k + G_{km}n_k n_m n_i \,, \tag{A.1}$$

and

$$\begin{aligned}\frac{dR^{|n}_{ij}}{dt} =& -(G^v_{ik} + 2\Omega^f_{ik})R^{|n}_{kj} - (G^v_{jk} + 2\Omega^f_{jk})R^{|n}_{ki} + (G^v_{km} + G^n_{km} + 2\Omega^f_{km})\times \\ & (R^{|n}_{im}n_k n_j + R^{|n}_{jm}n_k n_i) - \left[2C_1 R^{|n}_{ij} - C_2^2 R^{|n}_{qq}(\delta_{ij} - n_i n_j)\right].\end{aligned} \tag{A.2}$$

Regarding the evolution of the passive scalar field, the conditional expressions for the passive scalar variance and the scalar-flux vector are given by

$$\frac{d}{dt}\left(\frac{\Phi^{2|n}}{2}\right) = -Q^{|n}_i \Lambda_i - A_{ij}R^{|n}_{ij} \,, \tag{A.3}$$

and

$$\frac{d}{dt}Q_i^{|n} = -R_{ij}^{|n}\Lambda_j^{\phi} - (G_{ik}^{v} + 2\Omega_{ik}^{f})Q_k^{|n} - C_1 Q_i^{|n} + (G_{mk}^{v} + G_{mk}^{n} + 2\Omega_{mk}^{f})Q_k^{|n} n_m n_i \, , \tag{A.4}$$

where the effective gradients are given by

$$G_{ij}^{n} = G_{ij} + \frac{C_n}{\tau} r_{ik} d_{kj} \, , \quad G_{ij}^{v} = G_{ij} + \frac{C_v}{\tau} r_{ik} d_{kj} \, , \tag{A.5}$$

and

$$\Lambda_i^{\phi} = \Lambda_i + \frac{C_v \langle V_q \Phi \rangle}{\tau_\phi \langle V^2 \rangle} r_{is} d_{sq} \, , \qquad A_{ij} = \frac{C_v \langle \Phi^2 \rangle}{\tau_\phi \langle V^2 \rangle} r_{is} d_{sj} \, , \tag{A.6}$$

with $C_n = 2.2\, C_v = 2.2$. The turbulence and scalar time scales are given by

$$\tau = \frac{C_v \langle V^2 \rangle}{\epsilon} r_{is} d_{sm} r_{mi} \, , \quad \tau_\phi = C_v \frac{\langle \Phi^2 \rangle}{\epsilon_\phi} r_{ij} r_{is} d_{sj} \, . \tag{A.7}$$

The turbulent kinetic energy and scalar dissipation rates are determined by the algebraic models

$$\epsilon = F_\epsilon \kappa \tilde{\omega} + \nu \tilde{\omega}^2 \, , \qquad \epsilon_\phi = F_\phi \lambda \tilde{\omega} + \gamma \tilde{a}^2 \, , \tag{A.8}$$

with the model parameters F_ϵ and F_ϕ determined by

$$F_\epsilon = C_\epsilon \chi \, , \qquad \chi = 3 f_{ij} d_{ji} \, , \tag{A.9}$$

$$F_\phi = C_\epsilon \chi^{\phi} \, , \qquad \chi^{\phi} = 9 r_{iq} d_{qj}^{s} r_{ji} \, , \tag{A.10}$$

along with the set of scale evolutions equations of the ELSE model,

$$\frac{d\kappa}{dt} = -(2\kappa) r_{ij} S_{ji} - [F_\epsilon \kappa \tilde{\omega} + \nu \tilde{\omega}^2] \, , \tag{A.11a}$$

$$\frac{d\tilde{\omega}}{dt} = \tilde{\omega} f_{ij} S_{ji} - [C_{\tilde{\omega}^2_T} - \phi C_{\tilde{\omega}^2_P}]\tilde{\omega}^2 - \nu C_{\tilde{\omega}^2_\nu} \frac{\tilde{\omega}^3}{\kappa} \, , \tag{A.11b}$$

$$\frac{d\lambda}{dt} = -\overline{u_i' \phi'} \Lambda_i - [\gamma \tilde{a}^2 + F_\phi \lambda \tilde{\omega}], \tag{A.11c}$$

$$\frac{d\tilde{a}}{dt} = -C_{\tilde{a}^2_\gamma} \gamma \frac{\tilde{a}^3}{\lambda} - d_{mj}^{s} S_{jm} \tilde{a} - [C_{\tilde{\omega}^2_T} - \phi^{\phi} C_{\tilde{\omega}^2_P}]\tilde{a}\tilde{\omega} + [C_{\tilde{\omega}^2_T} - \phi^{\phi} C_{\tilde{\omega}^2_P}]\Lambda\tilde{\omega} \, . \tag{A.11d}$$

All model constants are summarised in Tables 3.1 and 3.2.

A.2 Analogy between f_{ij} and d^s_{ij}

We seek to show the connection between the scalar-variance and the mean-squared-magnitude scalar gradient with the scalar dimensionality tensor d^s_{ij}. The Fourier Representation of the dimensionality tensor is

$$D^s_{ij} = (\frac{L}{2\pi})^3 \int \frac{k_i k_j}{k^2} \langle \hat{\phi}\hat{\phi}^* \rangle d^3\mathbf{k} = \int \frac{k_i k_j}{k^2} E_\phi(\mathbf{k}) d^3\mathbf{k} \,. \tag{A.12}$$

Also, the Fourier representations of ϕ' and a'_w are

$$\phi' = \sum_k \hat{\phi} e^{-ik_m x_m} \,, \quad a'_w = \sum_k \hat{G}_w e^{-ik_m x_m} \,, \tag{A.13a}$$

$$a'_w = \phi'_{,w} = \sum_k -ik_w \hat{\phi} e^{-ik_m x_m} \,, \tag{A.13b}$$

$$\Rightarrow \hat{G}_w = -ik_w \hat{\phi} \,. \tag{A.13c}$$

Based on eq. (A.13) we can express $\langle a'_i a'_j \rangle$ as

$$\langle a'_i a'_j \rangle = \sum_k \sum_{k'} \langle \hat{G}_i(\mathbf{k}) \hat{G}_j(\mathbf{k}') \rangle e^{-i(k_m x_m + k'_m x'_m)} \,, \tag{A.14}$$

where here $\langle . \rangle$ denotes ensemble averaging. Since we consider one-point statistics, we set $x_m = x'_m$. Also, we define a new wave-number vector $k'' = -k'$. In order for a_i to be a real variable, $\hat{G}_q(\mathbf{k}') = \hat{G}_q(-\mathbf{k}'') = \hat{G}^*_q(\mathbf{k}'')$. Substituting back into eq. (A.14) leads

$$\langle a'_i a'_j \rangle = \sum_k \sum_{k''} \langle \hat{G}_i(\mathbf{k}) \hat{G}^*_j(\mathbf{k}'') \rangle e^{-i(k_m - k''_m) x_m} \,. \tag{A.15}$$

Next, we take into account the orthogonality condition

$$\frac{1}{L^3} \int e^{-i(k_m - k''_m) x_m} d\mathbf{x} = \delta(\mathbf{k} - \mathbf{k}'') \,. \tag{A.16}$$

Applying three dimensional spatial averaging on eq. (A.14) and using the orthogonality condition gives

$$\overline{\langle a_i' a_j' \rangle} = \sum_k \langle \hat{G}_i(\mathbf{k}) \hat{G}_j^*(\mathbf{k}) \rangle \,. \tag{A.17}$$

We set $\Delta k_i = \frac{2\pi}{L_i}$ and assume isotropic conditions, ($L_x = L_y = L_z = L$) so that eq. (A.17) becomes

$$\overline{\langle a_i' a_j' \rangle} = \sum_k \langle \hat{G}_i(\mathbf{k}) \hat{G}_j^*(\mathbf{k}) \rangle (\frac{L}{2\pi})^3 \Delta k_1 \Delta k_2 \Delta k_3 \,. \tag{A.18}$$

Based on eq. (A.18) we define the scalar gradient co-spectrum as

$$\tilde{Q}_{ij} = (\frac{L}{2\pi})^3 \langle \hat{G}_i(\mathbf{k}) \hat{G}_j^*(\mathbf{k}) \rangle \,. \tag{A.19}$$

For $\Delta k_i \to \infty$ the scalar gradient spectrum is defined through the expression

$$\hat{Q}_{ij} = \lim_{L \to \infty} \tilde{Q}_{ij} \,, \tag{A.20}$$

thus eq. (A.18) becomes

$$\overline{\langle a_i' a_j' \rangle} = \int \hat{Q}_{ij} d^3\mathbf{k} \,. \tag{A.21}$$

Next we relate $\tilde{Q}_{ij}$ with the scalar dimensionality tensor d_{ij}^s, through the identity

$$\frac{\tilde{Q}_{ij}}{k^2} = (\frac{L}{2\pi})^3 \left\langle \frac{(k_i \phi)(k_j \phi)^*}{k^2} \right\rangle = (\frac{L}{2\pi})^3 \frac{k_i k_j}{k^2} \langle \hat{\phi} \hat{\phi}^* \rangle \,. \tag{A.22}$$

We define the passive scalar-spectrum as

$$E_\phi(\mathbf{k}) = (\frac{L}{2\pi})^3 \langle \hat{\phi}(\mathbf{k}) \hat{\phi}^*(\mathbf{k}) \rangle \,, \tag{A.23}$$

at the limit $L \to \infty$, which yields the following expression

$$\frac{\hat{Q}_{ij}(\mathbf{k})}{k^2} = \frac{k_i k_j}{k^2} E_\phi(\mathbf{k}) \,. \tag{A.24}$$

Thus the scalar dimensionality tensor can be expressed as

$$D_{ij}^s = \int \frac{k_i k_j}{k^2} E_\phi(\mathbf{k}) d^3\mathbf{k} = \int \frac{\hat{Q}_{ij}}{k^2} d^3\mathbf{k} \,. \tag{A.25}$$

A.3 Dimensional analysis

The energy and passive scalar spectra $E_\kappa(k,t)$ and $E_\phi(k,t)$ respectively, can be expressed as a series of Taylor coefficients. Since large scale eddies contain most of the passive scalar or kinetic energy, the expansion is taken around $k = 0$, such as

$$\begin{aligned} E_\kappa(k,t) &= 2\pi k^2 (B_o + B_2 k^2 + ...)\,, \\ E_\phi(k,t) &= 2\pi k^2 (C_o + C_2 k^2 + ...)\,, \end{aligned} \tag{A.26}$$

from which the kinetic and scalar energy fields can be deduced by three-dimensional integration in the wave-space. Near $k = 0$, higher order terms can be neglected. If $B_o = 0$, only B_2 remains as the leading coefficient [90], whereas if $B_2 = 0$ and $B_o \neq 0$ [91], B_o drives the evolution of the flow. Using dimensional analysis, we find that

$$B_o \propto t^{-2} L^5 \,, \tag{A.27a}$$

$$B_2 \propto t^{-2} L^7 \,, \tag{A.27b}$$

$$C_o \propto \overline{\phi'^2} L^3 \,, \tag{A.27c}$$

$$C_2 \propto \overline{\phi'^2} L^5 \,, \tag{A.27d}$$

where L is a characteristic length scale.

High Reynolds and Peclet numbers

At high Reynolds and Peclet numbers, diffusion terms do not have major impact on the evolution of the fields, which are determined through nonlinear interactions. For $\{C_o, B_o\}$ leading coefficients, it can be shown to be invariants, so that the dimensional analysis results in

$$
\begin{aligned}
&\kappa \propto B_o^{\alpha} t^{\beta} \propto (t^{-2}L^5)^{\alpha} t^{\beta} = L^2 t^{-2}\\
\Rightarrow &\kappa \propto B_o^{2/5} t^{-6/5}\,,\\
&\overline{\phi'^2} \propto C_o B_o^{\alpha} t^{\beta} \propto \overline{\phi'^2} L^3 (t^{-2}L^5)^{\alpha} t^{\beta} = \overline{\phi'^2}\\
\Rightarrow &\overline{\phi'^2} \propto C_o B_o^{-3/5} t^{-6/5}\,,\\
&\overline{\omega'^2} \propto B_o^{\alpha} t^{\beta} \propto (L^5 t^{-2})^{\alpha} t^{\beta} = t^{-2}\\
\Rightarrow &\overline{\omega'^2} \propto t^{-2}\,,\\
&\overline{a'^2} \propto C_o B_o^{\alpha} t^{\beta} \propto \overline{\phi'^2} L^3 [L^5 t^{-2}]^{\alpha} t^{\beta} \propto \overline{\phi'^2} L^{-2}\,,\\
\Rightarrow &\overline{a'^2} \propto C_o B_o^{-1} t^{-2}\,,\\
\Rightarrow &\epsilon \propto \frac{d\kappa}{dt} \propto B_o^{2/5} t^{-11/5}\,,\\
\Rightarrow &\epsilon_{\phi} \propto \frac{d\overline{\phi'^2}}{dt} \propto C_o B_o^{-3/5} t^{-11/5}\,.
\end{aligned}
\tag{A.28}
$$

For zero $\{B_o, C_o\}$ and nonzero $\{B_2, C_2\}$, there are no longer strictly invariant quantities. Even so, making the assumption that $\{B_2, C_2\}$ vary slowly compared to the energy and scalar variance respectively, approximate expressions can be derived. The resulted similarity expressions are shown below

$$
\begin{aligned}
&\kappa \propto B_2^{\alpha} t^{\beta} \propto (t^{-2}L^7)^{\alpha} t^{\beta} = L^2 t^{-2}\\
\Rightarrow &\kappa \propto B_2^{2/7} t^{-10/7}\,,\\
&\overline{\phi'^2} \propto C_2 B_2^{\alpha} t^{\beta} \propto \overline{\phi'^2} L^5 (t^{-2}L^7)^{\alpha} t^{\beta} = \overline{\phi'^2}\\
\Rightarrow &\overline{\phi'^2} \propto C_2 B_2^{-5/7} t^{-10/7}\,,\\
&\overline{\omega'^2} \propto B_2^{\alpha} t^{\beta} \propto (L^7 t^{-2})^{\alpha} t^{\beta} = t^{-2}\\
\Rightarrow &\overline{\omega'^2} \propto t^{-2}\,,\\
&\overline{a'^2} \propto C_2 B_2^{\alpha} t^{\beta} \propto \overline{\phi'^2} L^5 [L^7 t^{-2}]^{\alpha} t^{\beta} \propto \overline{\phi'^2} L^{-2}\\
\Rightarrow &\overline{a'^2} \propto C_2 B_2^{-1} t^{-2}\,,\\
\Rightarrow &\epsilon \propto \frac{d\kappa}{dt} \propto B_2^{2/7} t^{-17/7}\,,\\
\Rightarrow &\epsilon_{\phi} \propto \frac{d\overline{\phi'^2}}{dt} \propto C_2 B_2^{-5/7} t^{-17/7}\,.
\end{aligned}
\tag{A.29}
$$

In the case of decaying turbulence in presence of a mean scalar gradient β, the leading coefficients of the passive scalar spectrum $\{C_o, C_2\}$ become functions of time which depend on the energy spectrum, defined as

$$C_o(t) \propto \beta^2 B_o t^2 \,, \tag{A.30a}$$

$$C_2(t) \propto \beta^2 B_2 t^2 \,. \tag{A.30b}$$

For $\{C_o, B_o\}$ leading coefficients, the dimensional analysis results in

$$\begin{aligned} &\overline{\phi'^2} \propto C_o B_o^{\alpha} t^{\beta} \propto \beta^2 t^2 [t^{-2} L^5]^{1+\alpha} t^{\beta} = \overline{\phi'^2} \\ \Rightarrow &\overline{\phi'^2} \propto C_o B_o^{-3/5} t^{-6/5} = \beta^2 B_o^{2/5} t^{4/5} \,, \\ &\overline{a'^2} \propto C_o B_o^{\alpha} t^{\beta} \propto \beta^2 t^2 [t^{-2} L^5]^{1+\alpha} t^{\beta} = \overline{\phi'^2} L^{-2} \\ \Rightarrow &\overline{a'^2} \propto C_o B_o^{-1} t^{-2} = \beta^2 \,. \end{aligned} \tag{A.31}$$

Respectively, when $\{C_2, B_2\}$ are the leading coefficients, dimensional analysis yields

$$\begin{aligned} &\overline{\phi'^2} \propto C_2 B_2^{\alpha} t^{\beta} \propto \beta^2 t^2 [t^{-2} L^7]^{1+\alpha} t^{\beta} = \overline{\phi'^2} \\ \Rightarrow &\overline{\phi'^2} \propto C_2 B_2^{-5/7} t^{-10/7} = \beta^2 B_2^{2/7} t^{4/7} \,, \\ &\overline{a'^2} \propto C_2 B_2^{\alpha} t^{\beta} \propto \beta^2 t^2 [t^{-2} L^7]^{1+\alpha} t^{\beta} = \overline{\phi'^2} L^{-2} \\ \Rightarrow &\overline{a'^2} \propto C_2 B_2^{-1} t^{-2} = \beta^2 \,. \end{aligned} \tag{A.32}$$

Low Reynolds and Peclet numbers

At low Reynolds and Peclet numbers, higher order interactions can be neglected, since the range of scales in which cascade process takes place becomes narrow. Thus, the behavior of the flow at large times depend solely on viscosity effects, and low wave-number spectrum. For $\{B_o, C_o\}$ spectra, one finds

$$\begin{aligned}
&\kappa \propto B_o\nu^\alpha t^\beta \propto (t^{-2}L^5)(L^2t^{-1})^\alpha t^\beta = L^2t^{-2} \\
\Rightarrow &\kappa \propto B_o(\nu t)^{-3/2}\,, \\
&\overline{\phi'^2} \propto C_o\gamma^\alpha t^\beta \propto \overline{\phi'^2}L^3(t^{-1}L^2)^\alpha t^\beta = \overline{\phi'^2} \\
\Rightarrow &\overline{\phi'^2} \propto C_o(\gamma t)^{-3/2}\,, \\
&\overline{\omega'^2} \propto B_o\nu^\alpha t^\beta \propto L^5t^{-2}(L^2t^{-1})^\alpha t^\beta = t^{-2} \\
\Rightarrow &\overline{\omega'^2} \propto B_o(\nu t)^{-5/2}\,, \\
&\overline{a'^2} \propto C_o\gamma^\alpha t^\beta \propto \overline{\phi'^2}L^3[L^2t^{-1}]^\alpha t^\beta \propto \overline{\phi'^2}L^{-2} \\
\Rightarrow &\overline{a'^2} \propto C_o(\gamma t)^{-5/2}\,, \\
\Rightarrow &\epsilon \propto \frac{d\kappa}{dt} \propto B_o(\nu t)^{-5/2}\,, \\
\Rightarrow &\epsilon_\phi \propto \frac{d\overline{\phi'^2}}{dt} \propto C_o(\gamma t)^{-5/2}\,,
\end{aligned} \tag{A.33}$$

whereas for $\{B_2, C_2\}$ spectra we have

$$\begin{aligned}
&\kappa \propto B_2\nu^\alpha t^\beta \propto (t^{-2}L^7)(L^2t^{-1})^\alpha t^\beta = L^2t^{-2} \\
\Rightarrow &\kappa \propto B_2(\nu t)^{-5/2}\,, \\
&\overline{\phi'^2} \propto C_2\gamma^\alpha t^\beta \propto \overline{\phi'^2}L^5(t^{-1}L^2)^\alpha t^\beta = \overline{\phi'^2}\,, \\
\Rightarrow &\overline{\phi'^2} \propto C_2(\gamma t)^{-5/2}\,, \\
&\overline{\omega'^2} \propto B_2\nu^\alpha t^\beta \propto L^7t^{-2}(L^2t^{-1})^\alpha t^\beta = t^{-2} \\
\Rightarrow &\overline{\omega'^2} \propto B_2(\nu t)^{-7/2}\,, \\
&\overline{a'^2} \propto C_2\gamma^\alpha t^\beta \propto \overline{\phi'^2}L^5[L^2t^{-1}]^\alpha t^\beta \propto \overline{\phi'^2}L^{-2} \\
\Rightarrow &\overline{a'^2} \propto C_2(\gamma t)^{-7/2}\,, \\
\Rightarrow &\epsilon \propto \frac{d\kappa}{dt} \propto B_2(\nu t)^{-7/2}\,, \\
\Rightarrow &\epsilon_\phi \propto \frac{d\overline{\phi'^2}}{dt} \propto C_2(\gamma t)^{-7/2}\,.
\end{aligned} \tag{A.34}$$

Appendix B

Preliminary work on the development of a Structure-based model for MagnetoHydroDynamic (MHD) flows.

B.1 Brief introduction

Magnetohydrodynamics deals with electrically conducting flows in the presence of magnetic fields. Those flows can be described by solving Navier-Stokes and Maxwell equations in a coupled manner. The reason for that is the existence in such flows of induced electric currents which lead to the appearance of an additional mechanism of energy dissipation which is based on Joule effects, namely as Joule dissipation. This kind of flows play an important role in the evolution of many physical phenomena, such as the evolution of planetary accretion disks, while they are present in engineering applications, such as fusion plasma and magnetic stirring. Most popular turbulence models used in CFD codes are based on traditional models, such as κ-ϵ, modified by adding ad-hoc terms in order to represent magnetic effects. These terms lack of information regarding the influence that the large-scale structure of the turbulent fields plays on the interaction between the velocity and the magnetic field. As it is already extensively described in this work, Structure-based Models are sensitized by construction to the turbulent structures through the use of structure-tensors, a trait that makes them elegant for use in the development of appropriate turbulence models for MHD applications. Preliminary work of Kassinos and Reynolds [92] in homogeneous unstrained MHD turbulence enforces the validity of this idea, while consequent work of Kassinos et al.

[47] served supportively by focusing on the further understanding of combined effects of frame rotation and mean rotation. Furthermore, Kassinos et al. [93] proposed a simplification of the coupled equations based on the quasi-linear assumption, in which the non-linear terms involving the fluctuating magnetic field are discarded. Their results agreed very well with the full MHD equations at least for magnetic Reynolds numbers up to $R_m = 50$. This conclusion is important for modeling purposes because it suggests that simplified equations can be solved instead of the full MhD equations for the study of MHD flows lying at the proposed range of validity.

B.1.1 General approach and objectives

The significant influence that the large-scale have on the dynamics of the turbulent statistics has urged us to explore the potential of constructing a complete Structure-based model for MHD applications, capable on taking into account these effects. Motivated by the success of the SBM for the passive scalar statistics, we put effort on extending the applicability of the Interaction Particle Representation Model for these flows. The Quasi-Linear assumption is adopted such that it leads to simpler modeling expressions, while some preliminary work is shown for the development of transport equations for the scales of the magnetic field which are also sensitized to the details of the large-scale field. In Section B.2 we introduce the governing equations of an incompressible, electrically conductive fluid. In order to describe the structure of the magnetic field, a set of relevant turbulence tensors is also presented. In Section B.3 we extend the IPRM model to account for the magnetic statistics, while in Section B.4 a set of transport equations for the structure-based magnetic scales is presented and discussed, which in future work will be used to bring the complete SBM into a closed form. In Section B.5 we introduce linearized expressions for the transport equations of the magnetic scales which are suitable for modeling purposes. Preliminary results for two test cases are shown in Section B.6, whereas conclusions and a list of future activities is given in Section B.7.

B.2 Mathematical Background

B.2.1 Governing equations

The transport equations of an electrically conductive fluid flow is governed by the continuity, momentum and induction equations,

$$\frac{\partial u_i}{\partial t} + u_q u_{i,q} = -\frac{1}{\rho} p_{,i} + b_q b_{i,q} + \nu u_{i,qq} \,, \tag{B.1a}$$

$$\frac{\partial b_i}{\partial t} + u_q b_{i,q} = b_q u_{i,q} + \eta b_{i,qq} \,, \tag{B.1b}$$

$$u_{q,q} = 0 \,, \tag{B.1c}$$

$$b_{q,q} = 0 \,, \tag{B.1d}$$

where b_i is the magnetic field expressed in alfven units $(1/\sqrt{\mu^* \rho})$, u_i and p are the instantaneous velocity and pressure fields respectively, η is the magnetic diffusivity, ν is the kinematic viscosity, ρ is the fluid density and μ^* is the fluid magnetic permeability.

The flow variables can be decomposed into a mean and a fluctuating part by applying the Reynolds decomposition

$$u_i = \overline{u}_i + u'_i \,, \quad b_i = \overline{b}_i + b'_i \,, \quad p = \overline{p} + p' \,. \tag{B.2}$$

For the case of homogeneous turbulence, use of eq. (B.2) into eqs. (B.1) leads to the following set of governing equations for the fluctuating and mean variables

$$u'_{q,q} = 0 \,, \quad \overline{u}_{q,q} = 0 \,, \tag{B.3a}$$

$$b'_{q,q} = 0 \,, \quad \overline{b}_{q,q} = 0 \,, \tag{B.3b}$$

$$\frac{\partial u'_i}{\partial t} + \overline{u}_q u'_{i,q} = -u'_q \overline{u}_{i,q} + \overline{b}_q b'_{i,q} - \frac{p'_{,i}}{\rho} - (u'_q u'_i)_{,q} + (b'_q b'_i)_{,q} + \nu u'_{i,qq} \,, \tag{B.3c}$$

$$\frac{\partial b'_i}{\partial t} + \overline{u}_q b'_{i,q} = \overline{b}_q u'_{i,q} + b'_q \, \overline{u}_{i,q} - (u'_q b'_i)_{,q} + (b'_q u'_i)_{,q} + \eta b'_{i,qq} \,, \tag{B.3d}$$

$$\frac{\partial \overline{u}_i}{\partial t} + \overline{u}_q \overline{u}_{i,q} = -\frac{\overline{p}_{,i}}{\rho} + \nu \overline{u}_{i,qq} \,, \tag{B.3e}$$

$$\frac{\partial \overline{b}_i}{\partial t} = \overline{b}_q \overline{u}_{i,q} \,. \tag{B.3f}$$

B.2.2 Quasi-Linear approach.

We further simplify eqs. (B.3) by adopting the so-called Quasi-Linear (hereafter QL) approximation, in which we discard all the non-linear terms involving the fluctuating magnetic field and keep the non-linear convective term in the fluctuating momentum equation. Thus eqs. (B.3c),(B.3d) are simplified to the following forms

$$\frac{\partial u_i'}{\partial t} + \overline{u}_q u_{i,q}' = -u_q'\overline{u}_{i,q} + \overline{b}_q b_{i,q}' - \frac{p_{,i}'}{\rho} - (u_q'u_i')_{,q} + \nu u_{i,qq}' \,, \tag{B.4a}$$

$$\frac{\partial b_i'}{\partial t} + \overline{u}_q b_{i,q}' = \overline{b}_q u_{i,q}' + b_q'\overline{u}_{i,q} + \eta b_{i,qq}' \,. \tag{B.4b}$$

Note that, compared to the analogous QL expression for the purely hydrodynamic case, eq. (B.4a) has an additional term which depends solely on the magnetic field. This term is linear, meaning it is also present in the RDT limit. Regarding eq. (B.4b), all terms are linear in terms of the fluctuating quantities, thus it has the same form at the RDT limit.

B.2.3 One point turbulence magnetic structure tensors

In the presence of magnetic fluctuations, additional effects occur in the flow in respect to the pure hydrodynamic case, which influence the status of the turbulent field. The orientation of the magnetic fluctuations determines the joule dissipation mechanism, thus having a significant impact on the morphology of the eddies and consequently to the velocity field. Furthermore, the correlation between the magnetic and the velocity fluctuations is known for playing important role to the dynamics of both fields, thus contributing to the turbulence anisotropy. As a result, additional one-point structure tensors are introduced which can be used to describe the contribution of the magnetic field to the anisotropy of the turbulent structure. In order to define the new tensors we introduce the fluctuating magnetic potential vector $\psi_i^{b'}$, which is used to define the magnetic field as follows

$$b_i' = \epsilon_{ijk}\psi_{k,j}^{b'} \,. \tag{B.5}$$

In analogy to the energy field, the magnetic stress tensor describes the spatial orientation of the magnetic intensities and it is related to the magnetic potential through the following identity,

$$R_{ij}^b = \overline{b_i'b_j'} = \epsilon_{ist}\epsilon_{jpq}\overline{\psi_{t,s}^{b'}\psi_{q,p}^{b'}} \,, \qquad r_{ij}^b = R_{ij}^b/(R_{qq}^b) \,. \tag{B.6}$$

The one-point structure tensors which describe solely the anisotropy of the magnetic field are defined by,

$$R^b_{ij} = \overline{b'_i b'_j}, \qquad r^b_{ij} = R^b_{ij}/R^b_{kk}, \qquad \tilde{r}^b_{ij} = r^b_{ij} - \delta_{ij}/3\,, \tag{B.7a}$$

$$D^m_{ij} = \overline{\psi^{b'}_{k,i}\psi^{b'}_{k,j}}, \qquad d^m_{ij} = D^m_{ij}/D^m_{kk}, \qquad \tilde{d}^m_{ij} = d^m_{ij} - \delta_{ij}/3\,. \tag{B.7b}$$

The correlation between the velocity and the magnetic field is represented by the cross-helicity tensor H_{ij}, defined by

$$H_{ij} = \overline{b'_i u'_j} = \epsilon_{ist}\epsilon_{jpq}\overline{\psi^{b'}_{t,s}\psi'_{q,p}}, \qquad h_{ij} = H_{ij}/\sqrt{R_{qq}R^b_{ss}}, \qquad \tilde{h}_{ij} = h_{ij} - \delta_{ij}/3\,, \tag{B.8}$$

where ψ'_i is the fluctuating stream function vector. Note that the cross-helicity tensor H_{ij} is not normalized by its trace H_{qq}. This happens because it might become ill-defined in cases where its trace takes zero or negative values. Since we consider homogeneous turbulence, it is useful to express these tensors as integrals in Fourier space,

$$R^b_{ij} = \int E^m_{ij}(\mathbf{k})d^3\mathbf{k}\,, \tag{B.9a}$$

$$D^m_{ij} = \int \frac{k_i k_j}{k^2} E^m_{qq}(\mathbf{k})d^3\mathbf{k}\,, \tag{B.9b}$$

$$H_{ij} = \int X_{ij}(\mathbf{k})d^3\mathbf{k}\,, \tag{B.9c}$$

where $E^m_{ij} \sim \langle \hat{b}_i \hat{b}^*_j \rangle$ is the magnetic energy spectrum and $X_{ij} \sim \langle \hat{b}_i \hat{u}^*_j \rangle$ is the cross-helicity spectrum. Note that the tensor trace D^m_{qq} is identical to the magnetic variance $\overline{b'_i b'_i}$.

B.2.4 Averaged equations

Starting from the quasi-linear expressions of eq. (B.4), a set of transport equations for the fluctuating statistics is derived. Firstly, the evolution of the Reynolds stress components is given by

$$\begin{aligned}\underbrace{\frac{d\overline{u'_i u'_j}}{dt}}_{\text{Langrangian term}} &= \underbrace{-\overline{u'_i u'_q}\,\overline{u}_{j,q} - \overline{u'_j u'_q}\,\overline{u}_{i,q}}_{\substack{\text{production due to}\\ \text{mean velocity field}}} \underbrace{-2\nu\overline{u'_{i,q}u'_{j,q}}}_{\substack{\text{viscous dissipation}\\ \text{related term}}} \underbrace{-\overline{u'_i u'_q u'_{j,q}} - \overline{u'_j u'_q u'_{i,q}}}_{\substack{\text{higher-order}\\ \text{re-distribution term}}} \\ &\underbrace{-\frac{1}{\rho}\overline{u'_i p'_{,j}} - \frac{1}{\rho}\overline{u'_j p'_{,i}}}_{\substack{\text{pressure-strain rate}\\ \text{re-distribution term}}} + \underbrace{\bar{b}_q\left(\overline{u'_i b'_{j,q}} + \overline{u'_j b'_{i,q}}\right)}_{\text{Joule dissipation term}} .\end{aligned} \tag{B.10}$$

The additional term compared to hydrodynamic case that appears in eq. (B.10) contains the mean magnetic field and is called Joule-dissipation term, because it is a sink term related to Joule energy losses. Note that Fourier analysis shows that this term acts evenly in all scales, thus it can not be neglected at high Reynolds number flows. The time history of the statistics of the magnetic fluctuations is found by the following equation

$$\underbrace{\frac{d(\overline{b'_i b'_j})}{dt}}_{\text{Langrangian term}} = \underbrace{-\bar{b}_q\left(\overline{u'_i b'_{j,q}} + \overline{u'_j b'_{i,q}}\right)}_{\substack{\text{production due to}\\ \text{mean magnetic field}}} + \underbrace{\left(\overline{b'_i b'_q}\,\overline{u}_{j,q} + \overline{b'_j b'_q}\,\overline{u}_{i,q}\right)}_{\substack{\text{production due to}\\ \text{mean stretching}}} \underbrace{-2\eta\overline{b'_{i,q}b'_{j,q}}}_{\substack{\text{magnetic dissipation}\\ \text{related term}}} , \tag{B.11}$$

where the magnetic tensor $\overline{b'_i b'_j}$ is the analogous for the magnetic fields to what the Reynolds stress tensor is for the energy field. In contrast to the Reynolds stress equation, the mean magnetic field acts now as a source term, accompanied with another production mechanism due to mean stretching and a dissipation mechanism due to magnetic diffusivity. This expression is elegant for modeling purposes due to its simplicity, since it stems from the linearized expression of eq. (B.4b). Additionally, the transport equation for the cross-helicity tensor $\overline{b'_i u'_j}$ is needed to be considered for modeling purposes, which at the QL limit becomes

$$\begin{aligned}\underbrace{\frac{d(\overline{b'_i u'_j})}{dt}}_{\text{Langrangian term}} &= \underbrace{-\overline{b'_i u'_q}\,\overline{u}_{j,q}}_{\substack{\text{production due to}\\ \text{mean velocity field}}} + \underbrace{\nu\overline{b'_i u'_{j,qq}}}_{\substack{\text{viscous dissipation}\\ \text{related term}}} - \underbrace{\frac{1}{\rho}\overline{b'_i p'_{,j}}}_{\substack{\text{pressure-magnetic}\\ \text{re-distribution term}}} - \underbrace{\overline{b'_i(u'_q u'_j)_{,q}}}_{\substack{\text{higher-order}\\ \text{re-distribution term}}} \\ &+ \underbrace{\bar{b}_q\overline{b'_i b'_{j,q}}}_{\substack{\text{Joule dissipation}\\ \text{related term}}} + \underbrace{\bar{b}_q\overline{u'_j u'_{i,q}}}_{\substack{\text{production due to}\\ \text{mean magnetic field}}} + \underbrace{\overline{b'_q u'_j}\,\overline{u}_{i,q}}_{\substack{\text{production due to}\\ \text{mean velocity field}}} + \underbrace{\eta\overline{u'_j b'_{i,qq}}}_{\substack{\text{magnetic diffusive}\\ \text{related term}}} .\end{aligned} \tag{B.12}$$

B.3 An extended Interaction Particle Representation Model for magnetic field transport

We seek to further extent this model to account for magnetic effects. We start by introducing an additional particle property, the magnetic vector **B**, which is the particle representation of the Fourier mode of the magnetic fluctuating field. Based on the exact expression (B.4b) the evolution of this property is a linear expression and can be given by

$$\frac{dB_i}{dt} = -\bar{B}_q V_i N_q + G_{iq} B_q - G^b_{iq} V_q \, , \tag{B.13}$$

where the dissipation term is modeled in terms of the magnetic effective gradient G^b_{ij} which is defined as

$$G^b_{iq} = \frac{C_v \langle V_i B_q \rangle}{\tau_b q^2} \, , \qquad q^2 = \langle V^2 \rangle \, , \tag{B.14}$$

where C_v is set to be equal to unity. The reason why we have used the concept of effective gradients stems from the standard view of energy transfer through a cascade mechanism, which assumes that at sufficiently high Reynolds number the dissipation of energy takes place mostly in the small scales, with a rate that is determined by the rate of energy transfer from the large-scale eddies to the smaller ones. In that sense, this term represents the non-linear turbulence interactions between large-scale structures and the smaller ones. More arguments that will justify the specific form of this term are given in the section regarding the magnetic scales, in which an alternative expression for the magnetic dissipation is given. Note that the same idea was successfully adopted for the development of a structure-based model for the passive-scalar model. The magnetic time-scale τ_b is defined by

$$\tau_b = C_v \frac{\langle B^2 \rangle}{\epsilon_b} r^b_{iq} r_{qi} \, , \tag{B.15}$$

which leads the following ratio between the turbulence and the magnetic time scale

$$\frac{\tau}{\tau_b} = \frac{\langle V^2 \rangle \epsilon_b}{\langle B^2 \rangle \epsilon} \frac{r_{iq} d_{qs} r_{si}}{r^b_{iq} r_{qi}} \, . \tag{B.16}$$

The conditional expressions for the one-point tensors are given by

$$B^{|n}_{ij} = \langle B_i B_j | n \rangle \, , \qquad D^{m|n}_{ij} = \langle B^2 n_i n_j | n \rangle \, , \qquad H^{|n}_{ij} = \langle B_i V_j | n \rangle \, . \tag{B.17}$$

The conditional evolution equations for the magnetic properties are

$$\frac{dB_{ij}^{|n}}{dt} = -\bar{B}_q N_q (H_{ij}^{|n} + H_{ji}^{|n}) + (G_{iq} B_{qj}^{|n} + G_{jq} B_{qi}^{|n}) - (G_{jq}^{b} H_{iq}^{|n} + G_{iq}^{b} H_{jq}^{|n})\,, \tag{B.18}$$

and

$$\begin{aligned}\frac{dH_{ij}^{|n}}{dt} &= -(G_{jk}^{v} + 2\Omega_{jk}^{f}) H_{ik}^{|n} + \left(G_{km}^{v} + G_{km}^{n} + 2\Omega_{km}^{f}\right) H_{im}^{|n} n_k n_j - C_1 H_{ij}^{|n} \\ &\quad + \bar{B}_q N_q \left(B_{ij}^{|n} - R_{ij}^{|n}\right) - G_{iq}^{b} R_{qj}^{|n} + G_{iq} H_{qj}^{|n}\,,\end{aligned} \tag{B.19}$$

Based on our experience, we have chosen to modify the expression for the conditional magnetic dissipation

$$G_{iq}^{b} \langle B_j V_q | n \rangle = \frac{C_v}{\tau_b q^2} \langle B_q V_i \rangle \langle B_j V_q | n \rangle\,. \tag{B.20}$$

We adopt instead the following approximation

$$\frac{C_v}{\tau_b q^2} \langle B_q V_i \rangle \langle B_j V_q | n \rangle \approx \frac{C_v}{\tau_b q^2} \langle B_j B_q \rangle R_{qi}^{|n}\,, \tag{B.21}$$

because this form is known to be more stable numerically, and it is successfully used to model the diffusive term in the structure-based model for the passive-scalar transport. Substituting back into eq. (B.18) yields

$$\frac{dB_{ij}^{|n}}{dt} = -\bar{B}_q N_q (H_{ij}^{|n} + H_{ji}^{|n}) + (G_{iq} B_{qj}^{|n} + G_{jq} B_{qi}^{|n}) - (A_{iq} R_{qj}^{|n} + A_{jq} R_{qi}^{|n})\,, \tag{B.22}$$

where the effective gradient is expressed as

$$A_{ij} = \frac{C_v}{\tau_b q^2} \langle B_i B_j \rangle\,. \tag{B.23}$$

Lastly, the transport for the conditional Reynolds stress tensor with the inclusion of the joule term becomes

$$\begin{aligned}\frac{dR^{|n}_{ij}}{dt} = &-\left(G^v_{jk} + 2\Omega^f_{jk}\right)R^{|n}_{ki} - \left(G^v_{ik} + 2\Omega^f_{ik}\right)R^{|n}_{kj} + [G^v_{km} + G^n_{km} + 2\Omega^f_{km}]\times \\ &\left(R^{|n}_{im}n_k n_j + R^{|n}_{jm}n_k n_i\right) + \overline{B}_q N_q\left(H^{|n}_{ij} + H^{|n}_{ji}\right) - \left[2C_1 R^{|n}_{ij} - C_2^2 R^{|n}_{qq}\left(\delta_{ij} - n_i n_j\right)\right] .\end{aligned} \tag{B.24}$$

B.4 A set of structure-based scales for the magnetic field

In this section, we have chosen the magnetic variance and the magnetic enstrophy as the eligible scales for the magnetic field, and we derive a set of transport equations which can be used in the future for the development of a two-equation structure-based model sensitized to large-scale anisotropies. Applying the triple decomposition method to eq. (B.4) leads to a set of transport equation for each contributor to the instantaneous magnetic field, which are

Mean magnetic squared magnitude:

$$\begin{aligned}\underbrace{\frac{\partial(\bar b_i\bar b_i/2)}{\partial t} + \bar u_q(\bar b_i\bar b_i/2)_{,q}}_{\substack{\text{mean Langrangian}\\ \text{increase}}} = &\underbrace{\bar b_i\bar b_q\overline{u}_{i,q}}_{\substack{\text{production by}\\ \text{self-stretching}}} \underbrace{-\bar b_{i,q}\left(\overline{\tilde b_q\tilde u_i} + \overline{\langle b''_q u''_i\rangle}\right)}_{\substack{\text{production by}\\ \text{cross-scale stretching}}} + \underbrace{\bar b_{i,q}\overline{\tilde u_q\tilde b_i}}_{\substack{\text{transfer to}\\ \text{large-scales}}} \underbrace{+\bar b_{i,q}\overline{\langle u''_q b''_i\rangle}}_{\substack{\text{transfer to}\\ \text{small-scales}}} \\ &- \underbrace{\eta\bar b_{i,q}\bar b_{i,q}}_{\substack{\text{dissipation from}\\ \text{mean}}} + \underbrace{\left[\bar b_i(\overline{\tilde b_q\tilde u_i} - \overline{\tilde u_q\tilde b_i}) + \bar b_i(\overline{\langle b''_q u''_i\rangle} - \overline{\langle u''_q b''_i\rangle}) + \eta(\bar b_i\bar b_i/2)_{,q}\right]_{,q}}_{\text{spatial flux}} ,\end{aligned} \tag{B.25}$$

Large-Scale magnetic variance:

$$\begin{aligned}\underbrace{\frac{\partial\overline{\tilde b_i\tilde b_i/2}}{\partial t} + \bar u_q\overline{(\tilde b_i\tilde b_i/2)}_{,q}}_{\substack{\text{mean Langrangian}\\ \text{increase}}} = &\underbrace{-\overline{\tilde b_i\tilde u_q}\bar b_{i,q}}_{\substack{\text{transfer from}\\ \text{mean}}} + \underbrace{\overline{\tilde b_i\tilde b_q}\bar u_{i,q}}_{\substack{\text{production by}\\ \text{mean stretching}}} \underbrace{-\left(\overline{\tilde b_q\tilde u_i\tilde b_{i,q}} - \overline{\tilde u_q\tilde b_i\tilde b_{i,q}}\right)}_{\substack{\text{production by}\\ \text{self-stretching}}} \underbrace{-\eta\overline{\tilde b_{i,q}\tilde b_{i,q}}}_{\substack{\text{dissipation by}\\ \text{large-scale}}} \\ &\underbrace{+\bar b_q\overline{\tilde b_i\tilde u_{i,q}} - \overline{\langle b''_q u''_i\rangle\tilde b_{i,q}}}_{\substack{\text{production by}\\ \text{cross-scale stretching}}} + \underbrace{\overline{\langle u''_q b''_i\rangle\tilde b_{i,q}}}_{\substack{\text{transfer to}\\ \text{small-scales}}} \\ &+ \underbrace{\left(\overline{\tilde b_i\tilde b_q\tilde u_i} + \overline{\tilde b_i\langle b''_q u''_i\rangle} - \overline{\tilde b_i\tilde u_q\tilde b_i} - \overline{\tilde b_i\langle u''_q b''_i\rangle} + \eta(\overline{\tilde b_i\tilde b_i/2})\right)_{,q}}_{\text{spatial flux}} ,\end{aligned} \tag{B.26}$$

Small-Scale magnetic variance:

$$
\begin{aligned}
\underbrace{\frac{\partial\overline{\langle b_i''b_i''/2\rangle}}{\partial t}+\bar{u}_q\overline{\langle b_i''b_i''/2\rangle}}_{\text{mean Langrangian increase}} = &-\underbrace{\overline{\langle b_i''u_q''\rangle}\bar{b}_{i,q}}_{\text{transfer from mean}}+\underbrace{\overline{\langle b_i''b_q''\rangle}\bar{u}_{i,q}}_{\text{production by mean stretching}}\underbrace{-\overline{\langle b_q''u_i''b_{i,q}''\rangle}-\overline{\langle u_q''b_i''b_{i,q}''\rangle}}_{\text{production by self-stretching}}-\underbrace{\overline{\langle u_q''b_i''\rangle\tilde{b}_{i,q}}}_{\text{transfer from large-scales}}\\
&\underbrace{+\bar{b}_q\overline{\langle b_i''u_{i,q}''\rangle}-\overline{\tilde{b}_q\langle u_i''b_{i,q}''\rangle}-\overline{\tilde{u}_i\langle b_q''b_{i,q}''\rangle}+\overline{\tilde{u}_q\langle b_i''b_{i,q}''\rangle}}_{\text{production by cross-scale stretching}}-\underbrace{\eta\overline{\langle b_{i,q}''b_{i,q}''\rangle}}_{\text{dissipation by small-scales}}\\
&+\underbrace{\left[\overline{\tilde{b}_q\langle b_i''u_i''\rangle}+\overline{\tilde{u}_i\langle b_i''b_q''\rangle}-\overline{\tilde{u}_q\langle b_i''b_i''\rangle}-\overline{\langle b_i''b_i''u_q''\rangle}+\overline{\langle b_i''b_q''u_i''\rangle}+\eta\left(\overline{\langle b_i''b_i''/2\rangle}\right)_{,q}\right]_{,q}}_{\text{spatial flux}}\;.
\end{aligned}
\tag{B.27}
$$

Comparison between eqs. (B.26), (B.27) suggests that magnetic variance is transfered from large-scales towards small scales in a similar fashion as occurs in both the analogous energy and passive scalar cases. This picture is consistent with Richardson's idea about cascade mechanism, a picture which will be used later on in order to re-express the magnetic dissipation term in an alternative form.

Applying the operator $\epsilon_{spi}\frac{\partial}{\partial x_p}$ in eq. (B.3) yields the analogous expressions for the magnetic enstrophy vector h_s. Below we summarize the transport equations for the mean and the large-scale contributors.

Mean magnetic enstrophy:

$$
\begin{aligned}
\frac{\partial(\bar{h}_s\bar{h}_s/2)}{\partial t}+\bar{u}_q(\bar{h}_s\bar{h}_s/2)_{,q} = &-\bar{u}_{q,m}\bar{b}_{n,q}\bar{b}_{n,m}+\bar{b}_{q,m}\bar{u}_{n,q}\bar{b}_{n,m}+\bar{b}_q\bar{h}_s\bar{\omega}_{s,q}\\
&-\left(\overline{\tilde{b}_q\tilde{\omega}_s}-\overline{\tilde{u}_q\tilde{h}_s}\right)\bar{h}_{s,q}-\left(\overline{\langle b_q''\omega_s''\rangle}-\overline{\langle u_q''h_s''\rangle}\right)\bar{h}_{s,q}-\eta\bar{h}_{s,q}\bar{h}_{s,q}\\
&+\left[\overline{\tilde{b}_{q,m}\tilde{u}_{n,q}}-\overline{\tilde{b}_{q,n}\tilde{u}_{m,q}}-\overline{\tilde{u}_{q,m}\tilde{b}_{n,q}}+\overline{\tilde{u}_{q,n}\tilde{b}_{m,q}}\right]\bar{b}_{n,m}\\
&+\left[\overline{\langle b_{q,m}''u_{n,q}''\rangle}-\overline{\langle b_{q,n}''u_{m,q}''\rangle}-\overline{\langle u_{q,m}''b_{n,q}''\rangle}+\overline{\langle u_{q,n}''b_{m,q}''\rangle}\right]\bar{b}_{n,m}\\
&+\left[\bar{h}_s(\overline{\tilde{b}_q\tilde{\omega}_s}-\overline{\tilde{u}_q\tilde{h}_s})+\bar{h}_s(\overline{\langle b_q''\omega_s''\rangle}-\overline{\langle u_q''h_s''\rangle})+\eta(\bar{h}_s\bar{h}_s/2)_{,q}\right]_{,q}
\end{aligned}
\tag{B.28}
$$

Large-Scale magnetic enstrophy:

$$
\begin{aligned}
&\frac{\partial(\overline{\tilde{h}_s\tilde{h}_s/2})}{\partial t} + \bar{u}_q(\overline{\tilde{h}_s\tilde{h}_s/2})_{,q} = -\overline{\tilde{b}_{n,q}\tilde{b}_{n,p}}\bar{u}_{q,p} + \overline{\tilde{b}_{q,m}\tilde{b}_{i,m}}\bar{u}_{i,q} + \left(\overline{\tilde{u}_{q,n}\tilde{b}_{n,i}} - \overline{\tilde{u}_{q,m}\tilde{b}_{i,m}}\right)\bar{b}_{i,q} \\
&+ \left(\overline{\tilde{u}_{n,q}\tilde{b}_{n,p}} - \overline{\tilde{u}_{m,q}\tilde{b}_{p,m}}\right)\bar{b}_{q,p} - \overline{\tilde{h}_s\tilde{u}_q}\bar{h}_{s,q} + \overline{\tilde{b}_q\tilde{h}_s}\bar{\omega}_{s,q} + \overline{\tilde{h}_s\tilde{\omega}_{s,q}}\bar{b}_q - \eta\overline{\tilde{h}_{s,q}\tilde{h}_{s,q}} \\
&- \overline{\left[\tilde{b}_q\tilde{\omega}_s + \langle b''_q\omega''_s\rangle - \langle u''_q h''_s\rangle\right]\tilde{h}_{s,q}} + \left[\overline{\tilde{h}_s(\tilde{b}_q\tilde{\omega}_s - \tilde{u}_q\tilde{h}_s)} + \overline{\tilde{h}_s\langle b''_q\omega''_s\rangle - \langle u''_q h''_s\rangle)} - \overline{\tilde{u}_q\tilde{h}_s\tilde{h}_s} + \eta\overline{(\tilde{h}_s\tilde{h}_s/2)_{,q}}\right]_{,q} \\
&+ \overline{\left[(\tilde{b}_{q,m}\tilde{u}_{n,q} - \tilde{b}_{q,n}\tilde{u}_{m,q}) - (\tilde{u}_{q,m}\tilde{b}_{n,q} - \tilde{u}_{q,n}\tilde{b}_{m,q})\right]\tilde{b}_{n,m}} \\
&+ \overline{\left[(\langle b''_{q,m}u''_{n,q}\rangle - \langle b''_{q,n}u''_{m,q}\rangle) - (\langle u''_{q,m}b''_{n,q}\rangle - \langle u''_{q,n}b''_{m,q}\rangle)\right]\tilde{b}_{n,m}}
\end{aligned}
\tag{B.29}
$$

As clearly shown from eqs. (B.28), (B.29), the derived expressions include a large number of complex terms, making further analysis of them a difficult task to perform. This is done at the next sub-section, in which the Quasi-Linear approach is adopted, which leads to simplified equations.

The magnetic field also contributes to the evolution of the enstrophy field ω, since additional terms depending solely to the magnetic field occur in its transport equation. The evolution equation for the instantaneous vorticity vector is derived by applying the operator $\epsilon_{spi}\frac{\partial}{\partial x_p}$ to eq. (B.4),

$$
\frac{\partial \omega_s}{\partial t} + u_q\omega_{s,q} = \omega_q u_{s,q} + \nu\omega_{s,qq} + b_q h_{s,q} - b_{s,q}h_q\,. \tag{B.30}
$$

Applying to eq. (B.30) the triple decomposition scheme yields the following transport equations for the contributors of the enstrophy field,

Mean enstrophy:

$$
\begin{aligned}
\frac{\partial(\bar{\omega}_s\bar{\omega}_s/2)}{\partial t} = \ldots + &\underbrace{\bar{\omega}_s\left(\bar{b}_q\bar{h}_{s,q} - \bar{b}_{s,q}\bar{h}_q\right)}_{\substack{\text{production by}\\ \text{self-stretching}}}\underbrace{-\left(\overline{\tilde{b}_q\tilde{h}_s} - \overline{\tilde{b}_s\tilde{h}_q}\right)\bar{\omega}_{s,q} - \left(\overline{\langle b''_q h''_s\rangle} - \overline{\langle b''_s h''_q\rangle}\right)\bar{\omega}_{s,q}}_{\substack{\text{production by}\\ \text{cross-scale stretching}}} \\
&+ \underbrace{\left[\bar{\omega}_s\left(\overline{\tilde{b}_q\tilde{h}_s} - \overline{\tilde{b}_s\tilde{h}_q}\right) + \bar{\omega}_s\left(\overline{\langle b''_q h''_s\rangle} - \overline{\langle b''_s h''_q\rangle}\right)\right]_{,q}}_{\text{diffusive flux}}
\end{aligned}
\tag{B.31}
$$

Large-scale enstrophy:

$$\frac{\partial\overline{(\tilde{\omega}_s\tilde{\omega}_s/2)}}{\partial t} = \ldots + \bar{b}_q\overline{\tilde{\omega}_s\tilde{h}_{s,q}} - \bar{b}_{s,q}\overline{\tilde{\omega}_s\tilde{h}_q} + \bar{h}_{s,q}\overline{\tilde{b}_q\tilde{\omega}_s} - \bar{h}_q\overline{\tilde{b}_{s,q}\tilde{\omega}_s} - \overline{\tilde{\omega}_{s,q}\tilde{b}_q\tilde{h}_s} - \overline{\tilde{\omega}_{s,q}\langle b''_q h''_s\rangle} \\ + \overline{\tilde{\omega}_{s,q}\tilde{b}_s\tilde{h}_q} + \overline{\tilde{\omega}_{s,q}\langle b''_s h''_q\rangle} + \left[\overline{\tilde{b}_q\tilde{\omega}_s\tilde{h}_s} + \overline{\tilde{\omega}_s\langle b''_q h''_s\rangle} - \overline{\tilde{\omega}_s\tilde{b}_s\tilde{h}_q} - \overline{\tilde{\omega}_s\langle b''_s h''_q\rangle}\right]_{,q} \tag{B.32}$$

Small-scale enstrophy:

$$\frac{\partial(\overline{\langle\omega''_s\omega''_s/2\rangle})}{\partial t} = \ldots + \bar{b}_q\overline{\langle\omega''_s h''_{s,q}\rangle} - \bar{b}_{s,q}\overline{\langle\omega''_s h''_q\rangle} + \bar{h}_{s,q}\overline{\langle b''_q\omega''_s\rangle} - \bar{h}_q\overline{\langle b''_{s,q}\omega''_s\rangle} - \overline{\tilde{b}_q\langle\omega''_{s,q}h''_s\rangle} + \overline{\tilde{h}_{s,q}\langle\omega''_s b''_q\rangle} \\ - \overline{\langle b''_q\omega''_{s,q}h''_s\rangle} + \overline{\tilde{b}_s\langle\omega''_{s,q}h''_q\rangle} + \overline{\tilde{h}_q\langle\omega''_{s,q}b''_s\rangle} + \overline{\langle b''_s\omega''_{s,q}h''_q\rangle} \\ + \left[\overline{\tilde{b}_q\langle\omega''_s h''_s\rangle} + \overline{\langle\omega''_s h''_s b''_q\rangle} - \overline{\tilde{b}_s\langle\omega''_s h''_q\rangle} - \overline{\tilde{h}_q\langle\omega''_s b''_s\rangle} - \overline{\langle\omega''_s b''_s h''_q\rangle}\right]_{,q} \tag{B.33}$$

B.5 Linearized equations

As mentioned above, the derived expressions include long and complicated terms, making them not elegant for modeling purposes. Instead, we choose as a starting point for the modeling process the corresponding expressions for the case of homogeneous turbulence at the QL limit. At this limit, the set of transport equations for the fluctuating statistics simplifies as follow:

$$\frac{\partial(\overline{u'_i u'_i/2})}{\partial t} + \bar{u}_q(\overline{u'_i u'_i/2})_{,q} = \underbrace{-R_{ij}\bar{u}_{i,j}}_{P_\kappa} \underbrace{+\bar{b}_q\overline{b'_{i,q}u'_i} - \nu\overline{\frac{\partial u'_i}{\partial x_i}\frac{\partial u'_i}{\partial x_j}}}_{\substack{\text{Total dissipation}\\ \epsilon_j+\epsilon_v}}, \tag{B.34}$$

$$\frac{\partial\overline{(\tilde{\omega}_s\tilde{\omega}_s/2)}}{\partial t} + \bar{u}_q(\overline{\tilde{\omega}_s\tilde{\omega}_s}/2)_{,q} = \underbrace{+\overline{\langle u''_j\omega''_i\rangle\tilde{\omega}_{i,j}}}_{\substack{\text{transfer to}\\ \text{small scales}}} + \underbrace{\overline{\tilde{\omega}_i\tilde{\omega}_j}\bar{u}_{i,j}}_{\substack{\text{production by}\\ \text{mean stretching}}} + \underbrace{\overline{\tilde{\omega}_i\tilde{\omega}_j\tilde{u}_{i,j}}}_{\substack{\text{production by}\\ \text{self stretching}}} + \underbrace{\overline{\tilde{\omega}_i\langle\omega''_j u''_{i,j}\rangle}}_{\substack{\text{production by}\\ \text{cross-scale stretching}}} \\ \underbrace{-\nu\overline{\tilde{\omega}_{i,j}\tilde{\omega}_{i,j}}}_{\substack{\text{dissipation by}\\ \text{large scales}}} \underbrace{+\bar{b}_q\overline{\tilde{\omega}_s\tilde{h}_{s,q}} - \overline{\tilde{\omega}_{s,q}\tilde{b}_q\tilde{h}_s}}_{\substack{\text{exchange with}\\ \text{magnetic enstrophy}}}, \tag{B.35}$$

$$\frac{\partial(\overline{b'_i b'_i/2})}{\partial t} + \bar{u}_q(\overline{b'_i b'_i/2})_{,q} = \underbrace{-\bar{b}_q\overline{b'_{i,q}u'_i} + \overline{b'_q b'_i}\bar{u}_{i,q}}_{\substack{\text{Total production}\\ P_j+P_b}} \underbrace{-\eta\overline{b'_{i,q}b'_{i,q}}}_{\epsilon_b}, \tag{B.36}$$

$$\begin{aligned}\frac{\partial\overline{(\tilde{h}_s\tilde{h}_s/2)}}{\partial t} + \bar{u}_q(\overline{\tilde{h}_s\tilde{h}_s/2})_{,q} = & \underbrace{-\overline{\tilde{b}_{n,q}\tilde{b}_{n,p}}\bar{u}_{q,p} + \overline{\tilde{b}_{q,m}\tilde{b}_{i,m}}\bar{u}_{i,q}}_{\substack{\text{production by}\\ \text{mean stretching}}} \quad \underbrace{-\eta\overline{\tilde{h}_{s,q}\tilde{h}_{s,q}}}_{\text{dissipative term}} \\ & \underbrace{-\overline{\tilde{\omega}_s\tilde{h}_{s,q}}\bar{b}_q + \overline{\tilde{\omega}_{s,q}\tilde{b}_q\tilde{h}_s}}_{\substack{\text{exchange with}\\ \text{large scale enstrophy}}} \underbrace{-\overline{\tilde{h}_{s,q}\langle\omega''_s b''_q\rangle}}_{\substack{\text{transfer to small}\\ \text{scale enstrophy}}} + \underbrace{\overline{\langle u''_q h''_s\rangle\tilde{h}_{s,q}}}_{\substack{\text{transfer to}\\ \text{small scales}}}\ .\end{aligned} \tag{B.37}$$

Note that the second term of the RHS of eq. (B.34) is related to the joule effects and acts as a sink term, while this term is also present in the evolution equation for the magnetic variance (B.36) in which it acts as a source term. The latter statement suggests the existence of an energy exchange mechanism which leads to a transfer of energy from the turbulent energy field to the magnetic variance field. Note also that, by comparing the enstrophy equations, we see the presence of an exchange mechanism in all scales. This observation is important since it further reduces the terms that we need to model.

B.5.1 Alternative expression for magnetic dissipation

Decomposing the magnetic dissipative term in eq. (B.36) into a large and a small part leads to the following alternative expression for the time evolution of the magnetic variance field,

$$\frac{\partial\overline{b'_i b'_i/2}}{\partial t} + \bar{u}_q(\overline{b'_i b'_i/2})_{,q} = -\bar{b}_q\overline{b'_{i,q}u'_i} + \overline{b'_q b'_i}\bar{u}_{i,q} - \left[\eta\overline{\langle b''_{i,q}b''_{i,q}\rangle} + \eta\overline{\tilde{b}_{i,q}\tilde{b}_{i,q}}\right]. \tag{B.38}$$

According to Richardson idea [51], the small scales adapt quickly to the changes that emerge to the large-scale structures. Consequently, these changes determine the rate at which the smallest scales dissipate magnetic energy, similarly to the energy and passive scalar fields. Thus, we assume that the rate at which magnetic variance is dissipated equals the rate at which magnetic variance is transfered through the cascade mechanism, such as

$$\left|\overline{\langle u''_q b''_i\rangle\tilde{b}_{i,q}}\right| \approx \left|\eta\overline{\langle b''_{i,q}b''_{i,q}\rangle}\right|. \tag{B.39}$$

Substitution of eq. (B.39) back into the dissipation term of eq. (B.40) yields

$$\frac{\partial \overline{b'_i b'_i/2}}{\partial t} + \bar{u}_q(\overline{b'_i b'_i/2})_{,q} = -\bar{b}_q \overline{b'_{i,q} u'_i} + \overline{b'_q b'_i}\bar{u}_{i,q} - \epsilon_b \,, \tag{B.40}$$

where the magnetic dissipation ϵ_b is alternatively expressed as

$$\epsilon_b = \underbrace{\overline{-\langle u''_q b''_i \rangle \tilde{b}_{i,q}}}_{\substack{\text{transfer from} \\ \text{large to small}}} + \underbrace{\overline{\eta \tilde{b}_{i,q} \tilde{b}_{i,q}}}_{\substack{\text{dissipation by} \\ \text{large scales}}} \quad . \tag{B.41}$$

The first term refers to the transfer of magnetic variance through the cascade mechanism and involves higher-order turbulence interactions. This alternative form is used to derive the modeled expression for the dissipation term in the Particle Representation Space based on the effective gradients concept (B.14). The second term refers to the dissipation of magnetic variance by the large-scales.

B.6 Preliminary results

Even though the structured-based model is incomplete and no computations can be performed, some preliminary results were obtained after approaching the Joule term that is present in the conditional evolution equation for the Reynolds stress tensor (B.24) as

$$\bar{B}_q N_q (H^{|n}_{ij} + H^{|n}_{ji}) \approx -2\sqrt{\bar{B}_q N_q \bar{B}_s N_s} R^{|n}_{ij} \,. \tag{B.42}$$

This form is valid at the limit of very low R_m, where the joule time scale is much smaller than the turbulence time scale. Thus, the magnetic field adapts rapidly to the changes of the velocity field, reaching the so-called quasi-static state. Expression (B.42) has the advantage that it brings eq. (B.24) into a closed form without the need to solve the transport equations for the conditional cross-helicity tensor $H^{|n}_{ij}$ and magnetic tensor $B^{|n}_{ij}$. The turbulence scales are provided by a κ-ϵ model with the addition of an ad-hoc magnetic term, given by

$$\frac{d\epsilon}{dt} = -\left[\frac{C_o \epsilon}{q^2} + C_s \bar{u}_{p,q} r_{qp} + C_\omega \sqrt{\Omega_n \Omega_m d_{nm}} + \frac{C_m}{\tau_m} \frac{\bar{B}_q \bar{B}_s}{\bar{B}^2} d_{qs} \right] \epsilon \,, \tag{B.43}$$

where τ_m is the Joule time scale, Ω_i is the mean vorticity vector and the constants are chosen to be

$$C_o = 11/3.0\,, \qquad C_s = 3.0\,, \qquad C_\omega = 0.01\,, \qquad C_\omega = 2.9\,. \tag{B.44}$$

We consider the case of homogeneous shear in a rotating frame at high Reynolds number for which DNS data is availiable[47]. A spanwise mean magnetic field and a transverse mean velocity gradient are imposed. The configuration of the mean flow is given by

$$\bar{u}_{i,j} = S\delta_{i1}\delta_{j2}\,, \qquad \Omega_i^f = \Omega^f\delta_{i3}\,, \qquad B_i = B\delta_{i3}\,. \tag{B.45}$$

In the presence of frame-rotation, an important parameter is the ratio of the frame rotation rate Ω_f to the mean shear rate S, given by

$$\eta_f = \frac{2\Omega_f}{S}\,. \tag{B.46}$$

where the frame-rotation rate is related to the frame-rotation tensor through the identity

$$\Omega_f = -\Omega_{12}^f\,, \tag{B.47}$$

and the initial conditions are determined by the shear parameter S^*, defined as

$$S^* = \frac{Sq^2}{\epsilon}\,. \tag{B.48}$$

Figure B.1 shows IPRM predictions for the time evolution of the turbulent kinetic energy at $Sq_o^2/\epsilon_o = 3.58$ and frame rotation rate $\eta_f = 0.5$ for two different magnetic Reynolds numbers, $R_m = 1$ and $R_m = 50$. This frame rotation rate is of particular interest since it corresponds to the most unstable hydrodynamic case. For the low R_m case, we observe that IPRM predictions are in good agreement with the DNS results except at large times, as expected due to the choice of eq. (B.42). For the high R_m case, IPRM is not capable of producing good matching with the DNS data, partly due to the fact that the quasi-static limit is not valid anymore. Even so, IPRM correctly predicts that the kinetic energy should increased at large times.

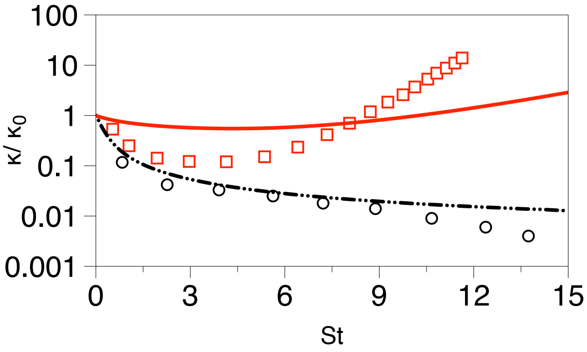

FIGURE B.1: IPRM model predictions (lines) for the time evolution of the turbulent kinetic energy. Comparison is made with DNS results (symbols) of Kassinos et al.[47] for homogeneous shear turbulence with transverse mean scalar-gradient at $Sq_o^2/\epsilon_o = 3.58$ and frame rotation rate $\eta_f = 0.5$. Two different magnetic Reynolds numbers are shown: (a) (○,—··—) $R_m = 1.0$; (□,———) $R_m = 50.0$.

B.7 Conclusions

The initial steps for the development of an extended IPRM model are presented which takes into account the presence of a magnetic field in a turbulent field. Additional transport equations for the evaluation of the magnetic scales are derived and discussed using the triple decomposition scheme. We propose the magnetic variance and the magnetic enstrophy as the proper scales to characterize the fluctuating magnetic field. These equations are strongly coupled to the corresponding scales for the velocity field, a trait that needs to be taken into account during the modeling process. An alternative expression for the magnetic dissipation is proposed based on the cascade mechanism which will be used to provide a modeled expression sensitized to the turbulence structure tensors. Further work is needed in order to reach a complete structure-based model, which needs to fulfill the following tasks:

- Obtain the asymptotic decay rates for the magnetic variance and the magnetic enstrophy in the limit of both very high and very low Reynolds numbers in order to evaluate the model parameters which appear in the magnetic scales.
- Model the additional magnetic terms which occur in the evolution equations for the turbulence scales through simple cases.
- Perform DNS computations for homogeneous shearless and shear turbulent flows in the presence of uniform external magnetic field for validation purposes.

Appendix C

Details on the extended stochastic models using effective gradients.

C.1 Model 1

C.1.1 Derivation of the transport equation for eddy-axis tensor a_{ij}.

The non-linear effects are incorporated into the differential of the eddy-axis vector through the effective gradients as follow

$$da_i = G^a_{ik} a_k dt - G^a_{ks} a_k a_s a_i dt \, , \tag{C.1a}$$

$$\Rightarrow \frac{da_i}{dt} = G^a_{ik} a_k - G^a_{ks} a_k a_s a_i \, . \tag{C.1b}$$

The differential of the velocity magnitude $V = (V_k V_k)^{1/2}$ is given by

$$dV = d([V_i V_i]^{1/2}) = \frac{1}{2}(V_i V_i)^{-1/2} d(V_i V_i) = \frac{1}{2V} d(V_i V_i) \, . \tag{C.2}$$

Expanding the expression for the differential of $d(V_i V_i)$ yields,

$$\frac{1}{2V} d(V_i V_i) = \frac{1}{2V}[(V_i + dV_i)(V_i + dV_i) - V_i V_i] = \frac{1}{2V}[2V_i dV_i + dV_i dV_i] \, . \tag{C.3}$$

Substituting eq. (C.3) in eq. (C.2) and using eq. (2.72) for the velocity differential in the absence of frame rotation gives,

$$\begin{aligned} dV =& \frac{1}{2V}[2V_i(-G^v_{ik}V_k dt + PN_i dt - C_1 V_i dt - C_2 V \epsilon_{ipq} dW_p n_q)] \\ &+ \frac{1}{2V}\Big[(-G^v_{ik}V_k dt + PN_i dt - C_1 V_i dt - C_2 V \epsilon_{ipq} dW_p n_q)(-G^v_{iq}V_q dt + PN_i dt \\ &- C_1 V_i dt - C_2 V \epsilon_{irs} dW_r n_s)\Big]\,. \end{aligned} \tag{C.4}$$

Keeping terms of order $O(dt)$ one finds

$$\begin{aligned} dV =& \frac{1}{2V}[-2G^v_{ik}V_iV_k dt + 2P\underbrace{N_iV_i}_{\text{zero}}dt - 2C_1V^2dt + C_2^2V^2\epsilon_{ipq}\epsilon_{irs}dW_pdW_rn_qn_s] \\ =& \frac{1}{2V}[-2G^v_{ik}V_iV_k dt - 2C_1V^2dt + C_2^2V^2(\delta_{pr}\delta_{qs} - \delta_{ps}\delta_{qr})dW_pdW_rn_qn_s] \\ \Rightarrow dV =& \frac{1}{2V}[-2G^v_{ik}V_iV_k dt - 2C_1V^2dt + C_2^2V^2(dW_pdW_pn_sn_s - dW_sdW_qn_qn_s)]\,. \end{aligned} \tag{C.5}$$

Combining eqs. (C.1), (C.5) yields an expression for the differential of the vector $A_i = Va_i$:

$$\begin{aligned} dA_i &= d(Va_i) = (V + dV)(a_i + da_i) - Va_i = Vda_i + a_idV + dVda_i \\ &= V[G^a_{ik}a_kdt - G^a_{ks}a_ka_sa_idt] + a_i\Big[\frac{1}{2V}[-2G^v_{iq}V_iV_qdt - 2C_1V^2dt \\ &+ C_2^2V^2(dW_pdW_pn_sn_s - dW_sdW_qn_qn_s)]\Big] \\ &= G^a_{ik}(Va_k)dt - G^a_{ks}a_ka_s(Va_i)dt - G^v_{qk}v_kv_q(Va_i)dt - C_1(Va_i)dt \\ &+ \frac{C_2^2}{2}(Va_i)[dW_pdW_p - dW_sdW_rn_sn_r] \\ \Rightarrow dA_i &= G^a_{ik}A_kdt - G^a_{ks}a_ka_sA_idt - G^v_{qk}v_kv_qA_idt - C_1A_idt \\ &+ \frac{C_2^2}{2}A_i[dW_pdW_p - dW_sdW_rn_sn_r]\,. \end{aligned} \tag{C.6}$$

The $dV.da_i$ has terms of higher order than $O(dt)$, thus it does not contribute to dA_i. In order to evaluate $d(A_iA_j)$ we use the following identity

$$d(A_iA_j) = (A_i + dA_i)(A_j + dA_j) - A_iA_j = A_idA_j + A_jdA_i + dA_idA_j\,. \tag{C.7}$$

Again, we retain terms up to $O(dt)$, thus we neglect dA_idA_j. Substituting eq. (C.6) in eq. (C.7) yields,

$$\begin{aligned} d(A_iA_j) = {} & G^a_{ik}A_kA_jdt + G^a_{jk}A_kA_idt - 2G^a_{ks}a_ka_sA_iA_jdt - 2G^v_{qk}v_kv_qA_iA_jdt \\ & - 2C_1A_iA_jdt + C_2^2A_iA_j[dW_pdW_p - dW_sdW_rn_sn_r]\,. \end{aligned} \tag{C.8}$$

A useful identity is

$$\langle A_iA_jdW_pdW_q\rangle \approx \langle A_iA_j\rangle\langle dW_pdW_q\rangle = A_{ij}dt\delta_{pq}\,. \tag{C.9}$$

Ensemble averaging eq. (C.8) and use of eq. (C.9) yields,

$$\begin{aligned} d(A_{ij}) = {} & G^a_{ik}A_{kj}dt + G^a_{jk}A_{ki}dt - 2G^a_{ks}\langle a_ka_sA_iA_j\rangle dt - 2G^v_{qk}\langle v_kv_qA_iA_j\rangle dt \\ & - 2C_1A_{ij}dt + C_2^2A_{ij}[\delta_{pp} - n_sn_s]dt\,. \end{aligned} \tag{C.10}$$

Dividing eq. (C.10) by dt yields the transport equation for A_{ij}

$$\frac{dA_{ij}}{dt} = G^a_{ik}A_{kj} + G^a_{jk}A_{ki} - 2G^a_{ks}q^2Z^a_{ijks} - 2G^v_{qk}\langle v_kv_qA_iA_j\rangle + 2[C_2^2 - C_1]A_{ij}\,, \tag{C.11}$$

where $Z^a_{ijks} = \frac{\langle V^2a_ia_ja_ka_s\rangle}{q^2}$ is a fully symmetric tensor and the model parameters C_1, C_2 are chosen to be

$$C_1 = C_2^2 = \frac{8.5}{\tau}\Omega^s f_{pq}n_pn_q, \quad \Omega^s = \sqrt{\Omega^s_k\Omega^s_k}, \quad \Omega^s_i = \epsilon_{ipq}r_{qk}d_{kp}\,. \tag{C.12}$$

A very good model for Z^a_{ijpq} has already been constructed by Kassinos et al. [2]. Substituting the expressions from eq. (C.12) in eq. (C.11) yields,

$$\frac{dA_{ij}}{dt} = G^a_{ik}A_{kj} + G^a_{jk}A_{ki} - 2G^a_{ks}q^2 Z^a_{ijks} - 2G^v_{qk}\langle v_k v_q A_i A_j\rangle \,. \tag{C.13}$$

Comparing eq. (C.13) with the analogous RDT equation as given in [2], we see that they are identical if instead of $G^{a,v}_{ij}$ we use G_{ij}.

Now, we seek to derive the transport equation for the normalized eddy-axis tensor $a_{ij} = \frac{A_{ij}}{A_{kk}}$. We start from the following equation

$$\frac{da_{ij}}{dt} = \frac{d}{dt}(\frac{A_{ij}}{A_{kk}}) = \frac{\dot{A}_{ij}}{A_{kk}} - \frac{A_{ij}}{A_{kk}}\frac{\dot{A}_{kk}}{A_{kk}} = \frac{\dot{A}_{ij}}{q^2} - a_{ij}\frac{\dot{A}_{kk}}{q^2}\,. \tag{C.14}$$

The transport equation of A_{kk} is found as follow

$$\begin{aligned}\frac{dA_{ww}}{dt} &= 2G^a_{wk}A_{kw} - 2G^a_{ks}Z^a_{wwks} - 2G^v_{qk}\langle V^2 \underbrace{a_w a_w}_{1} v_k v_q\rangle \\ &= 2G^a_{wk}A_{kw} - 2G^a_{ks}A_{ks} - 2G^v_{qk}R_{kq} = -2G^v_{qk}R_{kq} \\ &= -2(S_{qk} + \Omega_{qk} + \frac{C^v}{\tau}r_{qs}d_{sk})R_{kq} = -2(S_{qk} + \frac{C^v}{\tau}r_{qs}d_{sk})R_{kq} = -2\hat{S}_{qk}R_{kq}\,,\end{aligned} \tag{C.15}$$

where the term involving the mean rotation tensor is zero (symmetric-antisymmetric product) and $\hat{S}_{ij}$ is an effective strain rate tensor, defined by

$$\hat{S}_{qk} = S_{qk} + \frac{C^v}{\tau}r_{qs}d_{sk}\,. \tag{C.16}$$

Notice that $\hat{S}_{qk}$ is not a symmetric tensor. Substituting eq. (C.16) in eq. (C.15) yields,

$$\frac{da_{ij}}{dt} = G^a_{ik}a_{kj} + G^a_{jk}a_{ki} - 2G^a_{ks}Z^a_{ijks} - 2\frac{G^v_{qk}}{q^2}\langle v_k v_q A_i A_j\rangle + 2a_{ij}\hat{S}_{qk}r_{kq}\,. \tag{C.17}$$

Now we express the fourth and the fifth term of eq. (C.17) in terms of a_{ij} and the remaining structure parameters. For simplicity we deal with each term separately. We substitute the algebraic constitutive equation for the Reynolds stress into the fifth term to obtain

$$
\begin{aligned}
2a_{ij}\hat{S}_{qk}r_{kq} &= 2a_{ij}\hat{S}_{qk}[\frac{(1-\phi)}{2}(\delta_{kq}-a_{kq})+\phi a_{kq}+\frac{\gamma}{2}\frac{\Omega_s}{\Omega}(\epsilon_{ksy}a_{yq}+\epsilon_{qsy}a_{yk})] \\
&= (1-\phi)\hat{S}_{qk}(\delta_{kq}-a_{kq})a_{ij}+2\phi\hat{S}_{qk}a_{kq}a_{ij}+\gamma\frac{\Omega_s}{\Omega}\hat{S}_{qk}[\epsilon_{ksy}a_{yq}+\epsilon_{qsy}a_{yk}]a_{ij} \\
&= a_{ij}[2\phi\hat{S}_{qk}a_{kq}+(1-\phi)\hat{S}_{qq}-(1-\phi)\hat{S}_{qk}a_{kq}]+\frac{\gamma\Omega_s}{\Omega}[\hat{S}_{qk}\epsilon_{ksy}a_{yq}+\hat{S}_{qk}\epsilon_{qsy}a_{yk}]a_{ij}\,.
\end{aligned}
\tag{C.18}
$$

Substituting the expression for $\hat{S}_{ij}$ into eq. (C.18) yields,

$$
\begin{aligned}
2a_{ij}\hat{S}_{qk}r_{kq} &= a_{ij}[(3\phi-1)(S_{qk}+\frac{C^v}{\tau}r_{qw}d_{wk})a_{kq}+(1-\phi)\frac{C^v}{\tau}r_{qw}d_{wq}]+2\gamma\frac{\Omega_s}{\Omega}S_{qk}\epsilon_{ksy}a_{yq}a_{ij} \\
&+\gamma\frac{\Omega_s}{\Omega}a_{ij}\frac{C^v}{\tau}(r_{qs}d_{sk})[\epsilon_{ksy}a_{yq}+\epsilon_{qsy}a_{yk}]+(1-\phi)S_{qq}a_{ij} \\
&= a_{ij}(3\phi-1)S_{qk}a_{kq}+2\gamma\frac{\Omega_s}{\Omega}S_{qk}\epsilon_{ksy}a_{yq}a_{ij}+a_{ij}[(3\phi-1)\frac{C^v}{\tau}r_{qw}d_{wk}a_{kq}] \\
&+\gamma\frac{\Omega_s}{\Omega}a_{ij}\frac{C^v}{\tau}(r_{qs}d_{sk})[\epsilon_{ksy}a_{yq}+\epsilon_{qsy}a_{yk}]+(1-\phi)\frac{C^v}{\tau}r_{qs}d_{sq}a_{ij}+(1-\phi)S_{qq}a_{ij}\,.
\end{aligned}
\tag{C.19}
$$

Next, we deal with the fourth term of eq. (C.17). We use the conditioned expression for the Reynolds stress

$$
\langle V_kV_q|a\rangle a_ia_j = R^{|a}_{kq}a_ia_j = \tilde{V}^2[\frac{(1-\tilde{\phi})}{2}(\delta_{kq}-a_ka_q)+\tilde{\phi}a_ka_q+\frac{\tilde{\gamma}}{2}\frac{\Omega_s}{\Omega}(\epsilon_{kst}a_ta_q+\epsilon_{qst}a_ta_k)]a_ia_j\,,
\tag{C.20}
$$

where the symbol $|a\rangle$ denotes particle properties averaged over a constant eddy-axis vector a_i.

Substituting eq. (C.20) in the fourth term yields,

$$
\begin{aligned}
&-\frac{2G^v_{qk}}{q^2}\langle v_kv_qA_iA_j\rangle = -\frac{2G^v_{qk}}{q^2}\langle R_{kq}a_ia_j\rangle = -2\frac{G^v_{qk}}{q^2}\langle\frac{\tilde{V}^2(1-\tilde{\phi})}{2}(\delta_{kq}-a_ka_q)a_ia_j\rangle \\
&-2\frac{G^v_{qk}}{q^2}\langle\tilde{V}^2\tilde{\phi}a_ka_qa_ia_j\rangle-2\frac{G^v_{qk}}{q^2}\langle\frac{\tilde{V}^2\tilde{\gamma}}{2}\frac{\Omega_s}{\Omega}(\epsilon_{kst}a_ta_q+\epsilon_{qst}a_ta_k)a_ia_j\rangle \\
&= -\frac{G^v_{qk}}{q^2}\langle\tilde{V}^2(1-\tilde{\phi})[\delta_{kq}a_ia_j-a_ka_qa_ia_j]\rangle-\frac{2G^v_{qk}}{q^2}\langle\tilde{V}^2\tilde{\phi}a_ka_qa_ia_j\rangle \\
&-2\frac{\hat{S}_{qk}}{q^2}\langle\frac{\tilde{V}^2\tilde{\gamma}}{2}\frac{\Omega_s}{\Omega}(\epsilon_{kst}a_ta_q+\epsilon_{qst}a_ta_k)a_ia_j\rangle-2\frac{\Omega_{qk}}{q^2}\langle\frac{\tilde{V}^2\tilde{\gamma}}{2}\frac{\Omega_s}{\Omega}(\epsilon_{kst}a_ta_q+\epsilon_{qst}a_ta_k)a_ia_j\rangle\,.
\end{aligned}
\tag{C.21}
$$

The last term of eq. (C.21) is zero, as shown below

$$
\begin{aligned}
&-\frac{2}{q^2}[\langle\Omega_{qk}\frac{\tilde{V}^2\tilde{\gamma}}{2}\frac{\Omega_s}{\Omega}\epsilon_{kst}a_t a_q a_i a_j + \Omega_{qk}\frac{\tilde{V}^2\tilde{\gamma}}{2}\frac{\Omega_s}{\Omega}\epsilon_{qst}a_t a_k a_i a_j\rangle] = \\
&-\frac{2}{q^2}[\langle\Omega_{qk}\frac{\tilde{V}^2\tilde{\gamma}}{2}\frac{\Omega_s}{\Omega}\epsilon_{kst}a_t a_q a_i a_j - \Omega_{kq}\frac{\tilde{V}^2\tilde{\gamma}}{2}\frac{\Omega_s}{\Omega}\epsilon_{qst}a_t a_k a_i a_j\rangle]\,.
\end{aligned}
\tag{C.22}
$$

Interchanging the indices yields

$$
-\frac{2}{q^2}[\langle(\Omega_{qk} - \Omega_{qk})\frac{\tilde{V}^2\tilde{\gamma}}{2}\frac{\Omega_s}{\Omega}\epsilon_{kst}a_t a_q a_i a_j\rangle] = 0\,. \tag{C.23}
$$

Substituting eq. (C.23) into eq. (C.21) yields,

$$
\begin{aligned}
&-2\frac{G^v_{qk}}{q^2}\langle v_k v_q A_i A_j\rangle = -\frac{G^v_{qk}}{q^2}\langle\tilde{V}^2(1-\tilde{\phi})[\delta_{kq}a_i a_j - a_k a_q a_i a_j]\rangle - \frac{2G^v_{qk}}{q^2}\langle\tilde{V}^2\tilde{\phi}a_k a_q a_i a_j\rangle \\
&-2\frac{\hat{S}_{qk}}{q^2}\langle\frac{\tilde{V}^2\tilde{\gamma}}{2}\frac{\Omega_s}{\Omega}(\epsilon_{kst}a_t a_q + \epsilon_{qst}a_t a_k)a_i a_j\rangle \\
&= -\frac{1}{q^2}[G^v_{qq}\langle\tilde{V}^2(1-\tilde{\phi})a_i a_j\rangle + G^v_{qk}\langle-(1-\tilde{\phi})\tilde{V}^2 a_k a_q a_i a_j\rangle] - \frac{2G^v_{qk}}{q^2}\langle\tilde{V}^2\tilde{\phi}a_k a_q a_i a_j\rangle \\
&-\frac{1}{q^2}\frac{C^v}{\tau}\langle\tilde{V}^2\tilde{\gamma}\frac{\Omega_s}{\Omega}(\epsilon_{kst}a_t a_q a_i a_j)\rangle[r_{qp}d_{pk} + r_{kp}d_{pq}] - \frac{2S_{qk}}{q^2}\langle\frac{\tilde{V}^2\tilde{\gamma}}{2}\frac{2\Omega_s}{\Omega}(\epsilon_{kst}a_t a_q a_i a_j)\rangle \\
&= -\frac{1}{q^2}\frac{C^v}{\tau}r_{qw}d_{wq}\langle\tilde{V}^2(1-\tilde{\phi})a_i a_j\rangle + \frac{G^v_{qk}}{q^2}\langle(1-\tilde{\phi})\tilde{V}^2 a_k a_q a_i a_j\rangle - \frac{2G^v_{qk}}{q^2}\langle\tilde{V}^2\tilde{\phi}a_k a_q a_i a_j\rangle \\
&-\frac{1}{q^2}\frac{C^v}{\tau}\langle\tilde{V}^2\tilde{\gamma}\frac{\Omega_s}{\Omega}(\epsilon_{kst}a_t a_q a_i a_j)\rangle[r_{qp}d_{pk} + r_{kp}d_{pq}] - \frac{2S_{qk}}{q^2}\langle\tilde{V}^2\tilde{\gamma}\frac{\Omega_s}{\Omega}(\epsilon_{kst}a_t a_q a_i a_j)\rangle \\
&-\frac{1}{q^2}S_{qq}\langle\tilde{V}^2(1-\tilde{\phi})a_i a_j\rangle\,.
\end{aligned}
\tag{C.24}
$$

Averaging over all eddy-axis vectors yields,

$$
\begin{aligned}
-2\frac{G^v_{qk}}{q^2}\langle v_k v_q A_i A_j\rangle = &-\frac{C^v}{\tau}r_{qw}d_{wq}(1-\phi)a_{ij} + S_{qk}(1-\phi)Z^a_{kqij} + \frac{C^v}{\tau}r_{qw}d_{wk}(1-\phi)Z^a_{kqij} \\
&-2\phi S_{qk}Z^a_{kqij} - 2\phi\frac{C^v}{\tau}r_{qw}d_{wk}Z^a_{kqij} - 2\gamma\frac{\Omega_s}{\Omega}S_{qk}\epsilon_{kst}Z^a_{tqij} \\
&-\frac{C^v}{\tau}\gamma\frac{\Omega_s}{\Omega}\epsilon_{kst}Z^a_{tqij}(r_{qp}d_{pk} + r_{kp}d_{pq}) - (1-\phi)S_{qq}a_{ij}\,.
\end{aligned}
\tag{C.25}
$$

The final expression for the fourth term of a_{ij} transport equation is

$$\begin{aligned}
&-2\frac{G^v_{qk}}{q^2}\langle v_k v_q A_i A_j\rangle = \underbrace{(1-3\phi)S_{qk}Z^a_{kqij} - 2\gamma\frac{\Omega_s}{\Omega}S_{qk}\epsilon_{kst}Z^a_{tqij} - (1-\phi)S_{qq}a_{ij}}_{\text{RDT term}} \\
&-\underbrace{a_{ij}\frac{C^v}{\tau}r_{qw}d_{wq}(1-\phi) + (1-3\phi)\frac{C^v}{\tau}r_{qw}d_{wk}Z^a_{kqij} - \frac{C^v}{\tau}\gamma\frac{\Omega_s}{\Omega}\epsilon_{kst}Z^a_{tqij}(r_{qp}d_{pk}+r_{kp}d_{pq})}_{\text{slow term}}\,.
\end{aligned} \tag{C.26}$$

Adding the fourth and the fifth terms of eq. (C.17) together yields,

$$\begin{aligned}
&2a_{ij}\hat{S}_{qk}r_{kq} - \frac{2G^v_{qk}}{q^2}\langle v_k v_q A_i A_j\rangle = a_{ij}(3\phi-1)S_{qk}a_{kq} + 2\gamma\frac{\Omega_s}{\Omega}S_{qk}\epsilon_{ksy}a_{yq}a_{ij} \\
&+(1-3\phi)S_{qk}Z^a_{kqij} - 2\gamma\frac{\Omega_s}{\Omega}S_{qk}\epsilon_{kst}Z^a_{tqij} + a_{ij}[(3\phi-1)\frac{C^v}{\tau}r_{qs}d_{sk}a_{kq} + (1-\phi)\frac{C^v}{\tau}r_{qs}d_{sq}] \\
&-a_{ij}\frac{C^v}{\tau}r_{qs}d_{sq}(1-\phi) + (1-3\phi)\frac{C^v}{\tau}r_{qs}d_{sk}Z^a_{kqij} - \frac{C^v}{\tau}\gamma\frac{\Omega_s}{\Omega}\epsilon_{kst}Z^a_{tqij}(r_{qp}d_{pk}+r_{kp}d_{pq}) \\
&+\frac{C^v}{\tau}\gamma\frac{\Omega_s}{\Omega}\epsilon_{kst}a_{tq}a_{ij}(r_{qp}d_{pk}+r_{kp}d_{pq})\,.
\end{aligned} \tag{C.27}$$

The sixth term of eq. (C.27) cancels with the seventh term, leading to the expression

$$\begin{aligned}
&2a_{ij}\hat{S}_{qk}r_{kq} - \frac{2G^v_{qk}}{q^2}\langle v_k v_q A_i A_j\rangle = \underbrace{S_{qk}(3\phi-1)[a_{ij}a_{kq} - Z^a_{kqij}] + 2\gamma\frac{\Omega_s}{\Omega}S_{qk}\epsilon_{ksy}[a_{yq}a_{ij} - Z^a_{yqij}]}_{\text{RDT term}} \\
&+\underbrace{\frac{C^v}{\tau}r_{qw}d_{wk}(3\phi-1)[a_{ij}a_{kq} - Z^a_{kqij}] + \gamma\frac{\Omega_s}{\Omega}\frac{C^v}{\tau}(r_{qw}d_{wk}+r_{kw}d_{wq})\epsilon_{kst}[a_{tq}a_{ij} - Z^a_{tqij}]}_{\text{slow term}}\,.
\end{aligned} \tag{C.28}$$

Substituting eq. (C.28) in eq. (C.17) results to the following expression

$$\begin{aligned}
\frac{da_{ij}}{dt} &= G^a_{ik}a_{kj} + G^a_{jk}a_{ki} - 2G^a_{ks}Z^a_{ijks} + S_{qk}(3\phi-1)[a_{ij}a_{kq} - Z^a_{kqij}] \\
&+2\gamma\frac{\Omega_s}{\Omega}S_{qk}\epsilon_{ksy}[a_{yq}a_{ij} - Z^a_{yqij}] + \frac{C^v}{\tau}r_{qw}d_{wk}(3\phi-1)[a_{ij}a_{kq} - Z^a_{kqij}] \\
&+\gamma\frac{\Omega_s}{\Omega}\frac{C^v}{\tau}(r_{qw}d_{wk}+r_{kw}d_{wq})\epsilon_{kst}[a_{tq}a_{ij} - Z^a_{tqij}]\,.
\end{aligned} \tag{C.29}$$

In order to decompose eq. (C.29) into an RDT and a slow part, we need to find an expression for the effective gradient G^a_{jk}. Thus we assume that it has the following form

$$G^a_{ij} = G_{ij} + \frac{C^a}{\tau} s_{ik} w_{kj} \, , \tag{C.30}$$

where s_{ij}, w_{ij} might be normalized structure tensors. Substituting eq. (C.30) in eq. (C.29) and assuming that $s_{ij} = r_{ij}$, $w_{ij} = d_{ij}$ yields,

$$\begin{aligned}
\frac{da_{ij}}{dt} = & \underbrace{G_{ik}a_{kj} + G_{jk}a_{ki} - (3\phi + 1)S_{qk}Z^a_{ijkq} + S_{qk}(3\phi - 1)[a_{ij}a_{kq}] + 2\gamma\frac{\Omega_s}{\Omega}S_{qk}\epsilon_{ksy}[a_{yq}a_{ij} - Z^a_{yqij}]}_{\text{RDT term}} \\
& \underbrace{+\frac{C^v}{\tau}r_{qw}d_{wk}(3\phi - 1)[a_{ij}a_{kq} - Z^a_{kqij}] + \gamma\frac{\Omega_s}{\Omega}\frac{C^v}{\tau}(r_{qw}d_{wk} + r_{kw}d_{wq})\epsilon_{kst}[a_{tq}a_{ij} - Z^a_{tqij}]}_{\text{slow term-velocity contribution}} \\
& + \underbrace{\frac{C^a}{\tau}d_{qk}[r_{iq}a_{kj} + r_{jq}a_{ki}] - \frac{2C^a}{\tau}r_{kq}d_{qs}Z^a_{ijks}}_{\text{slow term-eddy contribution}} \, .
\end{aligned} \tag{C.31}$$

The specific form of eq. (C.31) reproduces correctly the RDT limit of the transport equations.

C.1.2 Derivation of the transport equation for the jetal parameter ϕ.

In order to achieve the closure of the system we need to incorporate modified transport equations for the remaining structure parameters which take into account the non-linear effects. Starting with the vortical parameter ϕ, its transport equation can be derived through the following equation

$$\frac{d\phi}{dt} = \frac{1}{q^2}[\langle\frac{dR^{|a}_{ij}}{dt}a_i a_j\rangle + \langle R^{|a}_{ij}\frac{d}{dt}(a_i a_j)\rangle - \frac{\langle R^{|a}_{ij}a_i a_j\rangle}{q^2}\langle\frac{dq^2}{dt}\rangle] \, . \tag{C.32}$$

We consider the second term first. Use of eq. (C.1) leads to the following expression

$$\frac{d(a_i a_j)}{dt} = G^a_{iq}a_q a_j + G^a_{jq}a_q a_i - 2G^a_{qs}a_q a_s a_i a_j \, . \tag{C.33}$$

Substituting back into eq. (C.32) yields,

$$\begin{aligned}&\langle R^{|a}_{ij}\frac{d}{dt}(a_i a_j)\rangle = \langle\tilde{V}^2[\frac{(1-\tilde{\phi})}{2}(\delta_{ij}-a_i a_j)+\tilde{\phi}a_i a_j](G^a_{ik}a_k a_j + G^a_{jk}a_k a_i - 2G^a_{ks}a_k a_s a_i a_j)\rangle + \gamma(...)\\ &= \langle\tilde{V}^2[G^a_{ik}\tilde{\phi}a_k a_i + G^a_{jk}\tilde{\phi}a_j a_k - 2\phi G^a_{ks}a_k a_s]\rangle + \langle\frac{\tilde{V}^2\gamma}{2}\frac{\Omega_k}{\Omega}[\epsilon_{ikt}a_t a_j G^a_{iq}a_q a_j + \epsilon_{jkt}a_t a_i G^a_{jq}a_q a_i]\rangle\\ &= 2\langle\frac{\tilde{V}^2\tilde{\gamma}}{2}\frac{\Omega_k}{\Omega}\epsilon_{ikt}[a_t G^a_{iq}a_q]\rangle\,.\end{aligned} \tag{C.34}$$

or

$$\langle R^{|a}_{ij}\frac{d}{dt}(a_i a_j)\rangle = \frac{\gamma\Omega_k}{\Omega}\epsilon_{ikt}G^a_{iq}A_{qt}\,. \tag{C.35}$$

The third term of eq. (C.32) is

$$\begin{aligned}\frac{\langle R^{|a}_{ij}a_i a_j\rangle}{q^2}\frac{d\langle q^2\rangle}{dt} &= \langle\frac{(1-\tilde{\phi})}{2}(\delta_{ij}-a_i a_j)a_i a_j\rangle \times -2S^v_{kq}R_{qk} + \langle\tilde{\phi}a_i a_j a_i a_j\rangle \times -2S^v_{kq}R_{qk}\\ &+ \langle\frac{\tilde{\gamma}}{2}\frac{\Omega_k}{\Omega}(\epsilon_{ikt}a_t a_j + \epsilon_{jkt}a_t a_i)a_i a_j\rangle \times -2S^v_{kq}R_{qk}\\ &= -2\phi S^v_{kq}R_{qk}\,.\end{aligned} \tag{C.36}$$

Next, we consider the first term of eq. (C.32), given by

$$\begin{aligned}&\langle\frac{dR^{|a}_{ij}}{dt}a_i a_j\rangle = -\langle G^v_{ik}R^{|a}_{kj}a_i a_j\rangle - G^v_{jk}\langle R^{|a}_{ki}a_i a_j\rangle\\ &+ (G^n_{km}+G^v_{km})\langle[R^{|a}_{im}n_k n_j + R^{|a}_{jm}n_k n_i]a_i a_j\rangle - \langle[2C_1 R^{|a}_{ij} - C_2^2 R^{|a}_{kk}(\delta_{ij}-n_i n_j)]a_i a_j\rangle\,.\end{aligned} \tag{C.37}$$

Re-expressing,

$$\begin{aligned}&-G^v_{ik}\langle R^{|a}_{kj}a_i a_j\rangle = -G^v_{ik}\langle\tilde{V}^2[\frac{(1-\tilde{\phi})}{2}(\delta_{kj}-a_k a_j)+\tilde{\phi}a_k a_j]a_i a_j\rangle\\ &- G^v_{ik}[\langle\frac{\tilde{V}^2\tilde{\gamma}}{2}\frac{\Omega_q}{\Omega}(\epsilon_{kqt}a_t a_j + \epsilon_{jqt}a_t a_k)a_i a_j\rangle]\\ &= -G^v_{ik}\langle\tilde{V}^2[\frac{(1-\tilde{\phi})}{2}(a_i a_k - a_i a_k)+\tilde{\phi}a_k a_i]\rangle - G^v_{ik}[\langle\frac{\tilde{V}^2\tilde{\gamma}}{2}\frac{\Omega_q}{\Omega}\epsilon_{kqt}a_t a_j a_i a_j\rangle]\\ &= -G^v_{ik}\langle\tilde{V}^2\tilde{\phi}a_k a_i\rangle - G^v_{ik}\epsilon_{kqt}\frac{\gamma}{2}\frac{\Omega_q}{\Omega}A_{ti}\,,\end{aligned} \tag{C.38}$$

yields the simplified equation

$$-G^v_{ik}\langle R^{|a}_{kj}a_ia_j\rangle = -G^v_{ik}\phi A_{ki} - \epsilon_{kqt}G^v_{ik}\frac{\gamma\Omega_q}{2\Omega}A_{ti}\,. \tag{C.39}$$

Summation of the first two terms of eq. (C.37) yields,

$$-G^v_{ik}\langle R^{|a}_{kj}a_ia_j\rangle - G^v_{jk}\langle R^{|a}_{ki}a_ia_j\rangle = -2G^v_{ik}\phi A_{ki} - \epsilon_{kqt}G^v_{ik}\frac{\gamma\Omega_q}{\Omega}A_{ti}\,. \tag{C.40}$$

Next, we consider the fourth term of eq. (C.37) which is given by

$$\begin{aligned} -\langle[2C_1R^{|a}_{ij} - C_2^2R^{|a}_{kk}(\delta_{ij}-n_in_j)]a_ia_j\rangle &= -2\phi\langle C_1\tilde{V}^2\rangle + \langle C_2^2\tilde{V}^2\rangle \\ &= (1-2\phi)\langle C_1\tilde{V}^2\rangle\,, \end{aligned} \tag{C.41}$$

where the slow rotational-randomization coefficient is expressed by

$$\langle C_1\tilde{V}^2\rangle = \frac{8.5}{\tau}\Omega^* f_{pq}D_{pq} = \frac{8.5}{2\tau}\Omega^* q^2[1-f_{pq}a_{qp}]\,. \tag{C.42}$$

Substituting eq. (C.42) in eq. (C.41) yields,

$$-\langle[2C_1R^{|a}_{ij} - C_2^2R^{|a}_{kk}(\delta_{ij}-n_in_j)]a_ia_j\rangle = (1-2\phi)\frac{8.5\Omega^*}{2\tau}q^2[1-f_{pq}a_{qp}]\,. \tag{C.43}$$

Substituting all simplified terms back to eq. (C.32) leads,

$$\frac{d\phi}{dt} = \underbrace{\gamma\frac{\Omega_k}{\Omega}\epsilon_{ikt}G^a_{iq}a_{qt} - \frac{\gamma\Omega_q}{\Omega}\epsilon_{kqt}G^v_{ik}a_{ti} + 2\phi(S^v_{kq}r_{qk} - S^v_{ik}a_{ki})}_{\text{RDT term}} + \underbrace{(1-2\phi)\frac{8.5\Omega^*}{2\tau}(1-f_{pq}a_{qp})}_{\text{slow term}}\,. \tag{C.44}$$

The first two terms of eq. (C.44) can be put into the form

$$\begin{aligned} \gamma\frac{\Omega_k}{\Omega}\epsilon_{ikt}G^a_{iq}a_{qt} - \gamma\frac{\Omega_k}{\Omega}\epsilon_{ikt}G^v_{si}a_{ts} &= \gamma\frac{\Omega_k}{\Omega}\epsilon_{ikt}[G^a_{is}a_{st} - G^v_{si}a_{ts}] \\ &= \gamma\frac{\Omega_k}{\Omega}\epsilon_{ikt}([\Omega_{is}a_{st} - \Omega_{si}a_{ts}] + a_{ts}[\frac{C_a}{\tau}r_{iq}d_{qs} - \frac{C_v}{\tau}r_{sq}d_{qi}])\,. \end{aligned} \tag{C.45}$$

Substituting eq. (C.45) in eq. (C.44) yields,

$$\begin{aligned}\frac{d\phi}{dt} &= 2\gamma\frac{\Omega_k}{\Omega}\epsilon_{ikt}\Omega_{is}a_s a_t + 2\phi S^v_{kq}[r_{qk} - a_{qk}] + (1-2\phi)\frac{8.5\Omega^*}{2\tau}(1 - f_{pq}a_{qp}) \\ &+ \gamma\frac{\Omega_k}{\Omega}\epsilon_{ikt}a_{ts}[\frac{C_a}{\tau}r_{iq}d_{qs} - \frac{C_v}{\tau}r_{sq}d_{qi}]\,.\end{aligned} \tag{C.46}$$

The relation between the antisymmetric part of the mean velocity gradient tensor and the mean rotation vector is given by

$$\Omega_{ij} = \frac{1}{2}\epsilon_{jiz}\Omega_z\,. \tag{C.47}$$

Substituting eq. (C.47) in eq. (C.46) yields,

$$\begin{aligned}\frac{d\phi}{dt} &= \epsilon_{ikt}\epsilon_{izs}\gamma\frac{\Omega_k}{\Omega}\Omega_z a_s a_t + 2\phi S^v_{kq}[r_{qk} - a_{qk}] + (1-2\phi)\frac{8.5\Omega^*}{2\tau}(1 - f_{pq}a_{qp}) \\ &+ \gamma\frac{\Omega_k}{\Omega}\epsilon_{ikt}a_{ts}[\frac{C_a}{\tau}r_{iq}d_{qs} - \frac{C_v}{\tau}r_{sq}d_{qi}] \\ &= (\delta_{kz}\delta_{ts} - \delta_{ks}\delta_{tz})\gamma\frac{\Omega_k}{\Omega}\Omega_z a_s a_t + 2\phi S^v_{kq}[r_{qk} - a_{qk}] + (1-2\phi)\frac{8.5\Omega^*}{2\tau}(1 - f_{pq}a_{qp}) \\ &+ \gamma\frac{\Omega_k}{\Omega}\epsilon_{ikt}a_{ts}[\frac{C_a}{\tau}r_{iq}d_{qs} - \frac{C_v}{\tau}r_{sq}d_{qi}] \\ &= \gamma\frac{\Omega_s\Omega_t}{\Omega}[\delta_{st} - a_s a_t] + 2\phi S^v_{kq}[r_{qk} - a_{qk}] \\ &+ (1-2\phi)\frac{8.5\Omega^*}{2\tau}(1 - f_{pq}a_{qp}) + \gamma\frac{\Omega_k}{\Omega}\epsilon_{ikt}a_{ts}[\frac{C_a}{\tau}r_{iq}d_{qs} - \frac{C_v}{\tau}r_{sq}d_{qi}]\,.\end{aligned} \tag{C.48}$$

Thus the final equation for the evolution of ϕ reduces to the following form

$$\begin{aligned}\frac{d\phi}{dt} &= \underbrace{\gamma\frac{\Omega_s\Omega_t}{\Omega}[\delta_{st} - a_s a_t] + 2\phi S^v_{kq}[r_{qk} - a_{qk}]}_{\text{RDT term}} \\ &+ \underbrace{(1-2\phi)\frac{8.5\Omega^*}{2\tau}(1 - f_{pq}a_{qp}) + \gamma\frac{\Omega_k}{\Omega}\epsilon_{ikt}a_{ts}[\frac{C_a}{\tau}r_{iq}d_{qs} - \frac{C_v}{\tau}r_{sq}d_{qi}]}_{\text{slow term}}\,.\end{aligned} \tag{C.49}$$

C.1.3 Derivation of the transport equation for the stropholysis scalar γ.

Next, we consider the stropholysis scalar γ. A useful identity is

$$\langle R_{ij}^{|a} \frac{\Omega_z}{\Omega} \epsilon_{izm} a_m a_j \rangle = \gamma \frac{\Omega_k \Omega_z}{\Omega^2} \frac{1}{2} (q^2 \delta_{kz} - A_{kz}) \,. \tag{C.50}$$

For our analysis, some useful identities are given below

$$\frac{d\Omega_k}{dt} = \Omega_r S_{kr} \,, \qquad \frac{d}{dt}(\frac{1}{\Omega}) = -\frac{\Omega_k}{\Omega^3} \frac{d\Omega_k}{dt} \,, \tag{C.51}$$

$$\frac{d\Omega^2}{dt} = 2\Omega_k \frac{d\Omega_k}{dt} \,, \qquad \frac{d}{dt}(\frac{1}{\Omega^2}) = -2\frac{\Omega_k}{\Omega^4} \frac{d\Omega_k}{dt} \,. \tag{C.52}$$

Taking the time-derivative of eq. (C.50) yields,

$$\begin{aligned} &\langle (\frac{dR_{ij}^{|a}}{dt}) \frac{\Omega_z}{\Omega} \epsilon_{izm} a_m a_j \rangle + \langle R_{ij}^{|a} \frac{d}{dt}(\frac{\Omega_z}{\Omega}) \epsilon_{izm} a_m a_j \rangle + \epsilon_{izm} \langle R_{ij}^{|a} \frac{\Omega_z}{\Omega} \frac{d}{dt}(a_m a_j) \rangle = \\ &(\frac{d\gamma}{dt}) \frac{\Omega_k \Omega_z}{\Omega^2} \frac{1}{2} (q^2 \delta_{kz} - A_{kz}) + \gamma \frac{d}{dt}(\frac{\Omega_k \Omega_z}{\Omega^2}) \frac{1}{2} (q^2 \delta_{kz} - A_{kz}) + \gamma \frac{\Omega_k \Omega_z}{2\Omega^2} \frac{d}{dt}(q^2 \delta_{kz} - A_{kz}) \,. \end{aligned} \tag{C.53}$$

Use of eqs. (C.51) leads to the following expression

$$\begin{aligned} \frac{d}{dt}(\frac{\Omega_k \Omega_z}{\Omega^2}) &= \frac{\Omega_k \Omega_r}{\Omega^2} S_{zr} + \frac{\Omega_z \Omega_r}{\Omega^2} S_{kr} + \Omega_k \Omega_z (-2\frac{\Omega_q}{\Omega^4} \frac{d\Omega_q}{dt}) \\ &= \frac{1}{\Omega^2} (\Omega_k \Omega_r S_{zr} + \Omega_z \Omega_r S_{kr}) - 2\frac{\Omega_k \Omega_z \Omega_q \Omega_r}{\Omega^4} S_{qr} \,. \end{aligned} \tag{C.54}$$

Substituting eq. (C.54) in the second term of the RHS of eq. (C.53) yields,

$$\begin{aligned} &\gamma \frac{d}{dt}(\frac{\Omega_k \Omega_z}{\Omega^2}) \frac{1}{2} (q^2 \delta_{kz} - A_{kz}) = \frac{\gamma}{2} [\frac{1}{\Omega^2} (\Omega_k \Omega_r S_{zr} + \Omega_z \Omega_r S_{kr}) - \frac{2\Omega_k \Omega_z \Omega_q \Omega_r S_{qr}}{\Omega^4}] (q^2 \delta_{kz} - A_{kz}) \\ &= \frac{\gamma}{2} \frac{q^2}{\Omega^2} [\Omega_z \Omega_r S_{zr} + \Omega_z \Omega_r S_{zr} - 2\Omega_q \Omega_r S_{qr}] - \frac{q^2 \gamma}{2\Omega^2} [(\Omega_k \Omega_r S_{zr} + \Omega_z \Omega_r S_{kr}) a_{kz} \\ &- 2\frac{\Omega_k \Omega_z \Omega_q \Omega_r}{\Omega^2} S_{qr} a_{kz}] \\ &= -\frac{q^2 \gamma}{2\Omega^2} [\Omega_z \Omega_r S_{kr} a_{zk} + \Omega_z \Omega_r S_{kr} a_{kz} - 2\frac{\Omega_k \Omega_z}{\Omega^2} \Omega_q \Omega_r S_{qr} a_{kz}] \\ &= -\frac{2q^2 \gamma}{2\Omega^2} [\Omega_z \Omega_r S_{kr} a_{zk} - \frac{\Omega_k \Omega_z \Omega_q \Omega_r}{\Omega^2} S_{qr} a_{kz}] \,. \end{aligned} \tag{C.55}$$

or

$$\gamma\frac{d}{dt}(\frac{\Omega_k\Omega_z}{\Omega^2})\frac{1}{2}(q^2\delta_{kz}-A_{kz}) = q^2\gamma[\frac{\Omega_k\Omega_z\Omega_q\Omega_r}{\Omega^4}S_{qr}a_{kz}-\frac{\Omega_z\Omega_r}{\Omega^2}S_{kr}a_{kz}]\,. \tag{C.56}$$

The third term of the RHS of eq. (C.53) is given by

$$\frac{d}{dt}(q^2\delta_{kz}-A_{kz}) = -2S^v_{km}R_{mk}\delta_{kz}-G^a_{kq}A_{qz}-G^a_{zq}A_{qk}+2G^a_{pq}q^2Z^a_{kzpq}+2G^v_{qs}\langle R^{|a}_{sq}a_ka_z\rangle\,. \tag{C.57}$$

Consequently,

$$\frac{\gamma\Omega_k\Omega_z}{2\Omega^2}\frac{d}{dt}(q^2\delta_{kz}-A_{kz}) = -\gamma S^v_{km}R_{mk}+\gamma\frac{\Omega_k\Omega_z}{\Omega^2}[-G^a_{kq}A_{qz}+S^a_{pq}q^2Z^a_{kzpq}+S^v_{qs}\langle R^{|a}_{sq}a_ka_z\rangle]\,. \tag{C.58}$$

Next, we deal with the LHS of eq. (C.53). The third term of this equation is treated as follow

$$\begin{aligned}
\epsilon_{izm}\langle R^{|a}_{ij}\frac{\Omega_z}{\Omega}\frac{d}{dt}(a_ma_j)\rangle &= \epsilon_{izm}\langle\tilde{V}^2[\frac{(1-\tilde{\phi})}{2}(\delta_{ij}-a_ia_j)]\frac{\Omega_z}{\Omega}[G^a_{mq}a_qa_j+G^a_{jq}a_qa_m\\
&-2G^a_{qs}a_qa_sa_ma_j]\rangle+\epsilon_{izm}\langle\tilde{V}^2\tilde{\phi}a_ia_j\frac{\Omega_z}{\Omega}[G^a_{mq}a_qa_j+G^a_{jq}a_qa_m-2G^a_{qs}a_qa_sa_ma_j]\rangle\\
&+\epsilon_{izm}\langle\tilde{V}^2\frac{\tilde{\gamma}}{2}\frac{\Omega_k}{\Omega}\frac{\Omega_z}{\Omega}(\epsilon_{ikt}a_ta_j+\epsilon_{jkt}a_ta_i)[G^a_{mq}a_qa_j+G^a_{jq}a_qa_m-2G^a_{qs}a_qa_sa_ma_j]\rangle\\
&=\epsilon_{izm}\langle\tilde{V}^2\frac{(1-\tilde{\phi})}{2}\frac{\Omega_z}{\Omega}[G^a_{mq}a_qa_i+G^a_{iq}a_qa_m-G^a_{qs}a_qa_sa_ma_i-G^a_{mq}a_qa_i]\rangle\\
&+\epsilon_{izm}\langle\tilde{V}^2\tilde{\phi}\frac{\Omega_z}{\Omega}[G^a_{mq}a_qa_ja_ia_j]\rangle+\epsilon_{izm}\langle\frac{\tilde{V}^2\tilde{\gamma}}{2}\frac{\Omega_k}{\Omega}\frac{\Omega_z}{\Omega}\epsilon_{ikt}a_ta_j[G^a_{mq}a_qa_j+G^a_{jq}a_qa_m\\
&-2G^a_{qs}a_qa_sa_ma_j]\rangle+\epsilon_{izm}\frac{\Omega_z}{\Omega}\langle\frac{\tilde{V}^2\tilde{\gamma}}{2}\frac{\Omega_k}{\Omega}\epsilon_{jkt}a_ta_iG^a_{mq}a_qa_j\rangle\\
&=\epsilon_{izm}\langle\frac{\tilde{V}^2(1-\tilde{\phi})}{2}\frac{\Omega_z}{\Omega}[G^a_{iq}a_qa_m-G^a_{qs}a_qa_sa_ma_i]\rangle+\epsilon_{izm}\langle\tilde{V}^2\tilde{\phi}\frac{\Omega_z}{\Omega}G^a_{mq}a_qa_i\rangle\\
&+\frac{\gamma}{2}\frac{\Omega_k\Omega_z}{\Omega^2}[\delta_{zk}\delta_{mt}-\delta_{zt}\delta_{mk}]\langle\tilde{V}^2a_ta_j[G^a_{mq}a_qa_j+G^a_{jq}a_qa_m-2G^a_{qs}a_qa_sa_ma_j]\rangle\\
&+\frac{\gamma}{2}\frac{\Omega_k\Omega_z}{\Omega^2}\epsilon_{izm}\epsilon_{jkt}G^a_{mq}\langle\tilde{V}^2a_ta_ia_qa_j\rangle\\
&=q^2\epsilon_{izm}\frac{(1-\phi)}{2}\frac{\Omega_z}{\Omega}[G^a_{iq}a_{qm}-G^a_{qs}Z^a_{qsmi}]+q^2\phi\epsilon_{izm}\frac{\Omega_z}{\Omega}G^a_{mq}a_{qi}\\
&+\frac{q^2\gamma}{2}\delta_{mt}[G^a_{mq}a_{qt}-G^a_{qs}Z^a_{qsmt}]-\frac{q^2\gamma}{2}\frac{\Omega_m\Omega_t}{\Omega^2}[G^a_{mq}a_{qt}-G^a_{qs}Z^a_{qsmt}]\,,
\end{aligned} \tag{C.59}$$

or

$$
\begin{aligned}
&\epsilon_{izm}\langle R_{ij}^{|a}\frac{\Omega_z}{\Omega}\frac{d}{dt}(a_m a_j)\rangle = q^2\epsilon_{izm}\frac{(1-\phi)}{2}\frac{\Omega_z}{\Omega}[G^a_{iq}a_{qm} - G^a_{qs}Z^a_{qsmi}] + q^2\phi\epsilon_{izm}\frac{\Omega_z}{\Omega}G^a_{mq}a_{qi} \\
&+ \frac{q^2\gamma}{2}(\delta_{mt} - \frac{\Omega_m\Omega_t}{\Omega^2})(G^a_{mq}a_{qt} - G^a_{qs}Z^a_{qsmt}) = q^2[\epsilon_{izm}\frac{(1-\phi)}{2}\frac{\Omega_z}{\Omega}G^a_{iq}a_{qm} + \phi\epsilon_{izm}\frac{\Omega_z}{\Omega}G^a_{mq}a_{qi}] \\
&- \frac{q^2\gamma}{2}\frac{\Omega_m\Omega_t}{\Omega^2}[G^a_{mq}a_{qt} - G^a_{qs}Z^a_{qsmt}]\,.
\end{aligned}
\tag{C.60}
$$

Now, the second term of the LHS of eq. (C.53) is given by

$$
\begin{aligned}
&\langle R_{ij}^{|a}\frac{d}{dt}(\frac{\Omega_z}{\Omega})\epsilon_{izm}a_m a_j\rangle = \langle\tilde{V}^2[\frac{(1-\phi)}{2}(\delta_{ij} - a_i a_j)\frac{d}{dt}(\frac{\Omega_z}{\Omega})\epsilon_{izm}a_m a_j]\rangle \\
&+ \langle\tilde{V}^2\tilde{\phi}a_i a_j\frac{d}{dt}(\frac{\Omega_z}{\Omega})\epsilon_{izm}a_m a_j\rangle + \langle\frac{\tilde{V}^2\tilde{\gamma}}{2}\frac{\Omega_k}{\Omega}(\epsilon_{ikt}a_t a_j + \epsilon_{jkt}a_t a_i)\frac{d}{dt}(\frac{\Omega_z}{\Omega})\epsilon_{izm}a_m a_j\rangle \\
&= \frac{q^2\gamma}{2}\frac{\Omega_k}{\Omega}\epsilon_{ikt}\langle a_t\frac{d}{dt}(\frac{\Omega_z}{\Omega})\epsilon_{izm}a_m\rangle = \frac{q^2\gamma}{2}(\delta_{kz}\delta_{mt} - \delta_{km}\delta_{tz})\frac{\Omega_k}{\Omega}\frac{d}{dt}(\frac{\Omega_z}{\Omega})a_{mt}\,.
\end{aligned}
\tag{C.61}
$$

The following useful identity is derived if we use eqs. (C.51)

$$
\begin{aligned}
\frac{d}{dt}(\frac{\Omega_z}{\Omega}) &= \frac{1}{\Omega}\frac{d}{dt}\Omega_z + \Omega_z\frac{d}{dt}(\frac{1}{\Omega}) = \frac{1}{\Omega}(\Omega_r S_{zr}) + \Omega_z[-\frac{\Omega_q}{\Omega^3}\frac{d}{dt}\Omega_q] \\
&= \frac{\Omega_r}{\Omega}S_{zr} - \frac{\Omega_z\Omega_q}{\Omega^3}\Omega_r S_{qr}\,.
\end{aligned}
\tag{C.62}
$$

Substituting back into eq. (C.61) yields,

$$
\begin{aligned}
\langle R_{ij}^{|a}\frac{d}{dt}(\frac{\Omega_z}{\Omega})\epsilon_{izm}a_m a_j\rangle &= \frac{q^2\gamma}{2}\frac{\Omega_k}{\Omega}(\frac{\Omega_r S_{zr}}{\Omega} - \frac{\Omega_z\Omega_q}{\Omega^3}\Omega_r S_{qr})(\delta_{kz}\delta_{mt} - \delta_{km}\delta_{tz})a_{mt} \\
&= \frac{q^2\gamma\Omega_k}{2\Omega}[\frac{\Omega_r}{\Omega}S_{kr} - \frac{\Omega_k\Omega_q}{\Omega^3}\Omega_r S_{qr}] - \frac{q^2\gamma}{2}\frac{\Omega_m}{\Omega}[\frac{\Omega_r S_{tr}}{\Omega} - \frac{\Omega_t\Omega_q\Omega_r S_{qr}}{\Omega^3}]a_{mt} \\
&= -\frac{q^2\gamma}{2\Omega}\frac{\Omega_m}{\Omega}\Omega_r S_{tr}a_{mt} + \frac{q^2\gamma}{2}\frac{\Omega_m\Omega_t\Omega_q\Omega_r}{\Omega^4}S_{qr}a_{mt}\,.
\end{aligned}
\tag{C.63}
$$

or

$$
\langle R_{ij}^{|a}\frac{d}{dt}(\frac{\Omega_z}{\Omega})\epsilon_{izm}a_m a_j\rangle = \frac{q^2\gamma\Omega_m\Omega_r}{2\Omega^2}a_{mt}[\frac{\Omega_t\Omega_q}{\Omega^2}S_{qr} - S_{tr}]\,.
\tag{C.64}
$$

Next, we deal with the first term of the LHS of eq. (C.53), which is the most complicated one

$$\begin{aligned}&\langle (\frac{dR^{|a}_{ij}}{dt})\frac{\Omega_z}{\Omega}\epsilon_{izm}a_m a_j\rangle = -G^v_{ik}\langle R^{|a}_{kj}\frac{\Omega_z}{\Omega}\epsilon_{izm}a_m a_j - G^v_{jk}\langle R^{|a}_{ki}\frac{\Omega_z}{\Omega}\epsilon_{izm}a_m a_j\rangle \\ &+ [G^n_{kq}+G^v_{kq}]\Bigg((\langle V_i V_q n_k n_j|a\rangle + \langle V_j V_q n_k n_i|a\rangle)\frac{\Omega_z}{\Omega}\epsilon_{izm}a_m a_j\Bigg) + \text{slow term}\,.\end{aligned} \tag{C.65}$$

The first term of eq. (C.65) is treated as follow

$$\begin{aligned}&-G^v_{ik}\langle R^{|a}_{kj}\frac{\Omega_z}{\Omega}\epsilon_{izm}a_m a_j\rangle = -G^v_{ik}\langle \tilde{V}^2[\frac{(1-\tilde{\phi})}{2}(\delta_{kj}-a_k a_j)]\frac{\Omega_z}{\Omega}\epsilon_{izm}a_m a_j\rangle \\ &- G^v_{ik}\langle \tilde{V}^2\tilde{\phi}a_k a_j\frac{\Omega_z}{\Omega}\epsilon_{izm}a_m a_j\rangle \\ &- G^v_{ik}\langle \frac{\tilde{V}^2\tilde{\gamma}}{2}\frac{\Omega_q}{\Omega}(\epsilon_{kqt}a_t a_j + \epsilon_{jqt}a_t a_k)\frac{\Omega_z}{\Omega}\epsilon_{izm}a_m a_j\rangle \\ &= -G^v_{ik}\langle \tilde{V}^2\frac{(1-\tilde{\phi})}{2}\frac{\Omega_z}{\Omega}\epsilon_{izm}a_m a_k\rangle + G^v_{ik}\langle \tilde{V}^2\frac{(1-\tilde{\phi})}{2}\frac{\Omega_z}{\Omega}\epsilon_{izm}a_m a_k\rangle \\ &- G^v_{ik}\langle \tilde{V}^2\tilde{\phi}\frac{\Omega_z}{\Omega}\epsilon_{izm}a_m a_k\rangle - G^v_{ik}\langle \frac{\tilde{V}^2\tilde{\gamma}\Omega_q\Omega_z}{2\Omega^2}[\epsilon_{kqt}\epsilon_{izm}a_t a_m + \epsilon_{jqt}\epsilon_{izm}a_t a_k a_m a_j]\rangle \\ &= -G^v_{ik}\langle \tilde{V}^2\tilde{\phi}\frac{\Omega_z}{\Omega}\epsilon_{izm}a_m a_k - G^v_{ik}\langle \frac{\tilde{V}^2\tilde{\gamma}\Omega_q\Omega_z}{2\Omega^2}\epsilon_{kqt}\epsilon_{izm}a_t a_m\rangle\,.\end{aligned} \tag{C.66}$$

Thus we obtain

$$-G^v_{ik}\langle R^{|a}_{kj}\frac{\Omega_z}{\Omega}\epsilon_{izm}a_m a_j\rangle = -G^v_{ik}\phi\frac{\Omega_z}{\Omega}\epsilon_{izm}A_{mk} - G^v_{ik}\gamma\frac{\Omega_q\Omega_z}{2\Omega^2}\epsilon_{kqt}\epsilon_{izm}A_{tm}\,. \tag{C.67}$$

Use of Mahoney's isotropic identities leads to the following expression for the second term of eq. (C.67)

$$
\begin{aligned}
&- G^v_{ik}\gamma\frac{\Omega_q\Omega_z}{2\Omega^2}[\delta_{ki}\delta_{qz}\delta_{tm}+\delta_{kz}\delta_{qm}\delta_{ti}+\delta_{km}\delta_{qi}\delta_{tz}-\delta_{ki}\delta_{qm}\delta_{tz}-\delta_{kz}\delta_{qi}\delta_{tm}-\delta_{km}\delta_{qz}\delta_{ti}]A_{tm}\\
&= -G^v_{ik}\gamma\frac{\Omega_q\Omega_q}{2\Omega^2}\delta_{ki}q^2 - G^v_{ik}\gamma\frac{\Omega_m\Omega_k}{2\Omega^2}A_{im} - G^v_{ik}\gamma\frac{\Omega_i\Omega_t}{2\Omega^2}A_{tk} + G^v_{kk}\gamma\frac{\Omega_m\Omega_t}{2\Omega^2}A_{tm} + G^v_{ik}\gamma\frac{\Omega_i\Omega_k}{2\Omega^2}q^2\\
&+ G^v_{ik}\gamma\frac{\Omega_q\Omega_q}{2\Omega^2}A_{ik}\\
&= -G^v_{kk}\gamma\frac{\Omega_q\Omega_q}{2\Omega^2}q^2 + G^v_{kk}\gamma\frac{\Omega_m\Omega_t}{2\Omega^2}A_{tm} - G^v_{ik}\gamma[\frac{\Omega_m\Omega_k}{2\Omega^2}A_{im} + \frac{\Omega_i\Omega_t}{2\Omega^2}A_{tk} - \frac{\Omega_i\Omega_k}{2\Omega^2}q^2 - \frac{\Omega_q\Omega_q}{2\Omega^2}A_{ik}]\\
&= -\gamma\frac{S^v_{kk}q^2}{2} + \gamma S^v_{kk}\frac{\Omega_m\Omega_t}{2\Omega^2}A_{tm} - G^v_{ik}\gamma\frac{\Omega_m\Omega_k}{2\Omega^2}A_{im} - G^v_{ik}\gamma\frac{\Omega_i\Omega_t}{2\Omega^2}A_{tk} + S^v_{ik}\gamma\frac{\Omega_i\Omega_k}{2\Omega^2}q^2\\
&+ S^v_{ik}\gamma\frac{\Omega_q\Omega_q}{2\Omega^2}A_{ik}\\
&= -\frac{\gamma S^v_{kk}}{2}q^2 + \gamma S^v_{kk}\frac{\Omega_m\Omega_t}{2\Omega^2}A_{tm} - S^v_{ik}\gamma\frac{\Omega_m\Omega_k}{2\Omega^2}A_{im} - S^v_{ik}\gamma\frac{\Omega_i\Omega_t}{2\Omega^2}A_{tk} + S^v_{ik}\gamma\frac{\Omega_i\Omega_k}{2\Omega^2}q^2 + S^v_{ik}\gamma\frac{\Omega_q\Omega_q}{2\Omega^2}A_{ik}\\
&= -\frac{\gamma S^v_{kk}}{2}q^2 + \gamma S^v_{kk}\frac{\Omega_m\Omega_t}{2\Omega^2}A_{tm} - \gamma S^v_{ik}(A_{im}\frac{\Omega_m\Omega_k}{2\Omega^2} + A_{km}\frac{\Omega_m\Omega_i}{2\Omega^2}) + S^v_{ik}\gamma\frac{\Omega_i\Omega_k}{2\Omega^2}q^2 + S^v_{ik}\gamma\frac{\Omega_q\Omega_q}{2\Omega^2}A_{ik}\,.
\end{aligned}
\tag{C.68}
$$

Substituting eq. (C.68) back into eq. (C.67) one obtains,

$$
\begin{aligned}
-G^v_{ik}\langle R^{|a}_{kj}\frac{\Omega_z}{\Omega}\epsilon_{izm}a_m a_j\rangle = -G^v_{ik}\phi\frac{\Omega_z}{\Omega}\epsilon_{izm}A_{mk} - \gamma\frac{S^v_{kk}}{2}q^2 + \gamma\frac{S^v_{kk}\Omega_m\Omega_t}{2\Omega^2}A_{tm}\\
+ S^v_{ik}\gamma\frac{\Omega_i\Omega_k}{2\Omega^2}q^2 + S^v_{ik}\gamma\frac{\Omega_q\Omega_q}{2\Omega^2}A_{ik} - \gamma S^v_{ik}(A_{im}\frac{\Omega_m\Omega_k}{2\Omega^2} + A_{km}\frac{\Omega_m\Omega_i}{2\Omega^2})\,.
\end{aligned}
\tag{C.69}
$$

The second term of eq. (C.65) is treated as follow

$$
\begin{aligned}
&- G^v_{jk}\langle R^{|a}_{ki}\frac{\Omega_z}{\Omega}\epsilon_{izm}a_m a_j\rangle = -G^v_{jk}\langle\tilde{V}^2\frac{(1-\tilde{\phi})}{2}(\delta_{ki}-a_k a_i)\frac{\Omega_z}{\Omega}\epsilon_{izm}a_m a_j\rangle\\
&- G^v_{jk}\langle\tilde{V}^2\tilde{\phi}a_k a_i\frac{\Omega_z}{\Omega}\epsilon_{izm}a_m a_j\rangle - G^v_{jk}\langle\frac{\tilde{V}^2\tilde{\gamma}}{2}\frac{\Omega_q}{\Omega}(\epsilon_{kqt}a_t a_i + \epsilon_{iqt}a_t a_k)\frac{\Omega_z}{\Omega}\epsilon_{izm}a_m a_j\rangle\\
&= -G^v_{jk}\frac{(1-\phi)}{2}\langle\tilde{V}^2\frac{\Omega_z}{\Omega}\epsilon_{kzm}a_m a_j\rangle + G^v_{jk}\frac{(1-\phi)}{2}\langle\tilde{V}^2\frac{\Omega_z}{\Omega}\epsilon_{izm}a_m a_j a_k a_i\rangle\\
&- G^v_{jk}\phi\frac{\Omega_z}{\Omega}\epsilon_{izm}\langle\tilde{V}^2 a_k a_i a_m a_j\rangle - G^v_{jk}\langle\frac{\tilde{V}^2\tilde{\gamma}}{2\Omega}\Omega_q\epsilon_{iqt}a_t a_k\frac{\Omega_z}{\Omega}\epsilon_{izm}a_m a_j\rangle\\
&= -G^v_{jk}\frac{(1-\phi)}{2}\epsilon_{kzm}\frac{\Omega_z}{\Omega}A_{mj} - G^v_{jk}\frac{\gamma\Omega_q}{2\Omega}(\delta_{qz}\delta_{tm}-\delta_{qm}\delta_{tz})\frac{\Omega_z}{\Omega}\langle\tilde{V}^2 a_t a_k a_m a_j\rangle\\
&= -G^v_{jk}\frac{(1-\phi)}{2}\epsilon_{kzm}\frac{\Omega_z}{\Omega}A_{mj} - G^v_{jk}\gamma\frac{\Omega_q\Omega_q}{2\Omega^2}\langle\tilde{V}^2 a_k a_j\rangle + G^v_{jk}\gamma\frac{\Omega_q\Omega_z}{2\Omega^2}\langle\tilde{V}^2 a_z a_k a_q a_j\rangle\\
&= -G^v_{jk}\frac{(1-\phi)}{2}\epsilon_{kzm}\frac{\Omega_z}{\Omega}A_{mj} - G^v_{jk}\gamma\frac{\Omega_q\Omega_z}{2\Omega^2}[A_{kj}\delta_{qz} - q^2 Z^a_{zkqj}]\,.
\end{aligned}
\tag{C.70}
$$

or

$$- G^v_{jk}\langle R^{|a}_{ki}\frac{\Omega_z}{\Omega}\epsilon_{izm}a_m a_j\rangle = -G^v_{jk}\frac{(1-\phi)}{2}\epsilon_{kzm}\frac{\Omega_z}{\Omega}A_{mj} - G^v_{jk}\gamma\frac{\Omega_q\Omega_z}{2\Omega^2}[A_{kj}\delta_{qz} - q^2 Z^a_{zkqj}]\,. \tag{C.71}$$

Adding eqs. (C.69) and (C.71) together, one finds

$$\begin{aligned}
&- [G^v_{jk}\langle R^{|a}_{ki}\frac{\Omega_z}{\Omega}\epsilon_{izm}a_m a_j\rangle + G^v_{ik}\langle R^{|a}_{kj}\frac{\Omega_z}{\Omega}\epsilon_{izm}a_m a_j\rangle] = -G^v_{jk}\frac{(1-\phi)}{2}\epsilon_{kzm}\frac{\Omega_z}{\Omega}A_{mj} \\
&- G^v_{jk}\gamma\frac{\Omega_q\Omega_z}{2\Omega^2}[A_{kj}\delta_{qz} - q^2 Z^a_{zkqj}] - G^v_{ik}\phi\frac{\Omega_z}{\Omega}\epsilon_{izm}A_{mk} + \gamma[-\frac{S^v_{kk}}{2}q^2 + S^v_{kk}\frac{\Omega_m\Omega_t}{2\Omega^2}A_{tm} \\
&- S^v_{ik}(A_{im}\frac{\Omega_m\Omega_k}{2\Omega^2} + A_{km}\frac{\Omega_m\Omega_i}{2\Omega^2}) + S^v_{ik}\frac{\Omega_i\Omega_k}{2\Omega^2}q^2 + S^v_{ik}\frac{\Omega_q\Omega_q}{2\Omega^2}A_{ik}] \\
&= -G^v_{jk}\frac{(1-\phi)}{2}\epsilon_{kzm}\frac{\Omega_z}{\Omega}A_{mj} - G^v_{ik}\phi\frac{\Omega_z}{\Omega}\epsilon_{izm}A_{mk} + \gamma[-\frac{S^v_{kk}}{2}q^2 + S^v_{kk}\frac{\Omega_m\Omega_t}{2\Omega^2}A_{tm} \\
&- S^v_{ik}(A_{im}\frac{\Omega_m\Omega_k}{2\Omega^2} + A_{km}\frac{\Omega_m\Omega_i}{2\Omega^2}) + S^v_{ik}\frac{\Omega_i\Omega_k}{2\Omega^2}q^2 + S^v_{ik}\frac{\Omega_q\Omega_q}{2\Omega^2}A_{ik} - G^v_{ik}\frac{\Omega_q\Omega_q}{2\Omega^2}A_{ki} + G^v_{ik}\frac{\Omega_q\Omega_z}{2\Omega^2}q^2 Z^a_{zkqi}] \\
&= -G^v_{jk}\frac{(1-\phi)}{2}\epsilon_{kzm}\frac{\Omega_z}{\Omega}A_{mj} - G^v_{ik}\phi\frac{\Omega_z}{\Omega}\epsilon_{izm}A_{mk} \\
&+ \gamma[-\frac{S^v_{kk}}{2}q^2 + S^v_{kk}\frac{\Omega_m\Omega_t}{2\Omega^2}A_{tm} - S^v_{ik}(A_{im}\frac{\Omega_m\Omega_k}{2\Omega^2} + A_{km}\frac{\Omega_m\Omega_i}{2\Omega^2}) + S^v_{ik}\frac{\Omega_i\Omega_k}{2\Omega^2}q^2 + S^v_{ik}\frac{\Omega_q\Omega_z}{2\Omega^2}q^2 Z^a_{zkqi}]\,,
\end{aligned} \tag{C.72}$$

or

$$\begin{aligned}
&- [G^v_{jk}\langle R^{|a}_{ki}\frac{\Omega_z}{\Omega}\epsilon_{izm}a_m a_j\rangle + G^v_{ik}\langle R^{|a}_{kj}\frac{\Omega_z}{\Omega}\epsilon_{izm}a_m a_j\rangle] = -G^v_{jk}\frac{(1-\phi)}{2}\epsilon_{kzm}\frac{\Omega_z}{\Omega}A_{mj} \\
&- G^v_{ik}\phi\frac{\Omega_z}{\Omega}\epsilon_{izm}A_{mk} + \gamma[-\frac{S^v_{kk}}{2}q^2 + S^v_{kk}\frac{\Omega_m\Omega_t}{2\Omega^2}A_{tm} - S^v_{ik}(\frac{\Omega_m\Omega_k}{2\Omega^2}A_{im} + \frac{\Omega_m\Omega_i}{2\Omega^2}A_{mk}) \\
&+ S^v_{ik}\frac{\Omega_i\Omega_k}{2\Omega^2}q^2 + S^v_{ik}\frac{\Omega_q\Omega_z}{2\Omega^2}q^2 Z^a_{zkqi}]\,.
\end{aligned} \tag{C.73}$$

Next, we consider the term involving the fourth moments, given by

$$[G^n_{kq} + G^v_{kq}]\langle(V_i V_q n_k n_j + V_j V_q n_k n_i)\frac{\Omega_z}{\Omega}\epsilon_{izm}a_m a_j|a\rangle\,. \tag{C.74}$$

The first term is zero due to the orthogonality condition $n_i a_i = 0$. The second term can be written in the more suitable form

$$[G^n_{kq} + G^v_{kq}]\langle M^{|a}_{jqki}\frac{\Omega_z}{\Omega}\epsilon_{izm}a_m a_j\rangle \,. \tag{C.75}$$

We deal with the term involving G^v_{ik} and generalize for $(G^v_{ik}+G^n_{ik})$. We decompose the fourth moment into three parts as follow

$$\begin{aligned} G^v_{kq}\langle M^{|a}_{jqki}\frac{\Omega_z}{\Omega}\epsilon_{izm}a_m a_j\rangle &= G^v_{kq}\langle M^{v|a}_{jqki}\frac{\Omega_z}{\Omega}\epsilon_{izm}a_m a_j\rangle + G^v_{kq}\langle M^{j|a}_{jqki}\frac{\Omega_z}{\Omega}\epsilon_{izm}a_m a_j\rangle \\ &+ G^v_{kq}\langle M^{h|a}_{jqki}\frac{\Omega_z}{\Omega}\epsilon_{izm}a_m a_j\rangle \,, \end{aligned} \tag{C.76}$$

where

$$M^{v|a}_{ijpq} = \frac{\tilde{V}^2(1-\tilde{\phi})}{8}\epsilon_{irt}\epsilon_{jzs}[(\delta_{rz}\delta_{pq} + \delta_{rp}\delta_{zq} + \delta_{rq}\delta_{zp}) - \delta_{rz}a_p a_q]a_t a_s \,, \tag{C.77a}$$

$$M^{j|a}_{ijpq} = \frac{\tilde{V}^2}{2}\tilde{\phi}[\delta_{pq}a_i a_j - a_i a_j a_p a_q] \,, \tag{C.77b}$$

$$M^{h|a}_{ijpq} = \tilde{\gamma}\tilde{V}^2\frac{\Omega_k}{\Omega}(\epsilon_{irt}a_t a_j + \epsilon_{jrt}a_t a_i)[\frac{1}{8}(\delta_{rk}\delta_{pq} + \delta_{rp}\delta_{kq} + \delta_{rq}\delta_{kp}) \tag{C.77c}$$

$$- \frac{1}{8}(\delta_{rk}a_p a_q + \delta_{rp}a_k a_q + \delta_{rq}a_k a_p)] \,. \tag{C.77d}$$

The vortical contribution is found to be zero,

$$G^v_{kq}\langle M^{v|a}_{jqki}\frac{\Omega_z}{\Omega}\epsilon_{izm}a_m a_j\rangle = 0 \,, \tag{C.78}$$

since we have $\epsilon_{jrt}a_t a_j = 0$. The jetal component is given by

$$\begin{aligned} G^v_{kq}\langle M^{j|a}_{jqki}\frac{\Omega_z}{\Omega}\epsilon_{izm}a_m a_j\rangle &= G^v_{kq}[\langle\frac{\tilde{V}^2\tilde{\phi}}{2}[\delta_{ki}a_j a_q - a_k a_i a_j a_q]\frac{\Omega_z}{\Omega}\epsilon_{izm}a_m a_j\rangle] \\ = G^v_{kq}\langle\frac{\tilde{V}^2\tilde{\phi}}{2}[\frac{\Omega_z}{\Omega}\epsilon_{kzm}a_m a_q - \frac{\Omega_z}{\Omega}\epsilon_{izm}a_k a_i a_q a_m]\rangle &= G^v_{kq}\frac{\phi}{2}\frac{\Omega_z}{\Omega}\epsilon_{kzm}A_{mq} \,. \end{aligned} \tag{C.79}$$

The contribution from the helical term is treated as follow

$$
\begin{aligned}
&G^v_{kq}\langle M^{h|a}_{jqki}\frac{\Omega_z}{\Omega}\epsilon_{izm}a_m a_j\rangle = G^v_{kq}\langle\tilde{\gamma}\tilde{V}^2\frac{\Omega_s}{\Omega}(\epsilon_{jrt}a_t a_q + \epsilon_{qrt}a_t a_j)[\frac{1}{8}(\delta_{rs}\delta_{ki} + \delta_{rk}\delta_{si} + \delta_{ri}\delta_{sk}) \\
&- \frac{1}{8}(\delta_{rs}a_k a_i + \delta_{rk}a_s a_i + \delta_{ri}a_s a_k)]\frac{\Omega_z}{\Omega}\epsilon_{izm}a_m a_j\rangle \\
&= G^v_{kq}\langle\tilde{\gamma}\tilde{V}^2\frac{\Omega_s}{\Omega}(\epsilon_{qrt}a_t a_j)[\frac{1}{8}(\delta_{rs}\delta_{ki} + \delta_{rk}\delta_{si} + \delta_{ri}\delta_{sk}) - \frac{1}{8}\delta_{ri}a_s a_k]\frac{\Omega_z}{\Omega}\epsilon_{izm}a_m a_j\rangle \\
&= G^v_{kq}\langle\tilde{\gamma}\tilde{V}^2\frac{\Omega_s}{\Omega}(\epsilon_{qrt}a_t a_j)[\frac{1}{8}(\delta_{rs}\delta_{ki} + \delta_{rk}\delta_{si} + \delta_{ri}\delta_{sk}) - \frac{1}{8}\delta_{ri}a_s a_k]\frac{\Omega_z}{\Omega}\epsilon_{izm}a_m a_j\rangle \\
&= G^v_{kq}\langle\frac{\tilde{\gamma}\tilde{V}^2}{8}[\epsilon_{qst}\epsilon_{kzm}\frac{\Omega_s\Omega_z}{\Omega^2}a_t a_m + \epsilon_{qkt}\epsilon_{szm}\frac{\Omega_s\Omega_z}{\Omega^2}a_t a_m + \epsilon_{itq}\epsilon_{izm}\frac{\Omega_k\Omega_z}{\Omega^2}a_t a_m]\rangle \\
&- G^v_{kq}\langle\frac{\tilde{\gamma}\tilde{V}^2}{8}\epsilon_{qit}\epsilon_{izm}\frac{\Omega_s\Omega_z}{\Omega^2}a_t a_m a_s a_k\rangle \\
&= G^v_{kq}\langle\frac{\tilde{\gamma}\tilde{V}^2}{8}[\epsilon_{qst}\epsilon_{kzm}\frac{\Omega_s\Omega_z}{\Omega^2}a_t a_m + [\delta_{tz}\delta_{qm} - \delta_{tm}\delta_{qz}]\frac{\Omega_k\Omega_z}{\Omega^2}a_t a_m \\
&- [\delta_{tz}\delta_{qm} - \delta_{tm}\delta_{qz}]\frac{\Omega_s\Omega_z}{\Omega^2}a_t a_m a_s a_k]\rangle \\
&= G^v_{kq}\langle\frac{\tilde{\gamma}\tilde{V}^2}{8}[\epsilon_{qst}\epsilon_{kzm}\frac{\Omega_z\Omega_s}{\Omega^2}a_t a_m + \frac{\Omega_k\Omega_t}{\Omega^2}a_t a_q - \frac{\Omega_k\Omega_q}{\Omega^2} - \frac{\Omega_s\Omega_t}{\Omega^2}a_t a_q a_s a_k + \frac{\Omega_s\Omega_q}{\Omega^2}a_s a_k]\rangle \\
&= G^v_{kq}\langle\frac{\tilde{\gamma}\tilde{V}^2}{8}\epsilon_{qst}\epsilon_{kzm}\frac{\Omega_s\Omega_z}{\Omega^2}a_t a_m\rangle + \langle\frac{\tilde{\gamma}\tilde{V}^2}{8}[G^v_{kq}(\frac{\Omega_k\Omega_t}{\Omega^2}a_{tq} + \frac{\Omega_q\Omega_t}{\Omega^2}a_{tk}) - S^v_{kq}\frac{\Omega_k\Omega_q}{\Omega^2} \\
&- S^v_{kq}\frac{\Omega_s\Omega_t}{\Omega^2}a_t a_q a_s a_k]\rangle \\
&= G^v_{kq}\frac{\gamma}{8}\epsilon_{qst}\epsilon_{kzm}\frac{\Omega_s\Omega_z}{\Omega^2}A_{tm} + \frac{\gamma}{8}G^v_{kq}(\frac{\Omega_k\Omega_t}{\Omega^2}A_{tq} + \frac{\Omega_q\Omega_t}{\Omega^2}A_{tk}) - \frac{\gamma}{8}S^v_{kq}\frac{\Omega_k\Omega_q}{\Omega^2}q^2 - \frac{\gamma}{8}S^v_{kq}\frac{\Omega_s\Omega_t}{\Omega^2}q^2 Z^a_{tqsk}\,.
\end{aligned}
\tag{C.80}
$$

or simply

$$
\begin{aligned}
&G^v_{kq}\langle M^{h|a}_{jqki}\frac{\Omega_z}{\Omega}\epsilon_{izm}a_m a_j\rangle = G^v_{kq}\frac{\gamma}{8}\epsilon_{qst}\epsilon_{kzm}\frac{\Omega_s\Omega_z}{\Omega^2}A_{tm} + \frac{\gamma}{8}G^v_{kq}(\frac{\Omega_k\Omega_t}{\Omega^2}A_{tq} + \frac{\Omega_q\Omega_t}{\Omega^2}A_{tk}) \\
&- \frac{\gamma}{8}S^v_{kq}\frac{\Omega_k\Omega_q}{\Omega^2}q^2 - \frac{\gamma}{8}S^v_{kq}\frac{\Omega_s\Omega_t}{\Omega^2}q^2 Z^a_{tqsk}\,.
\end{aligned}
\tag{C.81}
$$

Expanding the first term of eq. (C.81), one finds

$$
\begin{aligned}
&G^v_{kq}\frac{\gamma}{8}\epsilon_{qst}\epsilon_{kzm}\frac{\Omega_s\Omega_z}{\Omega^2}A_{tm} = G^v_{kq}\frac{\gamma}{8}[\delta_{qk}\delta_{sz}\delta_{tm} + \delta_{qz}\delta_{sm}\delta_{tk} + \delta_{qm}\delta_{sk}\delta_{tz} - \delta_{qk}\delta_{sm}\delta_{tz} - \delta_{qz}\delta_{sk}\delta_{tm} \\
&- \delta_{qm}\delta_{sz}\delta_{tk}]\frac{\Omega_s\Omega_z}{\Omega^2}A_{tm} \\
&= G^v_{qq}\frac{\gamma}{8}\frac{\Omega_z\Omega_z}{\Omega^2}q^2 + G^v_{tz}\frac{\gamma}{8}\frac{\Omega_m\Omega_z}{\Omega^2}A_{tm} + G^v_{sm}\frac{\gamma}{8}\frac{\Omega_s\Omega_z}{\Omega^2}A_{zm} - G^v_{qq}\frac{\gamma}{8}\frac{\Omega_m\Omega_t}{\Omega^2}A_{tm} - G^v_{sz}\frac{\gamma}{8}\frac{\Omega_s\Omega_z}{\Omega^2}q^2 \\
&- G^v_{tm}\frac{\gamma}{8}\frac{\Omega_s\Omega_s}{\Omega^2}A_{tm} \\
&= S^v_{qq}\frac{\gamma}{8}q^2 + S^v_{tz}\frac{\gamma}{8}\frac{\Omega_m\Omega_z}{\Omega^2}A_{tm} + S^v_{sm}\frac{\gamma}{8}\frac{\Omega_s\Omega_z}{\Omega^2}A_{zm} - S^v_{qq}\frac{\gamma}{8}\frac{\Omega_m\Omega_t}{\Omega^2}A_{tm} - S^v_{sz}\frac{\gamma}{8}\frac{\Omega_s\Omega_z}{\Omega^2}q^2 - S^v_{tm}\frac{\gamma}{8}A_{tm}\,.
\end{aligned}
\tag{C.82}
$$

Substituting back into eq. (C.81) yields,

$$
\begin{aligned}
&G^v_{kq}\langle M^{h|a}_{jqki}\frac{\Omega_z}{\Omega}\epsilon_{izm}a_m a_j\rangle = S^v_{qq}\frac{\gamma}{8}q^2 + S^v_{tz}\frac{\gamma}{8}\frac{\Omega_m\Omega_z}{\Omega^2}A_{tm} + S^v_{sm}\frac{\gamma}{8}\frac{\Omega_s\Omega_z}{\Omega^2}A_{zm} - S^v_{qq}\frac{\gamma}{8}\frac{\Omega_m\Omega_t}{\Omega^2}A_{tm} \\
&- S^v_{sz}\frac{\gamma}{8}\frac{\Omega_s\Omega_z}{\Omega^2}q^2 - S^v_{tm}\frac{\gamma}{8}A_{tm} + \underbrace{\frac{\gamma}{8}S^v_{kq}(\frac{\Omega_k\Omega_t}{\Omega^2}A_{tq} + \frac{\Omega_q\Omega_t}{\Omega^2}A_{tk})}_{\text{symmetric/antisymmetric}} - \frac{\gamma}{8}S^v_{kq}\frac{\Omega_k\Omega_q}{\Omega^2}q^2 - \frac{\gamma}{8}S^v_{kq}\frac{\Omega_s\Omega_t}{\Omega^2}q^2 Z^a_{tqsk}\,.
\end{aligned}
\tag{C.83}
$$

Simplifying,

$$
\begin{aligned}
&G^v_{kq}\langle M^{h|a}_{jqki}\frac{\Omega_z}{\Omega}\epsilon_{izm}a_m a_j\rangle = S^v_{qq}\frac{\gamma}{8}q^2 + \frac{\gamma}{4}(S^v_{sm}\frac{\Omega_s\Omega_z}{\Omega^2}A_{zm} + S^v_{tz}\frac{\Omega_m\Omega_z}{\Omega^2}A_{tm}) - S^v_{sz}\frac{\gamma}{4}\frac{\Omega_s\Omega_z}{\Omega^2}q^2 \\
&- S^v_{qq}\frac{\gamma}{8}\frac{\Omega_m\Omega_t}{\Omega^2}A_{tm} - S^v_{tm}\frac{\gamma}{8}A_{tm} - \frac{\gamma}{8}S^v_{kq}\frac{\Omega_s\Omega_t}{\Omega^2}q^2 Z^a_{tqsk}\,.
\end{aligned}
\tag{C.84}
$$

Substituting from eq. (C.84) in eq. (C.76) yields,

$$
\begin{aligned}
&G^v_{kq}\langle M^a_{jqki}\frac{\Omega_z}{\Omega}\epsilon_{izm}a_m a_j\rangle = q^2 G^v_{kq}\frac{\phi}{2}\frac{\Omega_z}{\Omega}\epsilon_{kzm}a_{mq} + q^2\gamma[\frac{S^v_{qq}}{8} + \frac{S^v_{tz}}{4}\frac{\Omega_m\Omega_z}{\Omega^2}a_{tm} \\
&+ \frac{S^v_{tz}}{4}\frac{\Omega_m\Omega_t}{\Omega^2}a_{zm} - \frac{S^v_{sz}}{4}\frac{\Omega_s\Omega_z}{\Omega^2} - \frac{S^v_{qq}}{8}\frac{\Omega_m\Omega_t}{\Omega^2}a_{tm} - \frac{S^v_{kq}}{8}\frac{\Omega_s\Omega_t}{\Omega^2}Z^a_{tqsk} - \frac{S^v_{tm}}{8}a_{tm}]\,.
\end{aligned}
\tag{C.85}
$$

Collecting all terms together gives the expression for the total term

$$
\begin{aligned}
&\langle(\frac{dR^{|a}_{ij}}{dt})\frac{\Omega_z}{\Omega}\epsilon_{izm}a_m a_j\rangle = -G^v_{jk}\frac{(1-\phi)}{2}\epsilon_{kzm}\frac{\Omega_z}{\Omega}q^2 a_{mj} - G^v_{ik}\phi\frac{\Omega_z}{\Omega}\epsilon_{izm}q^2 a_{mk} \\
&+\gamma[-\frac{S^v_{kk}}{2}q^2 + S^v_{kk}\frac{\Omega_m\Omega_t}{2\Omega^2}q^2 a_{tm} - S^v_{ik}(\frac{\Omega_m\Omega_k}{2\Omega^2}A_{im} + \frac{\Omega_m\Omega_i}{2\Omega^2}A_{mk}) + S^v_{ik}\frac{\Omega_i\Omega_k}{2\Omega^2}q^2 \\
&+S^v_{ik}\frac{\Omega_q\Omega_z}{2\Omega^2}q^2 Z^a_{zkqi}] + q^2 G^*_{kq}\frac{\phi}{2}\frac{\Omega_z}{\Omega}\epsilon_{kzm}a_{mq} + q^2\gamma[\frac{S^*_{qq}}{8} + \frac{S^*_{tz}}{4}(\frac{\Omega_m\Omega_z}{\Omega^2}a_{tm} + \frac{\Omega_m\Omega_t}{\Omega^2}a_{zm}) \\
&-\frac{S^*_{sz}}{4}\frac{\Omega_s\Omega_z}{\Omega^2} - \frac{S^*_{qq}}{8}\frac{\Omega_m\Omega_t}{\Omega^2}a_{tm} \\
&-\frac{S^*_{kq}}{8}\frac{\Omega_s\Omega_t}{\Omega^2}Z^a_{tqsk} - \frac{S^*_{tm}}{8}a_{tm}] + \text{slow term}\,,
\end{aligned}
\tag{C.86}
$$

where G^*_{ij} is defined by

$$
G^*_{ij} = G^v_{ij} + G^n_{ij}\,. \tag{C.87}
$$

Next, we deal with the slow term as follow

$$
\begin{aligned}
&\langle(\frac{dR^{|a}_{ij}}{dt})^s\frac{\Omega_z}{\Omega}\epsilon_{izm}a_m a_j\rangle = -\langle[2C_1 R^{|a}_{ij} - C_2^2 R^{|a}_{kk}(\delta_{ij} - n_i n_j)]\frac{\Omega_z}{\Omega}\epsilon_{izm}a_m a_j\rangle \\
&= -2\langle C_1 R^{|a}_{ij}\frac{\Omega_z}{\Omega}\epsilon_{izm}a_m a_j\rangle \\
&= -2\langle C_1[\tilde{V}^2\frac{(1-\tilde{\phi})}{2}(\delta_{ij} - a_i a_j)]\frac{\Omega_z}{\Omega}\epsilon_{izm}a_m a_j\rangle - 2\langle C_1\tilde{V}^2\tilde{\phi}a_i a_j\frac{\Omega_z}{\Omega}\epsilon_{izm}a_m a_j\rangle \\
&- 2\langle C_1\frac{\tilde{\gamma}}{2}\frac{\Omega_k}{\Omega}\tilde{V}^2(\epsilon_{ikt}a_t a_j + \epsilon_{jkt}a_t a_i)\frac{\Omega_z}{\Omega}\epsilon_{izm}a_m a_j\rangle \\
&= -2\gamma\frac{\Omega_k\Omega_z}{2\Omega^2}\epsilon_{ikt}\epsilon_{izm}\langle C_1\tilde{V}^2 a_t a_m\rangle \\
&= -2\gamma\frac{\Omega_k\Omega_z}{2\Omega^2}[\delta_{kz}\delta_{tm} - \delta_{km}\delta_{tz}]\langle\frac{8.5}{\tau}\Omega^* f_{pq}n_p n_q a_t a_m\tilde{V}^2\rangle \\
&= -2\gamma\frac{\Omega_z\Omega_z}{2\Omega^2}\langle\frac{8.5}{\tau}\Omega^* f_{pq}n_p n_q\tilde{V}^2\rangle + 2\gamma\frac{\Omega_m\Omega_t}{2\Omega^2}\langle\frac{8.5}{\tau}\Omega^* f_{pq}n_p n_q a_t a_m\tilde{V}^2\rangle \\
&= -\gamma\frac{8.5}{\tau}\langle\Omega^* f_{pq}D^{|a}_{pq}\rangle + \gamma\frac{\Omega_m\Omega_t}{\Omega^2}\frac{8.5}{\tau}\langle\Omega^* f_{pq}D^{|a}_{pq}a_t a_m\rangle\,.
\end{aligned}
\tag{C.88}
$$

Substituting the expression $D^{|a}_{ij} = \frac{\tilde{V}^2}{2}(\delta_{ij} - a_i a_j)$ in eq. (C.88) yields,

$$\begin{aligned}
&\langle(\frac{dR_{ij}^{|a}}{dt})^s\frac{\Omega_z}{\Omega}\epsilon_{izm}a_m a_j\rangle = -\gamma\frac{8.5}{\tau}\Omega^*[\frac{f_{pq}}{2}q^2(\delta_{pq}-a_{pq})]\\
&+\frac{\gamma\Omega_m\Omega_t}{\Omega^2}\frac{8.5}{\tau}\Omega^*[f_{pq}\frac{q^2}{2}\langle(\delta_{pq}-a_p a_q)a_t a_m\rangle]\\
&=\gamma\frac{8.5}{2\tau}\Omega^* q^2[f_{pq}\frac{\Omega_m\Omega_t}{\Omega^2}(\delta_{mt}a_{pq}-Z^a_{pqtm})]+\gamma\frac{8.5}{2\tau}\frac{\Omega_m\Omega_t}{\Omega^2}\Omega^* q^2[a_{tm}-\delta_{tm}]\,.
\end{aligned} \tag{C.89}$$

Thus the final expression for the slow term is given by

$$\langle(\frac{dR_{ij}^{|a}}{dt})^s\frac{\Omega_z}{\Omega}\epsilon_{izm}a_m a_j\rangle = \gamma\frac{8.5}{2\tau}\frac{\Omega_m\Omega_t}{\Omega^2}\Omega^* q^2[(a_{tm}-\delta_{tm})+f_{pq}(\delta_{mt}a_{pq}-Z^a_{pqtm})]\,. \tag{C.90}$$

Now we seek to further simplify the derived expressions for the terms of eq. (C.50). For simplicity we will deal with each term separately. Starting from the first term we have

$$\begin{aligned}
&\epsilon_{izm}\langle R_{ij}^{|a}\frac{\Omega_z}{\Omega}\frac{d}{dt}(a_m a_j)\rangle = q^2[\epsilon_{izm}\frac{(1-\phi)}{2}\frac{\Omega_z}{\Omega}G^a_{iq}a_{qm}+\phi\epsilon_{izm}\frac{\Omega_z}{\Omega}G^a_{mq}a_{qi}]\\
&-\frac{q^2\gamma}{2}\frac{\Omega_m\Omega_t}{\Omega^2}[G^a_{mq}a_{qt}-G^a_{qs}Z^a_{qsmt}]\\
&=q^2[\epsilon_{izm}\frac{(1-\phi)}{2}\frac{\Omega_z}{\Omega}S^a_{iq}a_{qm}+\phi\epsilon_{izm}\frac{\Omega_z}{\Omega}S^a_{mq}a_{qi}]+q^2[\epsilon_{izm}\frac{(1-\phi)}{2}\frac{\Omega_z}{\Omega}\Omega_{iq}a_{qm}+\phi\epsilon_{izm}\frac{\Omega_z}{\Omega}\Omega_{mq}a_{qi}]\\
&-\frac{q^2\gamma}{2}\frac{\Omega_m\Omega_t}{\Omega^2}[S^a_{mq}a_{qt}-S^a_{qs}Z^a_{qsmt}]-\frac{q^2\gamma}{2}\frac{\Omega_m\Omega_t}{\Omega^2}[\Omega_{mq}a_{qt}-\Omega_{qs}Z^a_{qsmt}]\\
&=q^2\epsilon_{izm}\frac{\Omega_z}{2\Omega}S^a_{iq}a_{qm}(1-3\phi)-\frac{q^2\gamma}{2}\frac{\Omega_m\Omega_t}{\Omega^2}(S^a_{mq}a_{qt}-S^a_{qs}Z^a_{qsmt})\\
&+q^2[\frac{(1-\phi)}{2}\epsilon_{izm}\epsilon_{irq}\frac{\Omega_z}{2\Omega}\Omega_r a_{qm}+\phi\frac{\Omega_z}{2\Omega}\epsilon_{miz}\epsilon_{mrq}\Omega_r a_{qi}]-\frac{q^2\gamma}{2}\frac{\Omega_m\Omega_t}{\Omega^2}[\frac{\epsilon_{qms}}{2}\Omega_s a_{qt}-\frac{\epsilon_{sqr}}{2}\Omega_r Z^a_{qsmt}]\\
&=q^2(1-3\phi)\epsilon_{izm}\frac{\Omega_z}{2\Omega}S^a_{iq}a_{qm}-\frac{q^2\gamma}{2}\frac{\Omega_m\Omega_t}{\Omega^2}(S^a_{mq}a_{qt}-S^a_{qs}Z^a_{qsmt})\\
&+q^2[\frac{(1-\phi)}{2}(\delta_{zr}\delta_{mq}-\delta_{zq}\delta_{mr})\frac{\Omega_z}{2\Omega}\Omega_r a_{qm}+\phi\frac{\Omega_z}{2\Omega}(\delta_{ir}\delta_{zq}-\delta_{iq}\delta_{zr})\Omega_r a_{qi}]\\
&-\frac{q^2\gamma}{4}\frac{\Omega_m\Omega_t}{\Omega^2}[\epsilon_{qms}\Omega_s a_{qt}-\epsilon_{sqr}\Omega_r Z^a_{qsmt}]
\end{aligned}$$

$$\begin{aligned}
&= q^2(1-3\phi)\epsilon_{izm}\frac{\Omega_z}{2\Omega}S^a_{iq}a_{qm} - \frac{q^2\gamma}{2}\frac{\Omega_m\Omega_t}{\Omega^2}(S^a_{mq}a_{qt} - S^a_{qs}Z^a_{qsmt}) \\
&+ q^2[\frac{(1-\phi)}{2}[\frac{\Omega_z\Omega_z}{2\Omega} - \frac{\Omega_q\Omega_m}{2\Omega}a_{qm}] + \frac{\phi}{2\Omega}[\Omega_q\Omega_i a_{qi} - \Omega_z\Omega_z]] \\
&- \frac{q^2\gamma}{4}\frac{\Omega_m\Omega_t}{\Omega^2}[\epsilon_{qms}\Omega_s a_{qt} - \epsilon_{sqr}\Omega_r Z^a_{qsmt}] \\
&= q^2(1-3\phi)\epsilon_{izm}\frac{\Omega_z}{2\Omega}S^a_{iq}a_{qm} - \frac{q^2\gamma}{2}\frac{\Omega_m\Omega_t}{\Omega^2}(S^a_{mq}a_{qt} - S^a_{qs}Z^a_{qsmt}) + q^2(\frac{(1-\phi)}{2}\frac{\Omega_z\Omega_z}{2\Omega} - \frac{\phi}{2\Omega}\Omega_z\Omega_z) \\
&+ q^2(\frac{\phi}{2\Omega}\Omega_q\Omega_i a_{qi} - \frac{(1-\phi)}{2}\frac{\Omega_q\Omega_m}{2\Omega}a_{qm}) - \frac{q^2\gamma}{4}\frac{\Omega_m\Omega_t}{\Omega^2}[\epsilon_{qms}\Omega_s a_{qt} - \epsilon_{sqr}\Omega_r Z^a_{qsmt}] \\
&= q^2(1-3\phi)\epsilon_{izm}\frac{\Omega_z}{2\Omega}S^a_{iq}a_{qm} - \frac{q^2\gamma}{2}\frac{\Omega_m\Omega_t}{\Omega^2}(S^a_{mq}a_{qt} - S^a_{qs}Z^a_{qsmt}) \\
&- \frac{q^2\gamma}{4}\frac{\Omega_m\Omega_t}{\Omega^2}[\epsilon_{qms}\Omega_s a_{qt} - \epsilon_{sqr}\Omega_r Z^a_{qsmt}] + q^2[\frac{\Omega_z\Omega_z}{4\Omega}(1-3\phi) + \frac{\Omega_i\Omega_q a_{qi}}{4\Omega}(2\phi - (1-\phi))] \\
&= q^2(1-3\phi)\epsilon_{izm}\frac{\Omega_z}{2\Omega}S^a_{iq}a_{qm} - \frac{q^2\gamma}{2}\frac{\Omega_m\Omega_t}{\Omega^2}(S^a_{mq}a_{qt} - S^a_{qs}Z^a_{qsmt}) \\
&- \frac{q^2\gamma}{4}\frac{\Omega_m\Omega_t}{\Omega^2}[\epsilon_{qms}\Omega_s a_{qt} - \epsilon_{sqr}\Omega_r Z^a_{qsmt}] + q^2[\frac{\Omega_z\Omega_z}{4\Omega}(1-3\phi) + \frac{\Omega_i\Omega_q a_{qi}}{4\Omega}(3\phi - 1)]\,.
\end{aligned} \tag{C.91}$$

Simplification of eq. (C.91) yields the final expression,

$$\begin{aligned}
\epsilon_{izm}\langle R^{|a}_{ij}\frac{\Omega_z}{\Omega}\frac{d}{dt}(a_m a_j)\rangle = {} & q^2(1-3\phi)\epsilon_{izm}\frac{\Omega_z}{2\Omega}S^a_{iq}a_{qm} - \frac{q^2\gamma}{2}\frac{\Omega_m\Omega_t}{\Omega^2}(S^a_{mq}a_{qt} - S^a_{qs}Z^a_{qsmt}) \\
& + q^2\frac{\Omega_i\Omega_q}{4\Omega}(1-3\phi)(\delta_{iq} - a_{iq})\,.
\end{aligned} \tag{C.92}$$

Next, we consider the third term of eq. (C.53),

$$\begin{aligned}
\frac{\gamma}{2}\frac{\Omega_k\Omega_z}{\Omega^2}\frac{d}{dt}(q^2\delta_{kz} - A_{kz}) &= -\gamma S^v_{km}R_{mk} + \gamma\frac{\Omega_k\Omega_z}{\Omega^2}[-G^a_{kq}A_{qz} + S^a_{pq}q^2Z^a_{kzpq} + S^v_{qs}\langle R^{|a}_{sq}a_k a_z\rangle] \\
&= -\gamma q^2 S^v_{km}r_{mk} + \gamma\frac{\Omega_k\Omega_z}{\Omega^2}[-S^a_{kq}q^2A_{qz} + S^a_{pq}q^2Z^a_{kzpq} + S^v_{qs}\langle R^{|a}_{sq}a_k a_z\rangle]\,.
\end{aligned} \tag{C.93}$$

The last term of eq. (C.93) can be put into the following form

$$
\begin{aligned}
&S^v_{qs}\langle R^{|a}_{sq} a_k a_z\rangle = S^v_{qs}\langle[\tilde{V}^2\frac{(1-\tilde{\phi})}{2}(\delta_{sq} - a_s a_q)a_k a_z + \tilde{V}^2\tilde{\phi} a_s a_q a_k a_z + \tilde{V}^2\tilde{\gamma}\frac{\Omega_m}{\Omega}\epsilon_{smt} a_t a_q a_k a_z]\rangle \\
&= q^2\frac{(1-\phi)}{2}S^v_{qq}a_{kz} + \frac{q^2}{2}S^v_{qs}Z^a_{sqkz}(3\phi - 1) + q^2\frac{\gamma}{2}S^v_{qs}\frac{\Omega_p}{\Omega}(\epsilon_{spy}Z^a_{yqkz} + \epsilon_{qpy}Z^a_{yskz})\,.
\end{aligned}
\tag{C.94}
$$

Substituting back into the third term of eq. (C.53) yields,

$$
\begin{aligned}
&\frac{\gamma}{2}\frac{\Omega_k\Omega_z}{\Omega^2}\frac{d}{dt}(q^2\delta_{kz} - A_{kz}) = -\gamma q^2 S^v_{km} r_{mk} + \gamma q^2\frac{\Omega_k\Omega_z}{\Omega^2}[-S^a_{kq}a_{qz} + S^a_{pq}Z^a_{kzpq}] \\
&+ \gamma\frac{\Omega_k\Omega_z}{\Omega^2}\frac{q^2}{2}[(1-\phi)S^v_{qq}a_{kz} + S^v_{qs}Z^a_{sqkz}(3\phi - 1) + \gamma\frac{\Omega_m}{\Omega}(\epsilon_{smt}Z^a_{tqkz} + \epsilon_{qmt}Z^a_{tskz})S^v_{qs}]\,.
\end{aligned}
\tag{C.95}
$$

Now we consider the most complicated term of eq. (C.53) as follow

$$
\begin{aligned}
&\langle(\frac{dR^{|a}_{ij}}{dt})\frac{\Omega_z}{\Omega}\epsilon_{izm}a_m a_j\rangle = -G^v_{jk}\frac{(1-\phi)}{2}\epsilon_{kzm}\frac{\Omega_z}{\Omega}q^2 a_{mj} - G^v_{ik}\phi\frac{\Omega_z}{\Omega}\epsilon_{izm}q^2 a_{mk} \\
&+ \gamma\Big[-\frac{S^v_{kk}}{2}q^2 + S^v_{kk}\frac{\Omega_m\Omega_t}{2\Omega^2}q^2 a_{tm} - S^v_{ik}(\frac{\Omega_m\Omega_k}{2\Omega^2}A_{im} + \frac{\Omega_m\Omega_i}{2\Omega^2}A_{mk}) + S^v_{ik}\frac{\Omega_i\Omega_k}{2\Omega^2}q^2 \\
&+ S^v_{ik}\frac{\Omega_q\Omega_z}{2\Omega^2}q^2 Z^a_{zkqi}\Big] + \text{slow term} + q^2 G^*_{kq}\frac{\phi}{2}\frac{\Omega_z}{\Omega}\epsilon_{kzm}a_{mq} + q^2\gamma\Big[\frac{S^*_{qq}}{8} + \frac{S^*_{tz}}{4}(\frac{\Omega_m\Omega_z}{\Omega^2}a_{tm} \\
&+ \frac{\Omega_m\Omega_t}{\Omega^2}a_{zm}) - \frac{S^*_{sz}}{4}\frac{\Omega_s\Omega_z}{\Omega^2} - \frac{S^*_{qq}}{8}\frac{\Omega_m\Omega_t}{\Omega^2}a_{tm} - \frac{S^*_{kq}}{8}\frac{\Omega_s\Omega_t}{\Omega^2}Z^a_{tqsk} - \frac{S^*_{tm}}{8}a_{tm}\Big] \\
&= -S^v_{jk}\frac{(1-\phi)}{2}\epsilon_{kzm}\frac{\Omega_z}{\Omega}q^2 a_{mj} - S^v_{ik}\phi\frac{\Omega_z}{\Omega}\epsilon_{izm}q^2 a_{mk} - \Omega_{jk}\frac{(1-\phi)}{2}\epsilon_{kzm}\frac{\Omega_z}{\Omega}q^2 a_{mj} \\
&- \Omega_{ik}\phi\frac{\Omega_z}{\Omega}\epsilon_{izm}q^2 a_{mk} + \gamma\Big[-\frac{S^v_{kk}}{2}q^2 + S^v_{kk}\frac{\Omega_m\Omega_t}{2\Omega^2}q^2 a_{tm} - S^v_{ik}(\frac{\Omega_m\Omega_k}{2\Omega^2}A_{im} + \frac{\Omega_m\Omega_i}{2\Omega^2}A_{mk}) \\
&+ S^v_{ik}\frac{\Omega_i\Omega_k}{2\Omega^2}q^2 + S^v_{ik}\frac{\Omega_q\Omega_z}{2\Omega^2}q^2 Z^a_{zkqi}\Big] + \text{slow term} + q^2\gamma\Big[\frac{S^v_{qq}}{8} + \frac{S^v_{tz}}{4}(\frac{\Omega_m\Omega_z}{\Omega^2}a_{tm} + \frac{\Omega_m\Omega_t}{\Omega^2}a_{zm}) \\
&- \frac{S^v_{sz}}{4}\frac{\Omega_s\Omega_z}{\Omega^2} - \frac{S^v_{qq}}{8}\frac{\Omega_m\Omega_t}{\Omega^2}a_{tm} - \frac{S^v_{kq}}{8}\frac{\Omega_s\Omega_t}{\Omega^2}Z^a_{tqsk} - \frac{S^v_{tm}}{8}a_{tm}\Big] + q^2 S^v_{kq}\frac{\phi}{2}\frac{\Omega_z}{\Omega}\epsilon_{kzm}a_{mq} \\
&+ 2q^2\Omega_{kq}\frac{\phi}{2}\frac{\Omega_z}{\Omega}\epsilon_{kzm}a_{mq} + q^2 S^n_{kq}\frac{\phi}{2}\frac{\Omega_z}{\Omega}\epsilon_{kzm}a_{mq} + q^2\gamma\Big[\frac{S^n_{qq}}{8} + \frac{S^n_{tz}}{4}(\frac{\Omega_m\Omega_z}{\Omega^2}a_{tm} + \frac{\Omega_m\Omega_t}{\Omega^2}a_{zm}) \\
&- \frac{S^n_{sz}}{4}\frac{\Omega_s\Omega_z}{\Omega^2} - \frac{S^n_{qq}}{8}\frac{\Omega_m\Omega_t}{\Omega^2}a_{tm} - \frac{S^n_{kq}}{8}\frac{\Omega_s\Omega_t}{\Omega^2}Z^a_{tqsk} - \frac{S^n_{tm}}{8}a_{tm}\Big]\,.
\end{aligned}
\tag{C.96}
$$

Collecting terms and simplifying yields,

$$\begin{aligned}\langle(\frac{dR_{ij}^{|a}}{dt})\frac{\Omega_z}{\Omega}\epsilon_{izm}a_m a_j\rangle &= -\epsilon_{kzm}\frac{\Omega_z}{2\Omega}q^2 a_{mi}[(1-\phi)S_{ik}^v + 2\phi S_{ki}^v] + q^2(1-3\phi)\frac{\Omega_m\Omega_i}{4\Omega}(\delta_{mi}-a_{mi}) \\ &+ q^2\gamma[-\frac{3}{8}S_{kk}^v + \frac{3}{8}S_{kk}^v\frac{\Omega_m\Omega_t}{\Omega^2}a_{mt} - \frac{S_{ik}^v}{4}(\frac{\Omega_m\Omega_k}{\Omega^2}a_{im} + \frac{\Omega_m\Omega_i}{\Omega^2}a_{mk}) + S_{ik}^v\frac{\Omega_i\Omega_k}{4\Omega^2} + \frac{3}{8}S_{ik}^v\frac{\Omega_q\Omega_z}{\Omega^2}Z_{kzqi}^a \\ &- \frac{S_{tm}^v}{8}a_{tm}] + q^2 S_{kq}^v\frac{\phi}{2}\frac{\Omega_z}{\Omega}\epsilon_{kzm}a_{mq} + \frac{q^2\phi}{2}\frac{\Omega_s\Omega_q}{\Omega}(\delta_{sq}-a_{sq}) + q^2 S_{kq}^n\frac{\phi}{2}\frac{\Omega_z}{\Omega}\epsilon_{kzm}a_{mq} \\ &+ q^2\gamma[\frac{S_{qq}^n}{8} + \frac{S_{tz}^n}{4}(\frac{\Omega_m\Omega_z}{\Omega^2}a_{tm} + \frac{\Omega_m\Omega_t}{\Omega^2}a_{zm}) - \frac{S_{sz}^n}{4}\frac{\Omega_s\Omega_z}{\Omega^2} - \frac{S_{qq}^n}{8}\frac{\Omega_m\Omega_t}{\Omega^2}a_{tm} - \frac{S_{kq}^n}{8}\frac{\Omega_s\Omega_t}{\Omega^2}Z_{tqsk}^a \\ &- \frac{S_{tm}^n}{8}a_{tm}] + \text{slow term}\end{aligned} \tag{C.97}$$

or

$$\begin{aligned}\langle(\frac{dR_{ij}^{|a}}{dt})\frac{\Omega_z}{\Omega}\epsilon_{izm}a_m a_j\rangle &= -\epsilon_{kzm}\frac{\Omega_z}{2\Omega}q^2 a_{mi}[(1-\phi)S_{ik}^v + 2\phi S_{ki}^v] + q^2(1-\phi)\frac{\Omega_m\Omega_i}{4\Omega}(\delta_{mi}-a_{mi}) \\ &+ q^2 S_{kq}^v\frac{\phi}{2}\frac{\Omega_z}{\Omega}\epsilon_{kzm}a_{mq} + q^2 S_{kq}^n\frac{\phi}{2}\frac{\Omega_z}{\Omega}\epsilon_{kzm}a_{mq} \\ &+ q^2\gamma[-\frac{3}{8}S_{kk}^v + \frac{3}{8}S_{kk}^v\frac{\Omega_m\Omega_t}{\Omega^2}a_{mt} - \frac{S_{ik}^v}{4}(\frac{\Omega_m\Omega_k}{\Omega^2}a_{im} + \frac{\Omega_m\Omega_i}{\Omega^2}a_{mk}) + S_{ik}^v\frac{\Omega_i\Omega_k}{4\Omega^2} + \frac{3}{8}S_{ik}^v\frac{\Omega_q\Omega_z}{\Omega^2}Z_{kzqi}^a \\ &- \frac{S_{tm}^v}{8}a_{tm}] + q^2\gamma[\frac{S_{qq}^n}{8} + \frac{S_{tz}^n}{4}(\frac{\Omega_m\Omega_z}{\Omega^2}a_{tm} + \frac{\Omega_m\Omega_t}{\Omega^2}a_{zm}) - \frac{S_{sz}^n}{4}\frac{\Omega_s\Omega_z}{\Omega^2} - \frac{S_{qq}^n}{8}\frac{\Omega_m\Omega_t}{\Omega^2}a_{tm} \\ &- \frac{S_{kq}^n}{8}\frac{\Omega_s\Omega_t}{\Omega^2}Z_{tqsk}^a - \frac{S_{tm}^n}{8}a_{tm}] + \underbrace{\langle(\frac{dR_{ij}^{|a,\text{slow}\rangle}}{dt})\frac{\Omega_z}{\Omega}\epsilon_{izm}a_m a_j\rangle}_{\text{slow term}},\end{aligned} \tag{C.98}$$

where the contribution of the slow term due to slow randomization is given by

$$\langle(\frac{dR_{ij}^{|a,\text{slow}\rangle}}{dt})\frac{\Omega_z}{\Omega}\epsilon_{izm}a_m a_j\rangle = \gamma\frac{8.5}{2\tau}\frac{\Omega_m\Omega_t}{\Omega^2}\Omega^s q^2[(a_{tm}-\delta_{tm}) + f_{pq}[\delta_{mt}a_{pq} - Z_{pqtm}^a]]\,. \tag{C.99}$$

We re-arrange eq. (C.53) to obtain

$$\begin{aligned}(\frac{d\gamma}{dt})\frac{\Omega_k\Omega_z}{\Omega^2}\frac{1}{2}(q^2\delta_{kz} - A_{kz}) &= -\gamma\frac{\Omega_k\Omega_z}{2\Omega^2}\frac{d}{dt}(q^2\delta_{kz} - A_{kz}) + \langle(\frac{dR_{ij}^{|a}}{dt})\frac{\Omega_z}{\Omega}\epsilon_{izm}a_m a_j\rangle \\ &+ \epsilon_{izm}\langle R_{ij}^{|a}\frac{\Omega_z}{\Omega}\frac{d}{dt}(a_m a_j)\rangle + \langle R_{ij}^{|a}\frac{d}{dt}(\frac{\Omega_z}{\Omega})\epsilon_{izm}a_m a_j\rangle - \gamma\frac{d}{dt}(\frac{\Omega_k\Omega_z}{\Omega^2})\frac{1}{2}(q^2\delta_{kz} - A_{kz})\,.\end{aligned} \tag{C.100}$$

In order to simplify our following calculations, we separate the terms based on their contribution. The eddy axis contribution is given by

$$
\begin{aligned}
F_a &= -\frac{2\gamma}{2}q^2\frac{\Omega_k\Omega_z}{\Omega^2}(-S^a_{kq}a_{qz} + S^a_{pq}Z^a_{kzpq}) - q^2\gamma\frac{\Omega_k\Omega_z}{2\Omega^2}(S^a_{kq}a_{qz} - S^a_{qp}Z^a_{qpkz})\\
&+ q^2(1-3\phi)\epsilon_{izm}\frac{\Omega_z}{2\Omega}S^a_{iq}a_{qm}\\
&= -\frac{\gamma}{2}q^2\frac{\Omega_k\Omega_z}{\Omega^2}(-2S^a_{kq}a_{qz} + 2S^a_{pq}Z^a_{kzpq} + S^a_{kq}a_{qz} - S^a_{pq}Z^a_{kzpq}) + q^2(1-3\phi)\epsilon_{izm}\frac{\Omega_z}{2\Omega}S^a_{iq}a_{qm}\\
&= -\frac{\gamma}{2}q^2\frac{\Omega_k\Omega_z}{\Omega^2}(-S^a_{kq}a_{qz} + S^a_{pq}Z^a_{kzpq}) + q^2(1-3\phi)\epsilon_{izm}\frac{\Omega_z}{2\Omega}S^a_{iq}a_{qm}\,,
\end{aligned}
\tag{C.101}
$$

whereas the vorticity contribution is

$$
\begin{aligned}
F^\Omega &= q^2\frac{\Omega_i\Omega_q}{4\Omega}(1-3\phi)(\delta_{iq} - a_{iq}) + q^2\frac{\gamma}{2}\frac{\Omega_m\Omega_r}{\Omega^2}a_{mt}(\frac{\Omega_t\Omega_q}{\Omega^2}S_{qr} - S_{tr}) + q^2(1-\phi)\frac{\Omega_m\Omega_i}{4\Omega}(\delta_{mi} - a_{mi})\\
&- q^2\gamma[\frac{\Omega_k\Omega_z\Omega_q\Omega_r}{\Omega^4}S_{qr}a_{kz} - \frac{\Omega_z\Omega_r}{\Omega^2}S_{kr}a_{kz}]\\
&= q^2\frac{\Omega_i\Omega_q}{4\Omega}(1-3\phi)(\delta_{iq} - a_{iq}) + q^2\frac{\Omega_q\Omega_i}{4\Omega}(1-\phi)(\delta_{qi} - a_{qi}) + q^2\frac{\gamma}{2}\frac{\Omega_m\Omega_r}{\Omega^2}a_{mt}(\frac{\Omega_t\Omega_q}{\Omega^2}S_{qr} - S_{tr})\\
&- 2q^2\frac{\gamma}{2}\frac{\Omega_m\Omega_r}{\Omega^2}a_{mt}(\frac{\Omega_t\Omega_q}{\Omega^2}S_{qr} - S_{tr})\\
&= q^2\frac{\Omega_i\Omega_q}{4\Omega}(\delta_{iq} - a_{iq})[1 - 3\phi + 1 - \phi] + q^2\frac{\gamma}{2}\frac{\Omega_m\Omega_r}{\Omega^2}a_{mt}(\frac{\Omega_t\Omega_q}{\Omega^2}S_{qr} - S_{tr} - 2\frac{\Omega_t\Omega_q}{\Omega^2}S_{qr} + 2S_{tr})\\
&= q^2\frac{\Omega_i\Omega_q}{2\Omega}(\delta_{iq} - a_{iq})[1 - 2\phi] + q^2\frac{\gamma}{2}\frac{\Omega_m\Omega_r}{\Omega^2}a_{mt}(-\frac{\Omega_t\Omega_q}{\Omega^2}S_{qr} + S_{tr})\,,
\end{aligned}
\tag{C.102}
$$

and the normal contribution is

$$
\begin{aligned}
F^n &= q^2S^n_{kq}\frac{\phi}{2}\frac{\Omega_z}{\Omega}\epsilon_{kzm}a_{mq} + q^2\gamma[\frac{S^n_{qq}}{8} + \frac{S^n_{tz}}{4}(\frac{\Omega_m\Omega_z}{\Omega^2}a_{tm} + \frac{\Omega_m\Omega_t}{\Omega^2}a_{zm}) - \frac{S^n_{sz}}{4}\frac{\Omega_s\Omega_z}{\Omega^2}\\
&- \frac{S^n_{qq}}{8}\frac{\Omega_m\Omega_t}{\Omega^2}a_{tm} - \frac{S^n_{kq}}{8}\frac{\Omega_s\Omega_t}{\Omega^2}Z^a_{tqsk} - \frac{S^n_{tm}}{8}a_{tm}]\,.
\end{aligned}
\tag{C.103}
$$

The most contribution is given by velocity, which is decomposed in two parts, the non-stropholysis part,

$$
\begin{aligned}
F^v_1 &= -\epsilon_{kzm}\frac{\Omega_z}{2\Omega}a_{mq}q^2[(1-\phi)S^v_{qk} + 2\phi S^v_{kq}] + q^2S^v_{kq}\frac{\phi}{2}\frac{\Omega_z}{\Omega}\epsilon_{kzm}a_{mq}\\
&= \epsilon_{kzm}\frac{\Omega_z}{2\Omega}a_{mq}q^2[\phi S^v_{kq} - (1-\phi)S^v_{qk} - 2\phi S^v_{kq}]\\
&= \epsilon_{kzm}\frac{\Omega_z}{2\Omega}a_{mq}q^2[-\phi S^v_{kq} - (1-\phi)S^v_{qk}]\\
&= -\epsilon_{kzm}\frac{\Omega_z}{2\Omega}a_{mq}q^2[\phi S^v_{kq} + (1-\phi)S^v_{qk}]\,,
\end{aligned}
\tag{C.104}
$$

and the stropholysis part

$$
\begin{aligned}
F_2^v &= q^2\gamma[S^v_{km}r_{mk} - \frac{4\Omega_k\Omega_z}{8\Omega^2}(1-\phi)S^v_{qq}a_{kz} - \frac{4\Omega_k\Omega_z}{8\Omega^2}S^v_{qs}Z^a_{sqkz}(3\phi-1) \\
&- \frac{\Omega_k\Omega_z}{2\Omega^2}\gamma\frac{\Omega_m}{\Omega}(\epsilon_{smt}Z^a_{tqkz} + \epsilon_{qmt}Z^a_{tskz})S^v_{qs} - \frac{3}{8}S^v_{kk} + \frac{3}{8}S^v_{kk}\frac{\Omega_m\Omega_t}{\Omega^2}a_{mt} - \frac{1}{4}S^v_{ik}(\frac{\Omega_m\Omega_k}{\Omega^2}a_{im} \\
&+ \frac{\Omega_m\Omega_i}{\Omega^2}a_{mk}) + S^v_{ik}\frac{\Omega_i\Omega_k}{4\Omega^2} + \frac{3}{8}S^v_{ik}\frac{\Omega_q\Omega_z}{\Omega^2}Z^a_{kzqi} - \frac{S^v_{tm}a_{tm}}{8}] \\
&= q^2\gamma[S^v_{km}r_{mk} + \frac{3}{8}S^v_{kk}\frac{\Omega_m\Omega_t}{\Omega^2}a_{mt} - \frac{4\Omega_m\Omega_t}{8\Omega^2}(1-\phi)S^v_{kk}a_{mt} - \frac{4\Omega_k\Omega_z}{8\Omega^2}S^v_{qs}Z^a_{sqkz}(3\phi-1) \\
&+ \frac{3\Omega_k\Omega_z}{8\Omega^2}S^v_{qs}Z^a_{qskz} - \frac{3}{8}S^v_{kk} - \frac{S^v_{tm}a_{tm}}{8} + S^v_{ik}\frac{\Omega_i\Omega_k}{4\Omega^2} - \frac{1}{4}S^v_{ik}(\frac{\Omega_m\Omega_k}{\Omega^2}a_{im} + \frac{\Omega_m\Omega_i}{\Omega^2}a_{mk}) \\
&- \frac{\Omega_k\Omega_z}{2\Omega^2}\gamma\frac{\Omega_m}{\Omega}(\epsilon_{smt}Z^a_{tqkz} + \epsilon_{qmt}Z^a_{tskz})S^v_{qs}] \\
&= q^2\gamma[S^v_{km}r_{mk} + S^v_{kk}\frac{\Omega_m\Omega_t}{8\Omega^2}a_{mt}(3-4+4\phi) + \frac{\Omega_k\Omega_z}{8\Omega^2}S^v_{qs}Z^a_{sqkz}(-12\phi+4+3) - \frac{3}{8}S^v_{kk} \\
&- \frac{S^v_{tm}a_{tm}}{8} + S^v_{ik}\frac{\Omega_i\Omega_k}{4\Omega^2} - \frac{1}{4}S^v_{ik}(\frac{\Omega_m\Omega_k}{\Omega^2}a_{im} + \frac{\Omega_m\Omega_i}{\Omega^2}a_{mk}) \\
&- \frac{\Omega_k\Omega_z}{2\Omega^2}\gamma\frac{\Omega_m}{\Omega}(\epsilon_{smt}Z^a_{tqkz} + \epsilon_{qmt}Z^a_{tskz})S^v_{qs}] \\
&= q^2\gamma[S^v_{km}r_{mk} + S^v_{kk}\frac{\Omega_m\Omega_t}{8\Omega^2}a_{mt}(4\phi-1) + \frac{\Omega_k\Omega_z}{8\Omega^2}S^v_{qs}Z^a_{sqkz}(7-12\phi) - \frac{3}{8}S^v_{kk} - \frac{S^v_{tm}a_{tm}}{8} \\
&+ S^v_{ik}\frac{\Omega_i\Omega_k}{4\Omega^2} - \frac{1}{4}S^v_{ik}(\frac{\Omega_m\Omega_k}{\Omega^2}a_{im} + \frac{\Omega_m\Omega_i}{\Omega^2}a_{mk}) - \frac{\Omega_k\Omega_z}{2\Omega^2}\gamma\frac{\Omega_m}{\Omega}(\epsilon_{smt}Z^a_{tqkz} + \epsilon_{qmt}Z^a_{tskz})S^v_{qs}]\,.
\end{aligned}
\tag{C.105}
$$

Adding all **-F** terms together yields the final expression for the transport equation of γ,

$$\begin{aligned}
&(\frac{d\gamma}{dt})\frac{\Omega_k\Omega_z}{\Omega^2}\frac{1}{2}(\delta_{kz}-a_{kz}) = \underbrace{-\frac{\gamma}{2}\frac{\Omega_k\Omega_z}{\Omega^2}(-S^a_{kq}a_{qz}+S^a_{pq}Z^a_{kzpq})+(1-3\phi)\epsilon_{izm}\frac{\Omega_z}{2\Omega}S^a_{iq}a_{qm}}_{\text{eddy contribution}} \\
&\underbrace{+\gamma\frac{8.5}{2\tau}\frac{\Omega_m\Omega_t}{\Omega^2}\Omega^*[(a_{tm}-\delta_{tm})+f_{pq}[\delta_{mt}a_{pq}-Z^a_{pqtm}]]}_{\text{pure slow term}} \\
&\underbrace{+\frac{\Omega_i\Omega_q}{2\Omega}(\delta_{iq}-a_{iq})[1-2\phi]+\frac{\gamma}{2}\frac{\Omega_m\Omega_r}{\Omega^2}a_{mt}(-\frac{\Omega_t\Omega_q}{\Omega^2}S_{qr}+S_{tr})}_{\text{pure vorticity contribution}} \\
&+\underbrace{S^n_{kq}\frac{\phi}{2}\frac{\Omega_z}{\Omega}\epsilon_{kzm}a_{mq}+\gamma[\frac{S^n_{qq}}{8}+\frac{S^n_{tz}}{4}(\frac{\Omega_m\Omega_z}{\Omega^2}a_{tm}+\frac{\Omega_m\Omega_t}{\Omega^2}a_{zm})-\frac{S^n_{sz}}{4}\frac{\Omega_s\Omega_z}{\Omega^2}-\frac{S^n_{qq}}{8}\frac{\Omega_m\Omega_t}{\Omega^2}a_{tm}}_{\text{gradient contribution}} \\
&\underbrace{-\frac{S^n_{kq}}{8}\frac{\Omega_s\Omega_t}{\Omega^2}Z^a_{tqsk}-\frac{S^n_{tm}}{8}a_{tm}]}_{\text{gradient contribution}} \\
&\underbrace{-\epsilon_{kzm}\frac{\Omega_z}{2\Omega}a_{mq}[\phi S^v_{kq}+(1-\phi)S^v_{qk}]}_{\text{velocity contribution}} \\
&\underbrace{+\gamma[S^v_{km}r_{mk}+S^v_{kk}\frac{\Omega_m\Omega_t}{8\Omega^2}a_{mt}(4\phi-1)+\frac{\Omega_k\Omega_z}{8\Omega^2}S^v_{qs}Z^a_{sqkz}(7-12\phi)-\frac{3}{8}S^v_{kk}-\frac{S^v_{tm}a_{tm}}{8}}_{\text{velocity contribution}} \\
&\underbrace{+S^v_{ik}\frac{\Omega_i\Omega_k}{4\Omega^2}-\frac{1}{4}S^v_{ik}(\frac{\Omega_m\Omega_k}{\Omega^2}a_{im}+\frac{\Omega_m\Omega_i}{\Omega^2}a_{mk})-\frac{\Omega_k\Omega_z}{2\Omega^2}\gamma\frac{\Omega_m}{\Omega}(\epsilon_{smt}Z^a_{tqkz}+\epsilon_{qmt}Z^a_{tskz})S^v_{qs}]}_{\text{velocity contribution}} \; .
\end{aligned} \tag{C.106}$$

The above equation captures correctly the RDT limit given in TF61.

C.2 Model 2.

The final goal of the following analysis is to construct a model which, in contrast to Model 1, predicts non-zero ϕ and γ for irrotational flows which are subjected to slow deformations. We start by introducing the expression for the effective eddy rotation rate

$$\Theta_z = \epsilon_{zrp} G^a_{rk} a_p a_k \, . \tag{C.107}$$

Some useful products regarding this vector are given below

$$\Omega^{*2} = \langle \Theta_i \Theta_i \rangle = G^a_{sk} G^a_{sq} a_{kq} - S^a_{tk} S^a_{pq} Z^a_{tkpq} \, , \tag{C.108a}$$

$$\langle \Theta_i \Theta_j \rangle = \delta_{ij} (G^a_{sk} G^a_{sq} a_{kq} - S^a_{tk} S^a_{pq} Z^a_{pqtk}) + S^a_{tk} (G^a_{iq} Z^a_{tkjq} + G^a_{jq} Z^a_{tkiq}) \tag{C.108b}$$

$$- G^a_{jk} G^a_{iq} a_{kq} - G^a_{sk} G^a_{sq} Z^a_{ijkq} \, . \tag{C.108c}$$

The constitutive equation of the Reynolds stress is given by

$$R_{ij} = q^2 [\frac{(1-\phi)}{2} (\delta_{ij} - a_{ij}) + \phi a_{ij} + \frac{\gamma}{2\Omega^*} (2 S^a_{tq} Z^a_{tqij} - G^a_{iq} a_{qj} - G^a_{jq} a_{qi})] \, . \tag{C.109}$$

A set of useful identities is given below

$$\frac{d\Theta_i}{dt} = \epsilon_{ijk} G^a_{jl} \frac{da_{kl}}{dt} \, , \tag{C.110a}$$

$$\frac{d}{dt} (\frac{\Theta_i}{\Theta}) = \frac{1}{\Theta} \frac{d\Theta_i}{dt} - \frac{\Theta_i \Theta_j}{\Theta^3} \frac{d\Theta_j}{dt} \, , \tag{C.110b}$$

$$\frac{d}{dt} (\frac{\Theta_i \Theta_j}{\Theta^2}) = \frac{1}{\Theta^2} (\Theta_i \frac{d\Theta_j}{dt} + \Theta_j \frac{d\Theta_i}{dt}) - 2 \frac{\Theta_k}{\Theta^2} \frac{\Theta_i \Theta_j}{\Theta^2} \frac{d\Theta_k}{dt} \, . \tag{C.110c}$$

The main idea is to use again the concept of effective gradients as described in [24], combined with the effective eddy rotation rate. Below we derive the transport equations of the structure parameters.

C.2.1 Derivation of the transport equation for the eddy-axis tensor a_{ij}.

We start by introducing the transport equation of A_{ij}

$$\frac{dA_{ij}}{dt} = G^a_{ik} A_{kj} + G^a_{jk} A_{ki} - 2 S^a_{ks} q^2 Z^a_{ijks} - 2 S^v_{qk} \langle v_k v_q A_i A_j \rangle \, . \tag{C.111}$$

The transport equation for the energy-weighted normalized eddy-axis tensor can be found through the identity

$$\frac{da_{ij}}{dt} = \frac{\dot{A}_{ij}}{q^2} - a_{ij}\frac{\dot{A}_{kk}}{q^2}\,. \tag{C.112}$$

We introduce the symmetric tensor $S_{ij}^{a,n,v}$ and the antisymmetric tensor $\Omega_{ij}^{a,n,v}$, which are defined as follow

$$S_{ik}^{a,v,n} = S_{ik} + \frac{C_{a,v,n}}{2\tau}(r_{iq}d_{qk} + r_{kq}d_{qi})\,, \tag{C.113a}$$

$$\Omega_{ik}^{a,v,n} = \Omega_{ik} + \frac{C_{a,v,n}}{2\tau}(r_{iq}d_{qk} - r_{kq}d_{qi})\,. \tag{C.113b}$$

Again, contraction of the A_{ij} transport equation yields the energy evolution equation

$$\frac{dA_{ss}}{dt} = -2S_{qk}^{v}R_{kq}\,, \tag{C.114}$$

where the transport equation of the normalized tensor is given by

$$\frac{da_{ij}}{dt} = G_{ik}^{a}a_{kj} + G_{jk}^{a}a_{ki} - 2S_{ks}^{a}Z_{ijks}^{a} - 2\frac{S_{qk}^{v}}{q^2}\langle v_k v_q A_i A_j\rangle + 2S_{qk}^{v}r_{kq}a_{ij}\,. \tag{C.115}$$

The last term of eq. (C.115) can be shown to be

$$2S_{qk}^{v}r_{kq}a_{ij} = (1-\phi)S_{qq}^{v}a_{ij} + (3\phi-1)S_{qk}^{v}a_{kq}a_{ij} + \frac{2\gamma}{\Omega^*}(S_{qk}^{v}S_{tp}^{a}Z_{kqtp}^{a} - S_{qk}^{v}G_{kp}^{a}a_{pq})a_{ij}\,. \tag{C.116}$$

Simplifying the fourth term yields,

$$-2\frac{S_{qk}^{v}}{q^2}\langle v_k v_q A_i A_j\rangle = -(1-\phi)S_{qq}^{v}a_{ij} + (1-3\phi)S_{qk}^{v}Z_{kqij}^{a} - \frac{2\gamma}{\Omega^*}S_{qk}^{v}(S_{tw}^{a}W_{twkqij} - G_{kw}^{a}Z_{wqij}^{a})\,, \tag{C.117}$$

where W_{ijklpq} is a fully-symmetric sixth-order tensor. A non-singular model for this tensor is already constructed by Kassinos in TF61, consistent with the model used here for Z tensor.

Substituting eqs. (C.117),(C.116) in eq. (C.115) yields the final expression for the transport equation of a_{ij} by

$$\begin{aligned}\frac{da_{ij}}{dt} &= S_{ik}^{a}a_{kj} + S_{jk}^{a}a_{ki} + (\Omega_{ik}^{a}a_{kj} + \Omega_{jk}^{a}a_{ki}) - 2S_{qk}^{a}Z_{ijkq}^{a} + (3\phi-1)S_{qk}^{v}[a_{kq}a_{ij} - Z_{kqij}^{a}] \\ &\quad + \frac{2\gamma}{\Omega^*}S_{qk}^{v}(S_{tp}^{a}Z_{tpkq}^{a}a_{ij} - G_{kp}^{a}a_{pq}a_{ij} - S_{tw}^{a}W_{twkqij} + G_{kw}^{a}Z_{wqij}^{a})\,.\end{aligned} \tag{C.118}$$

C.2.2 Derivation of the transport equation for the jetal parameter ϕ.

As before, the transport equation of scalar ϕ can be found through the expression

$$\frac{d\phi}{dt} = \frac{1}{q^2}[\langle \frac{dR^{|a}_{ij}}{dt} a_i a_j \rangle + \langle R^{|a}_{ij} \frac{d}{dt}(a_i a_j) \rangle - \frac{\langle R^{|a}_{ij} a_i a_j \rangle}{q^2} \frac{dq^2}{dt}] \,. \tag{C.119}$$

Re-expressing the RHS of eq. (C.119) yields,

$$\frac{1}{q^2} \langle R^{|a}_{ij} \frac{d}{dt}(a_i a_j) \rangle = \frac{\gamma}{\Omega^*}(S^a_{tq} S^a_{js} Z^a_{jqts} - G^a_{iq} G^a_{is} a_{qs}) \,. \tag{C.120}$$

Following similar analysis as before, the first part of the first term of eq. (C.119) is found to be

$$-2\frac{G^v_{ik}}{q^2} \langle R^{|a}_{kj} a_i a_j \rangle = -2\phi S^v_{ik} a_{ki} - \frac{\gamma}{\Omega^*}(S^v_{ik} S^a_{tq} Z^a_{iktq} - G^v_{ik} G^a_{kq} a_{qi}) \,, \tag{C.121}$$

while for the pure slow term we can obtain

$$-2\frac{\langle C_1 R^{|a}_{ij} a_i a_j \rangle}{q^2} + \frac{\langle C_2^2 R^{|a}_{kk} \rangle}{q^2} = (1-2\phi)\frac{8.5}{\tau}\Omega^s f_{pq} d_{qp} \,. \tag{C.122}$$

Adding both terms back into the first term of eq. (C.119) yields the simplified expression

$$\frac{1}{q^2}\langle \frac{dR^{|a}_{ij}}{dt} a_i a_j \rangle = -2\phi S^v_{ik} a_{ki} + (1-2\phi)\frac{8.5}{\tau}\Omega^s f_{pq} d_{qp} - \frac{\gamma}{\Omega^*}(S^v_{ik} S^a_{tq} Z^a_{iktq} - G^v_{ik} G^a_{kq} a_{qi}) \,. \tag{C.123}$$

Also, the third term of the RHS of eq. (C.119) is simply given by

$$\frac{1}{q^2}(-\frac{\langle R^{|a}_{ij} a_i a_j \rangle}{q^2} \frac{dq^2}{dt}) = 2\phi S^v_{qk} r_{kq} \,. \tag{C.124}$$

Lastly, addition of all terms yields the final expression for the ϕ transport equation

$$\frac{d\phi}{dt} = 2\phi S^v_{qk}(r_{kq} - a_{kq}) + (1-2\phi)\frac{8.5}{\tau}\Omega^s f_{pq} d_{qp} + \frac{\gamma}{\Omega^*}\left(S^a_{tq}(S^a_{js} - S^v_{js}) Z^a_{jstq} + (G^v_{si} - G^a_{is}) G^a_{iq} a_{qs} \right) . \tag{C.125}$$

C.2.3 Derivation of the transport equation for the stropholysis scalar γ.

The third term of the RHS of eq. (C.53) can be shown to be

$$\begin{aligned}&\langle R_{ij}^{|a}\frac{\Theta_z}{\Theta}\epsilon_{izm}\frac{d}{dt}(a_m a_j)\rangle = \frac{q^2(3\phi-1)}{2\Omega^*}[G_{rq}^a G_{rk}^a a_{kq} - S_{pq}^a S_{ik}^a Z_{pqik}^a]\\ &- q^2\frac{\gamma}{2}\frac{\langle\Theta_m\Theta_z\rangle}{\Omega^{*2}}(G_{mq}^a a_{qz} - S_{qs}^a Z_{qsmz}^a)\,.\end{aligned} \tag{C.126}$$

A simplified expression of the second term is

$$\langle R_{ij}^{|a}\frac{d}{dt}(\frac{\Theta_z}{\Theta})\epsilon_{izm}a_m a_j\rangle = \frac{q^2\gamma}{2}\langle\frac{\Theta_s}{\Theta}\frac{d}{dt}(\frac{\Theta_z}{\Theta})\rangle(\delta_{sz} - a_{sz})\,. \tag{C.127}$$

Regarding the manipulation of the fourth term of eq. (C.53), a useful identity is given by

$$\begin{aligned}S_{pq}^v\langle R_{pq}^{|a}a_z a_m\rangle &= q^2\frac{(1-\phi)}{2}S_{qq}^v a_{zm} + q^2\frac{(3\phi-1)}{2}S_{pq}^v Z_{pqzm}^a\\ &+ \frac{q^2\gamma}{\Omega^*}(S_{qs}^v S_{tw}^a W_{sqtwmz} - S_{qs}^v G_{sw}^a Z_{wqmz}^a)\,.\end{aligned} \tag{C.128}$$

while the fourth term of eq. (C.53) can be shown to be

$$\begin{aligned}&-\gamma\frac{\langle\Theta_z\Theta_m\rangle}{2\Omega^{*2}}\frac{d}{dt}(q^2\delta_{zm} - A_{zm}) = \gamma S_{qk}^v R_{kq} + \gamma q^2\frac{\langle\Theta_z\Theta_m\rangle}{\Omega^{*2}}(S_{zk}^a a_{km} - S_{pq}^a Z_{pqzm}^a)\\ &- q^2\gamma\frac{\langle\Theta_z\Theta_m\rangle}{2\Omega^{*2}}[(1-\phi)S_{qq}^v a_{zm} + (3\phi-1)S_{pq}^v Z_{pqzm}^a + \frac{2\gamma}{\Omega^*}(S_{qs}^v S_{tw}^a W_{sqtwmz} - S_{qs}^v G_{sw}^a Z_{wqmz}^a)]\\ &+ q^2\gamma\frac{\langle\Theta_z\Theta_m\rangle}{\Omega^{*2}}\Omega_{zk}^a a_{km}\,.\end{aligned} \tag{C.129}$$

Next, the first term of eq. (C.53) is decomposed as follow

$$\begin{aligned}\langle(\frac{dR_{ij}^{|a}}{dt})\frac{\Theta_z}{\Theta}\epsilon_{izm}a_m a_j\rangle &= -G_{ik}^v\langle R_{kj}^{|a}\frac{\Theta_z}{\Theta}\epsilon_{izm}a_m a_j\rangle - G_{jk}^v\langle R_{ki}^{|a}\frac{\Theta_z}{\Theta}\epsilon_{izm}a_m a_j\rangle \\ &+ [G_{kq}^n + G_{kq}^v]\langle(M_{iqkj}^{|a} + M_{jqki}^{|a})\frac{\Theta_z}{\Theta}\epsilon_{izm}a_m a_j\rangle \\ &- \langle[2C_1 R_{ij}^{|a} - C_2^2 R_{kk}^{|a}(\delta_{ij} - n_i n_j)]\frac{\Theta_z}{\Theta}\epsilon_{izm}a_m a_j\rangle\,.\end{aligned} \tag{C.130}$$

We deal with each term of eq. (C.130) individually. Thus, the first term is given by

$$\begin{aligned}&- G_{ik}^v\langle R_{kj}^{|a}\frac{\Theta_z}{\Theta}\epsilon_{izm}a_m a_j\rangle = -\frac{q^2\phi}{\Omega^*}[S_{pk}^v S_{mq}^a Z_{kpqm}^a - G_{rk}^v G_{rq}^a a_{kq}] - \frac{q^2\gamma}{2}S_{kk}^v \\ &+ \frac{q^2\gamma}{2}S_{kk}^v\frac{\langle\Theta_m\Theta_y\rangle}{\Omega^{*2}}a_{ym} - q^2\gamma S_{yz}^v\frac{\langle\Theta_m\Theta_z\rangle}{\Omega^{*2}}a_{ym} + \gamma q^2 S_{sz}^v\frac{\langle\Theta_s\Theta_z\rangle}{2\Omega^{*2}} + \gamma q^2\frac{S_{ym}^v}{2}a_{ym}\,,\end{aligned} \tag{C.131}$$

while the second term can be shown to be

$$\begin{aligned}-\frac{G_{jk}^v}{q^2}\langle R_{ki}^{|a}\frac{\Theta_z}{\Theta}\epsilon_{izm}a_m a_j\rangle &= -\frac{(1-\phi)}{2\Omega^*}(S_{mq}^a S_{jp}^v Z_{pqmj}^a - G_{kq}^a G_{jk}^v a_{qj}) \\ &- \gamma G_{jk}^v\frac{\langle\Theta_q\Theta_z\rangle}{2\Omega^{*2}}(\delta_{qz}a_{kj} - Z_{zqkj}^a)\,.\end{aligned} \tag{C.132}$$

Adding both terms yields the expression

$$\begin{aligned}&- G_{ik}^v\langle R_{kj}^{|a}\frac{\Theta_z}{\Theta}\epsilon_{izm}a_m a_j\rangle - G_{jk}^v\langle R_{ki}^{|a}\frac{\Theta_z}{\Theta}\epsilon_{izm}a_m a_j\rangle = \frac{1}{2\Omega^*}[-(1+\phi)S_{pk}^v S_{mq}^a Z_{pkmq}^a \\ &+ G_{rq}^a(2\phi G_{rk}^v + (1-\phi)G_{kr}^v)a_{qk}] + \gamma q^2[S_{jk}^v\frac{\langle\Theta_m\Theta_y\rangle}{2\Omega^{*2}}Z_{ykmj}^a - \frac{S_{kk}^v}{2} + S_{kk}^v\frac{\langle\Theta_m\Theta_y\rangle}{2\Omega^{*2}}a_{ym} \\ &- S_{yz}^v\frac{\langle\Theta_m\Theta_z\rangle}{\Omega^{*2}}a_{ym} + S_{sz}^v\frac{\langle\Theta_s\Theta_z\rangle}{2\Omega^{*2}}]\,.\end{aligned} \tag{C.133}$$

Next, the pure slow part of eq. (C.130) is shown to be

$$\begin{aligned}-\langle 2C_1 R_{ij}^{|a}\frac{\Theta_z}{\Theta}\epsilon_{izm}a_m a_j\rangle &= -q^2\gamma\frac{8.5}{\tau}\Omega^s f_{pq}(d_{pq} - \frac{\langle\Theta_m\Theta_y\rangle}{\Omega^{*2}}\langle n_p n_q a_y a_m\rangle) \\ &= \gamma\frac{8.5}{2\tau}\frac{\langle\Theta_m\Theta_t\rangle}{\Omega^{*2}}\Omega^s[(a_{tm} - \delta_{tm}) + f_{pq}(\delta_{mt}a_{pq} - Z_{pqtm}^a)]\,.\end{aligned} \tag{C.134}$$

The third term of eq. (C.53) involves the fourth order pressure-strain tensor, which is decomposed at three parts, similarly to the previous analysis. Again, the vortical contribution is zero

$$G^v_{kq}\langle M^{v|a}_{jqki}\frac{\Theta_z}{\Theta}\epsilon_{izm}a_m a_j\rangle = 0\,, \tag{C.135}$$

where the jetal contribution is not, given by

$$G^v_{kq}\langle M^{j|a}_{jqki}\frac{\Theta_z}{\Theta}\epsilon_{izm}a_m a_j\rangle = \frac{q^2\phi}{2\Omega^*}(S^v_{kq}S^a_{ms}Z^a_{mskq} - G^v_{kq}G^a_{ks}a_{sq})\,. \tag{C.136}$$

The expression for the helical contribution is found to be

$$\begin{aligned} G^v_{kq}\langle M^{h|a}_{jqki}\frac{\Theta_z}{\Theta}\epsilon_{izm}a_m a_j\rangle &= \frac{q^2\gamma}{8}[S^v_{kk} - S^v_{kk}\frac{\langle\Theta_t\Theta_m\rangle}{\Omega^{*2}}a_{mt} - 2S^v_{kq}\frac{\langle\Theta_q\Theta_k\rangle}{\Omega^{*2}} - S^v_{kq}a_{qk} \\ &+ 2G^v_{kq}\frac{\langle\Theta_q\Theta_m\rangle}{\Omega^{*2}}a_{mk} + 2G^v_{km}\frac{\langle\Theta_t\Theta_k\rangle}{\Omega^{*2}}a_{mt} - S^v_{kq}\frac{\langle\Theta_t\Theta_s\rangle}{\Omega^{*2}}Z^a_{sktq}]\,. \end{aligned} \tag{C.137}$$

Adding all contributions together yields,

$$\begin{aligned} G^v_{kq}\langle M^{|a}_{jqki}\frac{\Theta_z}{\Theta}\epsilon_{izm}a_m a_j\rangle &= \frac{q^2\phi}{2\Omega^*}(S^v_{kq}S^a_{ms}Z^a_{mskq} - G^v_{kq}G^a_{ks}a_{sq}) + \frac{q^2\gamma}{8}[S^v_{kk} - S^v_{kk}\frac{\langle\Theta_t\Theta_m\rangle}{\Omega^{*2}}a_{mt} \\ &- 2S^v_{kq}\frac{\langle\Theta_q\Theta_k\rangle}{\Omega^{*2}} - S^v_{kq}a_{qk} + 2S^v_{kq}(\frac{\langle\Theta_q\Theta_m\rangle}{\Omega^{*2}}a_{mk} + \frac{\langle\Theta_k\Theta_m\rangle}{\Omega^{*2}}a_{mq}) - S^v_{kq}\frac{\langle\Theta_t\Theta_s\rangle}{\Omega^{*2}}Z^a_{sktq}]\,. \end{aligned} \tag{C.138}$$

which leads to the final expression for the first term of γ transport equation

$$
\begin{aligned}
&\frac{1}{q^2}\langle \frac{dR^{|a}_{ij}}{dt}\frac{\Theta_z}{\Theta}\epsilon_{izm}a_m a_j\rangle = \frac{1}{2\Omega^*}[-S^v_{pk}S^a_{mq}Z^a_{pkmq} + G^a_{rq}(\phi G^v_{rk} + (1-\phi)G^v_{kr})a_{qk}] \\
&+ \frac{\phi}{2\Omega^*}[S^n_{kq}S^a_{ms}Z^a_{mskq} - G^n_{kq}G^a_{ks}a_{sq}] \\
&+ \gamma[-\frac{3}{8}S^v_{kk} + \frac{3}{8}S^v_{kk}\frac{\langle\Theta_m\Theta_y\rangle}{\Omega^{*2}}a_{ym} - \frac{3}{4}S^v_{yz}\frac{\langle\Theta_m\Theta_z\rangle}{\Omega^{*2}}a_{ym} + S^v_{sz}\frac{\langle\Theta_s\Theta_z\rangle}{4\Omega^{*2}} - \frac{S^v_{kq}a_{qk}}{8} \\
&+ S^v_{kq}\frac{\langle\Theta_q\Theta_m\rangle}{4\Omega^{*2}}a_{mk} + \frac{3}{8}S^v_{jk}\frac{\langle\Theta_m\Theta_y\rangle}{\Omega^{*2}}Z^a_{ykmj}] \\
&+ \gamma[\frac{S^n_{kk}}{8} - \frac{S^n_{kk}}{8}\frac{\langle\Theta_t\Theta_m\rangle}{\Omega^{*2}}a_{mt} - S^n_{kq}\frac{\langle\Theta_q\Theta_k\rangle}{4\Omega^{*2}} - \frac{S^n_{kq}}{8}a_{qk} + S^n_{kq}(\frac{\langle\Theta_q\Theta_m\rangle}{4\Omega^{*2}}a_{mk} + \frac{\langle\Theta_k\Theta_m\rangle}{4\Omega^{*2}}a_{mq}) \\
&- \frac{S^n_{kq}}{8}\frac{\langle\Theta_t\Theta_s\rangle}{\Omega^{*2}}Z^a_{sktq}] - \gamma\frac{8.5}{\tau}\Omega^s f_{pq}(d_{pq} - \frac{\langle\Theta_m\Theta_y\rangle}{\Omega^{*2}}\langle n_p n_q a_y a_m\rangle)\,.
\end{aligned}
\tag{C.139}
$$

Summarizing, all the simplified expressions for the RHS terms of eq. (C.53) are given below

$$
\begin{aligned}
\langle R^{|a}_{ij}\frac{\Theta_z}{\Theta}\epsilon_{izm}\frac{d}{dt}(a_m a_j)\rangle &= \frac{q^2(3\phi-1)}{2\Omega^*}[G^a_{rq}G^a_{rk}a_{kq} - S^a_{pq}S^a_{ik}Z^a_{pqik}] \\
&- q^2\frac{\gamma}{2}\frac{\langle\Theta_m\Theta_z\rangle}{\Omega^{*2}}(G^a_{mq}a_{qz} - S^a_{qs}Z^a_{qsmz})\,,
\end{aligned}
\tag{C.140}
$$

$$
\langle R^{|a}_{ij}\frac{d}{dt}(\frac{\Theta_z}{\Theta})\epsilon_{izm}a_m a_j\rangle = \frac{q^2\gamma}{2}\langle\frac{\Theta_s}{\Theta}\frac{d}{dt}(\frac{\Theta_z}{\Theta})\rangle(\delta_{sz} - a_{sz})\,,
\tag{C.141}
$$

$$
-\frac{\gamma}{2}\frac{d}{dt}(\frac{\langle\Theta_z\Theta_m\rangle}{\Omega^{*2}})(\delta_{zm} - a_{zm}) = -\frac{\gamma}{2}\frac{d}{dt}(\frac{\langle\Theta_z\Theta_m\rangle}{\Omega^{*2}})(\delta_{zm} - a_{zm})\,,
\tag{C.142}
$$

$$
\begin{aligned}
&-\gamma\frac{\langle\Theta_z\Theta_m\rangle}{2\Omega^{*2}}\frac{d}{dt}(q^2\delta_{zm} - A_{zm}) = \gamma S^v_{qk}R_{kq} + \gamma q^2\frac{\langle\Theta_z\Theta_m\rangle}{\Omega^{*2}}(S^a_{zk}a_{km} - S^a_{pq}Z^a_{pqzm}) \\
&- q^2\gamma\frac{\langle\Theta_z\Theta_m\rangle}{2\Omega^{*2}}\Bigg[(1-\phi)S^v_{qq}a_{zm} + (3\phi-1)S^v_{pq}Z^a_{pqzm} \\
&+ \frac{2\gamma}{\Omega^*}(S^v_{qs}S^a_{tw}W_{sqtwmz} - S^v_{qs}G^a_{sw}Z^a_{wqmz})\Bigg] + q^2\gamma\frac{\langle\Theta_z\Theta_m\rangle}{\Omega^{*2}}\Omega^a_{zk}a_{km}\,.
\end{aligned}
\tag{C.143}
$$

Adding all the above expressions and further simplifying yields the final expression for the transport equation of γ

$$
\begin{aligned}
&(\frac{d\gamma}{dt})\frac{\langle\Theta_z\Theta_m\rangle}{2\Omega^{*2}}(\delta_{zm}-a_{zm}) = \frac{(3\phi-1)}{2\Omega^*}(G^a_{rq}G^a_{rk}a_{kq} - S^a_{pq}S^a_{ik}Z^a_{pqik}) \\
&+ \frac{1}{2\Omega^*}\left[- S^v_{pk}S^a_{mq}Z^a_{pkmq} + G^a_{rq}(\phi G^v_{rk} + (1-\phi)G^v_{kr})a_{qk}\right] + \frac{\phi}{2\Omega^*}(S^n_{kq}S^a_{ms}Z^a_{mskq} - G^n_{kq}G^a_{ks}a_{sq}) \\
&- \frac{\gamma}{2}\frac{d}{dt}(\frac{\langle\Theta_z\Theta_m\rangle}{\Omega^{*2}})(\delta_{zm}-a_{zm}) + \frac{\gamma}{2}\langle\frac{\Theta_s}{\Theta}\frac{d}{dt}(\frac{\Theta_z}{\Theta})\rangle(\delta_{sz}-a_{sz}) - \gamma\frac{8.5}{\tau}\Omega^s f_{pq}(d_{pq} \\
&- \frac{\langle\Theta_m\Theta_y\rangle}{\Omega^{*2}}\langle n_p n_q a_y a_m\rangle) + \gamma\left[\frac{S^n_{kk}}{8} - \frac{S^n_{kk}}{8}\frac{\langle\Theta_t\Theta_m\rangle}{\Omega^{*2}}a_{mt} - S^n_{kq}\frac{\langle\Theta_q\Theta_k\rangle}{4\Omega^{*2}} - \frac{S^n_{kq}}{8}a_{qk}\right. \\
&\left. + S^n_{kq}\frac{\langle\Theta_q\Theta_m\rangle}{2\Omega^{*2}}a_{mk} - \frac{S^n_{kq}}{8}\frac{\langle\Theta_t\Theta_s\rangle}{\Omega^{*2}}Z^a_{sktq}\right] + \gamma\frac{\langle\Theta_z\Theta_m\rangle}{2\Omega^{*2}}(G^a_{zk}a_{km} - S^a_{pq}Z^a_{pqzm}) \\
&+ \gamma\left[S^v_{qk}r_{kq} - \frac{3}{8}S^v_{qq} + \frac{(4\phi-1)}{8}S^v_{qq}\frac{\langle\Theta_m\Theta_y\rangle}{\Omega^{*2}}a_{ym} + \frac{(7-12\phi)}{8}S^v_{jk}\frac{\langle\Theta_m\Theta_y\rangle}{\Omega^{*2}}Z^a_{ykmj}\right. \\
&\left. - S^v_{yz}\frac{\langle\Theta_z\Theta_m\rangle}{2\Omega^{*2}}a_{ym} + S^v_{sz}\frac{\langle\Theta_s\Theta_z\rangle}{4\Omega^{*2}} - \frac{S^v_{kq}}{8}a_{qk} - \gamma\frac{\langle\Theta_z\Theta_m\rangle}{\Omega^{*3}}(S^v_{qs}S^a_{tw}W_{sqtwmz} - S^v_{qs}G^a_{sw}Z^a_{wqmz})\right].
\end{aligned}
\tag{C.144}
$$

Endly, the following expressions are needed in order to bring the system of equations into a closed form

$$
\begin{aligned}
\langle\Theta_i\frac{d\Theta_z}{dt}\rangle &= \delta_{iz}G^a_{rl}[G^a_{kw}(G^a_{rk}a_{wl} - G^a_{pk}Z^a_{plwr}) - 2S^a_{sw}(G^a_{rk}Z^a_{lswk} - G^a_{pk}W_{plsrwk})] \\
&+ G^a_{pl}[G^a_{kw}(G^a_{ik}Z^a_{zlwp} - G^a_{pk}Z^a_{wizl}) - 2S^a_{sw}(G^a_{ik}W_{zlspwk} - G^a_{pk}W_{zlsiwk})] \\
&+ G^a_{zl}[G^a_{kw}(G^a_{rk}Z^a_{wirl} - G^a_{ik}a_{wl}) - 2S^a_{sw}(G^a_{rk}W_{rlsiwk} - G^a_{ik}Z^a_{slwk})] .
\end{aligned}
\tag{C.145}
$$

C.2.4 Derivation of the transport equation of the normalized Dimensionality tensor d_{ij}.

Next, we derive the transport equation for the normalized dimensionality tensor at the slow limit. We start from the differential of the normal vector, given by

$$
dN_i = -G^n_{ki}N_k dt\,. \tag{C.146}
$$

The transport equation of its normalized vector can be expressed as follow

$$
\frac{d}{dt}(\frac{N_i}{N}) = \frac{dn_i}{dt} = N_i\frac{d}{dt}(\frac{1}{N}) + \frac{1}{N}\frac{dN_i}{dt} = -\frac{N_i}{N^2}\frac{dN}{dt} + \frac{1}{N}\frac{dN_i}{dt}\,, \tag{C.147}
$$

while the transport equation of its magnitude is simply

$$\begin{aligned}\frac{dN}{dt} &= \frac{d(N_kN_k)^{1/2}}{dt} = \frac{1}{2}(N_kN_k)^{-1/2}\frac{d}{dt}(N_kN_k) = \frac{1}{2N}2N_k\frac{dN_k}{dt} \\ &= n_k\frac{dN_k}{dt} = n_k[-G^n_{qk}N_q] = -G^n_{qk}n_kN_q \\ \Rightarrow \frac{dN}{dt} &= -G^n_{qk}n_kN_q\,.\end{aligned} \tag{C.148}$$

Substituting eq. (C.148) in eq. (C.147) one finds

$$\begin{aligned}\frac{dn_i}{dt} &= -\frac{n_i}{N}\frac{dN}{dt} + \frac{1}{N}(-G^n_{ki}N_k) = -\frac{n_i}{N}(-G^n_{qk}n_kN_q) - G^n_{ki}n_k \\ \Rightarrow \frac{dn_i}{dt} &= -G^n_{ki}n_k + G^n_{qk}n_kn_qn_i\,.\end{aligned} \tag{C.149}$$

The differential of the vector Vn_i is

$$d(Vn_i) = (V+dV)(n_i+dn_i) - Vn_i = Vdn_i + n_idV + dVdn_i = dD_i\,. \tag{C.150}$$

Substituting the expressions for dV and dn_i in eq. (C.150) yields,

$$\begin{aligned}dD_i &= V[-G^n_{ki}n_k + G^n_{qk}n_kn_qn_i]dt + \frac{n_i}{2V}[-2G^v_{pk}V_pV_kdt - 2C_1V^2dt \\ &+ C_2^2V^2(dW_pdW_pn_sn_s - dW_sdW_qn_qn_s)] \\ &= G^n_{ki}D_kdt + G^n_{qk}n_kn_qD_idt - G^v_{pk}v_pv_kD_idt - C_1D_idt + \frac{C_2^2}{2}D_i(dW_pdW_p - dW_sdW_qn_qn_s)\,.\end{aligned} \tag{C.151}$$

Using eq. (C.151) one finds

$$\begin{aligned}d(D_iD_j) &= (D_i+dD_i)(D_j+dD_j) - D_iD_j = D_idD_j + D_jdD_i + dD_idD_j \\ &= -G^n_{ki}D_kD_jdt + 2G^n_{qk}n_kn_qD_iD_jdt - 2G^v_{pk}v_pv_kD_iD_jdt - 2C_1D_iD_jdt \\ &+ C_2^2D_iD_j(dW_pdW_p - dW_sdW_rn_sn_r) - G^n_{kj}D_kD_idt\,.\end{aligned} \tag{C.152}$$

Averaging over all particles yields,

$$\begin{aligned}
dD_{ij} &= -G^n_{ki}D_{kj}dt - G^n_{kj}D_{ki}dt + 2G^n_{qk}\langle D_iD_jn_kn_q\rangle dt - 2G^v_{pk}\langle v_pv_kD_iD_j\rangle dt \\
&- 2\langle C_1D_iD_j\rangle dt + \langle C_2^2D_iD_jdW_pdW_p\rangle - C_2^2\langle D_iD_jdW_sdW_rn_sn_r\rangle \\
dD_{ij} &= -G^n_{ki}D_{kj}dt - G^n_{kj}D_{ki}dt + 2G^n_{qk}\langle D_iD_jn_kn_q\rangle dt - 2G^v_{pk}\langle v_pv_kD_iD_j\rangle dt \\
&+ \langle D_iD_jdt(-2C_1 + 3C_2^2 - C_2^2)\rangle \\
\Rightarrow \frac{dD_{ij}}{dt} &= -G^n_{ki}D_{kj} - G^n_{kj}D_{ki} + 2G^n_{qk}\langle D_iD_jn_kn_q\rangle - 2G^v_{pk}\langle v_pv_kD_iD_j\rangle\,,
\end{aligned} \tag{C.153}$$

or

$$\frac{dD_{ij}}{dt} = -G^n_{ki}D_{kj} - G^n_{kj}D_{ki} + 2G^n_{qk}q^2Z^n_{ijkq} - 2G^v_{pk}M_{pkij}\,, \tag{C.154}$$

where the higher order tensors are defined as

$$Z^n_{ijkq} = \frac{\langle V^2n_in_jn_kn_q\rangle}{q^2}, \quad M_{pkij} = \langle V_pV_kn_in_j\rangle\,. \tag{C.155}$$

Now, the normalized energy-weighted tensor is given by

$$d_{ij} = \frac{D_{ij}}{D_{kk}}\,. \tag{C.156}$$

A useful identity is

$$\frac{dd_{ij}}{dt} = \frac{1}{q^2}\frac{dD_{ij}}{dt} - d_{ij}\frac{1}{q^2}\frac{dD_{kk}}{dt}\,. \tag{C.157}$$

Substituting eq. (C.154) in eq. (C.157) one obtains,

$$\frac{dd_{ij}}{dt} = -G^n_{ki}d_{kj} - G^n_{kj}d_{ki} + 2G^n_{qk}Z^n_{ijkq} - 2\frac{G^v_{pk}}{q^2}M_{pkij} + 2S^v_{qk}r_{kq}d_{ij}\,. \tag{C.158}$$

C.3 Derivation of M_{ijpq} using eddy effective rotation rate vector.

We start our analysis by introducing the conditioned form of this tensor, which can be decomposed in three components

$$\frac{M^{v|a}_{ijpq}}{q^2} = \frac{(1-\phi)}{8}\epsilon_{irt}\epsilon_{jzs}[(\delta_{rz}\delta_{pq} + \delta_{rp}\delta_{zq} + \delta_{rq}\delta_{zp}) - \delta_{rz}a_p a_q]a_t a_s\,, \tag{C.159a}$$

$$\frac{M^{j|a}_{ijpq}}{q^2} = \frac{\phi}{2}[\delta_{pq}a_i a_j - a_i a_j a_p a_q]\,, \tag{C.159b}$$

$$\frac{M^{h|a}_{ijpq}}{q^2} = \frac{\gamma}{8}\frac{\Omega^*_k}{\Omega^*}(\epsilon_{irt}a_t a_j + \epsilon_{jrt}a_t a_i)[(\delta_{rk}\delta_{pq} + \delta_{rp}\delta_{kq} + \delta_{rq}\delta_{kp}) - (\delta_{rk}a_p a_q + \delta_{rp}a_k a_q + \delta_{rq}a_k a_p)]\,, \tag{C.159c}$$

where v,j and h refer to the vortical, jettal and helical components respectively.
Compare to the original expression derived by Kassinos & Reynolds in TF61, in eq. (C.159) we have replaced the mean rotation vector Ω_i with the eddy effective rotation rate vector, in an attempt to incorporate additional structural information through a modified stropholysis term. A useful identity is given by

$$\epsilon_{irt}\epsilon_{jzs} = (\delta_{ij}\delta_{rz}\delta_{ts} + \delta_{iz}\delta_{rs}\delta_{tj} + \delta_{is}\delta_{rj}\delta_{tz}) - (\delta_{ij}\delta_{rs}\delta_{tz} + \delta_{iz}\delta_{rj}\delta_{ts} + \delta_{is}\delta_{rz}\delta_{tj})\,. \tag{C.160}$$

Applying eq. (C.160) into the vortical part of eq. (C.159) yields,

$$\begin{aligned}
\frac{M^{v|a}_{ijpq}}{V^2} &= \frac{(1-\phi)}{8}\delta_{ij}[(\delta_{zz}\delta_{pq}+\delta_{zp}\delta_{zq}+\delta_{zq}\delta_{zp}-\delta_{zz}a_pa_q)a_ta_t \\
&- (\delta_{sz}\delta_{pq}+\delta_{sp}\delta_{zq}+\delta_{sq}\delta_{zp}-\delta_{sz}a_pa_q)a_za_s] \\
&+ \frac{(1-\phi)}{8}[(\delta_{si}\delta_{pq}+\delta_{sp}\delta_{iq}+\delta_{sq}\delta_{ip}-\delta_{si}a_pa_q)a_ja_s-(\delta_{ji}\delta_{pq}+\delta_{jp}\delta_{iq}+\delta_{jq}\delta_{ip}-\delta_{ij}a_pa_q)a_sa_s] \\
&+ \frac{(1-\phi)}{8}[(\delta_{jz}\delta_{pq}+\delta_{jp}\delta_{zq}+\delta_{jq}\delta_{zp}-\delta_{jz}a_pa_q)a_za_i-(\delta_{zz}\delta_{pq}+\delta_{zp}\delta_{zq}+\delta_{zq}\delta_{zp}-\delta_{zz}a_pa_q)a_ia_j] \\
&= \frac{(1-\phi)}{8}\delta_{ij}[(3\delta_{pq}+\delta_{pq}+\delta_{pq}-3a_pa_q)-(\delta_{pq}a_za_z+a_pa_q+a_pa_q-a_za_za_pa_q)] \\
&+ \frac{(1-\phi)}{8}[a_j(a_i\delta_{pq}+a_p\delta_{iq}+a_q\delta_{ip}-a_ia_pa_q)-(\delta_{ij}\delta_{pq}+\delta_{jp}\delta_{iq}+\delta_{jq}\delta_{ip}-\delta_{ij}a_pa_q)] \\
&+ \frac{(1-\phi)}{8}[a_i(a_j\delta_{pq}+a_q\delta_{jp}+a_p\delta_{jq}-a_ja_pa_q)-a_ia_j(3\delta_{pq}+\delta_{pq}+\delta_{pq}-3a_pa_q)] \\
&= \frac{(1-\phi)}{8}\delta_{ij}[5\delta_{pq}-3a_pa_q-\delta_{pq}-a_pa_q] \\
&+ \frac{(1-\phi)}{8}[a_ia_j\delta_{pq}+\delta_{iq}a_pa_j+\delta_{ip}a_qa_j-a_ia_ja_pa_q-\delta_{ij}\delta_{pq}-\delta_{jp}\delta_{iq}-\delta_{jq}\delta_{ip}+\delta_{ij}a_pa_q] \\
&+ \frac{(1-\phi)}{8}[a_ia_j\delta_{pq}+\delta_{jp}a_ia_q+\delta_{jq}a_ia_p-a_ia_ja_pa_q-a_ia_j(5\delta_{pq}-3a_pa_q)]\,.
\end{aligned} \tag{C.161}$$

Averaging over all particles (carrying different a_i) one finds

$$\begin{aligned}
\frac{M^{v}_{ijpq}}{q^2} &= \frac{(1-\phi)}{2}\delta_{ij}(\delta_{pq}-a_{pq})+\frac{(1-\phi)}{8}[\delta_{pq}(a_{ij}-\delta_{ij})+(a_{pj}\delta_{iq}+a_{qj}\delta_{ip})-(\delta_{jp}\delta_{iq}+\delta_{jq}\delta_{ip}) \\
&+ \delta_{ij}a_{pq}-Z^a_{ijpq}]+\frac{(1-\phi)}{8}[a_{ij}\delta_{pq}+\delta_{jp}a_{iq}+\delta_{jq}a_{ip}-Z^a_{ijpq}-5\delta_{pq}a_{ij}+3Z^a_{pqij}] \\
&= \frac{(1-\phi)}{8}[4\delta_{ij}\delta_{pq}-4\delta_{ij}a_{pq}+\delta_{pq}a_{ij}-\delta_{pq}\delta_{ij}+a_{pj}\delta_{iq}+a_{qj}\delta_{ip}-\delta_{jp}\delta_{iq}-\delta_{jq}\delta_{ip}+\delta_{ij}a_{pq} \\
&- Z^a_{ijpq}+a_{ij}\delta_{pq}+\delta_{jp}a_{iq}+\delta_{jq}a_{ip}-Z^a_{ijpq}-5\delta_{pq}a_{ij}+3Z^a_{ijpq}] \\
&= \frac{(1-\phi)}{8}[3\delta_{ij}(\delta_{pq}-a_{pq})-3\delta_{pq}a_{ij}+Z^a_{ijpq}+(a_{pj}\delta_{iq}+a_{qj}\delta_{ip})+(\delta_{jp}a_{iq}+\delta_{qj}a_{ip}) \\
&- (\delta_{jp}\delta_{iq}+\delta_{qj}\delta_{ip})]\,.
\end{aligned} \tag{C.162}$$

Thus the final form of the vortical component of M_{ijpq} is given by

$$\begin{aligned}
\frac{M^{v}_{ijpq}}{q^2} &= \frac{(1-\phi)}{8}[3\delta_{ij}(\delta_{pq}-a_{pq})-3\delta_{pq}a_{ij}+Z^a_{ijpq}+(a_{pj}\delta_{iq}+a_{qj}\delta_{ip})+(\delta_{jp}a_{iq}+\delta_{qj}a_{ip}) \\
&- (\delta_{jp}\delta_{iq}+\delta_{qj}\delta_{ip})]\,.
\end{aligned} \tag{C.163}$$

Contracting eq. (C.163) by setting $p=q$ yields,

$$\frac{M^v_{ijpp}}{q^2} = \frac{(1-\phi)}{2}(\delta_{ij} - a_{ij}) = r_{ij}\,. \tag{C.164}$$

Also, the continuity condition is satisfied if we set $i = p$

$$\frac{M^v_{pjpq}}{q^2} = \frac{(1-\phi)}{8}[3\delta_{jq} - 3a_{jq} - 3a_{qj} + a_{jq} + a_{jq} + 3a_{qj} + a_{jq} + \delta_{jq} - \delta_{jq} - 3\delta_{jq}] = 0\,. \tag{C.165}$$

The jetal component is simply given by

$$\frac{M^j_{ijpq}}{q^2} = \frac{\phi}{2}(\delta_{pq}a_{ij} - Z^a_{ijpq})\,. \tag{C.166}$$

Next, we deal with the most complicated component, which is the helical part

$$\frac{M^h_{ijpq}}{q^2} = \frac{\gamma\Omega^*_k}{8\Omega^*}(\underbrace{\epsilon_{irt}a_t a_j}_{\text{part 1}} + \underbrace{\epsilon_{jrt}a_t a_i}_{\text{Part 2}})[(\delta_{rk}\delta_{pq} + \delta_{rp}\delta_{kq} + \delta_{rq}\delta_{kp}) - (\delta_{rk}a_p a_q + \delta_{rp}a_k a_q + \delta_{rq}a_k a_p)]\,. \tag{C.167}$$

The first part is treated as follow

$$\begin{aligned}
&\frac{M^{h|a}_{ijpq}}{q^2}|_{\text{Part 1}} = \frac{\gamma\Theta_k}{8\Omega^*}[\epsilon_{ikt}a_t a_j\delta_{pq} + \epsilon_{ipt}a_t a_j\delta_{kq} + \epsilon_{iqt}a_t a_j\delta_{kp} - \epsilon_{ikt}a_t a_j a_p a_q \\
&- \epsilon_{ipt}a_t a_j a_k a_q - \epsilon_{iqt}a_t a_j a_k a_p] \\
&= \frac{\gamma\epsilon_{krs}G^a_{rn}a_s a_n}{8\Omega^*}[\epsilon_{ikt}a_t a_j\delta_{pq} - \epsilon_{ikt}a_t a_j a_p a_q + \epsilon_{ipt}(\delta_{kq}a_t a_j - a_t a_j a_k a_q) \\
&+ \epsilon_{iqt}(a_t a_j\delta_{kp} - a_t a_j a_k a_p)] \\
&= \frac{\gamma}{8\Omega^*}[(\delta_{rt}\delta_{si} - \delta_{ri}\delta_{st})G^a_{rn}a_s a_n a_t a_j\delta_{pq} - (\delta_{rt}\delta_{si} - \delta_{ri}\delta_{st})G^a_{rn}a_s a_n a_t a_j a_p a_q \\
&+ \epsilon_{krs}G^a_{rn}a_s a_n\epsilon_{ipt}\delta_{kq}a_t a_j + \epsilon_{krs}G^a_{rn}a_s a_n\epsilon_{iqt}\delta_{kp}a_t a_j - \epsilon_{krs}G^a_{rn}a_s a_n\epsilon_{ipt}a_k a_q a_t a_j \\
&- \epsilon_{krs}G^a_{rn}a_s a_n\epsilon_{iqt}a_k a_p a_t a_j] \\
&= \frac{\gamma}{8\Omega^*}[G^a_{rn}a_i a_n a_r a_j\delta_{pq} - G^a_{in}a_t a_n a_t a_j\delta_{pq} - G^a_{rn}a_i a_n a_r a_j a_p a_q + G^a_{in}a_t a_n a_t a_j a_p a_q \\
&+ \epsilon_{qrs}G^a_{rn}a_s a_n\epsilon_{ipt}a_t a_j + \epsilon_{prs}G^a_{rn}a_s a_n\epsilon_{iqt}a_t a_j] \\
&\Rightarrow \frac{M^h_{ijpq}}{q^2}|_{\text{Part 1}} = \frac{\gamma}{8\Omega^*}[G^a_{rn}\delta_{pq}Z^a_{ijnr} - G^a_{in}\delta_{pq}a_{nj} - G^a_{rn}W_{ijpqnr} + G^a_{in}Z^a_{njpq} \\
&+ \epsilon_{qrs}\epsilon_{ipt}G^a_{rn}Z^a_{sntj} + \epsilon_{prs}\epsilon_{iqt}G^a_{rn}Z^a_{sntj}]\,.
\end{aligned} \tag{C.168}$$

Using eq. (C.160), we expand the term $\epsilon_{qrs}\epsilon_{ipt}G^a_{rn}Z_{sntj}$ to obtain

$$\begin{aligned}
&\epsilon_{qrs}\epsilon_{ipt}G^a_{rn}Z^a_{sntj} = [\delta_{qi}\delta_{rp}\delta_{st} + \delta_{qp}\delta_{rt}\delta_{si} + \delta_{qt}\delta_{ri}\delta_{sp} - \delta_{qi}\delta_{rt}\delta_{sp} - \delta_{qp}\delta_{ri}\delta_{st} - \delta_{qt}\delta_{rp}\delta_{si}]G^a_{rn}Z^a_{sntj} \\
&= G^a_{pn}Z^a_{tntj}\delta_{qi} + \delta_{qp}G^a_{tn}Z^a_{intj} + G^a_{in}Z^a_{pnqj} - G^a_{tn}Z^a_{pntj}\delta_{qi} - \delta_{pq}G^a_{in}Z^a_{snsj} - G^a_{pn}Z^a_{inqj} \\
&= G^a_{pn}a_{nj}\delta_{qi} + G^a_{rn}\delta_{pq}Z^a_{ijnr} + G^a_{in}Z^a_{pqnj} - G^a_{rn}Z^a_{pnrj}\delta_{qi} - \delta_{pq}G^a_{in}a_{nj} - G^a_{pn}Z^a_{inqj}\,.
\end{aligned} \tag{C.169}$$

Substituting eq. (C.169) back into eq. (C.168) yields,

$$\begin{aligned}
\frac{M^h_{ijpq}}{q^2}|_{\text{Part 1}} = \frac{\gamma}{8\Omega^*}&[3\delta_{pq}G^a_{rn}Z^a_{ijnr} - 3\delta_{pq}G^a_{in}a_{nj} + 3G^a_{in}Z^a_{pqnj} + G^a_{pn}(a_{nj}\delta_{qi} - Z^a_{njqi}) \\
&+ G^a_{qn}(a_{nj}\delta_{pi} - Z^a_{njip}) - G^a_{rn}(W_{ijpqnr} + Z^a_{qnrj}\delta_{pi} - G^a_{rn}Z^a_{pnrj}\delta_{qi})]\,.
\end{aligned} \tag{C.170}$$

The second part is treated similarly, leading to the final form for the helical part of the fourth moment

$$\begin{aligned}
\frac{M^h_{ijpq}}{q^2} = \frac{\gamma}{8\Omega^*}&[6\delta_{pq}G^a_{rn}Z^a_{ijnr} - 2G^a_{rn}W_{ijpqnr} - 3\delta_{pq}(G^a_{in}a_{nj} + G^a_{jn}a_{ni}) + 3(G^a_{in}Z^a_{pqnj} + G^a_{jn}Z^a_{pqni}) \\
&- G^a_{rn}(Z^a_{qnrj}\delta_{pi} + Z^a_{qnri}\delta_{pj}) + G^a_{pn}(a_{nj}\delta_{qi} + a_{ni}\delta_{qj}) - 2G^a_{pn}Z^a_{nqij} - 2G^a_{qn}Z^a_{ijnp} \\
&+ G^a_{qn}(a_{nj}\delta_{pi} + a_{ni}\delta_{pj} - G^a_{rn}(Z^a_{pnrj}\delta_{qi} + Z^a_{pnri}\delta_{qj})]\,.
\end{aligned} \tag{C.171}$$

Contracting eq. (C.171) by setting $p = q$ gives

$$\begin{aligned}
\frac{M^h_{ijpp}}{q^2} &= \frac{\gamma}{8\Omega^*}[G^a_{rn}Z^a_{ijnr}(18 - 2 - 2 - 2) + (G^a_{in}a_{nj} + G^a_{jn}a_{ni})[-9 + 1 + 3 + 1] - 4G^a_{pn}Z^a_{ijnp} \\
&= \frac{\gamma}{8\Omega^*}[8G^a_{pn}Z^a_{ijnp} - 4(G^a_{in}a_{nj} + G^a_{jn}a_{ni})] = \frac{\gamma}{2\Omega^*}[2G^a_{pn}Z^a_{ijnp} - (G^a_{in}a_{nj} + G^a_{jn}a_{ni})]\,.
\end{aligned} \tag{C.172}$$

which coincides with the stropholysis part of the Reynolds stress constitutive equation.

Appendix D

Details of the stability manipulation of the ASBM closure.

D.1 Blending method.

The idea behind the blending concept is to relate a fraction of the solution with a more stable algorithm, particularly that of an eddy viscosity model (EVM), and the remaining fraction with a less stable closure, such as ASBM. The fraction, expressed by a blending factor α, starts from zero (pure EVM) and progressively increases until it reaches unity (purely ASBM). O'Sullivan [94] already developed and successfully implemented a blending method for incompressible momentum equations. Here we derive suitable blending expressions for the momentum and energy transport equations, used in order to improve the robustness of the ASBM closure when low-compressibility flows cases are conisdered, such the ones described in Chapter 7. In order to derive the blended expressions, the Reynolds stress tensor is expressed as a sum of two distinct parts,

$$-\frac{\partial}{\partial x_j}(\overline{\rho u_i' u_j'}) = -\frac{\partial}{\partial x_j}[\alpha \overline{\rho u_i' u_j'}^{exact} + (1-\alpha)\overline{\rho u_i' u_j'}^{Bous}]\,. \tag{D.1}$$

Substituting eq. (D.1) into the incompressible mean momentum equations and applying the Boussineq approximation yields,

$$\frac{\partial(\overline{\rho}\bar{u}_i)}{\partial t} + \frac{\partial(\overline{\rho}\bar{u}_i\bar{u}_j)}{\partial x_j} + \frac{\partial}{\partial x_j}\{[\bar{p} + \frac{2\overline{\rho}\kappa}{3}(1-\alpha)]\delta_{ij}\} = -\alpha\frac{\partial\overline{\rho u_i' u_j'}}{\partial x_j} + \frac{\partial}{\partial x_j}\left\{\mu\frac{\partial\bar{u}_i}{\partial x_j} + (1-\alpha)\mu_T[\frac{\partial\bar{u}_i}{\partial x_j} + \frac{\partial\bar{u}_j}{\partial x_i}]\right\}. \tag{D.2}$$

Here this idea is extended in order to account for compressible flows. Accordingly, the mean momentum and energy equations are given by

$$\frac{\partial(\overline{\rho}\bar{u}_i)}{\partial t} + \frac{\partial}{\partial x_j}(\overline{\rho}\bar{u}_i\bar{u}_j) + \frac{\partial}{\partial x_j}[(\bar{p} + \frac{2}{3}\overline{\rho}\kappa)\delta_{ij}] = \frac{\partial}{\partial x_j}[\mu[\frac{\partial\bar{u}_i}{\partial x_j} + \frac{\partial\bar{u}_j}{\partial x_i} - \frac{2}{3}\mu\frac{\partial\bar{u}_k}{\partial x_k}\delta_{ij}] - \overline{\rho u_i' u_j'}], \tag{D.3a}$$

$$\frac{\partial(\overline{\rho}\bar{e})}{\partial t} + \frac{\partial}{\partial x_j}(\overline{\rho}\bar{u}_i(\bar{e} + \bar{p})\delta_{ij}) = \frac{\partial}{\partial x_i}\{\bar{u}_j(\mu[\frac{\partial\bar{u}_i}{\partial x_j} + \frac{\partial\bar{u}_j}{\partial x_i}] - \frac{2}{3}\mu\frac{\partial\bar{u}_k}{\partial x_k}\delta_{ij} - \overline{\rho u_i' u_j'}) + q_j^{tot}\delta_{ij}\}. \tag{D.3b}$$

Applying the Boussineq approximation yields,

$$\frac{\partial(\overline{\rho}\tilde{u}_i)}{\partial t} + \frac{\partial}{\partial x_j}(\overline{\rho}\tilde{u}_i\tilde{u}_j) + \frac{\partial}{\partial x_j}[(p + \frac{2}{3}\overline{\rho}\kappa)\delta_{ij}] = \frac{\partial}{\partial x_j}[(\mu + \mu_T)[\frac{\partial\tilde{u}_i}{\partial x_j} + \frac{\partial\tilde{u}_j}{\partial x_i} - \frac{2}{3}\mu\frac{\partial\tilde{u}_k}{\partial x_k}\delta_{ij}]], \tag{D.4a}$$

$$\frac{\partial(\overline{\rho}\tilde{e})}{\partial t} + \frac{\partial}{\partial x_j}(\overline{\rho}\tilde{u}_i(\tilde{e} + p)\delta_{ij}) = \frac{\partial}{\partial x_i}\{\tilde{u}_j[(\mu + \mu_T)[\frac{\partial\tilde{u}_i}{\partial x_j} + \frac{\partial\tilde{u}_j}{\partial x_i} - \frac{2}{3}\mu\frac{\partial\tilde{u}_k}{\partial x_k}\delta_{ij}] - \frac{2}{3}\overline{\rho}\kappa\delta_{ij}] + q_j^{tot}\delta_{ij}\}. \tag{D.4b}$$

Substituting eq. (D.1) into eqs. (D.4) and after a little bit of algebra yields the final blending expressions

$$\frac{\partial(\overline{\rho}\bar{u}_i)}{\partial t} + \frac{\partial(\overline{\rho}\bar{u}_i\bar{u}_j)}{\partial x_j} + \frac{\partial}{\partial x_j}\{[\bar{p} + \frac{2\overline{\rho}\kappa}{3}(1-\alpha)]\delta_{ij}\} = -\alpha\frac{\partial\overline{\rho u_i' u_j'}}{\partial x_j} + \frac{\partial}{\partial x_j}\left\{\mu[\frac{\partial\bar{u}_i}{\partial x_j} + \frac{\partial\bar{u}_j}{\partial x_i} - \frac{2}{3}\frac{\partial\bar{u}_k}{\partial x_k}\delta_{ij}] + (1-\alpha)\mu_T[\frac{\partial\bar{u}_i}{\partial x_j} + \frac{\partial\bar{u}_j}{\partial x_i}]\right\}, \tag{D.5}$$

and

$$\frac{\partial(\overline{\rho}\bar{e})}{\partial t} + \frac{\partial}{\partial x_j}(\overline{\rho}\bar{u}_i(\bar{e}+p)\delta_{ij}) = -\alpha\frac{\partial}{\partial x_i}[\bar{u}_j\overline{\rho u_i' u_j'}] + \frac{\partial}{\partial x_i}[\bar{u}_j\mu(\frac{\partial \bar{u}_i}{\partial x_j} + \frac{\partial \bar{u}_j}{\partial x_i} - \frac{2}{3}\mu\frac{\partial \bar{u}_k}{\partial x_k}\delta_{ij})$$
$$+ (1-\alpha)\bar{u}_j\mu_T(\frac{\partial \bar{u}_i}{\partial x_j} + \frac{\partial \bar{u}_j}{\partial x_i} - \frac{2}{3}\mu\frac{\partial \bar{u}_k}{\partial x_k}\delta_{ij}) + q_j^{tot}\delta_{ij}]\,. \tag{D.6}$$

Bibliography

[1] P. Spalart and S. Allmaras. A one-equation turbulence model for aerodynamic flows. *Recherche Aerospatiale*, 1:5–21, 1994.

[2] K. Kassinos and W. Reynolds. A structure-based model for the rapid distortion of homogeneous turbulence. PhD thesis, Thermosciences Division Department of Mechanical Engineering Stanford, California 94305, 1994.

[3] S. Kassinos, W. Reynolds, and M. Rogers. One-point turbulence structure tensors. *J. Fluid Mech.*, 428:213–248, 2001.

[4] S. Poroseva, S. Kassinos, C. Langer, and W. Reynolds. Structure-based turbulence model: Application to a rotating pipe flow. *Phys. Fluids*, 14:1523–1532, 2002.

[5] C. Langer and W. Reynolds. A new algebraic structure-based turbulence model for rotating wall-bounded flows. PhD thesis, Thermosciences Division Department of Mechanical Engineering Stanford, California 94305, 2003.

[6] S. Kassinos, C. Langer, G. Kalitzin, and G. Iaccarino. A simplified structure-based model using standard turbulence scale equations: Computation of rotating wall-bounded flows. *Int. J. Heat Fluid*, 27:653–660, 2006.

[7] W. Reynolds, C. Langer, and S. Kassinos. Structure and scales in turbulence modeling. *Phys. Fluids*, 14(7):2485–2492, 2002.

[8] G. Kalitzin, G. Iacarrino, C. Langer, and S. Kassinos. Combining eddy-viscosity models and the algebraic structure-based Reynolds stress closure. pages 171–182. Annual Research Briefs, Center for Turbulence Research, 2004.

[9] J. Benton. Evaluation of v^2-f and ASBM turbulence models for transonic aerofoil RAE2822. pages 439–450. Progress in Wall Turbulence: Understanding and modeling, ERCOFTAC Series, 2011.

[10] B. Aupoix, K. Kassinos, and C. Langer. ASBM-BSL: An easy access to the structure based model technology. In *Sixth International Symposium on Turbulence and Shear Flow Phenomena, Seoul-Korea, June 22-24*, 2009.

[11] A. Kolmogorov. The local structure of turbulence in incompressible viscous fluid for very large Reynolds numbers. *Dokl. Akad. Nauk SSSR*, 30:301–305, 1941.

[12] A. Obukhov. Structure of the temperature field in a turbulent current. *Izv. Akad. Nauk SSSR Ser. Geogr. Geofiz*, 13:58–69, 1949.

[13] S Corrsin. On the spectrum of isotropic temperature fluctuations in an isotropic turbulence. *J. Appl. Phys.*, 22:469–473, 1951.

[14] L. Danaila, R. Antonia, and P. Burattini. Comparison between kinetic energy and passive scalar energy transfer in locally homogeneous isotropic turbulence. *Physica D*, 241:224–231, 2012.

[15] B. Ma and Z. Warhaft. Some aspects of the thermal mixing layer in grid turbulence. *Phys. Fluids*, 29:3114–3120, 1986.

[16] J. Chasnov. Similarity states of passive scalar transport in isotropic turbulence. *Phys. Fluids*, 6(2):1036–1051, February 1994.

[17] K. Sreenivasan. On local isotropy of passive scalars in turbulent shear flows. *Proc. R. Soc. London.*, Ser. A434:165–182, 1991.

[18] Z. Warhaft and J. Lumley. An experimental study of the decay of temperature fluctuations in grid-generated turbuience. *J. Fluid Mech.*, 88:659, 1978.

[19] Z. Warhaft. Passive scalars in turbulent flows. *Annu. Rev. Fluid Mech.*, 32:203–240, 2000.

[20] A. Johansson and P. Wikstrom. DNS and modeling of passive scalar transport in turbulent channel flow with a focus on scalar dissipation rate modeling. *Flow Turbul. Combust.*, 63:223–245, 2000.

[21] A. Yoshizawa. Statistical modeling of passive-scalar diffusion in turbulent shear flows. *J. Fluid Mech.*, 195:541–555, 1988.

[22] S. Kassinos and W. Reynolds. An extended structured-based model based on a stochastic eddy-axis evolution equation. pages 133–148. Annual Research Briefs, Center for Turbulence Research, 1995.

[23] L. Arnold. *Stochastic differential equations.* John Wiley & Sons.

[24] S. Kassinos and W. Reynolds. A particle representation model for the deformation of homogeneous turbulence. pages 31–51. Annual Research Briefs, Center for Turbulence Research, 1996.

[25] O. Reynolds. On the dynamical theory of incompressible viscous fluids and the determination of the criterion. *Philos. Trans. R. Soc. Lond. A*, 186:123–164, 1895.

[26] W. Reynolds and A. Hussain. The mechanics of an organized wave in turbulent shear flow. Part 3: Theoretical models and comparisons with experiments. *J. Fluid Mech.*, 54 (263), 1972.

[27] A. Kolmogorov. Equations of turbulent motion of an incompressible fluid. *Izv. Akad. Nauk SSSR*, 1/2:56, 1942.

[28] P.G. Saffman. A model for inhomogeneous turbulent flow. *Proc. Roy. Soc. London*, A317:417–433, February 1970.

[29] D Wilcox. Reassessment of the scale determining equation for advanced turbulence models. *AIAA J.*, 26(11):1299–1310, 1988.

[30] D. Wilcox. *Turbulence modeling for CFD.* 2nd edition, DCW Industries, Inc., La Canada CA, 1998.

[31] F. Menter. Two-equation eddy-viscosity turbulence models for engineering applications. *AIAA J.*, 32(8):1598–1605, 1994.

[32] S. Kassinos, C. Langer, S. Haire, and W. Reynolds. Structure-based turbulence modeling for wall-bounded flows. *Int. J. Heat Fluid*, 21:599–605, 2000.

[33] W. Reynolds and S. Kassinos. One-point modeling of rapidly deformed homogeneous turbulence. *Proc. R. Soc. London*, Ser. A 451:87, 1995.

[34] F. Stylianou, R. Pecnik., and S. Kassinos. A general framework for computing the turbulence structure tensors. *Comput. Fluids*, 106:54–66, 2015.

[35] J. Mahoney. Tensor and isotropic tensor identities. *The Matrix and Tensor Quarterly*, 34(5)1:85–91, 1985.

[36] S. Kassinos and E. Akylas. Advances in particle representation modeling of homogeneous turbulence. From the linear PRM version to the interacting viscoelastic IPRM. *New approaches in modeling multiphase flows and dispersion in turbulence, fractal methods and synthetic turbulence ERCOFTAC*, 18:81–101, 2012.

[37] J. Lumley and G. Newman. The return to isotropy of homogeneous turbulence. *J. Fluid Mech.*, 82:161–178, 1977.

[38] J. Lumley and K. Choi. The return to isotropy of homogeneous turbulence. *J. Fluid Mech.*, 436:59–84, 2001.

[39] W. Rodi. A new algebraic relation for calculating the Reynolds stress. *Z. Angew. Math. Mech.*, 56(T219-221), 1976.

[40] S. Haire and W. Reynolds. Toward an affordable two-equation structure-based turbulence model. Technical report TF-84, Thermosciences Division Department of Mechanical Engineering Stanford University, California 94305., 2003.

[41] C. Tong and Z. Warhaft. On passive scalar derivative statistics in grid turbulence. *Phys. Fluids*, 6:2165–2176, 1994.

[42] K. Sreenivasan, R. Antonia, and H. Danh. Temperature dissipation fluctuations in a turbulent boundary layer. *Phys. Fluids*, (20):1238–1249, 1977.

[43] R. Stewart. Turbulence and waves in stratified atmosphere. *Radio Sci.*, 4:1269–1278, 1969.

[44] K. Sreenivasan and S. Tavoularis. On the skewness of the temperature derivative in turbulent flows. *J. Fluid Mech.*, (101):783–795, 1980.

[45] P. Mestayer. Local isotropy and isotropy in a high-Reynolds-number turbulent boundary layer. *J. Fluid Mech.*, (125):475–503, 1982.

[46] G. Brethouwer. The effect of rotation on rapidly sheared homogeneous turbulence and passive scalar transport. Linear theory and direct numerical simulation. *J. Fluid Mech.*, 542:305, 2005.

[47] S. Kassinos, B. Knaepen, and D. Carati. The transport of a passive scalar in magnetohydrodynamic turbulence subjected to mean shear and frame rotation. *Phys. Fluids*, 19: 015105, 2007.

[48] B. Shraiman and E. Sigga. Scalar turbulence. *Nature.*, 405:639–646, 2000.

[49] C. Panagiotou and S. Kassinos. The ASBM-SA turbulence closure: Taking advantage of structure-based modeling in current engineering CFD codes. *Int. J. Heat Fluid Fl.*, 52: 111–128, 2015.

[50] W. Reynolds, S. Kassinos, C. Langer, and S. Haire. New directions in turbulence modeling. Third International Symposium on Turbulence, Heat, and Mass Transfer, 2000.

[51] L. Richardson. Weather prediction by numerical process. In *Cambridge: Cambridge University Press*, 1922.

[52] K. Sreenivasan. The passive scalar spectrum and the Obukhov-Corrsin constant. *Phys.Fluids*, 8:189–196, 1996.

[53] H. Kolla, J. Rogerson, N. Chakraborty, and N. Swaminathan. Scalar dissipation rate modeling and its validation. *Combust. Sci. Technol.*, 181(3):518–535, 2009.

[54] M. Lesieur and J. Herring. Diffusion of a passive scalar in two-dimensional turbulence. *J. Fluid Mech.*, 61:77–95, May 1985.

[55] M. Rogers, N. Mansour, and W. Reynolds. An algebraic model for the turbulent flux of a passive scalar. *J. Fluid Mech.*, 203:77–101, June 1989.

[56] Y. Younis, C. Speziale, and T. Clark. A rational model for the turbulent scalar fluxes. *Proc. R. Soc. A*, 461:575–594, 2005.

[57] A. Gylfason and Z. Warhaft. Effects of axisymmetric strain on a passive scalar field: modeling and experiment. *J. Fluid Mech.*, 628:339–356, 2009.

[58] M. Lee and W. Reynolds. Numerical experiments on the structure of homogeneous turbulence. PhD thesis, Thermosciences Division Department of Mechanical Engineering Stanford, California 9430, 1985.

[59] M. Rahman, T. Siikonen, and R. Agarwal. Improved low Re-number one-equation turbulence model. *AIAA J.*, 49(4):735–747, 2011.

[60] H. Dryden. Recent advances in the mechanics of boundary layer flow. In ed. R. V. Mises and T. V. Karman, editors, *Adv. Appl. Mech. Vol. 1*, pages 1–40, 1946.

[61] P. Bradshaw, D. Ferriss, and N. Atwell. Calculation of boundary layer development using the turbulent energy equation. *J. Fluid Mech.*, 28(3):593–616, 1967.

[62] E. Fares and W. Schroder. A general one-equation turbulence model for free shear and wall-bounded flows. *Flow Turbul. Combust.*, 73:187–215, 2005.

[63] Y. Nagano, C. Pei, and H. Hattori. A new low-Reynolds number one-equation model of turbulence. *Flow Turbul. Combust.*, 63:135–151, 2000.

[64] V. Patel, W. Rodi, and G. Scheuerer. Turbulence models for near-wall and low Reynolds number flow: A review. *AIAA J.*, 23(9):1308–1319, 1985.

[65] F. Lien, G. Kalitzin, and P. Durbin. RANS modeling for compressible and transitional flows. pages 267–286. Annual Research Briefs, Center for Turbulence Research, 1998.

[66] F. Ham, K. Mattson, and G. Iaccarino. Accurate and stable finite volume operators for unstructured flow solvers. pages 243–261. Annual Research Briefs, Center for Turbulence Research, 2006.

[67] J. Alamo and J. Jimenez. Spectra of very large anisotropic scales in turbulent channels. *Phys. Fluids*, 15, 2003.

[68] S. Hoyas and J. Jimenez. Scaling of the velocity fluctuations in turbulent channels up to Re_τ=2003. *Phys. Fluids*, 18:011702, 2006.

[69] J. Loureiro, F. Pinho, and F. Silva. Near wall characterization of the flow over a two-dimensional steep smooth hill. *Exp. Fluids*, 42(3):441–457, 2007.

[70] S. Jovic and D. Driver. Reynolds number effects on the skin friction in separated flows behind a backward facing step. *Exp. Fluids*, 18:464–467, 1995.

[71] H. Le, P. Moin, and J. Kim. Direct numerical simulation of turbulent flow over a backward-facing step. *J. Fluid Mech.*, 330:349–374, 1997.

[72] C. Buice and J. Eaton. Experimental investigation of flow through an asymmetric plane diffuser. *J. Fluids Eng.*, 122:433–435, 2000.

[73] H. Kaltenbach, M. Fatica, R. Mittal, T. Lund, and P. Moin. Study of flow in a planar asymmetric diffuser using large-eddy simulation. *J. Fluid Mech.*, 390:151–185, 1999.

[74] T. DalBello, V. Dippold, and N. Georgiadis. Computational study of separating flow in a planar subsonic diffuser. Tech. Mem. 213894, NASA, 2005.

[75] URL `http://ucy-compsci.org/index.php?link=US-ASBM.html`.

[76] C. Rumsey, T. Gatski, L. Sellers, V. Vatsa, and S. Viken. Summary of the 2004 CFD validation workshop on synthetic jets and turbulent separation control. *In AIAA 2004-2217*, 2004.

[77] D. Greenblatt, K. Paschal, N. Schaeffler, A. Washburn, J. Harris, and C. Yao. A separation control CFD validation test case. Part 1: Baseline and steady suction. *AIAA Paper*, pages 2004–2220, 2004.

[78] A. Seifert and L. Pack. Active flow separation control on wall-mounted hump at high Reynolds numbers. *AIAA J.*, 40(7):1363–1372, 2002.

[79] T. Gatski and C. Rumsey. Langley Research Center Workshop: CFD validation of synthetic jets and turbulent separation control., (Cited 24 December 2014) . URL `http://cfdval2004.larc.nasa.gov/case3grids`.

[80] X. Albets-Chico, S. Kassinos, H. Radhakrishnan, and B Knaepen. Numerical simulation of a liquid-metal flow in a poorly conducting pipe subjected to a strong fringing magnetic field. *Phys. Fluids*, 23:047101, 2011.

[81] M. Rahman, R. Agarwal, M. Lampinen, and T. Siikonen. Improvements to Rahman-Agarwal-Siikonen one-equation turbulence model based on κ-ϵ closure. In *7th AIAA Theoretical Fluid Mechanics Conference, Atlanta, GA*, 2014.

[82] B. Baldwin and T. Barth. One-equation turbulence transport model for separated turbulent flows. *AIAA Paper*, pages 91–0610, 1991.

[83] K. Nadarajah. The discrete adjoint approach to aerodynamic shape optimization. PhD Thesis, Department of Aeronautics and Astronautics Stanford, California 94305, 2003.

[84] W. McCroskey, K. McAlister, L. Carr, and S. Pucci. An experimental study of dynamic stall on advanced airfoil sections. Tech. Memo. 84245, NASA, 1982.

[85] N. Eastman and A. Sherman. Airfoil section characteristics as affected by variations of the Reynolds number. Tech. Mem. 586, NASA, 1939.

[86] M. Moulton and M. Smith. The prediction and validation of static and dynamic stall. Presented in Heli Japan, Saitama - Japan, November 1-3, 2010.

[87] C. Consul. Hydrodynamic analysis of a tidal cross-flow turbine. PhD thesis, University of Oxford, 2011.

[88] D. Sharpe. *Wind turbine aerodynamics.* In Wind Energy Conversion Systems, Prentice Hall, 1990.

[89] R. Green and M. Giuni. Dynamic stall database. Tech. Memo. 1570-AM-01, Aerospace Sciences Division, School of Engineering, University of Glasgow, 2013.

[90] G. Batchelor and I. Proudman. The large-scale structure of homogeneous turbulence. *Philos. Trans. R. Soc. London*, 248(949):369–405, January 1956.

[91] P. Saffman. The large-scale structure of homogeneous turbulence. *J. Fluid Mech.*, 27: 581–593, February 1967.

[92] S. Kassinos and W. Reynolds. Structure-based modeling for homogeneous MHD turbulence. pages 301–315. Annual Research Briefs, Center for Turbulence Research, 1999.

[93] S. Kassinos, B. Knaepen, and D. Carati. MHD turbulence in the presence of a strong magnetic field. pages 191–201. Annual Research Briefs, Center for Turbulence Research, 2002.

[94] J. O'Sullivan, R. Pecnik, and G. Iaccarino. Investigating turbulence in wind flow over complex terrain. pages 129–139. In Proceedings of the Summer Program, Center for Turbulence Research, 2010.